UNCLASSIFIED

AD NUMBER

AD859194

NEW LIMITATION CHANGE

TO

Approved for public release, distribution unlimited

FROM

Distribution authorized to U.S. Gov't. agencies and their contractors; Critical Technology; JUL 1969. Other requests shall be referred to Air Force Weapons Laboratory, Attn: WLDC, Kirtland AFB, NM 87117.

AUTHORITY

AFWL ltr dtd 30 Nov 1971

THIS PAGE IS UNCLASSIFIED

AD-859194

AFWL-TR-
68-153

PHOTOELASTIC STUDY OF WAVE PROPAGATION IN LAYERED MEDIA

I. M. Daniel

IIT RESEARCH INSTITUTE
Technology Center
Chicago, Illinois 60616

Contract F29601-67-C-0079

TECHNICAL REPORT NO. AFWL-TR-68-153

July 1969

AIR FORCE WEAPONS LABORATORY
Air Force Systems Command
Kirtland Air Force Base
New Mexico

20070924040

This document is subject to special export controls and each transmittal to foreign governments or foreign nationals may be made only with prior approval of AFWL (WLDC), Kirtland AFB, NM, 87117.

AIR FORCE WEAPONS LABORATORY
Air Force Systems Command
Kirtland Air Force Base
New Mexico

When U. S. Government drawings, specifications, or other data are used for any purpose other than a definitely related Government procurement operation, the Government thereby incurs no responsibility nor any obligation whatsoever, and the fact that the Government may have formulated, furnished, or in any way supplied the said drawings, specifications, or other data, is not to be regarded by implication or otherwise, as in any manner licensing the holder or any other person or corporation, or conveying any rights or permission to manufacture, use, or sell any patented invention that may in any way be related thereto.

This report is made available for study with the understanding that proprietary interests in and relating thereto will not be impaired. In case of apparent conflict or any other questions between the Government's rights and those of others, notify the Judge Advocate, Air Force Systems Command, Andrews Air Force Base, Washington, D. C. 20331.

DO NOT RETURN THIS COPY. RETAIN OR DESTROY

PHOTOELASTIC STUDY OF WAVE PROPAGATION IN LAYERED MEDIA

I. M. DANIEL

IIT RESEARCH INSTITUTE
Technology Center
Chicago, Illinois 60616
Contract F29601-67-C-0079

TECHNICAL REPORT NO. AFWL-TR-68-153

This document is subject to special export controls and each transmittal to foreign governments or foreign nationals may be made only with prior approval of AFWL (WLDC), Kirtland AFB, New Mexico 87117.

FOREWORD

This report was prepared by the IIT Research Institute, Chicago, Illinois, under Contract F29601-67-C-0079. The research was performed under Program Element 61102H, Project 5710, Subtask SB144, and was funded by the Defense Atomic Support Agency (DASA).

Inclusive dates of research were 31 May 1967 to 30 September 1968. The report was submitted 20 May 1969 by the Air Force Weapons Laboratory Project Officer, Dr. Henry F. Cooper, Jr. (WLDC).

Dr. I. M. Daniel of IIT Research Institute was the project leader. Additional IITRI personnel who made contributions to the work reported herein include Drs. F. J. Ahimaz, J.E. Kennedy, R.E. Rowlands and Messrs. J. Devery, R.P. Joyce, R.H. Marloff, C. Mayhew, T. Niiro and J. Staulcup. Professors W.F. Riley and R.L. Marino of Iowa State University and Valparaiso University, respectively, acted as consultants. Professor R.L. Marino contributed to Sections III and IV of this report.

Information in this report is embargoed under the U.S. Export Control Act of 1949, administered by the Department of Commerce. This report may be released by departments or agencies of the U.S. Government to departments or agencies of foreign governments with which the United States has defense treaty commitments, subject to approval of AFWL (WLDC), Kirtland AFB, New Mexico 87117.

Contractor's report number is IITRI Research Project No. D6038.

This technical report has been reviewed and is approved.

HENRY F. COOPER
Project Officer

CLIFF M. WHITEHEAD
Colonel, USAF
Chief, Civil Engineering Branch

for GEORGE C. DARBY, JR.
Colonel, USAF
Chief, Development Division

ABSTRACT

(Distribution Limitation Statement No. 2)

This program studies photoelastically the transmitted, reflected and refracted waves resulting when a wave generated by explosive or air-shock loading reaches the plane interface between two birefringent materials of different impedances. Dynamic photoelastic and photoviscoelastic methods complemented by moiré techniques were used. A special explosive loading system using PETN (Pentaerythritol Tetranitrate) was developed. A shock tube was used for air-shock loading. The photoelastic and moiré fringe patterns in the explosively loaded models were photographed with a Cranz-Schardin multiple spark camera operating at a rate of 200,000 frames per second. A Fastax camera was used in recording similar patterns in the air-shock loaded models. A class of birefringent model materials with controllable impedance was developed. All models consisted of two layers of birefringent materials having an impedance ratio of 2:1. The models were loaded by a buried explosive source in the low-impedance medium, a buried explosive source in the high-impedance medium. The distance of the point of loading from the interface was varied. Propagation and attenuation characteristics of incident, reflected and refracted waves were studied. The formation of headwaves at the interface was clearly evident in one case. Stress determinations were made in some instances using photoelastic and moiré data.

This page intentionally left blank.

CONTENTS

Section		Page
I	INTRODUCTION	1
II	WAVE PROPAGATION IN LAYERED MEDIA	3
	1. Reflection and Refraction of Plane Waves at an Interface	3
	2. Wave Propagation in Two Semi-Infinite Media for Point Source Loading	8
III	EXPERIMENTAL METHODS	13
	1. Dynamic Photoelasticity and Photoviscoelasticity	13
	2. Moiré Method	16
	3. Methods of Loading	18
	a. Buried Source Explosive Loading	18
	b. Air Shock Loading	22
	4. Cranz-Schardin Multiple Spark Camera	23
	a. General	23
	b. Spark Gap Bank	25
	c. Optical System	26
	d. Control Circuits	28
IV	DEVELOPMENT OF MODEL MATERIALS	31
	1. Preliminary Investigations	31
	2. Materials for Explosive Loading Experiments	31
	3. Materials for Air Shock Loading Experiments	52
V	PROPERTIES OF MODEL MATERIALS	56
	1. Introduction	56
	2. Dynamic Properties of Columbia Resin (CR-39)	56

CONTENTS (Cont'd.)

Section		Page
V	3. Properties of DER 50/40	59
	4. Properties of DER 73/27 and DER 85/15	70
VI	WAVE PROPAGATION IN LAYERED MODEL DUE TO AIR-BLAST LOADING ON ONE EDGE	78
	1. Introduction	78
	2. Experimental Procedure	78
	3. Results and Discussion	80
VII	WAVE PROPAGATION IN LAYERED MODEL DUE TO EXPLOSIVE LOADING IN LOW-IMPEDANCE MEDIUM	100
	1. Introduction	100
	2. Experimental Procedure	100
	3. Results and Discussion	102
VIII	WAVE PROPAGATION IN LAYERED MODEL DUE TO EXPLOSIVE LOADING IN HIGH-IMPEDANCE MEDIUM	143
	1. Introduction	143
	2. Experimantal Procedure	143
	3. Results and Discussion	143
IX	SUMMARY, CONCLUSIONS AND RECOMMENDATIONS FOR FUTURE WORK	172
	REFERENCES	180

ILLUSTRATIONS

Figure		Page
1	Reflection and Refraction of a Dilatational (P) Wave at an Interface Between Two Elastic Media	5
2	Path of "Refraction Arrival" ($\alpha_2 > \alpha_1$)	9
3	Complete Set of Waves Generated in Two Elastic Media by a Point Source of Dilatational Waves in Low-Impedance Medium ($\alpha_2 > \beta_2 > \alpha_1 > \beta_1$; After Cagniard) (Ref. 8)	11
4	Optical Indication of Impact Pressure Pulse of PETN	19
5	Isochromatic Fringe Patterns in Columbia Resin (CR-39) Plate under PETN Explosive Loading at Center (Camera Speed: 200,000 Frames/Second)	20
6	Pressure-Time Record in Shock Tube at Model Location	24
7	Lite-Mike Record Showing Time of Firing of Individual Sparks	30
8	Isochromatic Fringe Patterns in Columbia Resin (CR-39) Under Explosive Loading (Camera Speed: 193,000 Frames/Second)	33
9	Wave Propagation in Columbia Resin (CR-39) Plate as a Function of Fringe Order	34
10	Wave Propagation in CR-39 Bar as a Function of Fringe Order	35
11	Isochromatic Fringe Patterns in Plexiglas Under Explosive Loading (Camera Speed: 193,000 Frames/Second)	37
12	Isochromatic Fringe Patterns in Homalite-100 Plate Under Explosive Loading (Camera Speed: 193,000 Frames/Second)	38
13	Isochromatic Fringe Patterns in Laminac Exp. 126-3 Plate Under Explosive Loading (Camera Speed: 193,000 Frames/Second)	39
14	Isochromatic Fringe Patterns in Cellulose Acetate Butyrate Under Explosive Loading (Camera Speed: 193,000 Frames/Second)	40
15	Isochromatic Fringe Patterns in Epoxy Resin (60 Percent DER 732 and 40 Percent DER 331) Plate Under Explosive Loading (Camera Speed: 193,000 Frames/Second)	41
16	Isochromatic Fringe Patterns in Epoxy Resin (70 Percent DER 732, 30 Percent DER 331) Plate Under Explosive Loading (Camera Speed: 193,000 Frames/Second)	42

ILLUSTRATIONS (Cont'd.)

Figure		Page
17	Wave Propagation in Plexiglas Plate as a Function of Fringe Order	43
18	Wave Propagation in Homalite-100 Plate as a Function of Fringe Order	44
19	Wave Propagation in Laminac Plate as a Function of Fringe Order	45
20	Wave Propagation in Cellulose Acetate Butyrate Plate as a Function of Fringe Order	46
21	Wave Propagation in PSM-1 Plate as a Function of Fringe Order	47
22	Wave Propagation in DER 50/50 Plate as a Function of Fringe Order	48
23	Wave Propagation in DER 60/40 Plate as a Function of Fringe Order	49
24	Wave Propagation in DER 70/30 Plate as a Function of Fringe Order	50
25	Wave Propagation Velocity as a Function of Fringe Order for Three Candidate Model Materials for Air Shock Loading Experiments	55
26	Young's Modulus and Stress Fringe Value of CR-39 as Functions of Time (Based on Results by Clark) (Ref. 12)	57
27	Uniaxial Tensile Specimen used for Creep Tests at Various Temperatures	60
28	Young's Relaxation Modulus as a Function of Time at Various Temperatures for DER 60/40	61
29	Individual and Composite Curves for Relaxation Modulus of DER 60/40	62
30	Simple-Shear Specimen used for Creep Tests at Various Temperatures	64
31	Shear Relaxation Modulus as a Function of Time at Various Temperatures for DER 60/40	66
32	Stress Fringe Value as a Function of Time at Various Temperatures for DER 60/40	67

ILLUSTRATIONS (Cont'd.)

Figure		Page
33	Individual and Composite Curves for Stress Fringe Value of DER 60/40	68
34	Temperature-Time Shift Function for Relaxation Modulus and Stress Fringe Value for DER 60/40	71
35	Young's and Shear Relaxation Moduli, Stress Fringe Value and Poisson's Ratio as Functions of Time for DER 60/40	72
36	Stress Fringe Value as a Function of Time at Various Temperatures for DER 73/27	73
37	Stress Fringe Value as a Function of Time at Various Temperatures for DER 85/15	74
38	Individual and Composite Curves for Stress Fringe Value of DER 73/27	75
39	Individual and Composite Curves for Stress Fringe Value of DER 85/15	76
40	Sketch of Model Subjected to Air Blast Loading on the Edge (Phase I)	79
41	Series of 30 Consecutive Photographs Showing Transient Isochromatic Fringe Patterns in Layered Model I-1 (Camera Speed: 7700 Frames/Second)	81
42	Series of 30 Consecutive Photographs Showing Transient Isochromatic Fringe Patterns in Layered Model I-2 (Camera Speed: 7700 Frames/Second)	82
43	Series of 30 Consecutive Photographs Showing Transient Isochromatic Fringe Patterns in Layered Model I-3 (Camera Speed: 8100 Frames/Second)	83
44	Series of 30 Consecutive Photographs Showing Transient Isochromatic Fringe Patterns in Layered Model I-5 (Camera Speed: 7500 Frames/Second)	84
45	Series of 12 Consecutive Photographs Showing Transient Moiré Fringe Patterns in Layered Model I-5 (Camera Speed: 7500 Frames/Second)	85
46	Fringe Position as a Function of Time in Model I-1	87
47	Wave Propagation Velocity in Two Layers of Model I-1 as a Function of Fringe Order	88

ILLUSTRATIONS (Cont'd.)

Figure		Page
48	Fringe Position as a Function of Time in Model I-2	90
49	Wave Propagation Velocity in Two Layers of Model I-2 as a Function of Fringe Order	91
50	Fringe Position as a Function of Time in Model I-3	92
51	Wave Propagation Velocity in Two Layers of Model I-3 as a Function of Fringe Order	93
52	Angle of Fringe Inclination in Model I-3 as a Function of Time	94
53	Fringe Position as a Function of Time in Model I-5	96
54	Wave Propagation Velocity in Two Layers of Model I-5 as a Function of Fringe Order	97
55	Angle of Fringe Inclination in Model I-5 as a Function of Time	98
56	Sketch of Model Showing Dimensions and Location of Explosive Loading Source in Low-Impedance Medium (Phase II)	101
57	Isochromatic Fringe Patterns in Model II-1D (Explosive Source in Low-Impedance Medium 1 in. from Interface; Impedance Ratio 2.40:1; Camera Speed 187,000 Frames/Second	103
58	Velocity of Wave Propagation as a Function of Fringe Order in Two Media of Model II-1D	104
59	Fringe Order as a Function of Position with Time as a Parameter for Incident Wave P_1 in Low-Impedance Medium of Model II-1D	106
60	Fringe Order as a Function of Position with Time as a Parameter, for Refracted Wave P_1P_2 in High-Impedance Medium of Model II-1D	107
61	Fringe Order as a Function of Position with Time as a Parameter for Refracted Waves in High-Impedance Medium Along Interface (Model II-1D; Frame Nos. are Marked)	109
62	Fringe Order as a Function of Position with Time as a Parameter in Low-Impedance Medium Along Interface (Model II-1D; Frame Nos. are Marked)	110
63	Wave Propagation in Time Period $h/\alpha_1 \leq t \leq h/\alpha_1 \cos \theta_{CR}$ or 29 μ sec $< t <$ 34 μ sec for Model II-1D	113

ILLUSTRATIONS (Cont'd.)

Figure		Page
64	Wave Propagation in Time Period $h/\alpha_1 \cos \theta_{CR} < t < h/\alpha_1 \cos \phi_{CR}$ or 34 μ sec < t < 42 μ sec	115
65	Detail of Frame 6 (t = 57 μ sec) Showing Two Headwaves	116
66	Detail of Frame 12 (t = 86 μ sec) Showing Three Headwaves	117
67	Detail of Frame 16 (t = 109 μ sec) Showing Three Headwaves	118
68	Variation of Fringe Order with Time in High-Impedance Medium for Model II-1D	120
69	Radial (Vertical) Displacements in High-Impedance Medium as a Function of Distance from Interface with Time as a Parameter for Specimen II-1D (Frame Nos. are Marked on the Curves)	122
70	Principal Stresses in High-Impedance Medium as a Function of Distance from Interface with Time as a Parameter for Specimen II-1D (Frame Nos. are Marked on the Curves; Results Obtained from Photoelastic Data)	123
71	Moiré Fringe Patterns for Horizontal Displacements in Model II-1F (Explosive Source in Low-Impedance Medium 1 In. from Interface; Camera Speed: 190,000 Frames/Second)	125
72	Moiré Fringe Patterns for Vertical Displacements in Model II-1F (Explosive Source in Low-Impedance Medium 1 In. from Interface; Camera Speed: 190,000 Frames/Second)	126
73	Vertical Displacements in High-Impedance Medium as a Function of Distance from Interface with Time as a Parameter for Specimens II-1D and II-1F (Frame Nos. are Marked on the Curves)	127
74	Principal Stresses in High-Impedance Medium as a Function of Distance from Interface with Time as a Parameter for Specimen II-1F (Frame Nos. are Marked on the Curves; Results Obtained from Moiré Data)	128
75	Horizontal and Vertical Stresses in High-Impedance Medium Along Interface in Specimen II-1F	129
76	Horizontal and Vertical Stresses in High-Impedance Medium Along Interface in Specimen II-1F	130

Figure		Page
77	Isochromatic Fringe Patterns in Model II-2D (Explosive Source in Low-Impedance Medium 2 In. from Interface; Impedance Ratio 2.31:1; Camera Speed 200,000 Frames/Second)	131
78	Velocity of Wave Propagation as a Function of Fringe Order in Two Media of Model II-2D	133
79	Fringe Order as a Function of Position with Time as a Parameter for Incident Wave P_1 in Low-Impedance Medium of Model II-2D (Frame Nos. and Times in Microseconds are Indicated)	134
80	Fringe Order as a Function of Position with Time as a Parameter Along Line Through Explosive Source Normal to Interface (Model II-2D; Frame Nos. are Indicated)	135
81	Fringe Order as a Function of Position with Time as a Parameter in Low-Impedance Medium Along Interface (Model II-2D; Frame Nos. are Indicated)	136
82	Fringe Order as a Function of Position with Time as a Parameter for Refracted Waves in High-Impedance Medium Along Interface (Model II-2D; Frame Nos. are Marked)	137
83	Detail of Frame 16 (t = 101 μ sec) for Model II-2D	139
84	Isochromatic Fringe Patterns in Model II-3D (Explosive Source in Low-Impedance Medium 3 In. from Interface; Impedance Ratio 2.16:1; Camera Speed 200,000 Frames/Second)	140
85	Fringe Order as a Function of Position with Time as a Parameter Along Line Through Explosive Source Normal to Interface (Model II-3D; Frame Nos. are Indicated)	141
86	Fringe Order as a Function of Position with Time as a Parameter in Low-Impedance Medium Along Interface (Model II-3D; Frame Nos. are Indicated)	142
87	Sketch of Model Showing Dimensions and Location of Explosive Loading Source in High-Impedance Medium (Phase III)	144
88	Isochromatic Fringe Patterns in Model III-1D (Explosive Source in High-Impedance Medium 1 In. from Interface; Impedance Ratio 2.23:1; Camera Speed 200,000 Frames/Second)	145

ILLUSTRATIONS (Cont'd.)

Figure		Page
89	Velocity of Wave Propagation as a Function of Fringe Order in Two of Model III-1D	146
90	Fringe Order as a Function of Position with Time as a Parameter for Refracted P_2P_1 Wave in Low-Impedance Medium of Model III-1D	148
91	Fringe Order as a Function of Position with Time as a Parameter in High-Impedance Medium Along Interface (Model III-1D; Frame Nos. are Marked)	149
92	Fringe Order as a Function of Position with Time as a Parameter for Refracted Waves in Low-Impedance Medium Along Interface (Model III-1D; Frame Nos. are Marked)	150
93	Enlargement of Frame 10 (t = 70 μ sec) Showing Reflected and Refracted Waves	152
94	Enlargement of Frame 12 (t = 80 μ sec) Showing Reflected and Refracted Waves	153
95	Isochromatic Fringe Patterns in Model III-2D (Explosive Source in High-Impedance Medium 2 In. from Interface; Impedance Ratio 2.20:1; Camera Speed 200,000 Frames/Second)	154
96	Velocity of Wave Propagation as a Function of Fringe Order in Two Media of Model III-2D	155
97	Fringe Order as a Function of Position with Time as a Parameter for Refracted P_2P_1 Wave in Low-Impedance Medium of Model III-2D	157
98	Fringe Order as a Function of Position with Time as a Parameter in High-Impedance Medium Along Interface (Model III-2D; Frame Nos. are Marked)	158
99	Fringe Order as a Function of Position with Time as a Parameter for Refracted Waves in Low-Impedance Medium Along Interface (Model III-2D; Frame Nos. are Marked)	159
100	Enlargement of Frame 12 (t = 81 μ sec) Showing Reflected and Refracted Waves in Model III-2D	161
101	Isochromatic Fringe Patterns in Model III-3D (Explosive Source in High-Impedance Medium 3 In. from Interface; Impedance Ratio 2.18:1; Camera Speed 200,000 Frames/Second)	162
102	Velocity of Wave Propagation as a Function of Fringe Order in Two Media of Model III-3D	163

ILLUSTRATIONS (Cont'd.)

Figure		Page
103	Fringe Order as a Function of Position in High-Impedance Medium Along Line Through Explosive Source Normal to Interface for Model III-3D (Frame Nos. are Marked)	164
104	Fringe Order as a Function of Position with Time as a Parameter for Refracted P_2P_1 Wave in Low-Impedance Medium of Model III-3D	165
105	Fringe Order as a Function of Position with Time as a Parameter in High-Impedance Medium Along Interface (Model III-3D; Frame Nos. are Marked)	167
106	Fringe Order as a Function of Position with Time as a Parameter for Refracted Waves in Low-Impedance Medium Along Interface (Model III-3D; Frame Nos. are Marked)	168
107	Enlargement of Frame 12 (t = 85 μ sec) Showing Reflected and Refracted Waves in Model III-3D	170

SECTION I

INTRODUCTION

This program is aimed at developing technical information on the propagation of stress waves in earth produced by high-intensity surface or subsurface explosions. The nature and intensity of these stress waves and their interaction with material and geometrical discontinuities, such as interfaces between geological strata, is of vital significance to the design of underground structures. Experimental field data do exist, but they do not yield a complete picture of the phenomenon. Besides, it is very impractical to make experimental field observations for the study of the influence of parameters such as impedance ratio of adjacent layers, distance of explosive source from interface, type of explosive detonation (surface or buried), inclination of wavefront with interface, etc. A complete knowledge of stress wave interaction phenomena and their dependence on the geometrical and material parameters of the media is desired.

One approach in studying the fundamental aspects of stress-wave propagation and interaction with discontinuities has been the use of photoelastic and moiré techniques with plastic models. A number of such programs have been sponsored by the Air Force Weapons Laboratory with the IIT Research Institute. Models with cavities of various shapes and inclusions of various rigidities subjected to falling weight, explosive, and air-shock loadings have been studied. Both elastic and viscoelastic studies have been conducted (Ref. 1 and 2). One major conclusion from these investigations has been that in most cases dynamic stresses around discontinuities, such as cavities and inclusions simulating underground structures, can be computed from the free-field state of stress using static stress ratios which are not appreciably different from dynamic ones. The most recently concluded study dealt with wave propagation in layered media (Ref. 3). Explosively loaded models, consisting of layers of CR-39 and aluminum with an impedance ratio of 6:1 were used.

The objective of the present study is to employ all previously developed experimental techniques of dynamic photoelasticity and moiré to the study of wave propagation in layered media. More particularly, the objective is to study photoelastically the transmitted, reflected and refracted waves resulting when a wave generated by explosive or air shock loading reaches the plane interface between two birefringent materials having an impedance ratio of 2:1. The program consists of the following three Phases:

Phase I: Air-Blast Loading on the Free Surface

Phase II: Buried Source in the Low-Impedance Medium

Phase III: Buried Source in the High-Impedance Medium

The distance between the source of loading and the interface was varied.

A new explosive charge, Pentaerythritol Tetranitrate (PETN), was used in this investigation and is described in Section III along with other experimental methods and techniques. Also described is the Schardin multiple spark camera, which was operated at a rate of 200,000 frames per second to record dynamic photoelastic and moiré fringe patterns.

A significant phase of the work was the development of birefringent model materials with controllable impedance. Thus, it was possible to make both layers of the model transparent and birefringent as opposed to the previous study where one layer (aluminum) was opaque. The development of these materials and their property determinations are described in Sections IV and V. The remaining sections of the report describe the application of the materials, methods, and techniques to the solution of the particular problems of Phases I, II, and III above. In the closing section, results are summarized, some conclusions are drawn and recommendations for future work are made.

SECTION II

WAVE PROPAGATION IN LAYERED MEDIA

1. Reflection and Refraction of Plane Waves at an Interface

In general, a disturbance of any kind reaching the interface of two dissimilar media produces two reflected and two refracted waves. Under special circumstances, depending on the incident wave and the impedances of the media, additional waves may be generated. In the case, for example, where the source of the disturbance is in the low-impedance medium the two refracted waves can generate five different headwaves. Thus, a maximum of nine different waves can be generated by a single incident wave at the interface of two layers. This problem is extremely complex for a complete mathematical analysis. The analytical formulation of the problem for elastic waves is given by Ewing, Jardetsky, and Press (Ref. 4). The corresponding problem for viscoelastic waves is much more complex. Several aspects of that problem dealing with the interaction of viscoelastic waves with plane boundaries have been discussed by Cooper and Reiss (Ref. 5).

An incident wave of any type, impinging on the interface of the two elastic media will produce, in general, compressional and distortional waves in both media.

The potential functions describing the waves at the interface are:

$$\varphi_1 = A_1 \exp\left[i k (ct - x + a_1 y)\right] + A_{11} \exp\left[i k (ct - x - a_1 y)\right] \quad (1)$$

$$\psi_1 = B_1 \exp\left[i k (ct - x + b_1 y)\right] + B_{11} \exp\left[i k (ct - x - b_1 y)\right] \quad (2)$$

$$\varphi_2 = A_{12} \exp\left[i k (ct - x + a_2 y)\right] \quad (3)$$

$$\psi_2 = B_{12} \exp\left[i k (ct - x + b_2 y)\right] \quad (4)$$

where

$$k = \frac{2\pi \cos e}{\lambda} = \frac{2\pi \cos f}{\lambda'}$$

λ, λ' = wavelengths for compressional and distortional waves, respectively.

c = wave velocity along interface

$$a_1 = \tan e_1 = \left[\left(\frac{c}{\alpha_1}\right)^2 - 1\right]^{1/2}$$

$$b_1 = \tan f_1 = \left[\left(\frac{c}{\beta_1}\right)^2 - 1\right]^{1/2}$$

$$a_2 = \tan e_2 = \left[\left(\frac{c}{\alpha_2}\right)^2 - 1\right]^{1/2}$$

$$b_2 = \tan f_2 = \left[\left(\frac{c}{\beta_2}\right)^2 - 1\right]^{1/2}$$

$$\alpha_i = \left(\frac{\lambda_i + 2\mu_i}{\rho_i}\right)^{1/2} = \text{dilatational wave velocity } (i = 1, 2)$$

$$\beta_i = \left(\frac{\mu_i}{\rho_i}\right)^{1/2} = \text{distortional wave velocity } (i = 1, 2)$$

e_1, f_1, e_2 and f_2 are defined in Fig. 1,

subscripts 1 and 2 refer to media 1 and 2,

λ_i, μ_i = Lamé constants of materials

ρ_i = densities

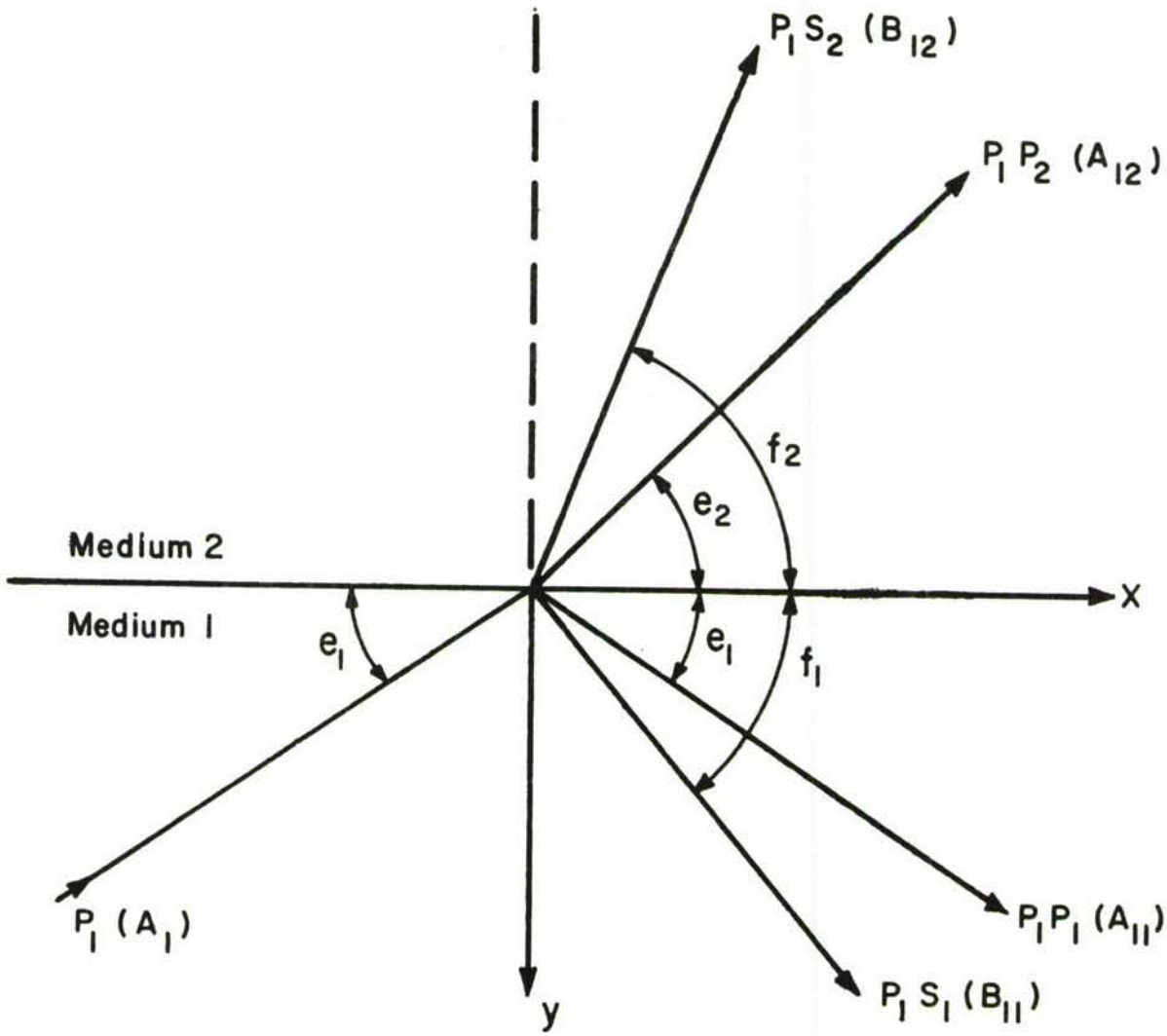


Figure 1. REFLECTION AND REFRACTION OF A DILATATIONAL (P) WAVE AT AN INTERFACE BETWEEN TWO ELASTIC MEDIA

A and B (with appropriate subscripts) refer to amplitudes of dilatational and distortional waves.

From the elementary laws of reflection and refraction we have:

$$c = \frac{\alpha_1}{\cos e_1} = \frac{\beta_1}{\cos f_1} = \frac{\alpha_2}{\cos e_2} = \frac{\beta_2}{\cos f_2} \tag{5}$$

These conditions imply that for real e_1, f_1, e_2, f_2 the interface velocity c must be greater than α_1, β_1, α_2, and β_2. It is possible, however, that some coefficients, say a_2 and b_2, are imaginary, i.e., that

$$c < \alpha_2 \quad \text{and} \quad c < \beta_2$$

In this case, phase changes would occur upon refraction.

The displacements and stresses are expressed in terms of the potential functions as follows:

$$u = \frac{\partial \phi}{\partial x} - \frac{\partial \psi}{\partial y}, \quad v = \frac{\partial \phi}{\partial y} + \frac{\partial \psi}{\partial y} \tag{6}$$

and

$$\sigma_{yx} = \mu \left(\frac{2 \partial^2 \phi}{\partial x \partial y} + \frac{\partial^2 \psi}{\partial x^2} - \frac{\partial^2 \psi}{\partial y^2} \right) \tag{7}$$

$$\sigma_{yy} = \lambda \nabla^2 \phi + 2 \mu \left(\frac{\partial^2 \phi}{\partial y^2} + \frac{\partial^2 \psi}{\partial x \partial y} \right) \tag{8}$$

The boundary conditions at $y = 0$ require that

$$\begin{aligned} u_1 &= u_2 \\ v_1 &= v_2 \end{aligned} \tag{9}$$

and

$$(\sigma_{yy})_1 = (\sigma_{yy})_2$$
$$(\sigma_{yx})_1 = (\sigma_{yx})_2 \tag{10}$$

By substituting the potential functions from Eqs. (1), (2), (3), and (4) in Eqs. (6), (7), and (8) and applying the boundary conditions, we obtain the following system of four linear equations in terms of the wave amplitudes A_1, A_{11}, A_{12}, B_1, B_{11}, and B_{12}:

$$A_1 + A_{11} + b_1 (B_1 - B_{11}) = A_{12} + b_2 B_{12} \tag{11}$$

$$a_1 (A_1 - A_{11}) - (B_1 + B_{11}) = a_2 A_{12} - B_{12} \tag{12}$$

$$\mu_1 \left[- (b_1^2 - 1) (A_1 + A_{11}) + 2 b_1 (B_1 - B_{11}) \right]$$
$$= \mu_2 \left[- (b_2^2 - 1) A_{12} + 2 b_2 B_{12} \right] \tag{13}$$

$$\mu_1 \left[2 a_1 (A_1 - A_{11}) + (b_1^2 - 1) (B_1 + B_{11}) \right]$$
$$= \mu_2 \left[2 a_2 A_{12} + (b_2^2 - 1) B_{12} \right] \tag{14}$$

In the case where only an incident dilatational wave is considered $B_1 = 0$. Then, the four amplitude coefficients A_{11}, B_{11}, A_{12}, and B_{12} can be expressed in terms of the incident wave amplitude A_1. Values of reflection and transmission coefficients have been tabulated by Muskat and Meres (Ref. 6).

2. Wave Propagation in Two Semi-Infinite Media for Point Source Loading

When the incident wave is generated by a point source at a finite distance from the interface the problem becomes more complicated than in the case of plane waves discussed above. This problem is of practical importance in seismology in the determination of the "refraction arrival." When a point source and a receiver are located in the low-impedance medium at a distance from each other large compared to their distance from the interface, it is observed that the first disturbance arriving at the receiver corresponds to a propagation along the path shown in Fig. 2. This propagation takes place in three parts; (1) source to interface at a velocity α_1, (2) along the interface at a velocity α_2, and (3) interface to receiver at a velocity α_1. The angle of incidence is equal to the critical angle

$$\theta_{cr} = \text{arc sin } \frac{\alpha_1}{\alpha_2} \tag{15}$$

The analytical formulation of this problem is quite complex as it involves expressions for the potential functions in terms of improper integrals of Bessel functions (Ref. 4). One characteristic result of these analyses is that, for wavelengths short compared to the thickness of the layer, in addition to ordinary waves with velocities depending only on the properties of the individual layers, a modified Rayleigh wave could exist with velocity depending on the properties of both media. This interface wave, known also as Stoneley wave, occurs when the shear wave velocities in the two media are nearly equal. Its velocity falls between the velocity of Rayleigh waves and that of the distrotional wave in the high-impedance medium.

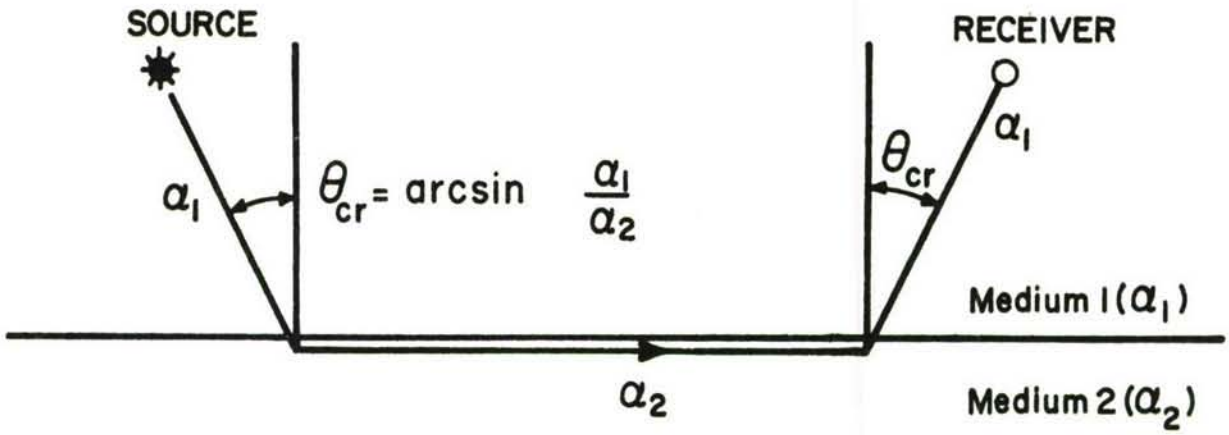


Figure 2. PATH OF "REFRACTION ARRIVAL" ($\alpha_2 > \alpha_1$)

A complete set of waves generated by a point source in the low-impedance medium was described graphically by Cagniard (Ref. 8) and is shown in Fig. 3. The incident P_1 wave in medium 1 impinges on the interface between the two media and generates a reflected dilatational wave P_1P_1, a reflected shear wave P_1S_1, a refracted dilatational wave P_1P_2 and a refracted shear wave P_1S_2. If the wave velocities in the two media are related as

$$\alpha_2 > \beta_2 > \alpha_1 > \beta_1 \tag{16}$$

then, at some time after wave initiation the two refracted waves will have outrun the incident and reflected waves along the interface. Each one of the refracted waves P_1P_2 and P_1S_2 will in turn generate two refracted waves in medium 1, $P_1P_2P_1$, $P_1P_2S_1$, $P_1S_2P_1$ and $P_1S_2S_1$. The "refraction arrival" mentioned earlier corresponds to the arrival of wave $P_1P_2P_1$ at the receiver location prior to arrival of any other wave including the incident P_1 wave. The refracted P_1P_2 wave produces also a reflected shear wave in medium 2, the $P_1P_2S_2$ wave. These second order waves have plane wavefronts and are usually referred to as headwaves. Their plane wavefronts are tangent to the curved wavefronts of the corresponding reflected and refracted dilatational and shear waves.

Referring to Fig. 3, point A located at a distance from point 0 (the intersection of the interface and the centerline) equal to

$$(OA) = h \tan \theta_{cr} \tag{17}$$

where θ_{cr} is given by Eq. (15), corresponds to the point where the interface velocity in medium 1 equals the dilatational velocity in medium 2.

$$c = \frac{\alpha_1}{\sin \theta_{cr}} = \alpha_2 \tag{18}$$

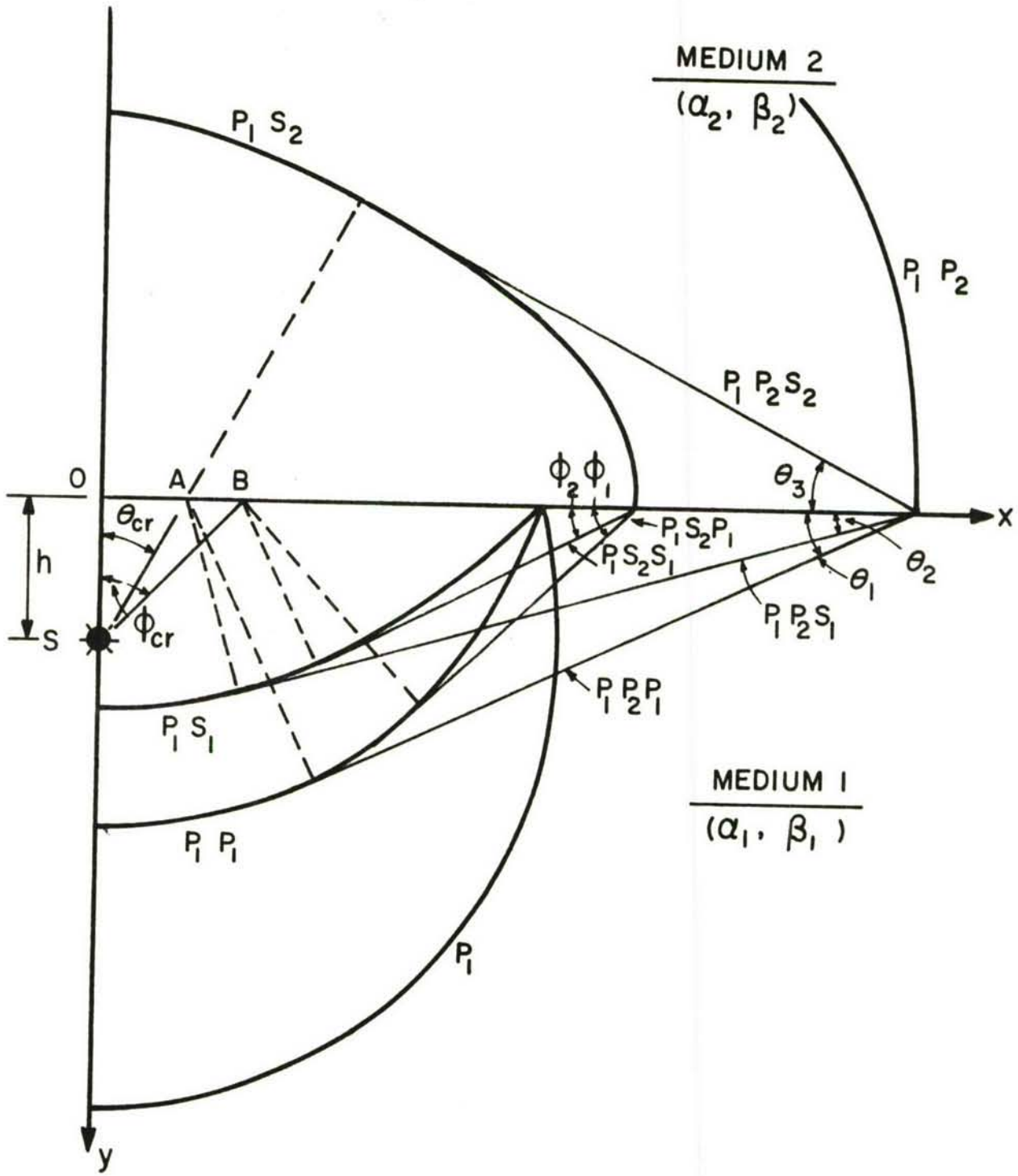


Figure 3. COMPLETE SET OF WAVES GENERATED IN TWO ELASTIC MEDIA BY A POINT SOURCE OF DILATATIONAL WAVES IN LOW-IMPEDANCE MEDIUM ($\alpha_2 > \beta_2 > \alpha_1 > \beta_1$; AFTER CAGNIARD) (Ref. 8)

Beyond this point, the refracted wave P_1P_2 outruns the incident P_1 wave and produces the three headwaves discussed above. Considering point A as a source of waves P_1P_2, P_1S_2, P_1S_1 and P_1P_1 it follows that the angles that the wavefronts $P_1P_2P_1$, $P_1P_2S_1$ and $P_1P_2S_2$ form with the interface are

$$\theta_1 = \theta_{cr} = \text{arc sin } \frac{\alpha_1}{\alpha_2} \tag{19}$$

$$\theta_2 = \text{arc sin } \frac{\beta_1}{\alpha_2} \tag{20}$$

$$\theta_3 = \text{arc sin } \frac{\beta_2}{\alpha_2} \tag{21}$$

Point B corresponds to a critical angle

$$\phi_{cr} = \text{arc sin } \frac{\alpha_1}{\beta_2} \tag{22}$$

when the incident wave velocity along the interface equals the shear wave velocity in medium 2:

$$c = \frac{\alpha_1}{\sin \phi_{cr}} = \beta_2 \tag{23}$$

Beyond this point the refracted shear wave P_1S_2 outruns the incident P_1 wave along the interface and generates the two headwaves discussed earlier. Their plane wavefronts form the following angles with the interface

$$\phi_1 = \phi_{cr} = \text{arc sin } \frac{\alpha_1}{\beta_2} \tag{24}$$

$$\phi_2 = \text{arc sin } \frac{\beta_1}{\beta_2} \tag{25}$$

SECTION III

EXPERIMENTAL METHODS

1. Dynamic Photoelasticity and Photoviscoelasticity

In dynamic photoelasticity, as in the static case, a model is fabricated out of a birefringent material and subjected to dynamic loadings similar to those encountered in the prototype. The model is viewed in monochromatic polarized light and the resulting isochromatic fringe patterns are recorded by means of appropriate electronic and photographic instrumentation.

The interpretation of fringe orders is the same as in the static case, i.e., the fringe order is related to the principal stress difference by the stress-optic law

$$\sigma_1 - \sigma_2 = \frac{2nf_\sigma}{h} \tag{26}$$

where

f_σ is the material fringe value

h is the model thickness.

The value of f_σ is determined by suitable calibration for a dynamic loading of similar duration and rate as the one used in the model.

The separation of stresses, i.e., the determination of individual values of σ_1 and σ_2, requires additional experimental data, such as strains. In the past, the moiré method of strain analysis has been used extensively for this purpose. In certain select cases of wave propagation, however, principal stress separation is possible without any additional data. In the case of a pure dilatational wave, stresses are present both in the direction of wave propagation and perpendicular thereto; however, deformations occur

only in the direction of wave propagation. Thus, the displacements are:

$$u_r = f(r), \quad u_\theta = 0 \tag{27}$$

For a point source, the incident P_1 wave exhibits polar symmetry, which makes possible the determination of individual strains (and stresses) from purely photoelastic data as follows:

$$\varepsilon_\theta = \frac{u_r}{r} = -\frac{(1+\nu)}{E}\,\frac{f_\sigma}{h}\int_r \frac{n}{r}\,dr \tag{28}$$

$$\varepsilon_r = \varepsilon_\theta - \frac{1+\nu}{E}\,\frac{n}{h}\,f_\sigma \tag{29}$$

Separation of principal stresses using only photoelastic data is also possible in the case of a pure distortional wave (S type) since for a state of pure shear it is known that

$$\sigma_1 = -\sigma_2 \tag{30}$$

Thus, it is seen that separation of principal stresses is easily accomplished whenever there is a distinct separation of P and S waves.

Most birefringent materials used in model studies are viscoelastic in nature and, therefore, exhibit rate (or time, or frequency) dependence in all mechanical and optical properties. Polymers, used as model materials, usually exhibit three time regions of characteristic behavior: a glassy region at very short times (or high rates) where the material behaves elastically, a rubbery region corresponding to very long times where the material also behaves elastically, and an intermediate region of pronounced viscoelastic behavior. The elastic analysis described above is valid when the rate dependence is negligible over the timescale of the experiment, e.g., when the material is in the glassy region of behavior. The same is true when the material is in the rubbery region, although purely elastic rubbery

behavior is not common under dynamic loading conditions.

Whenever material behavior falls in the transition region, where rate effects cannot be neglected, a photoviscoelastic analysis of the fringe patterns is necessary. Methods and techniques for such an analysis have been developed and successfully applied to wave propagation problems (Refs. 2,9). The stress-optic law in this case takes more complicated forms, one of which is the following:

$$\sigma_{xx} - \sigma_{yy} = \frac{2}{h} \int_0^t f_\sigma (t-\tau) \frac{d}{d\tau} \left[(n_1 - n_2)\cos 2\phi_n \right] d\tau \qquad (31)$$

and

$$\sigma_{xy} = \frac{1}{h} \int_0^t f_\sigma (t - \tau) \frac{d}{d\tau} \left[(n_1 - n_2) \sin 2 \phi_n \right] d\tau \qquad (32)$$

where

h = the model thickness

$f_\sigma (t)$ = the time-dependent stress fringe value

$n_1 - n_2$ = relative birefringence

ϕ_n = isoclinic parameter

$\sigma_{xx} - \sigma_{yy}$ = difference in normal stresses

σ_{xy} = shear stress

The value of $f_\sigma (t)$ is obtained by means of sinusoidal oscillation tests for dynamic applications. They can also be obtained by means of creep tests at low temperatures and by applying the temperature-time equivalence principle. These methods of material characterization have been proven valid and useful (Refs. 2,10).

2. Moiré Method

The moiré effect is an optical phenomenon observed when two closely spaced arrays of lines are superimposed and viewed with either transmitted or reflected light. If the two arrays consist of opaque parallel lines which are not identical in either spacing (pitch) or orientation, then interference between the two arrays occurs and moiré fringes are produced.

In actual practice, one array is photo-printed or etched on the surface of the specimen. A transparent reference array usually of the same pitch is placed adjacent to the specimen and aligned parallel to the specimen array. As the specimen is loaded, the specimen array deforms and follows the surface displacements induced by the loads. The reference array, of course, does not deform since it is not loaded and as a consequence a moire interference pattern is formed when light is transmitted through the two arrays.

Moiré fringe patterns can most easily be interpreted by relating them to the displacement field since moire fringes are loci of points having the same component of displacement in a direction perpendicular to the grid lines of the undistorted reference array.

Once two orthogonal displacement surfaces (u and v) have been established by using line arrays parallel to the x and y axes of a specimen, the cartesian strain components can be computed from the derivatives of the displacements. Two specimens are normally required for these determinations unless an axis of symmetry exists so that mutually perpendicular arrays can be placed on the same specimen. When strains are sufficiently small, the classical strain-displacement equations are used:

$$\varepsilon_{xx} = \frac{\partial u}{\partial x}$$

$$\varepsilon_{yy} = \frac{\partial v}{\partial y} \qquad (33)$$

$$\varepsilon_{xy} = \frac{1}{2}\left(\frac{\partial u}{\partial y} + \frac{\partial v}{\partial x}\right)$$

The fineness of the line images required to obtain satisfactory information from a moiré pattern depends only upon the magnitude of the deformations. These deformations are related to the modulus of elasticity of the specimen material the geometry of the specimen, and the manner of loading. The pitch of the array should be small enough to give sufficient response but not so fine as to produce fringes that can no longer be distinguished clearly.

In the present application, it was decided to use arrays of 1,000 lines per inch. These arrays were photoprinted on the specimens using the Kodak Photosensitive Resist Process (KPR). This photosensitive resist is an organic solvent solution of a durable, ultraviolet-sensitive plastic. It can be applied to almost any material to form thin coatings insoluble in water and resistant to it. After proper exposure to ultraviolet light the coated specimen is developed in an organic solvent which disolves the coating in the unexposed areas. A dye solution is then used to make the exposed areas more visible.

The procedure used in the present case was as follows: The specimen surface was cleaned with soap and water and then with acetone. The liquid Kodak Photo Resist (KPR) was poured over the specimen and the latter was spun on a spinning table for approximately 2 minutes. The coating was subsequently cured for 10 minutes at 140°F. The film master with the desired array of 1,000 lines per inch was placed in contact with the coated surface in a vacuum table and exposed to the light of a carbon arc for 2-1/2 minutes. The vacuum was adjusted to insure proper contact of the master and to avoid excessive pressure on the specimen. The specimen is then developed in a special developer (KPR developer) for approximately 4 minutes, washed with water, then immersed in a dye for 15 seconds and washed again. After drying, the specimen is ready for testing. During the test the moire film master is kept in contact with the printed side of the specimen by means of a film of oil and is adjusted so that a minimum mismatch fringe pattern appears.

3. Methods of Loading

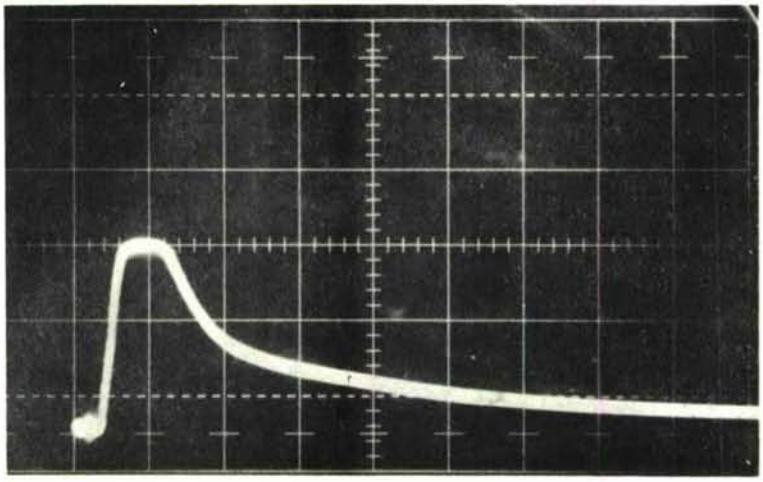
a. Buried Source Explosive Loading

Internal point source loading was produced by detonating a charge of Pentaerythritol Tetranitrate (PETN). This explosive is most readily available in Primacord and is ideally suited for dynamic loading of photoelastic models. It was selected for this investigation and preferred over lead azide for a number of reasons. It is very stable and much safer than lead azide requiring a high level of energy for detonation. It has a higher detonation velocity (8,300 meters/second) and its energy output is at least as high as that of lead azide. An indication of the time characteristics of the explosive pulse can be seen in the photocell trace of a typical detonation (Fig. 4). The rise time is approximately one microsecond and the mean width six microseconds. A relatively slow decay is evident. Another advantage of PETN is that it does not give off too much smoke or too much light, thus allowing photography of fringe patterns in close vicinity of the explosive source. A typical photoelastic record illustrating some of these facts is shown in Fig. 5. The record shows a satisfactory cylindrical P-wave generated by the explosive.

In preliminary studies, it was found that 50 mg of PETN would provide model loads which would yield sufficient response (in the form of photoelastic fringes) without producing significant fractures to dissipate the energy of the explosive.

A suitable detonator system was designed and fabricated and subsequent tests showed that the following requirements were satisfied:

(1) The PETN detonated consistently with no misfires. (This required providing a suitable energy source and a device for transferring this energy to the explosive. It also required that the PETN be of suitable particle size.)



Time: 5 Micro sec/cm

Figure 4. OPTICAL INDICATION OF IMPACT PRESSURE PULSE OF PETN (Ref. 11)

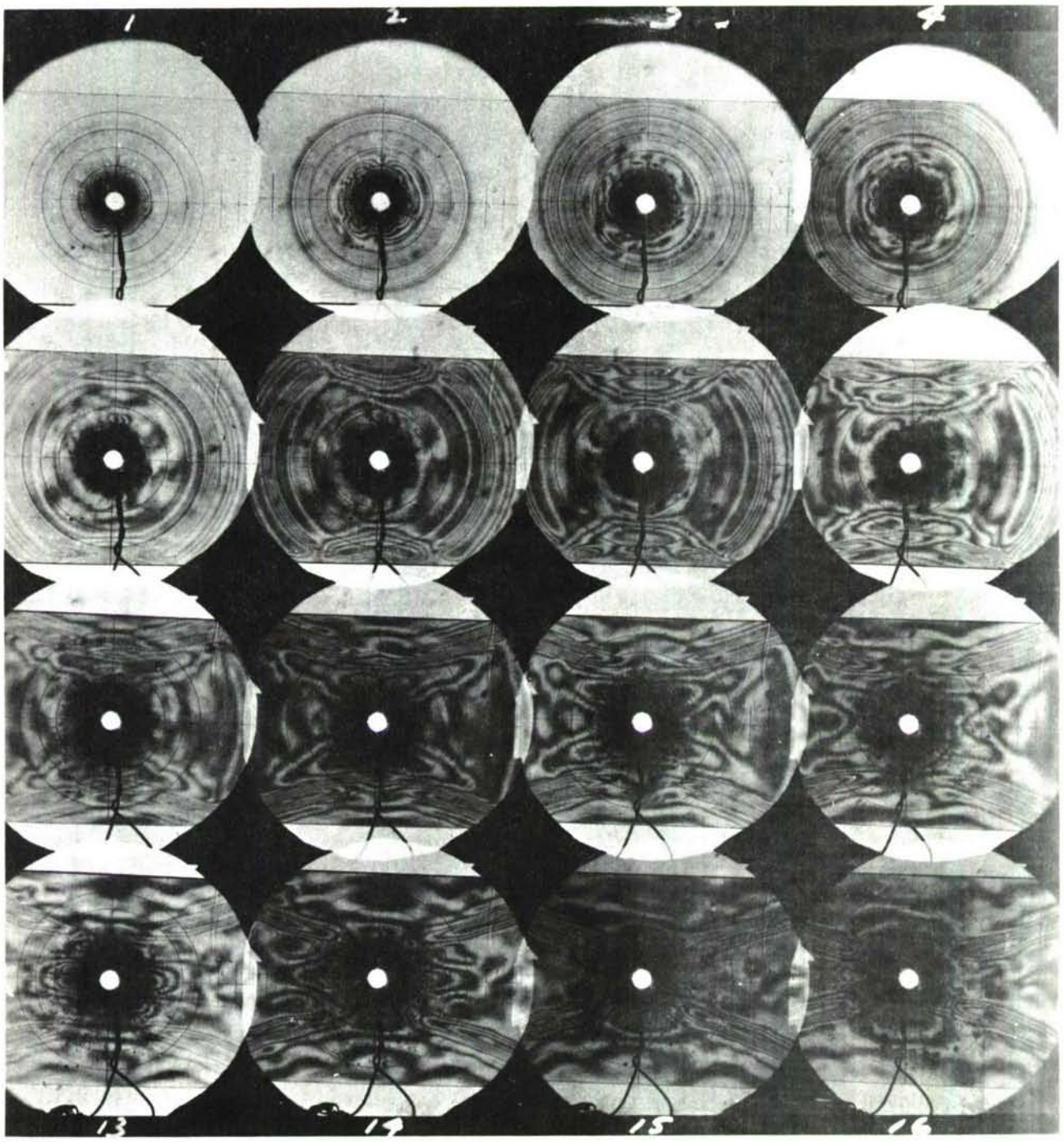


Figure 5. ISOCHROMATIC FRINGE PATTERNS IN COLUMBIA RESIN (CR-39) PLATE UNDER PETN EXPLOSIVE LOADING AT CENTER (CAMERA SPEED: 200,000 FRAMES/SECOND)

2. The PETN yielded a loading which was reproducible from one shot to the next.

3. The PETN burned uniformly producing a symmetrical incident P wave emanating from the point source.

4. The burning rate of the 50 mg charge produced a loading rate in the model which was consistent with the loading rate normally occurring in larger charges.

To satisfy these design specifications, it was found desirable to reduce the diameter size of the PETN particles normally found in Primacord and to compact these finer grains into the detonator to a density of 900 mg per cc. A particle size of 20 to 40 μ was achieved by dissolving the coarse particles (taken directly from the Primacord) in acetone and then precipitating the finer grains by pouring the acetone with the dissolved PETN into a beaker of ice water. The precipitate was gathered on filter paper and allowed to dry.

The actual detonator assemblies (i.e., explosive containers) were manufactured from disks 3/8 in. dia. by 0.230 in. thick cut from a 3/8 in. dia. plexiglas rod. A No. R size drill (0.339 in. dia.) was employed to machine a blind hole in the center of one end of the plexiglas disk to provide a snug fit for an exploding bridge wire header used to detonate the explosive. The 0.339 in. dia. hole was drilled to a depth of 0.176 in. including the cone formed by the drill tip.

After the plexiglas disks had been machined and drilled to the proper dimensions, they were each filled with a 50 mg charge of PETN that had been weighed on an analytical balance sensitive to 0.1 mg. The loose PETN was compacted to a density of 900 mg per cc by inserting the exploding bridge wire header into the 0.339 in. diameter hole, pressing down firmly until the header was seated on its flange and then bonding the header in place with a quick setting adhesive (Eastman 910 Cement). This procedure not only established the volume of the compacted PETN at 0.00339 in.^{3} (the volume for the

required density of a 50 mg charge) but also insured that there was intimate contact between the exploding bridge wire (EBW) and the PETN.

The EBW headers, which are commercially available, consist of two terminal pins embedded in the longitudinal direction of a cylinder of electrical insulating material. These terminal pins are flush with the cylinder at one end and at the other end they are connected to lead wires. The terminal pin spacing (approximately 1/16 in.) at the flush end of the cylinder is then bridged with a 0.0015 in. diameter gold wire soldered at each end to the terminal pins. The resistance of this very short length of thin gold wire is less than 1 ohm and when a high voltage (2000 v) is rapidly (1 μ sec) imposed across the header terminals, the gold wire literally explodes releasing a sufficient level of energy to initiate the detonation of the fine grain PETN.

The completed detonator assemblies (EBW header and plexiglas container filled with PETN) were then inserted into a 3/8 in. dia. hole in the model which had been drilled at the proper location for the point source explosive loading. These assemblies were bonded in place with a thin layer of epoxy adhesive to insure an adequate mechanical coupling between the model and the detonator so that the majority of the energy from the explosive would be transferred to the model.

In bonding the detonator assemblies in place, the models were laid flat on a table and the detonator was inserted into the hole in the model until the flat end of the detonator was flush with the model face that was in contact with the table. The dimensions of the detonator assembly were such that with the detonator in this position, the center of mass of the explosive was placed in the central plane of the model so as to eliminate flexural loading.

b. Air Shock Loading

This type of loading was accomplished by means of a shock tube described in earlier reports (Refs. 1,2). The shock tube used is 6 in. in diameter (I.D.) and 28 ft. long. A 2-ft. section of this tube is

filled with nitrogen under 600 psi pressure. A 24-gage drawing quality steel is used for the diaphragm that separates the driver section from the rest of the tube. The plate model to be loaded is inserted in a specially machined slot in the tube approximately 16 ft from the pressure section and 10 ft from the other end. The model is held in a plexiglas housing with a metal frame attached to the tube so that the loaded edge of the model is flush with the inside surface of the tube. A thin rubber diaphragm is used between the tube slot and the model to prevent air from the tube from entering the spaces between the model and the housing.

The "goose" control unit of a Fastax camera in conjunction with a falling weight device is used to trigger and coordinate three events: the start of the camera, the flashing of the lights and the detonation of the blasting cap which punctures the metal diaphragm and initiates the shock wave. The downstream end of the tube is filled with shock-absorbent foam and is left partially open to minimize the intensity of the reflected shock wave. The magnitude and shape of the pressure pulse is measured with a Kistler pressure gage. A typical oscilloscope record obtained in the present study is shown in Fig. 6.

4. Cranz-Schardin Multiple Spark Camera

a. General

The same multiple spark camera used by Dally and Riley (Ref. 3) for their photoelastic studies of wave propagation was also employed (with a few minor modifications) for the current investigation of wave propagation in layered media. This camera system is capable of photographically recording (at rates which can be varied from 185,000 to 700,000 frames per second) a time-sequenced series of 16 dynamic photoelastic fringe patterns. The line definition of the photographic records is such that a fringe array of approximately 12 lines per inch moving at a velocity of 100,000 in./sec can be resolved

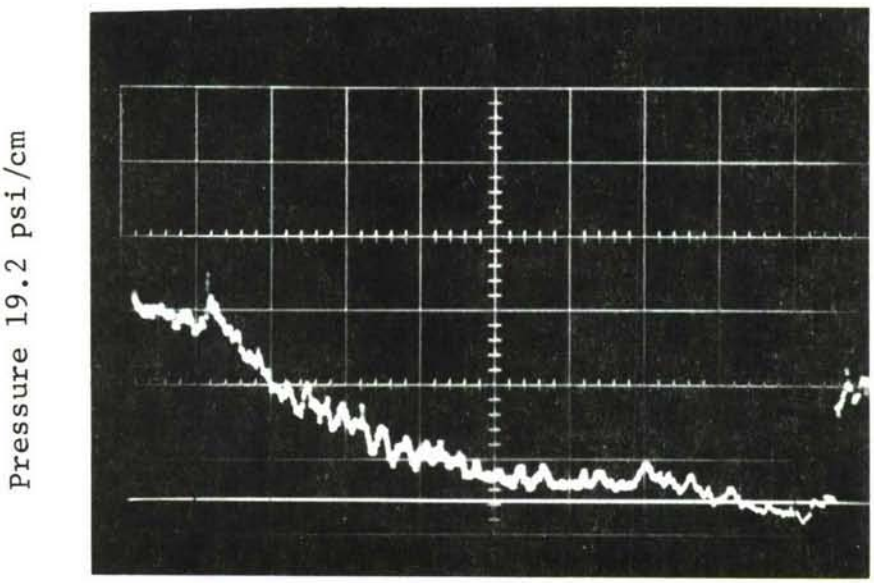


Figure 6. PRESSURE-TIME RECORD IN SHOCK TUBE AT MODEL LOCATION

on the film. For the current investigation, the slowest framing rates of 185,000 to 200,000 frames per second were employed.

The Cranz-Schardin multiple spark camera is composed of three basic systems: spark gap bank, optics, and control circuits. Each of these systems is discussed in detail in the following sections.

b. Spark Gap Bank

The spark gap bank consists of 16 separate spark gaps arranged in a 4 by 4 array and mounted on the front face of a standard floor model instrument cabinet. Each of the 16 spark gap circuits consists of two chrome plated brass spheres, two 0.05 μ f (15 kv) capacitors (one for each electrode) and a 1 Meg ohm resistor placed in parallel with the spark gap to bridge it during the operation of charging the capacitors. An inductor is placed between adjacent spark gap circuits forming an LC loop to control the discharge rate of a capacitor as the previous spark gap in the circuit is fired. Each inductor is a single winding on an air core and is tapped at five discrete values of inductance from 3 to 100 μ H.

A commercially available Trigger Module Unit (EG and G Model TM-11) and a Trigger Gap Unit (EG and G Model GP-12A) were used to initiate the sequential firing of the spark gaps. The Trigger Module is designed to provide a 15 kv pulse of fast rise time (0.3 μ sec) to fire the Trigger Gap Unit. It is an integrated package consisting of a d-c power supply, a primary triggering circuit, a Krytron switch tube, and a pulse output transformer. The Trigger Module was fired remotely by adding a silicon controlled rectifier (SCR) to the "Remote Trigger" circuit of the Module. The gating pulse for the SCR was provided by the Time Delay Pulse Generator (Tektronix Model 531) to be discussed in a later section.

The initial step in operating the spark gap bank is to charge all of the capacitors to a potential of 16 kv. The first LC circuit (between the trigger gap and the first spark gap) is then closed by firing the Trigger Gap Unit with the Trigger Module. Closing this

first LC circuit causes the first capacitor (and the corresponding electrode of the first spark gap) to discharge so rapidly that the voltage on the electrode overshoots zero and goes from the original positive value of 16 kv to a negative value of approximately 14 kv. This oscillation places an electrical potential of nearly 30 kv across the first spark gap. Since the 5/16 in. air space between the electrodes cannot stand off this voltage, a short duration, intense spark jumps the gap and provides the first source of light in the sequence. As the second capacitor in the first spark gap circuit is discharged through the spark gap, the first capacitor in the second spark gap circuit is discharged through the second LC circuit and again the voltage overshoots zero to a negative value of 14 kv. This now places 30 kv across the second spark gap causing it to fire and so on down the entire line. The delay time between the firing of successive spark gaps is governed by the value of the inductance in the LC circuit for each spark gap. Any one of five inductance values can be selected to give different delay times by plugging jumper wires into the proper terminals on the incudtance patch board at the rear of the cabinet housing the spark gap bank.

c. Optical System

The optical system of the multiple spark camera performs five distinct functions: polarization of light, image separation, monochromatic filtering of light, image magnification, and image recording. The complete optical system consists of two circular polaroid elements (one placed on each side of the model), a field lens with 9 in. dia. and a 21 in. focal length, 16 camera lenses (f 4.5, focal length 7.5 in.) mounted in a 4 by 4 array on a specially designed lens board of a commercially available 11 x 14 portrait camera, and 16 monochromatic filters mounted in the portrait camera on the inside face of the lens board.

In operation, the light given by one of the spark gaps in the 4 by 4 array passes first through a circular polaroid element (Polaroid Corp. Type HNCP-38) where it emerges as circularly polarized light. This light then passes through the model and the second circular polaroid element. The emerging light is then collected by

the 9 in. diameter field lens and is focused on one (and only one) of the camera lenses in the 4 by 4 array. The light then passes through a monochromatic filter mounted on the inside face of the special lens board and is focused on the plane of the camera back containing the sheet of film.

In recording the passage of a dynamic event on film, the light from each of the 16 sparks is focused on a separate camera lens. This produces 16 separate images or frames on the film corresponding to the 16 instances of time during the event when the individual sparks fire in sequence. This image separation is accomplished by the proper location of the field lens and by the proper spacing of the spark gaps and the camera lenses.

In this camera, the spark gaps were placed at 2.75 in. on centers and the camera lenses at 2.00 in. on centers. The 9 in. dia. field lens was positioned so that the light emerging from the four corner spark gaps would be focused at the center of the four corner camera lenses. In this way, it was assured that light from each spark would fall on the center of a camera lens in a corresponding (but inverted) position on the lens board.

The image magnification is governed primarily by the focal length of the field lens (21 in.) and the focal length of the camera lenses (7.5 in.). With this optical system, a magnification ratio having a negative value of 0.3 (i.e., a reduction) was obtained. This means that a 9 in. diameter circle of light passing through the field lens is reduced to an image of approximately 2.7 in. diameter on the plane of the film.

In order to obtain a band width of light which was sufficiently narrow to approximate a monochromatic light source without losing a major portion of the available light from the sparks, it was decided to employ Kodak Gelatin Film Wratten Filters Type No. 47B. These filters are violet in color and they have the maximum transmission between the wave lengths of 4,200 and 4,400 angstroms. In this range, these filters transmit approximately 45 percent of the intensity of these wavelengths. For wavelengths above and below these values

there is a sharp decrease in transmission. For example, at 4000 angstroms and 4700 angstroms, the Type 47B filter transmits only about 15 percent of the intensity of these wavelengths. A Spark Spectrum Table in the Handbook of Chemistry and Physics listing the intensity of the various wavelengths for a spark discharbed in air shows the majority of the available light occurring for the wavelengths between approximately 3900 and 4600 angstroms.

The film selected to record the images of the dynamic event was Kodak Gravure Positive. This is a blue sensitive film of moderately high speed and medium contrast. It has a fine grain emulsion and is designed primarily for use in the graphic arts industry. Although its ASA exposure index for a Tungsten light source is only 8, its actual speed when exposed to the light from the spark gap is considerably faster. This is because the film has its greatest sensitivity in the wavelength range from 4000 angstroms to 4400 angstroms which is the same range where the maximum intensity of the spark light source occurs.

d. Control Circuits

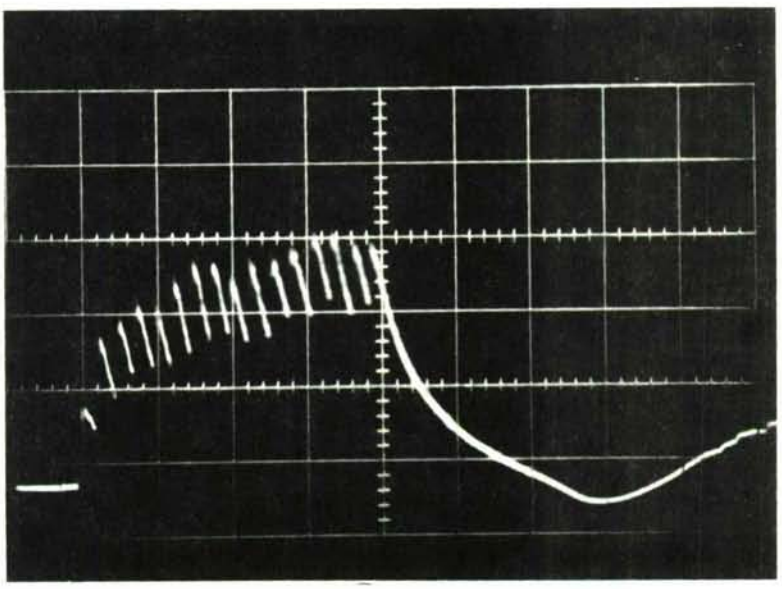
In order to obtain meaningful photographic records of dynamic fringe patterns with the multiple spark camera, it is necessary to employ electronic circuits which control precisely (on a microsecond time scale) the sequence of events during the required time period. These events which must occur at precise times include: the detonation of the explosive charge, the initiation of the horizontal sweep of the oscilloscope, and the triggering of the spark gap bank after a predetermined delay time.

This sequence of events is initiated by closing a switch in a firing circuit discharging a 5 μ f capacitor which had been charged to 2 kv. This firing circuit emits simultaneously three pulses: (1) a 2 kv pulse which explodes the gold bridge wire and detonates the PETN, (2) a 20 v pulse which triggers the horizontal sweep of the oscilloscope, and (3) a 20 v pulse which initiates a Time Delay Pulse Generator (Tektronix - Model 531). After a predetermined

elapsed time (in microseconds) from initiation, the Time Delay Generator emits a 25 v pulse which is used as a gating pulse for a silicon controlled rectifier (SCR). This gating pulse fires the Trigger Module which in turn fires the Trigger Gap and starts the sequential discharge of the 16 spark gaps.

The light output from the sparks is sensed by a high-frequency photomultiplier device (EG and G Lite Mike - Model 560A) which has a response range from 3,700 to 11,000 angstroms. The output signal from the photocell is displayed on the oscilloscope and a polaroid photograph is taken of this display which yields a light intensity versus time record. This establishes the instant during the passage of the event when each of the sparks was discharged and the corresponding photograph of the dynamic fringe pattern recorded. A typical record is shown in Fig. 7. Time measurements taken from the polaroid photograph of the oscilloscope trace for the Lite-Mike output signal show that there is a minimum delay of approximately 18 μ sec from the time the switch in the firing circuit is closed until the first spark gap fires. Since 5 μ sec is the minimum delay time which can be set on the Time Delay Generator, this time can be eliminated from the 18 μ sec by bypassing the Delay Generator altogether. Another 7 μ sec can be eliminated by bypassing the inductor in the LC circuit between the Trigger Gap and the first spark gap. The remaining 6 μ sec cannot be eliminated and represent the inherent delay in the combined system of Trigger Module, Trigger Gap, and first spark gap. Any delay time greater than 11 μ sec (6 μ sec + 5 μ sec) can be selected and controlled within 1 μ sec with the Time Delay Generator.

The position of the fringes obtained from the photographic records of the dynamic fringe patterns indicates that the initiation of the PETN charge occurs in less than 1 μ sec from the time the switch in the firing circuit is closed.



Time: 20 Micro sec/cm

Figure 7. LITE-MIKE RECORD SHOWING TIME OF FIRING OF INDIVIDUAL SPARKS

SECTION IV

DEVELOPMENT OF MODEL MATERIALS

1. Preliminary Investigations

The specific objective of this task was to develop or select birefringent model materials for use as layers of the two-layer models needed. The requirement was that the impedance (ρc_L) ratio of the two materials be 2:1.

Since the two loading conditions planned, explosive point source and air shock loading, are different in nature and intensity, and since the impedances must be evaluated under the same loading conditions encountered in the model experiment, it was decided to select two groups of materials for the two loading conditions.

Most birefringent plastics have approximately the same density, therefore the preliminary screening and evaluation of candidate model materials was based on the plate wave propagation velocity c_L. Two groups of materials were evaluated; high-modulus materials with wave propagation velocity between 25,000 and 100,000 in./sec, and low-modulus materials with wave propagation velocities in the range between 5,000 and 25,000 in./sec. The first group was investigated for use in the explosive loading experiments, the second for use in the air shock loading experiments. An extensive listing of all candidate materials was made and samples of all promising ones were procured.

2. Materials for Explosive Loading Experiments

Candidate materials considered for this group include the following: Columbia Resin (Homalite CR-39), Plexiglas, rigid polyester resin (Paraplex, Rohm and Haas; Homalite 100; and Photolastic PSM-1), flexible polyester resins (Laminac Exp. 126-3, American Cyanamid; and Photolastic PL-2), polycarbonate resin (Lexan, General Electric Co.), Cellulose Acetate Butyrate, and combinations of flexible (DER 732) and rigid (DER 331) Dow epoxy resins.

These materials were evaluated by conducting explosive loading tests in 1/4 in. thick plates of dimensions 4 in. x 10 in. These plates were loaded explosively with a 50 mg charge of PETN at a point on the longitudinal centerline near one end. Subsequent layered models were tested using the same explosive charge. Photographic records of the dynamic fringe patterns were obtained using the Schardin camera operating at an effective rate of approximately 200,000 frames per second.

Figure 8 shows the dynamic isochromatic fringe patterns produced in a specimen of Columbia Resin (CR-39) by the explosive loading. The incident P-wave is clearly manifested by the circular-arc shape of the fringes. The nearly parallel fringes inclined with respect to the sides of the specimen are produced by the distortional (shear) PS-wave reflected from the free edges of the specimen.

The propagation velocity of several fringe orders of the incident P-wave was determined by computing the slope of the curve of fringe order position vs. time (i.e., the instant of exposure of each photographic frame). It was found that this velocity (slope) remained nearly constant with time for each fringe order. It can be noted, however, from Fig. 9 which shows the variation of propagation velocity with fringe order for the Columbia Resin (CR-39) specimen that the velocity decreases slightly with increasing fringe order. This small change in propagation velocity indicates that under explosive loading, the behavior of the Columbia Resin (CR-39) is nearly elastic.

The velocity of propagation of the wavefront (zero order fringe) is obtained by extrapolating the above curve to the zero order fringe. As can be seen from the curve, the incident P-wave front travels with a velocity of 73,000 in./sec in the Columbia Resin.

A similar test with a Columbia Resin strip was conducted to determine the uniaxial wave propagation velocity in the material. A bar 1/4 in. x 1/4 in. was used. The propagation velocity as a function of fringe order is depicted in Fig. 10, whereby extrapolation to zero

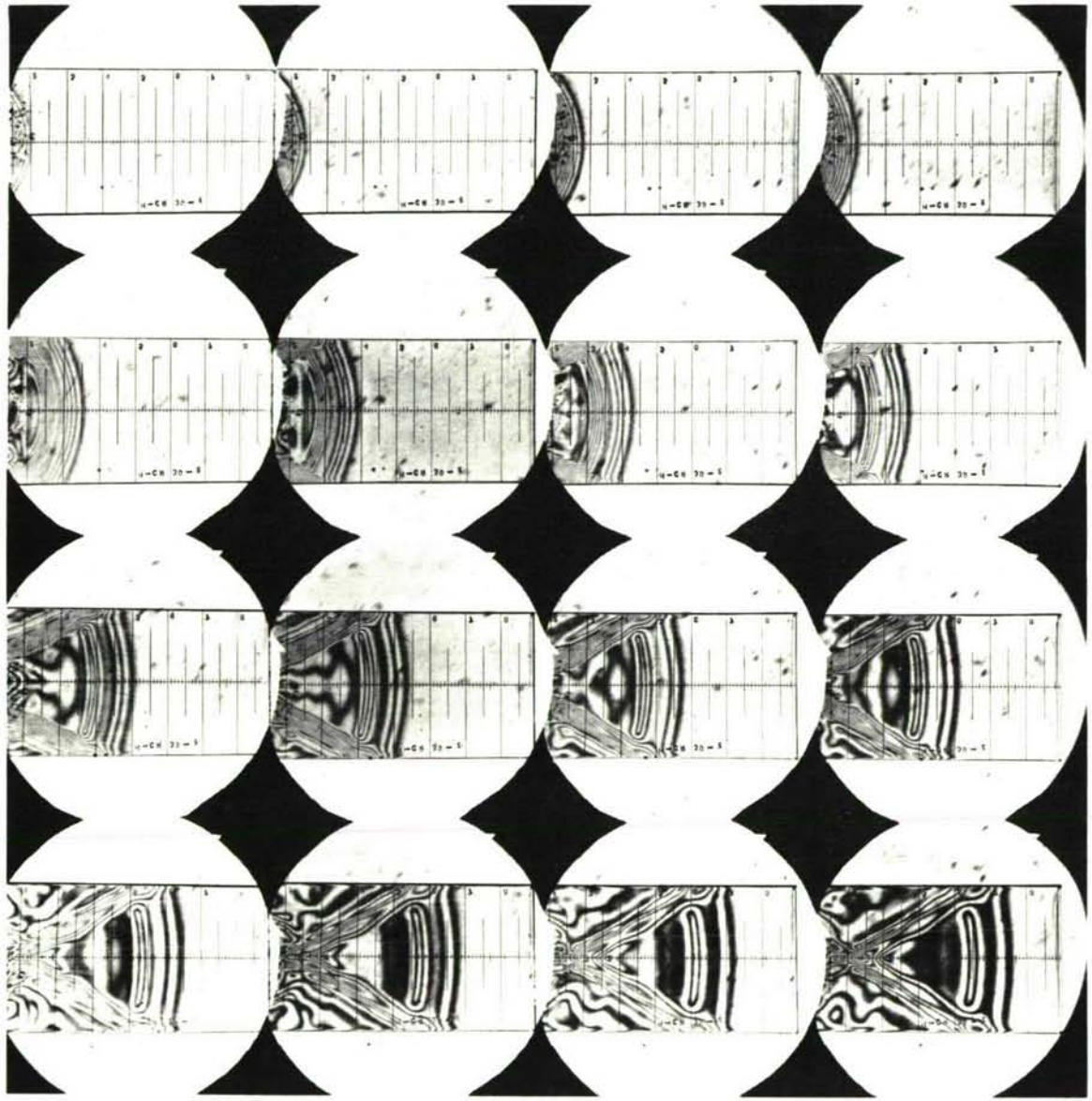


Figure 8. ISOCHROMATIC FRINGE PATTERNS IN COLUMBIA RESIN (CR-39) UNDER EXPLOSIVE LOADING (CAMERA SPEED: 193,000 FRAMES/SECOND)

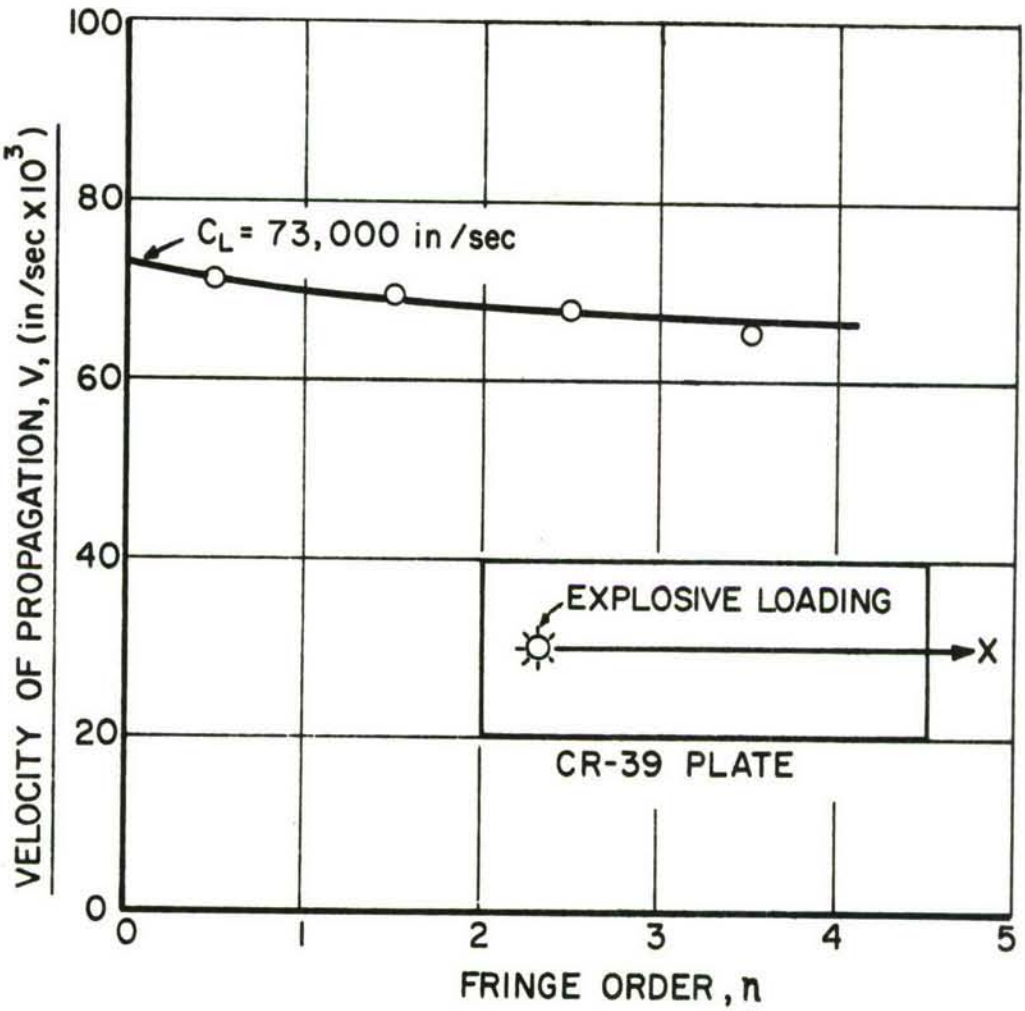


Figure 9. WAVE PROPAGATION IN COLUMBIA RESIN (CR-39) PLATE AS A FUNCTION OF FRINGE ORDER

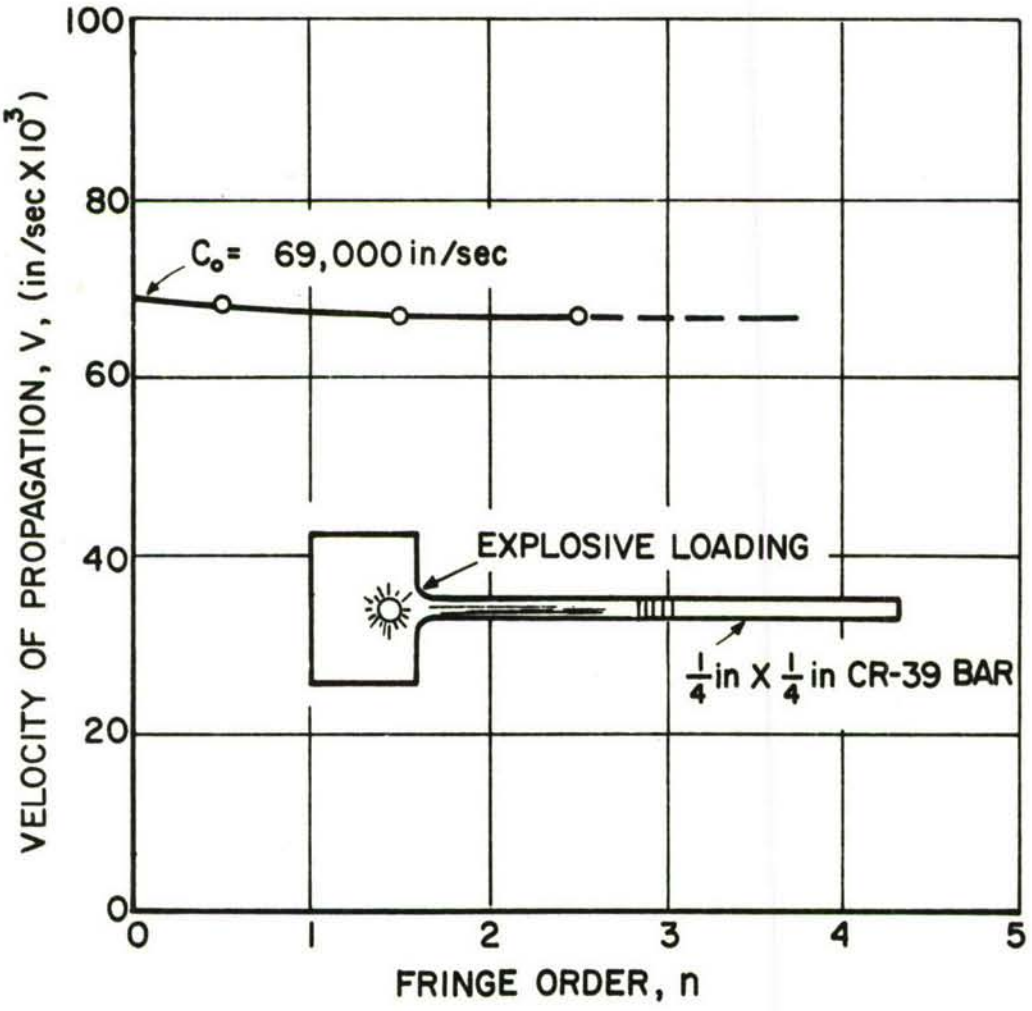


Figure 10. WAVE PROPAGATION IN CR-39 BAR AS A FUNCTION OF FRINGE ORDER

fringe order a uniaxial propagation velocity of

$$c_o = 69{,}000 \text{ in./sec}$$

is obtained.

Similar evaluation studies were conducted on other candidate materials. Isochromatic fringe patterns for similarly loaded plates of Plexiglas, Homalite-100, Laminac Exp. 126-3, Cellulose Acetate Butyrate, and two combinations of Dwo Epoxy Resins 732 and 331 (DER 60/40 and DER 70/30) are shown in Figs. 11 through 16. These patterns were analyzed to obtain the velocity of propagation of various fringe orders. The velocity of the wavefront was then obtained by extrapolation to the zero order fringe. The propagation velocities as a function of fringe order with the velocity of the wavefront obtained by extrapolation for the materials tested are shown in Figs. 17 through 24.

From these results, it can be seen that all "hard" birefringent materials have wave propagation velocities ranging from 60,000 to 100,000 in./sec. The combinations of Dow epoxy resins, however, offer the greatest variability in velocity of propagation and hence in impedance. The densities of all materials tested were measured and the impedances computed as shown in Table I. On the basis of these results, it was decided to use Columbia Resin (CR-39) as the high impedance medium and a mixture of 60 parts (by weight) of Dow flexible epoxy resin (DER 732) to 40 parts of Dow rigid epoxy resin (DER 331) as the low impedance medium for the layered model subjected to explosive loading. The impedance ratio of these two materials is:

$$\frac{(\rho\, c_L)\ \text{CR-39}}{(\rho\, c_L)\ \text{DER 60/40}} = \frac{8.84}{4.40} = 2.01$$

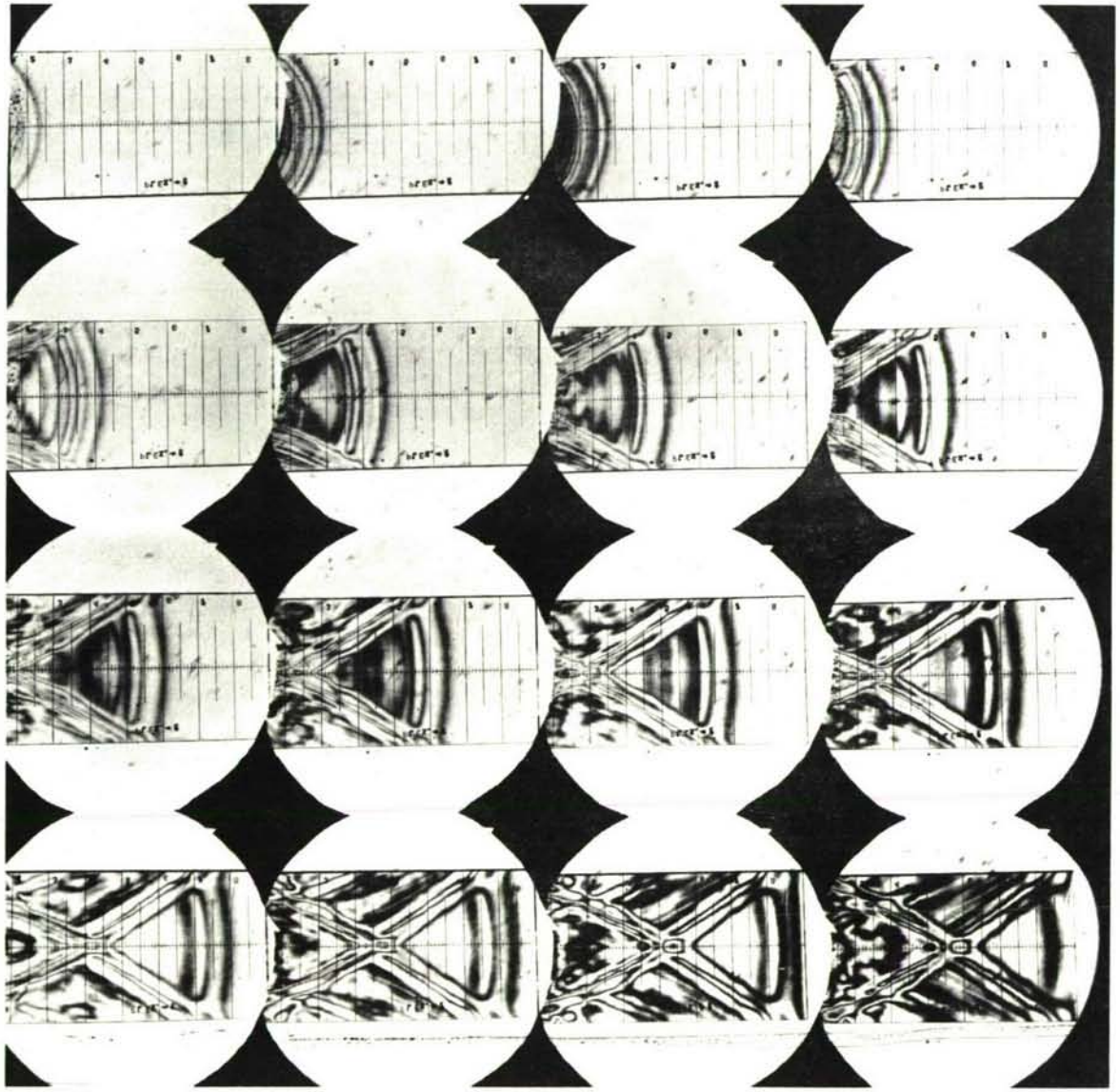


Figure 11. ISOCHROMATIC FRINGE PATTERNS IN PLEXIGLAS UNDER EXPLOSIVE LOADING (CAMERA SPEED: 193,000 FRAMES/SECOND)

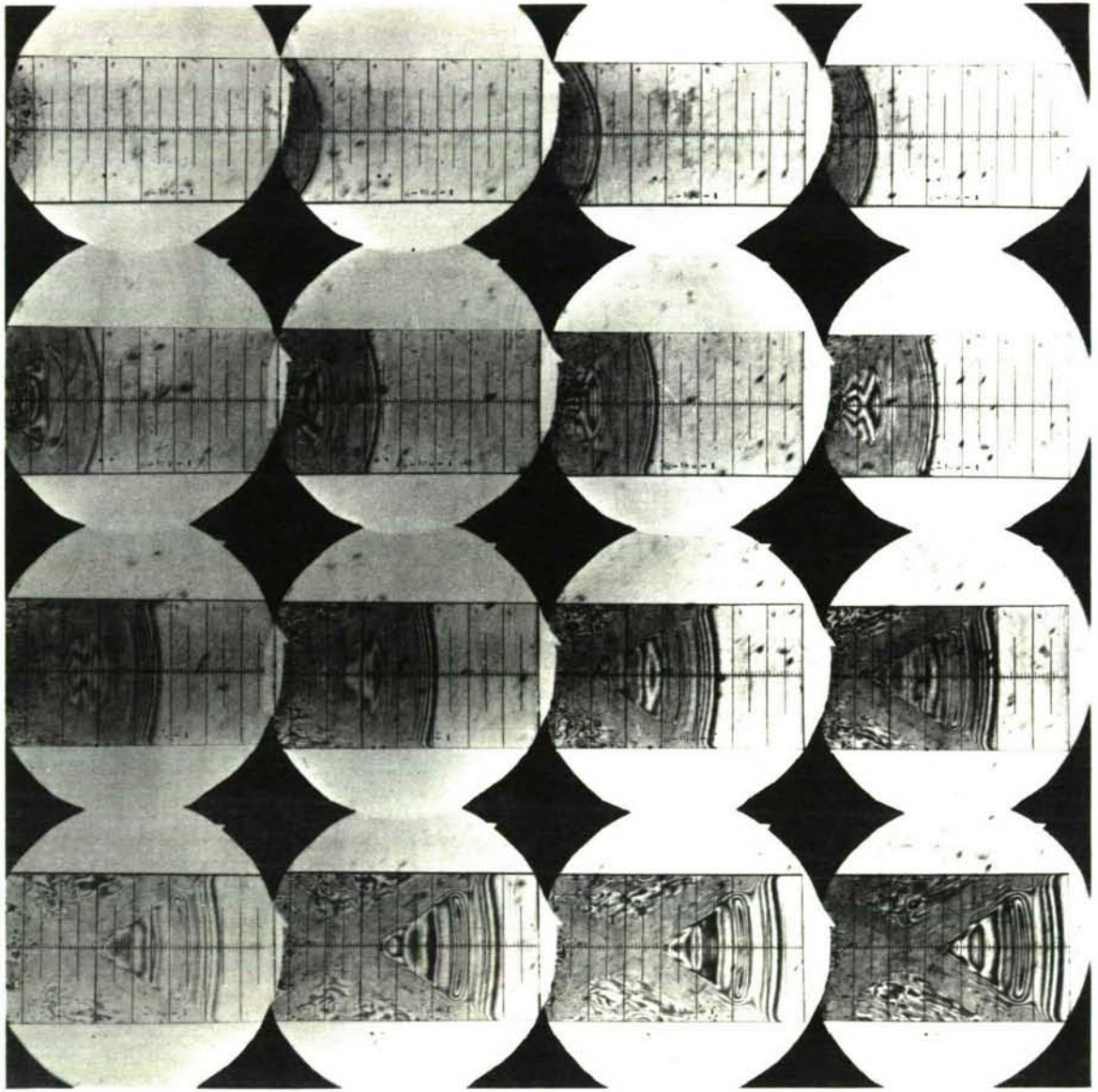


Figure 12. ISOCHROMATIC FRINGE PATTERNS IN HOMALITE-100 PLATE UNDER EXPLOSIVE LOADING (CAMERA SPEED: 193,000 FRAMES/SECOND)

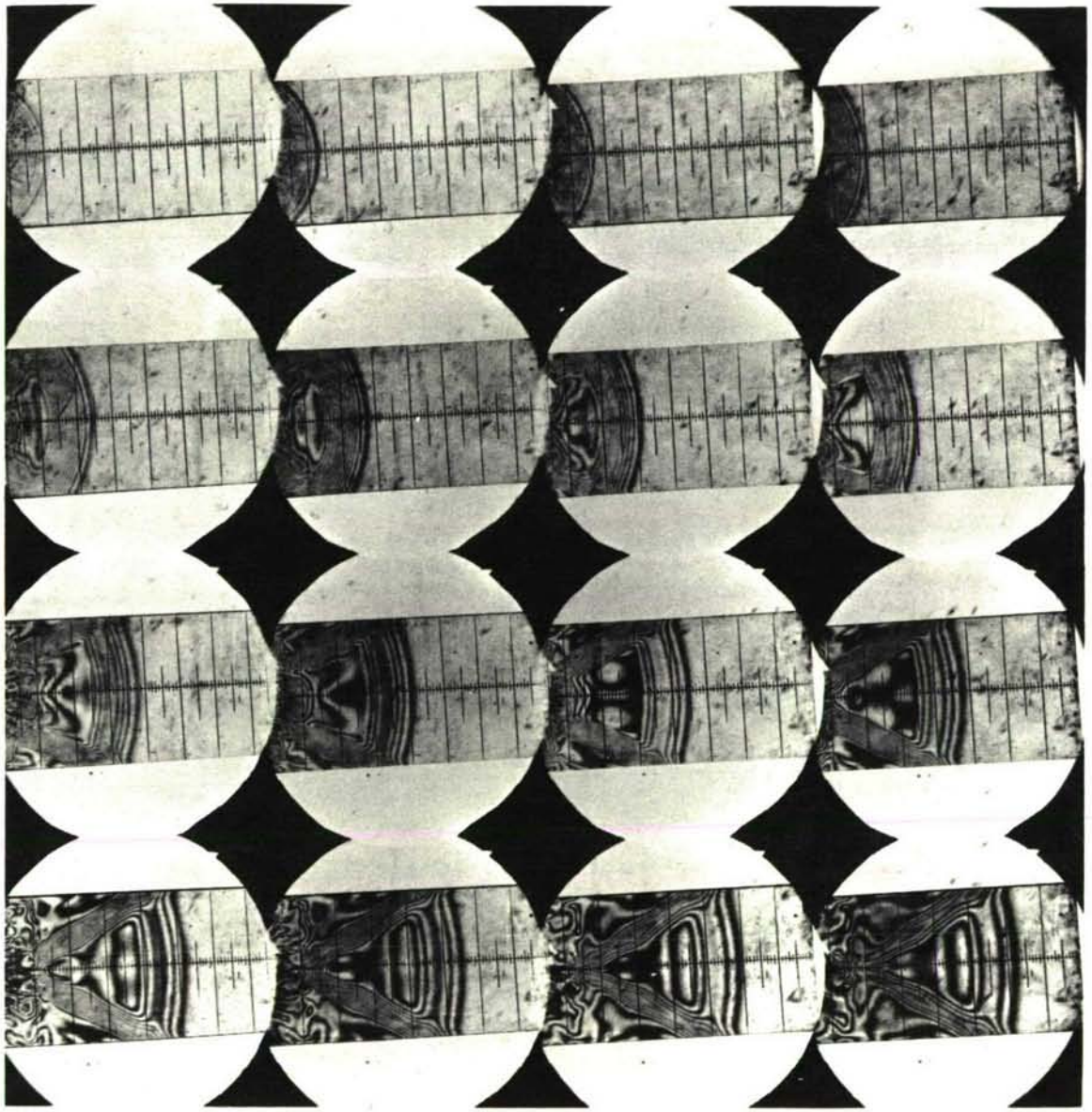


Figure 13. ISOCHROMATIC FRINGE PATTERNS IN LAMINAC EXP. 126-3 PLATE UNDER EXPLOSIVE LOADING (CAMERA SPEED: 193,000 FRAMES/SECOND)

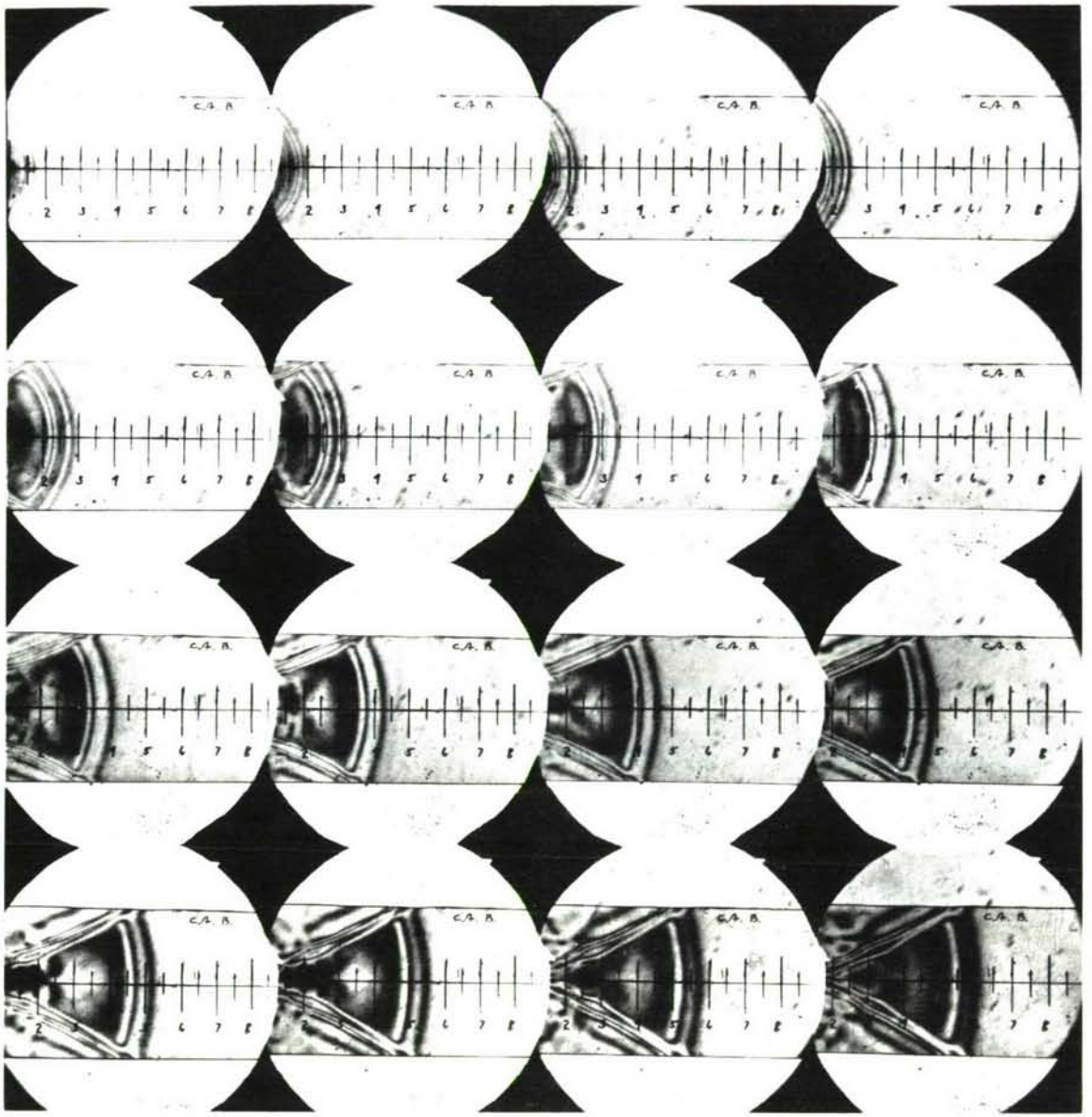


Figure 14. ISOCHROMATIC FRINGE PATTERNS IN CELLULOSE ACETATE BUTYRATE UNDER EXPLOSIVE LOADING (CAMERA SPEED: 193,000 FRAMES/SECOND)

MEDIUM 3 IN. FROM INTERFACE; IMPEDANCE RATIO 2.18:1; CAMERA SPEED: 200,000

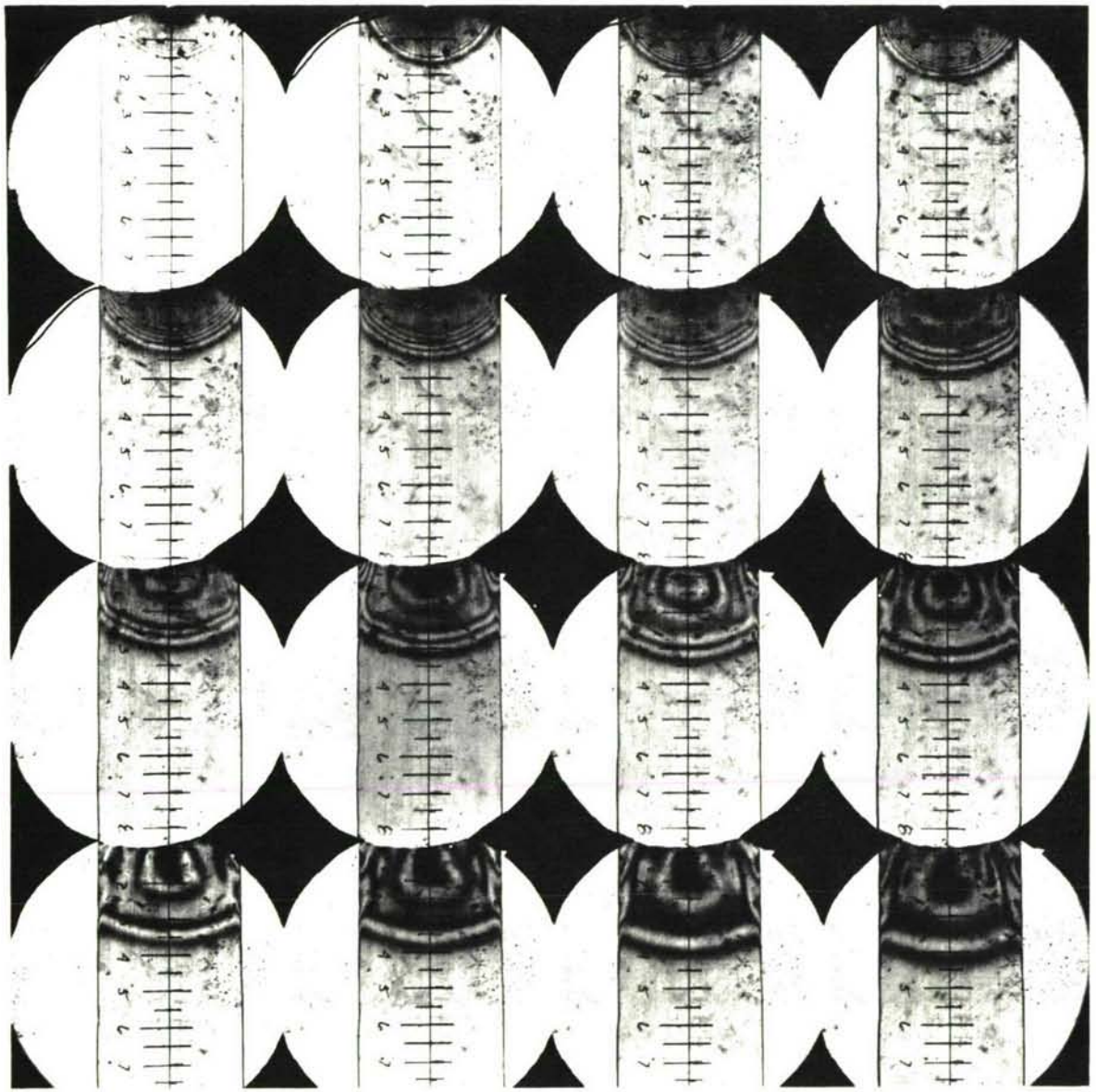


Figure 15. ISOCHROMATIC FRINGE PATTERNS IN EPOXY RESIN (60 PERCENT DER 732 AND 40 PERCENT DER 331) PLATE UNDER EXPLOSIVE LOADING (CAMERA SPEED: 193,000 FRAMES/SECOND)

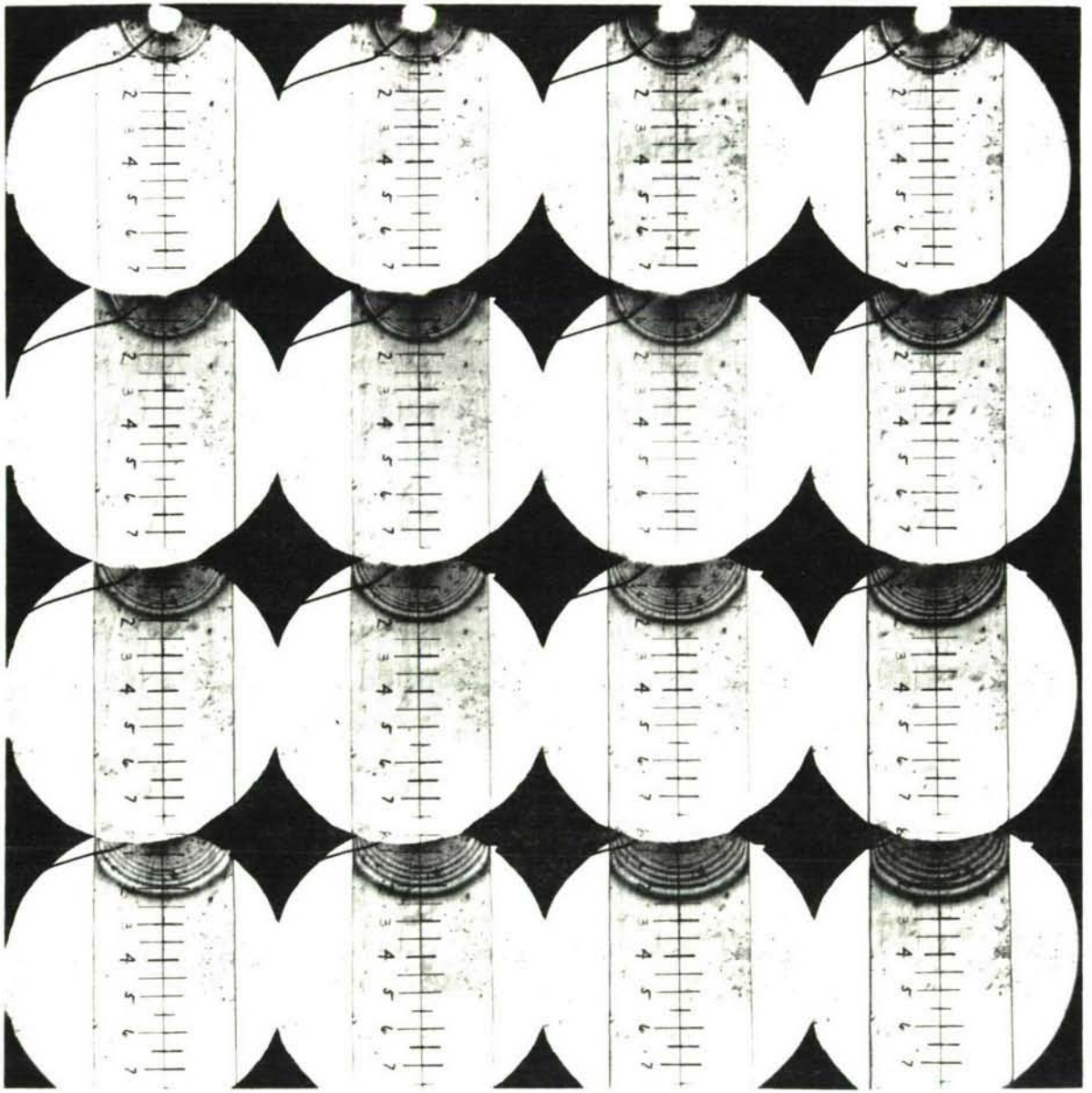


Figure 16. ISOCHROMATIC FRINGE PATTERNS IN EPOXY RESIN (70 PERCENT DER 732, 30 PERCENT DER 331) PLATE UNDER EXPLOSIVE LOADING (CAMERA SPEED: 193,000 FRAMES/SECOND)

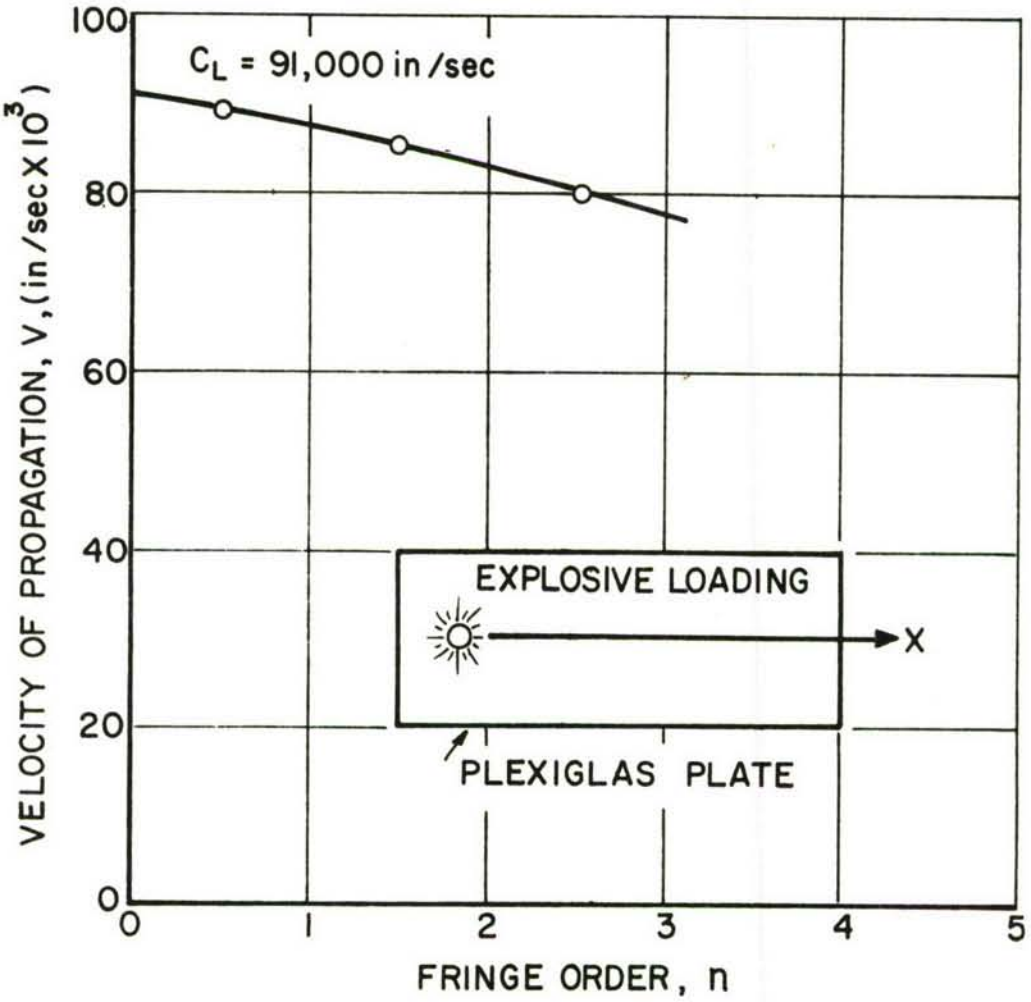


Figure 17. WAVE PROPAGATION IN PLEXIGLAS PLATE AS A FUNCTION OF FRINGE ORDER

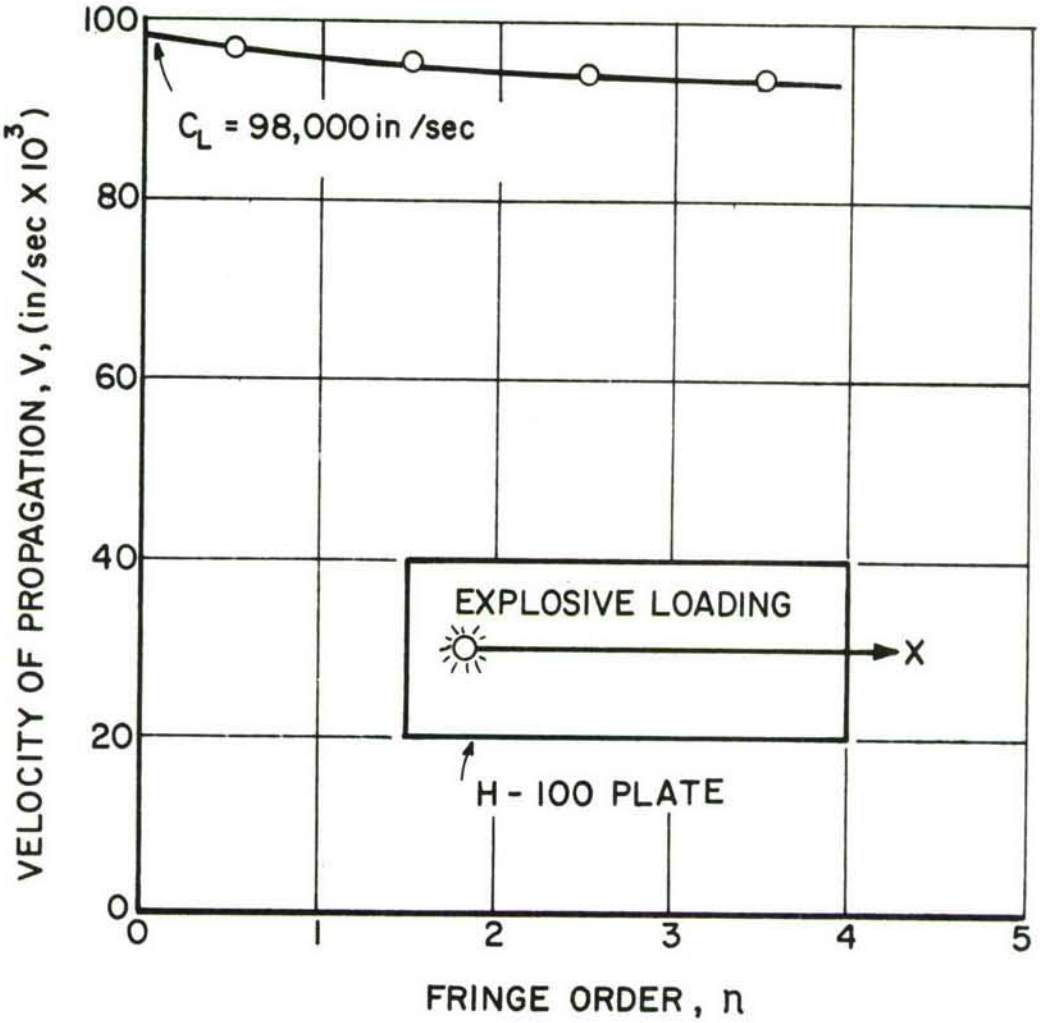


Figure 18. WAVE PROPAGATION IN HOMALITE-100 PLATE AS A FUNCTION OF FRINGE ORDER

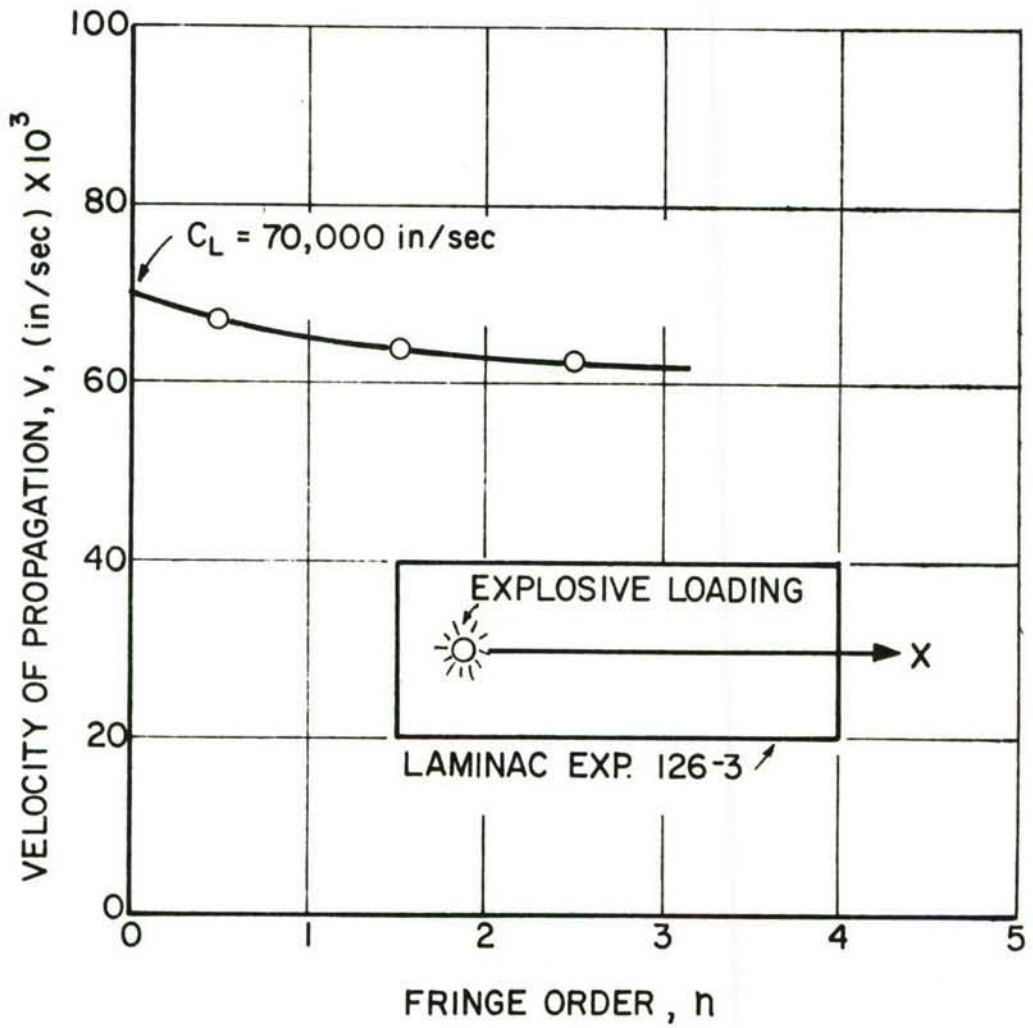


Figure 19. WAVE PROPAGATION IN LAMINAC PLATE AS A FUNCTION OF FRINGE ORDER

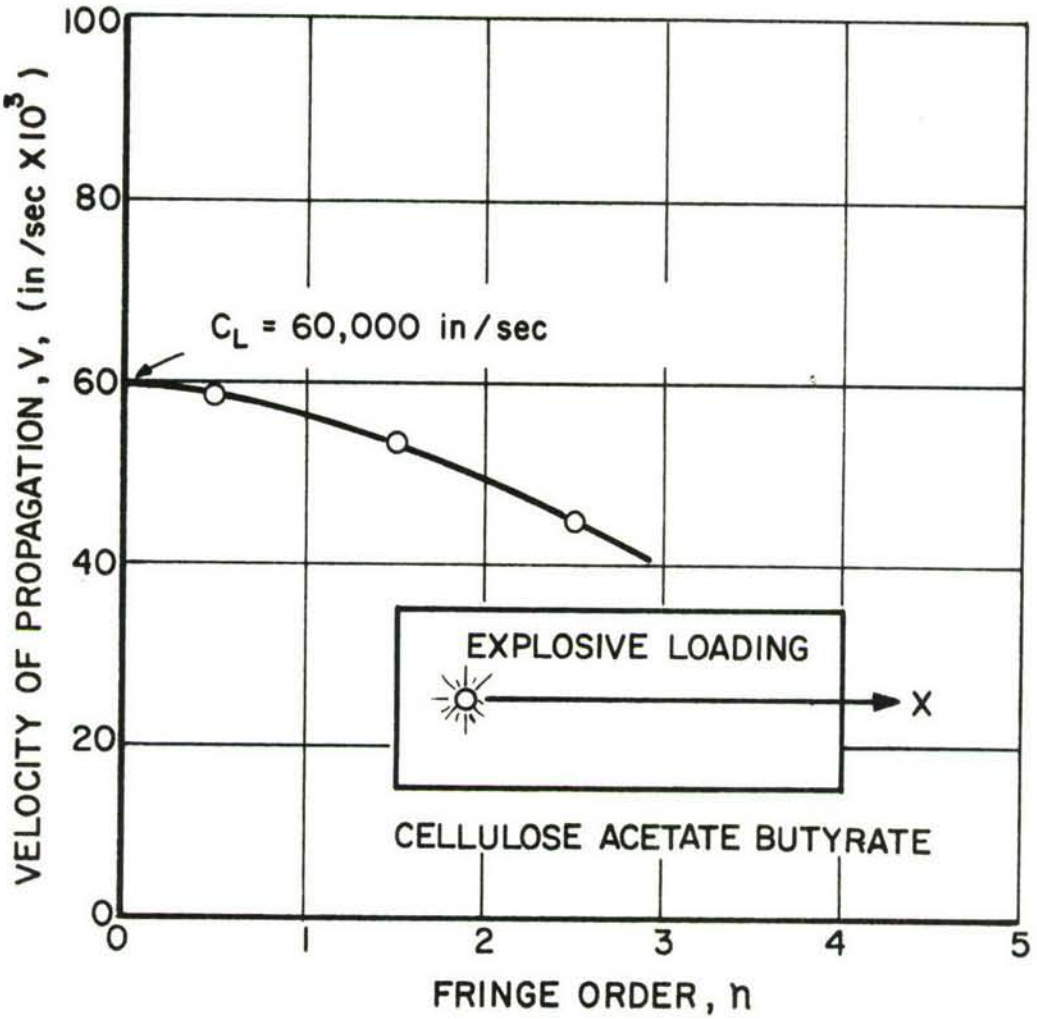


Figure 20. WAVE PROPAGATION IN CELLULOSE ACETATE BUTYRATE PLATE AS A FUNCTION OF FRINGE ORDER

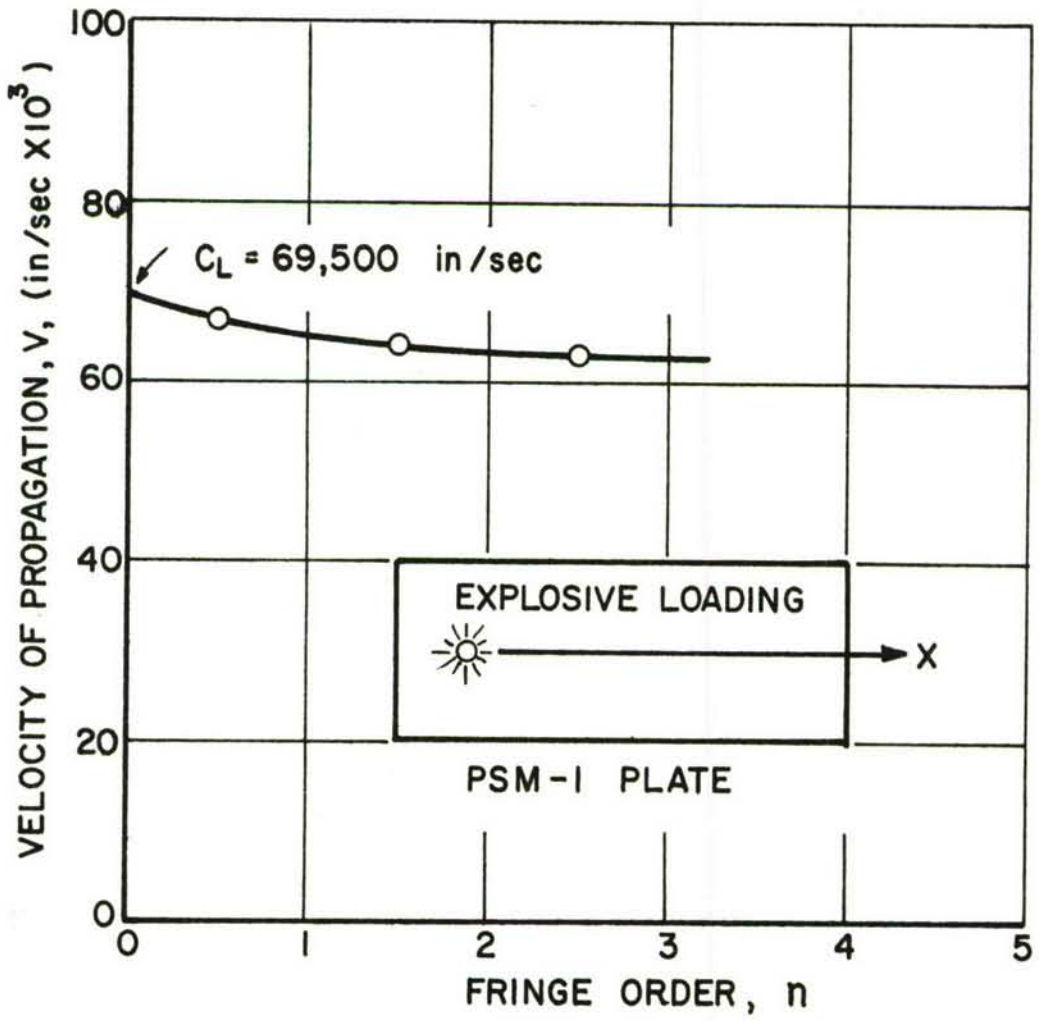


Figure 21. WAVE PROPAGATION IN PSM-1 PLATE AS A FUNCTION OF FRINGE ORDER

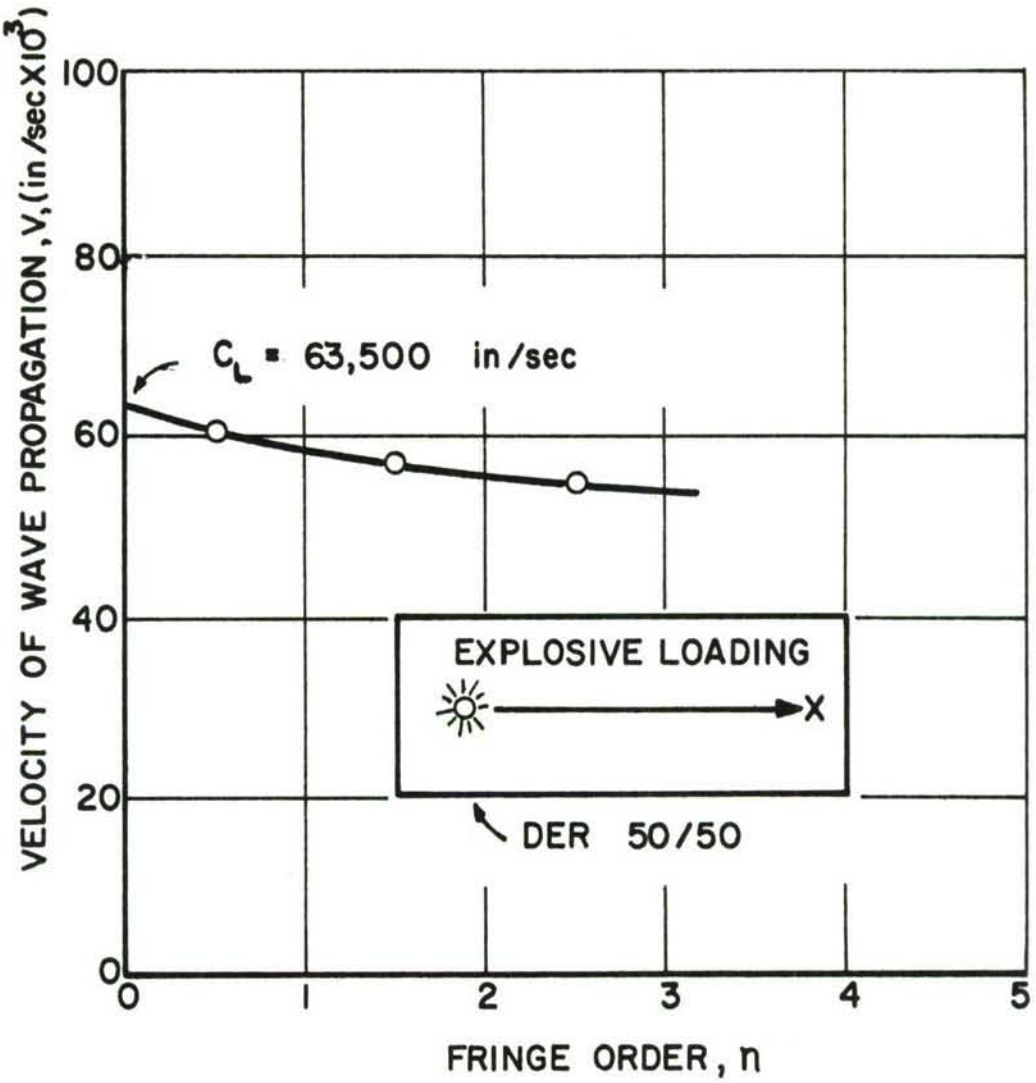


Figure 22. WAVE PROPAGATION IN DER 50/50 PLATE AS A FUNCTION OF FRINGE ORDER

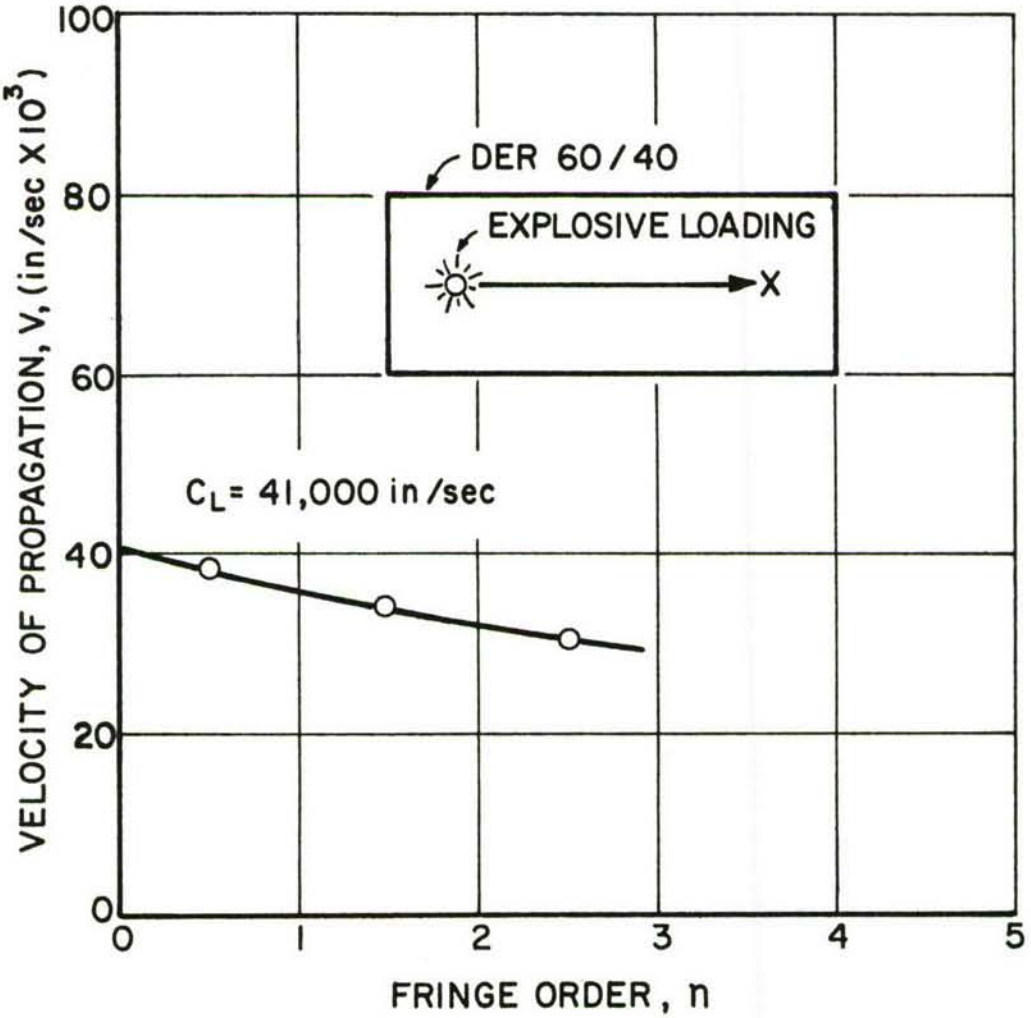


Figure 23. WAVE PROPAGATION IN DER 60/40 PLATE AS A FUNCTION OF FRINGE ORDER

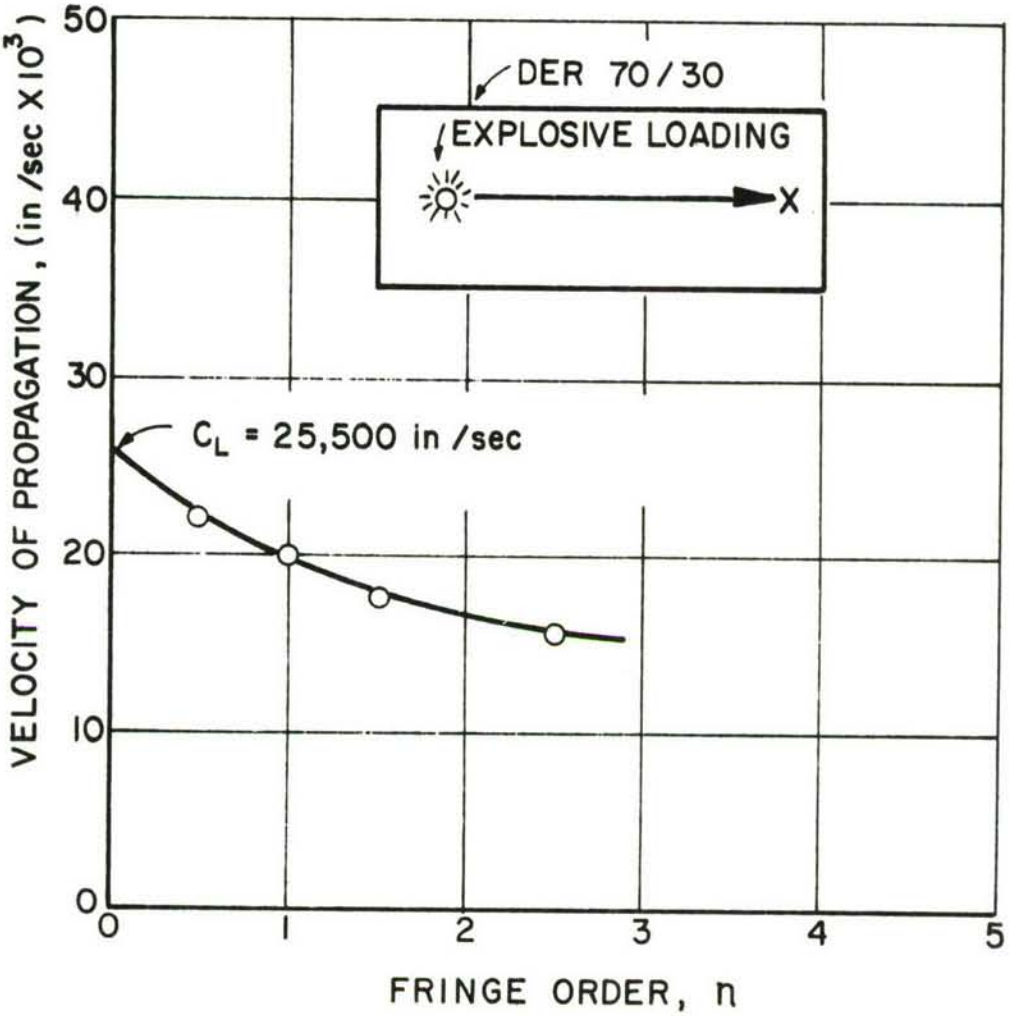


Figure 24. WAVE PROPAGATION IN DER 70/30 PLATE AS A FUNCTION OF FRINGE ORDER

Table I

PROPERTIES OF CANDIDATE MODEL MATERIALS FOR EXPLOSIVE LOADING EXPERIMENTS

Material	Wave Propagation Velocity in Plate c_L (in./sec)	Density ρ $(\frac{\text{lb sec}^2}{\text{in.}^4})$	Impedance ρc_L $(\frac{\text{lb sec}}{\text{in.}^3})$
Columbia Resin (CR-39)	73,000	0.000121	8.84
Plexiglas	91,000	0.000110	10.03
Homalite-100	98,000	0.000110	10.78
Laminac (Exp. 126-3)	70,000	0.000115	8.05
Polyester PSM-1	65,000	0.000107	6.94
DER 50/50*	63,500	0.000108	6.85
DER 60/40*	41,000	0.000107	4.40
DER 70/30*	25,500	0.000105	2.68
Cellulose Acetate Butyrate	60,000	0.000108	6.48

*DER x/y denotes mixture of x-parts of Dow Epoxy Resin DER 732 and y-parts of DER 331.

3. Materials for Air Shock Loading Experiments

The study of candidate materials to be employed for the air shock loading was carried out by machining 3/8 in. thick plate specimens having the dimensions 6 in. x 16 in. The list of low-modulus photoelastic materials which were studied and evaluated as potential materials for the two-layered air blast model includes:

1. Solithane 113 (with 29 pph Catalyst 300 and 9 pph Catalyst 328).
2. Solithane 113 (with 51 pph Catalyst 300 4.5 pph Catalyst 328).
3. Scotchcast No. 221.
4. Hysol Urethane (static modulus, 1300 psi).
5. Hysol Urethane CP5-4485 (static modulus, 500 psi).
6. Mixture of Hysol Urethane (90 parts) and Hysol Epoxy (10 parts).
7. Mixture of Dow epoxy resins; 75 parts flexible DER 732 and 25 parts rigid DER 331.
8. Mixture of Dow epoxy resins; 85 parts flexible DER 732 and 15 parts rigid DER 331.
9. Polybutadiene rubber (Diene 35).

These evaluation studies were conducted by placing the plate specimens of these materials in the model support fixture and subjecting one of the 16 in. edges to an air-blast loading from the shock tube. The material evaluation specimens were subjected to exactly the same air-shock pressure pulse selected for the two-layered air-blast model. A driver pressure of 600 psi was used and the pressure pulse at the specimen location was monitored for each loading with a piezoelectric pressure gage (Kistler, Model 601A). The oscilloscope trace of the output signal from the gage showed a pressure pulse having a sharp rise (μ sec range) to a maximum level

of approximately 52 psi and then an exponential decay to zero pressure in 18 m sec. Transient isochromatic fringe patterns for all candidate materials were recorded with a Fastax camera operating at a rate of approximately 7,500 frames per second.

A preliminary analysis of these photographic records was conducted for the purpose of selecting the most promising candidate materials for the two-layered model. In this initial screening, the approximate propagation velocity of the one-half order fringe of each material was determined by computing the slope of the curve showing the position of the one-half order fringe as a function of time (i.e., the elapsed time between successive frames as defined by the operating framing rate of the Fastax camera). It was found that this velocity remained nearly constant with time for all materials. Results of this analysis are tabulated in Table II.

Table II
PROPAGATION VELOCITY OF CANDIDATE MODEL MATERIALS
FOR AIR-SHOCK LOADING EXPERIMENTS

Material	Propagation Velocity of Half-Order Fringe, in./sec
Solithane 113 (29 pph Catalyst 300)	Velocity too high for Analysis
Solithane 113 (51 pph Catalyst 300)	15,000
Scotchcast No. 221	15,000
Hysol Urethane (E_{static} = 1,300 psi)	5,000
Hysol Urethane CP5-4485 (E_{static} = 500 psi)	4,700
Hysol 90/10 (90 parts Urethane, 10 parts Epoxy)	15,000
DER 75/25*	8,400
DER 85/15*	5,200

*DER x/y denotes mixture of x-parts of Dow Epoxy Resin DER 732 and y-parts of DER 331.

On the basis of the results above, a more detailed evaluation was undertaken of the three most promising materials, Hysol CP5-4485, DER 75/25 and DER 85/15. The propagation velocity of several fringe orders for these materials was determined as before and results are plotted in Fig. 25. It can be noted that the propagation velocity decreases sharply with increasing fringe order, indicating pronounced viscoelastic behavior of these materials under air shock loading. The velocities of the wavefront, obtained by extrapolation to the zero order fringe, are as follows:

DER 75/25:* c_L = 10,400 in./sec

DER 85/15:* c_L = 5,800 in./sec

Hysol CP5-4485: c_L = 5,400 in./sec

It was decided to use Dow epoxy resins for both media of the layered model because of their similarity in mechanical and chemical properties and light transmission characteristics. DER 85/15 was chosen as the low impedance material. In order to obtain the exact formulation of the high impedance material, wave propagation velocities were obtained for various mixtures of flexible (DER 732) and rigid (DER 331) Dow epoxy resin. By plotting these propagation velocities as a function of the mixture rario, it was found that the mixture DER 73/27 had exactly twice the impedance of DER 85/15.

*DER x/y denotes mixture of x-parts of Dow Epoxy Resin DER 732 and y-parts of DER 331.

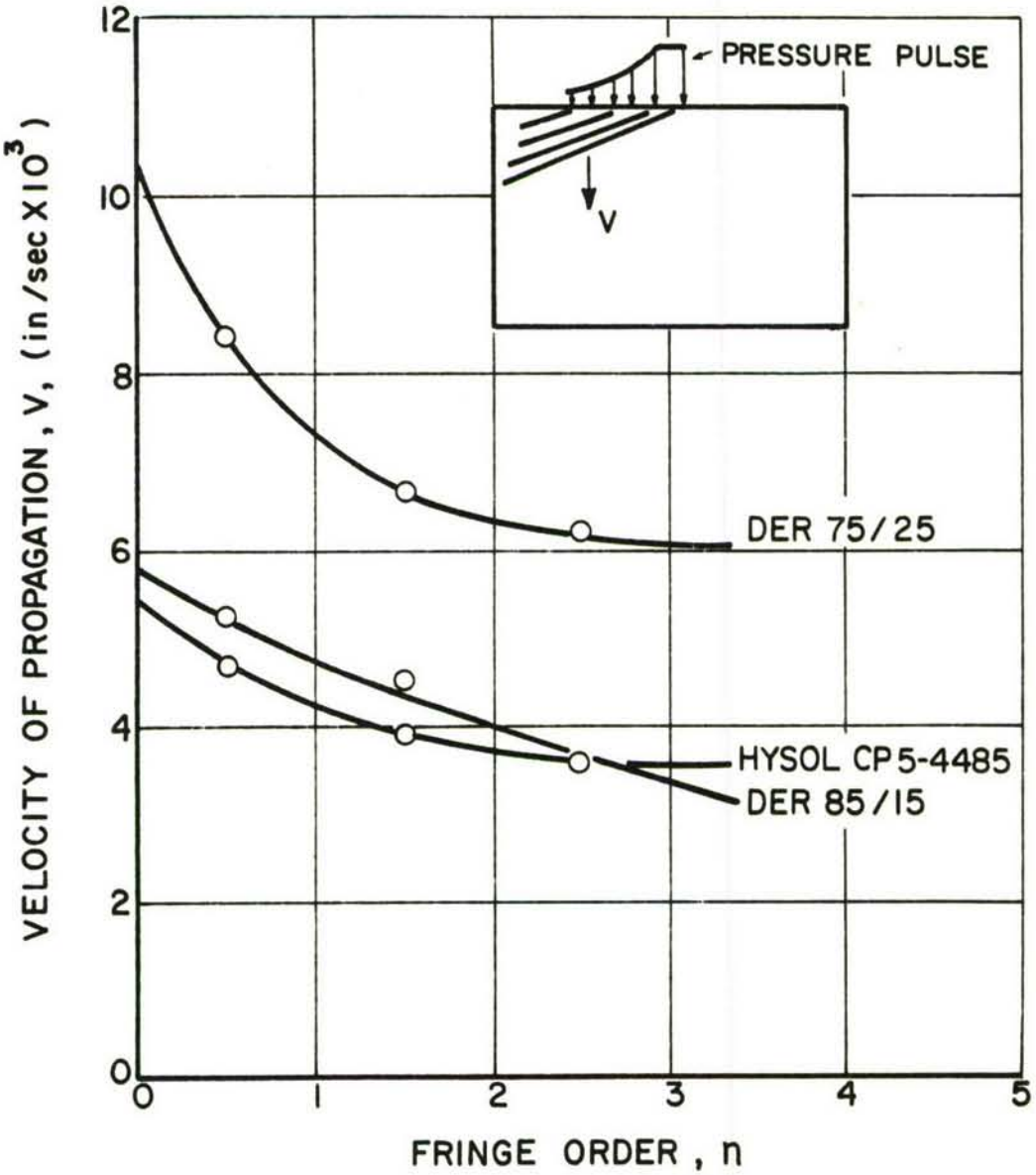


Figure 25. WAVE PROPAGATION VELOCITY AS A FUNCTION OF FRINGE ORDER FOR THREE CANDIDATE MODEL MATERIALS FOR AIR-SHOCK LOADING EXPERIMENTS

SECTION V

PROPERTIES OF MODEL MATERIALS

1. Introduction

To translate birefringence and moiré data into stresses, it is necessary to know the relevant mechanical and optical properties of the model materials. It was realized early that all model materials used exhibit viscoelastic behavior to varying degrees. A full mechanical and optical characterization of these materials was undertaken following previously developed procedures (Ref. 10). It was required to obtain mechanical and optical properties, i.e., relaxation modulus and time-dependent stress fringe value, under conditions of time of loading or strain rate or frequency encountered in the subsequent experiments to be analyzed. Properties of Columbia resin (CR-39) were extracted from the published results by Clark (Ref. 12), whereas most of the properties of the combinations of Dow epoxy resins were obtained by creep tests at low temperatures and a few sinusoidal oscillation tests at room temperature.

2. Dynamic Properties of Columbia Resin (CR-39)

Some properties of Columbia resin have been reported by Clark (Ref. 12) as functions of time from zero to peak loading. His results extend down to approximately 30 μ sec. These curves, plotted on a log-log scale, were extrapolated down to 0.1 μ sec and plotted over the range between 0.1 and 1,000 μ sec in Fig. 26. It is seen that Young's modulus varies from 410,000 psi at 1,000 μ sec to 590,000 psi at 0.1 μ sec. Based on the propagation velocity in a CR-39 bar (Fig. 10) the following modulus is computed:

$$c_o = 69{,}000 \text{ in./sec}$$

$$\rho = 122 \times 10^{-6} \text{ lb sec}^2/\text{in.}^4$$

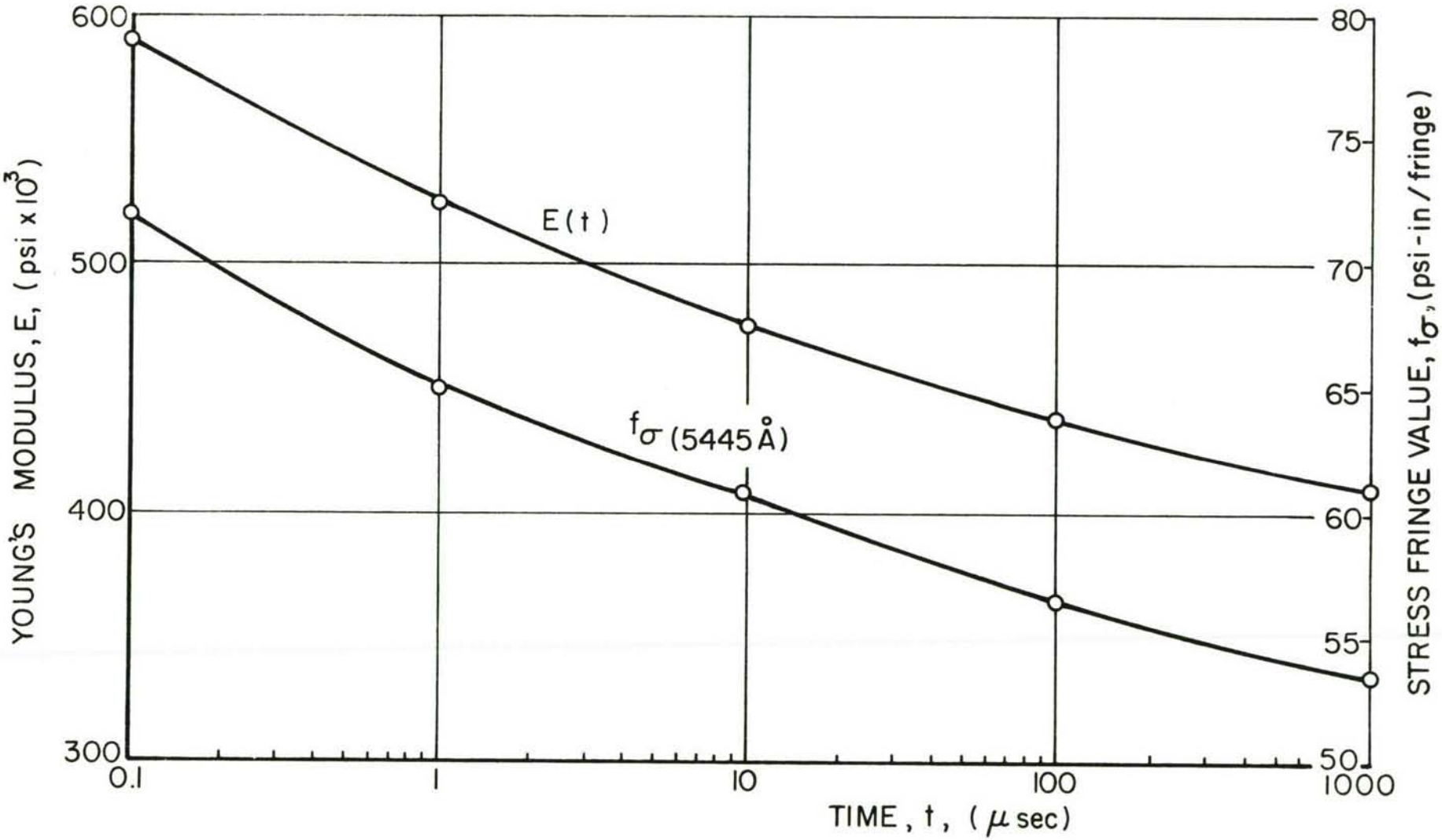


Figure 26. YOUNG'S MODULUS AND STRESS FRINGE VALUE OF CR-39 AS FUNCTIONS OF TIME (BASED ON RESULTS BY CLARK) (Ref. 12)

hence,

$$E = c_o^2 \rho = 580{,}000 \text{ psi} \tag{34}$$

This value of Young's modulus corresponds, according to the curve of Fig. 26, to a loading time of a fraction of a microsecond which is compatible with the known rise time of the PETN explosive charge.

The dynamic Poisson's ratio is obtained by comparing the wave velocity in the bar with that in a plate. From the results shown in Fig. 9

$$c_L = 73{,}000 \text{ in./sec}$$

The ratio of the two velocities is a function of Poisson's ratio only:

$$\frac{c_o}{c_L} = (1 - \nu^2)^{1/2} \tag{35}$$

hence,

$$1 - \nu^2 = \left(\frac{69{,}000}{73{,}000}\right)^2 = 0.893$$

and

$$\nu = 0.33 \tag{36}$$

corresponding to a loading time less than a microsecond.

The stress fringe value varies from a value of 53 psi-in./fringe at 1000 μ sec to 72 psi-in./fringe at 0.1 μ sec. The value corresponding to the time for the Young's modulus given above is approximately 70 psi-in./fringe. The stress fringe values given here correspond to a wavelength of 5445 Å, i.e., that of mercury green. To reduce them for the actual wavelength of 4300 Å used in the Schardin camera it is necessary to multiply them by the ratio of wavelengths $\frac{4300}{5445}$

In reducing strain or birefringent data to obtain stresses the time dependency of the modulus and stress fringe value must be taken into consideration. This is done either by a rigorous viscoelastic analysis or by using the appropriate values corresponding to the time between zero and peak loading at the point in question in a quasi-elastic analysis.

3. Properties of DER 60/40*

This is the material used, in combination with Columbia resin, as the low-impedance medium in the explosive loading experiments. Material characterization in this case was based primarily on creep tests at different temperatures by applying the temperature-time equivalence principle. According to this principle, which has been used successfully in the past (Refs. 2,10), short-time or dynamic properties can be obtained by quasi-static tests at low temperatures.

Creep tests were conducted by subjecting a double tensile specimen (Fig. 27) to a constant load maintained for a period of approximately 24 hours. The specimen is made by cementing two 1.50 in. x 0.50 in. x 0.25 in. prismatic bars of the material to two aluminum end plates. The specimen is suspended from a frame on one end and loaded on the other end through metal rods threaded at the center of these aluminum plates. The probe rod of a differential transformer (DCDT) was threaded to the upper end plate and the core cylinder was attached to the bottom end plate. These tests were conducted inside an environmental chamber at the following temperatures: 75°, 35°, 15°, and 0°F. The axial strain was monitored with the DCDT.

The relaxation Young's modulus as a function of time determined from these creep tests is shown in Fig. 28. Values of this modulus at discrete times were multiplied by the ratio $\frac{T_o}{T}$ of the reference absolute temperature (535°R room temperature) to the absolute temperature of the particular test, were tabulated in Table III and plotted in Fig. 29. In applying the temperature-time equivalence principle, all curves of Fig. 29, except the one corresponding to

*DER x/y denotes mixture of x-parts of Dow Epoxy Resin DER 732 and y-parts of DER 331.

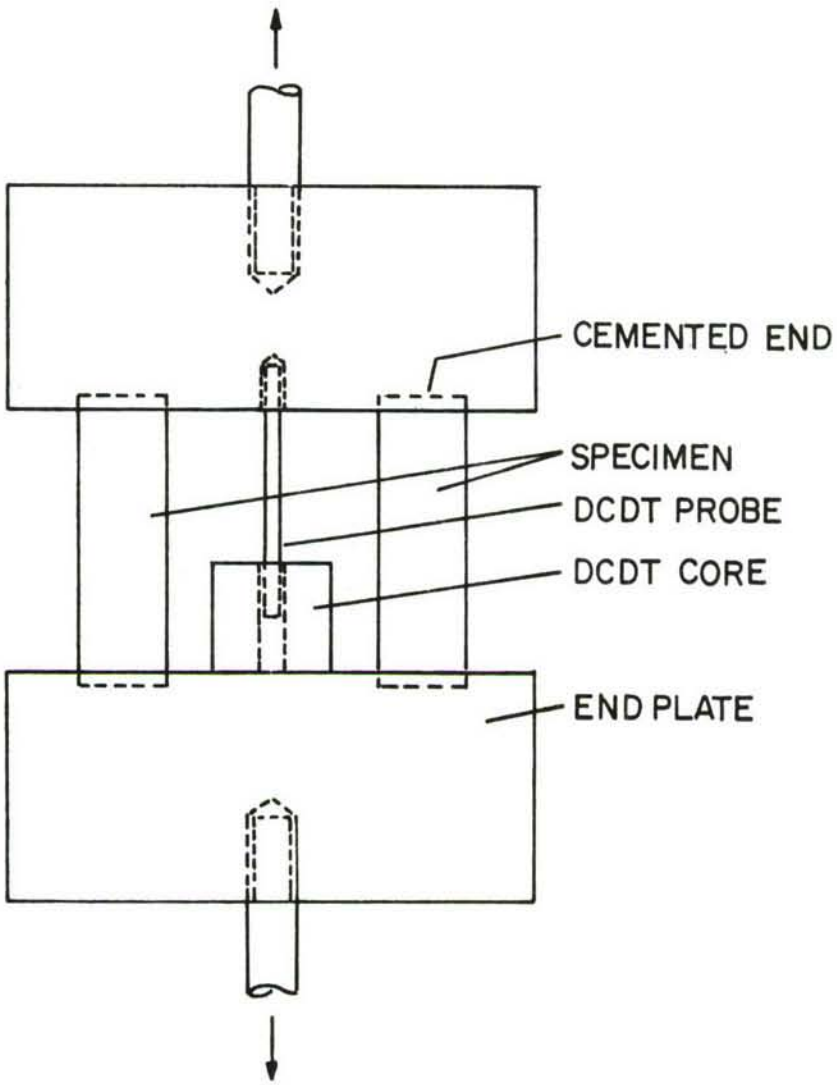


Figure 27. UNIAXIAL TENSILE SPECIMEN USED FOR CREEP TESTS AT VARIOUS TEMPERATURES

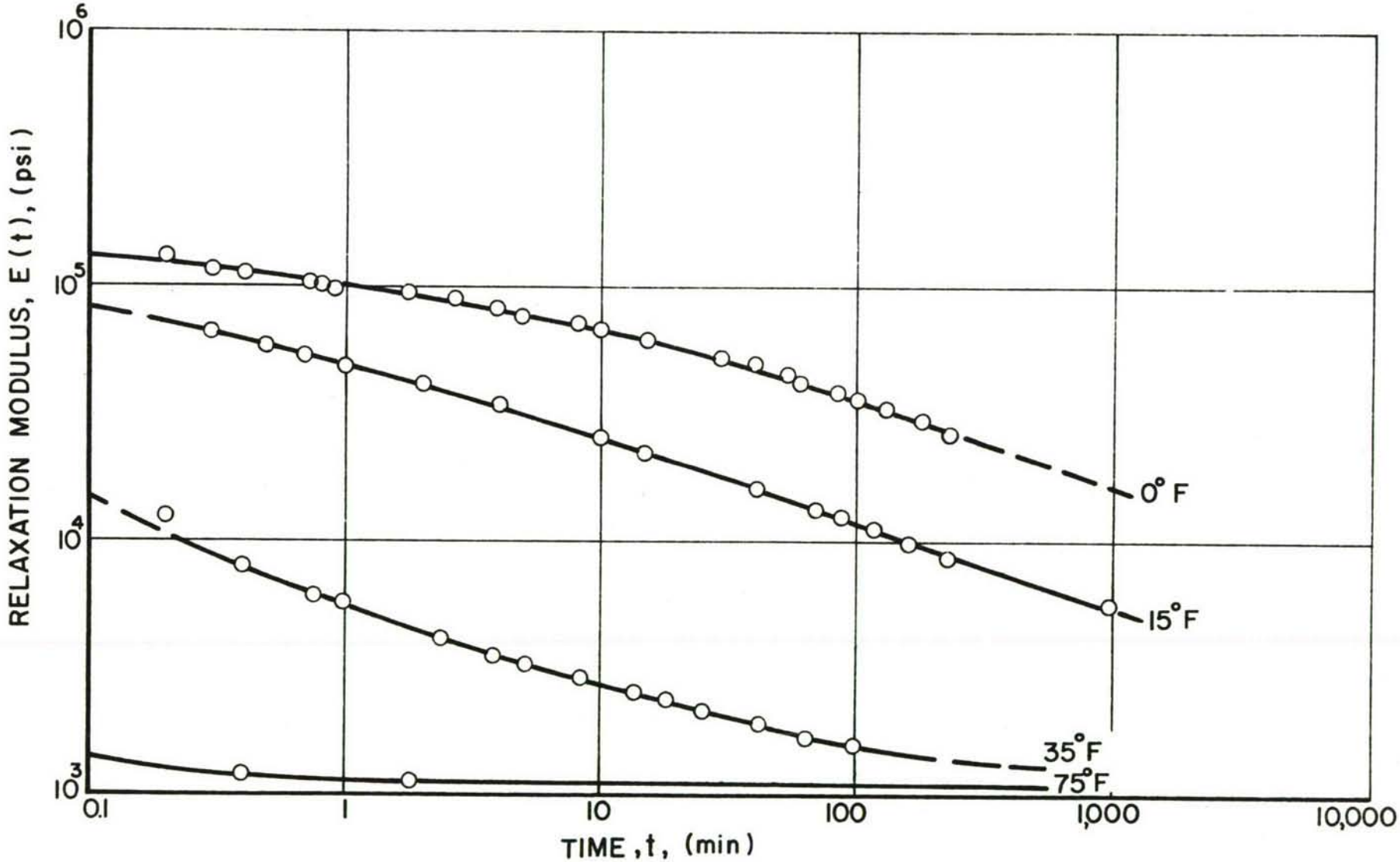


Figure 28. YOUNG'S RELAXATION MODULUS AS A FUNCTION OF TIME AT VARIOUS TEMPERATURES FOR DER 60/40

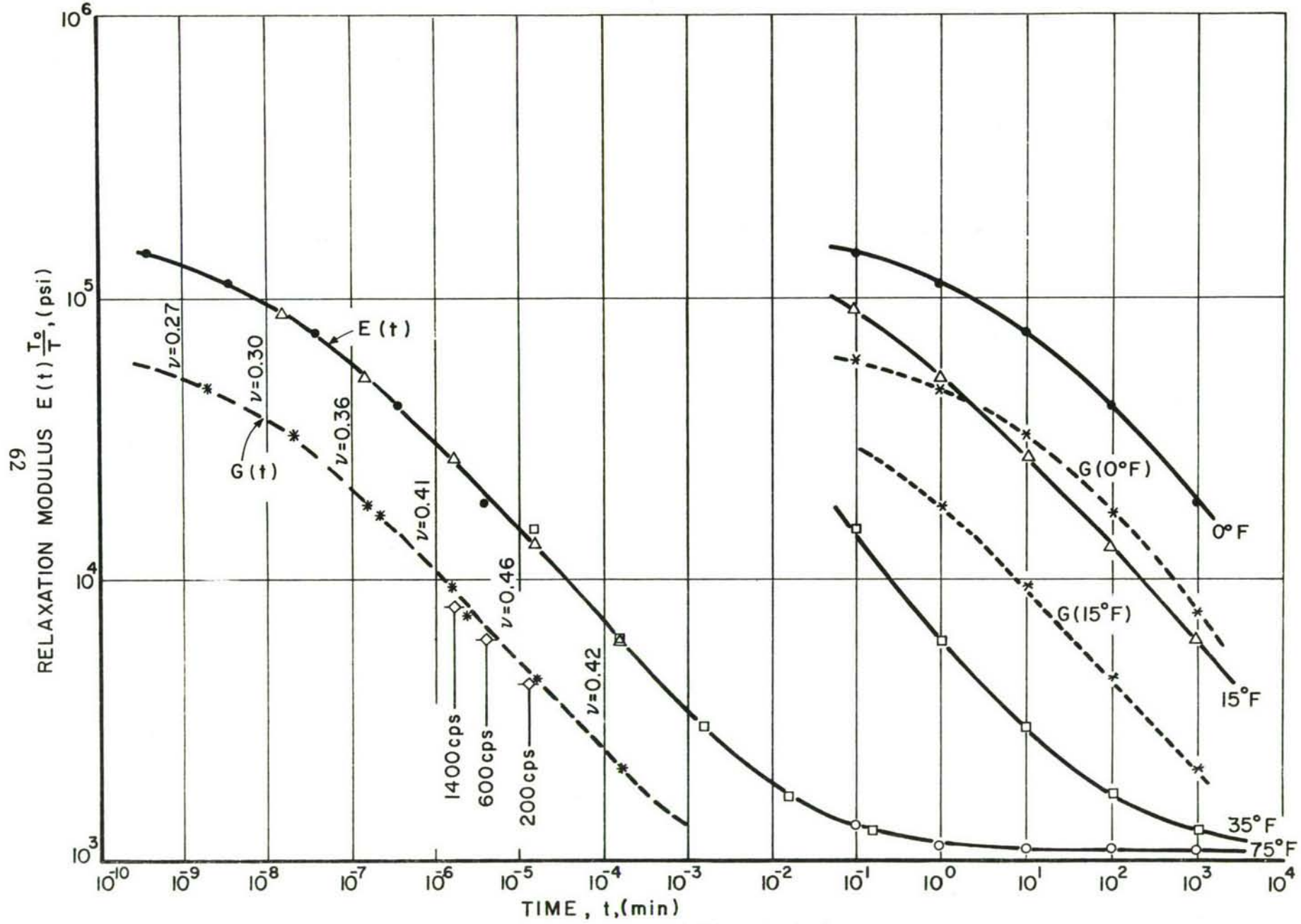


Figure 29. INDIVIDUAL AND COMPOSITE CURVES FOR RELAXATION MODULUS OF DER 60/40

room temperature, were shifted horizontally until one continuous composite curve corresponding to room temperature was obtained. This curve extends over about 14 decades of time and gives a broad spectrum of properties.

The relaxation shear modulus in the time range of interest was obtained independently by conducting simple-shear creep tests

Table III

VALUES OF RELAXATION MODULUS OF DER 60/40* AT VARIOUS TEMPERATURES AND TIMES AFTER LOADING

Time (Min.)	Relaxation Modulus: $E(t)\ \frac{T^*_o}{T}$ (psi)			
	Temperature (°F)			
	75	35	15	0
0.1	1,350	15,000	92,000	144,000
1	1,140	6,000	53,000	113,000
10	1,120	3,000	27,500	75,000
100	1,110	1,700	13,500	41,000
100	1,100	1,300	6,100	18,700

$^*\frac{T_o}{T}$ is the ratio of the reference absolute temperature to the given temperature in degrees Rankine.

*DER x/y denotes mixture of x-parts of Dow Epoxy Resin DER 732 and y-parts of DER 331.

at 15°F and 0°F. This was accomplished by subjecting two prismatic bars (1.50 in. x 0.30 in. x 0.25 in.) of the material to simple shear by means of the fixture shown in Fig. 30. The specimens were cemented along their long edges to the arms of a metal fork on one side and to

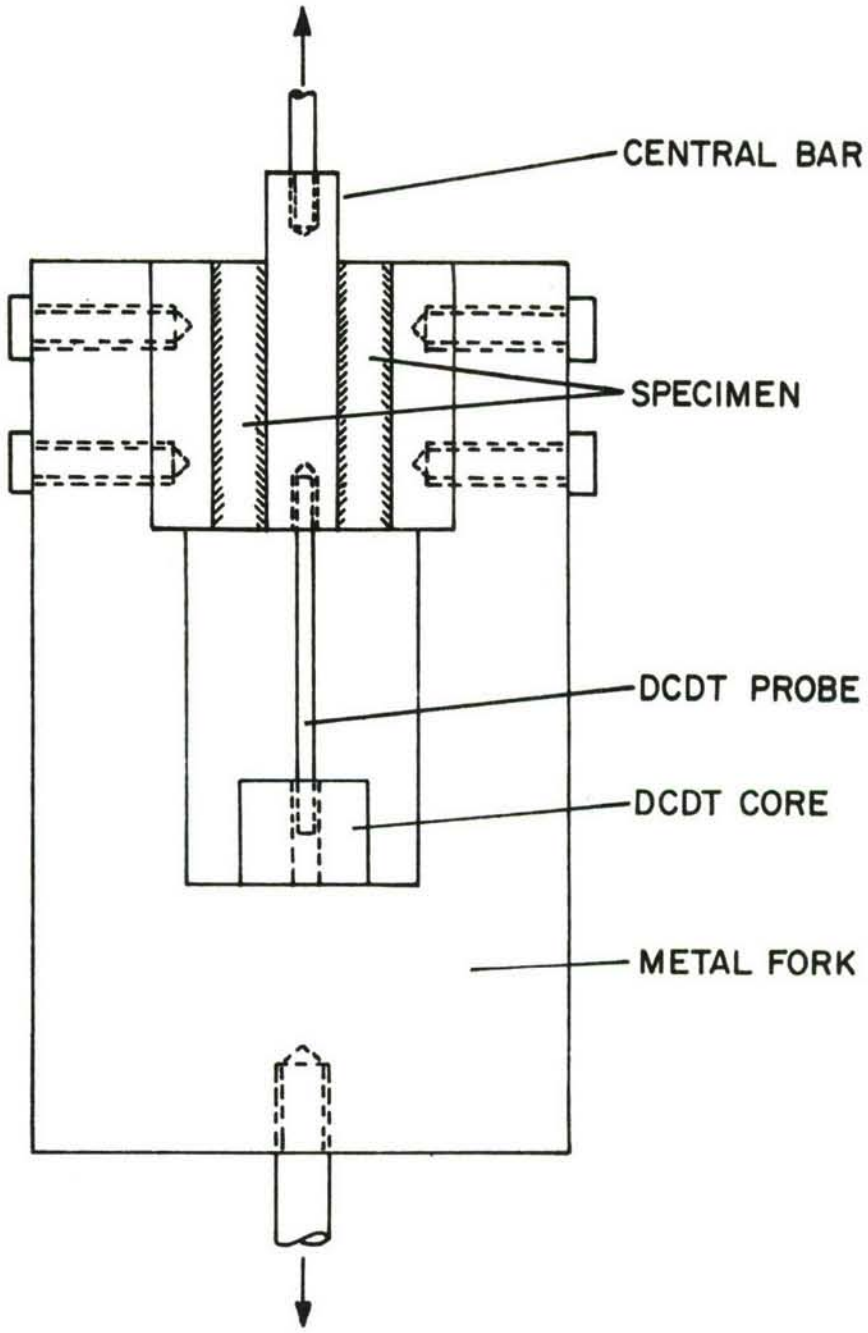


Figure 30. SIMPLE-SHEAR SPECIMEN USED FOR CREEP TEST AT VARIOUS TEMPERATURES

a central metal bar on the other. A DCDT was mounted as shown in Fig. 30 with the probe attached to the central bar and the core cylinder to the fork, thus, measuring the relative displacement of the opposite edges of the specimens. The shear relaxation modulus as a function of time is plotted in Fig. 31. Values of this modulus multiplied by the appropriate absolute temperature ratio were plotted in Fig. 29 and shifted similarly as the values of Young's modulus. A composite curve extending over seven decades of time was thus obtained for the shear relaxation modulus.

The dynamic shear modulus was also checked by means of sinusoidal oscillation tests at various frequencies. The same shear specimen described above was mounted with load cells and accelerometers at the two ends of the specimen and tested in a shaker as described previously (Refs. 2,10). A complex modulus as a function of frequency was obtained and was converted to a relaxation modulus as a function of time by means of an approximate interrelationship. Values computed for some discrete values of frequency are plotted on the composite curve of Fig. 29. The check seems to be satisfactory.

The optical properties of DER 60/40 were determined by taking birefringence readings simultaneously with the elongation readings in the uniaxial tensile creep tests discussed earlier. The four elements of a circular polariscope were inserted in the environmental chamber and measurements were made by the Tardy method of compensation where only the analyzer is rotated. The analyzer was rotated from outside the chamber by means of a flexible shaft. An additional series of photocreep tests using disks under diametral compression was conducted at temperatures 75°, 40°, 20°, and 2°F. Results of these tests in the form of a time-dependent stress fringe value are given in Fig. 32. The stress fringe value at discrete times was multiplied by the aboslute temperature ratio $\frac{T_o}{T}$, tabulated in Table IV and plotted in Fig. 33. By shifting the individual curves for different temperatures, except the one corresponding to room temperature, a composite (master) curve corresponding to room temperature was obtained. This curve is similar in shape to that for the relaxation modulus and shows a very broad transition region. The curve extends over 14 decades to time.

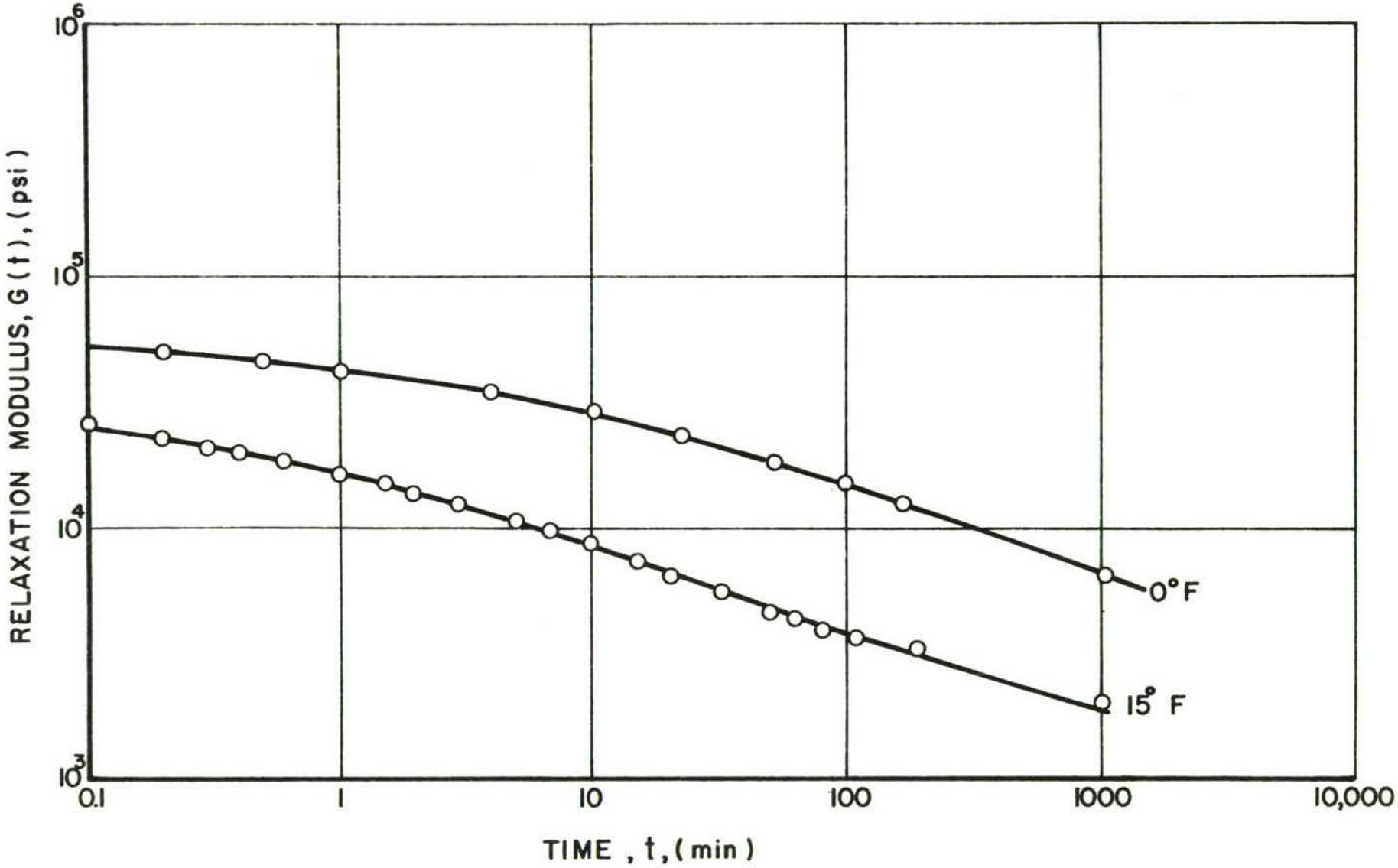


Figure 31. SHEAR RELAXATION MODULUS AS A FUNCTION OF TIME AT VARIOUS TEMPERATURES FOR DER 60/40

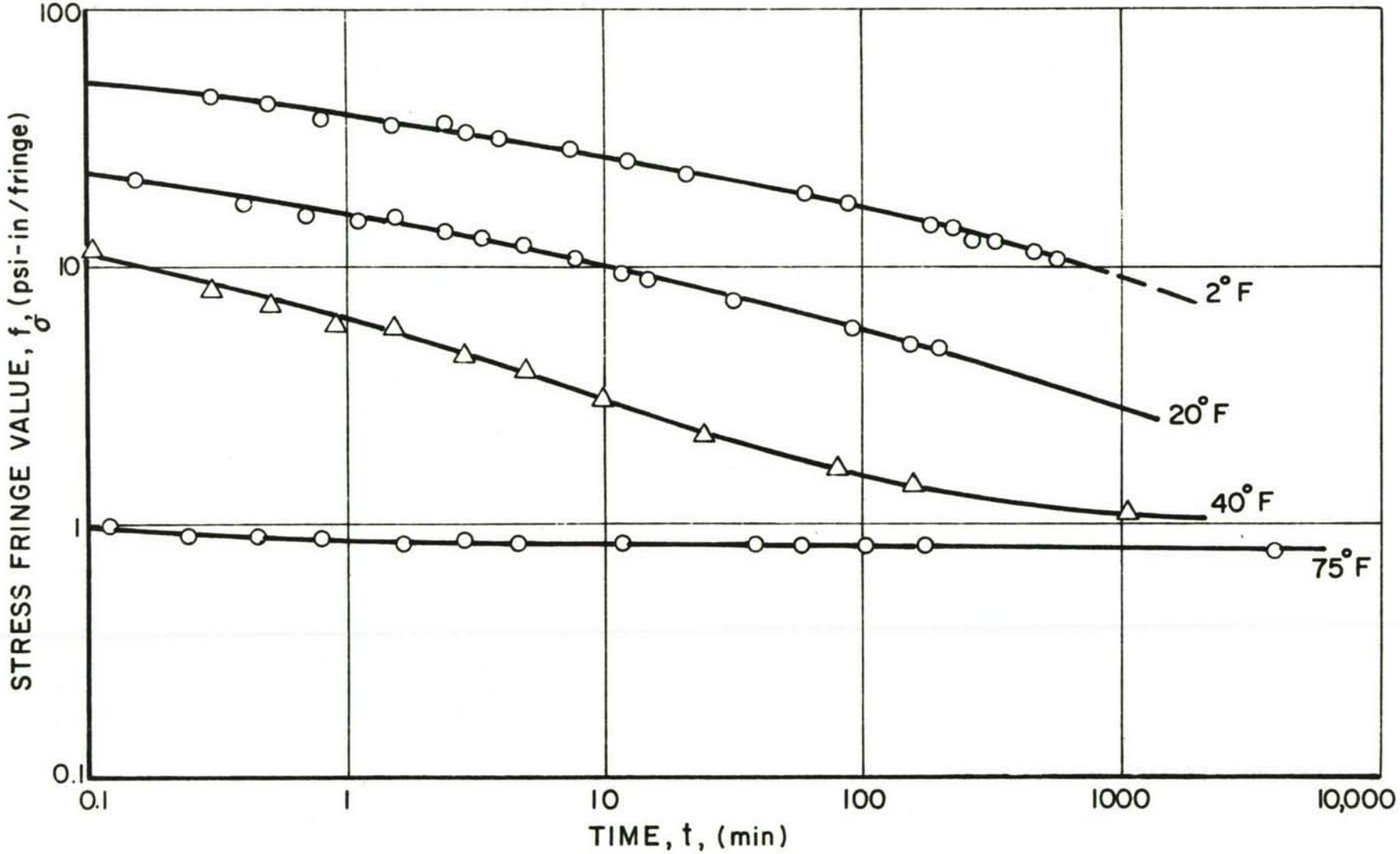


Figure 32. STRESS FRINGE VALUE AS A FUNCTION OF TIME AT VARIOUS TEMPERATURES FOR DER 60/40

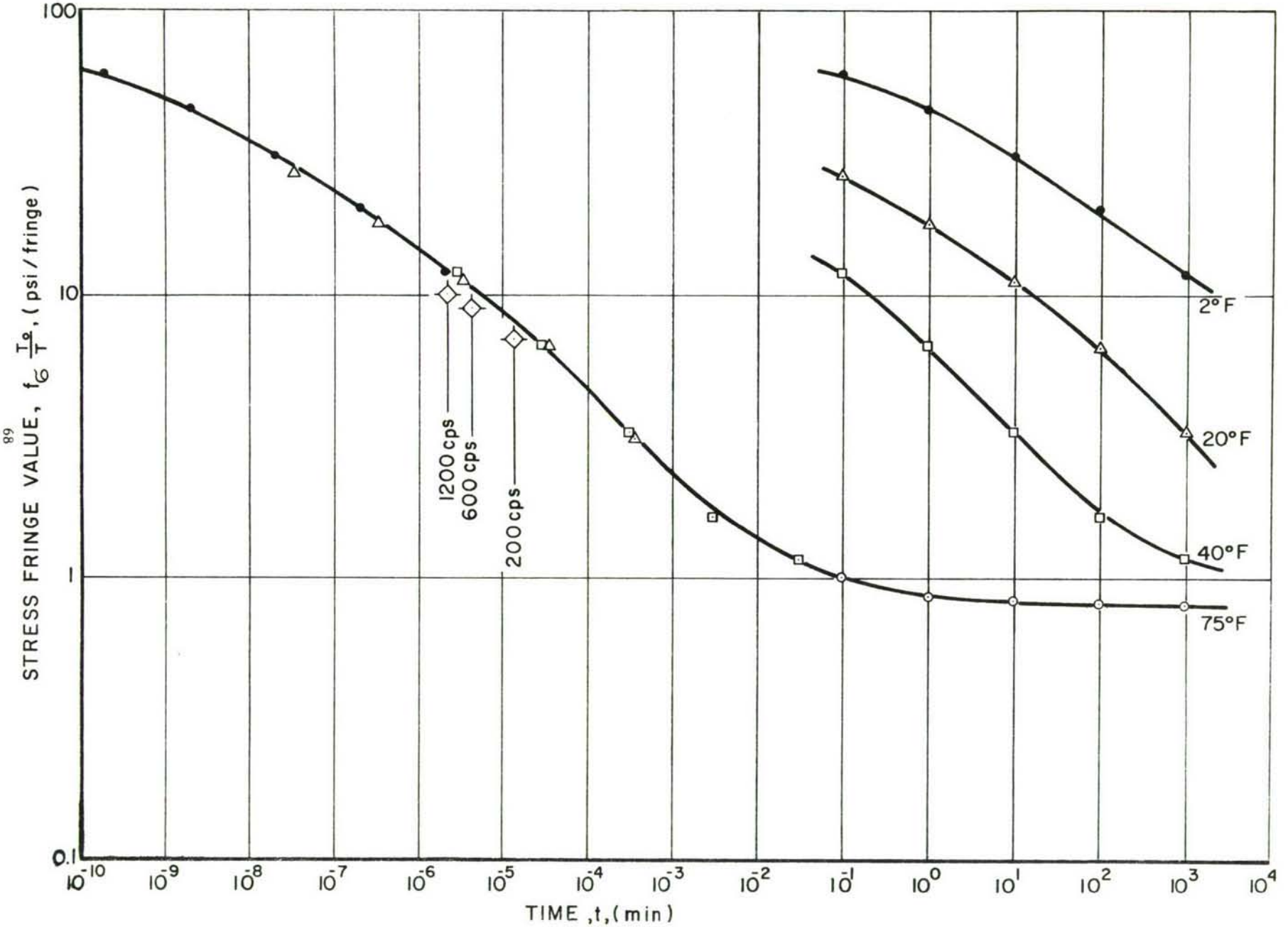


Figure 33. INDIVIDUAL AND COMPOSITE CURVES FOR STRESS FRINGE VALUE OF DER 60/40

Table IV

VALUES OF STRESS FRINGE VALUE OF DER 60/40* AT VARIOUS TEMPERATURES AND TIMES AFTER LOADING

Time (Min.)	Stress Fringe Value: $f_\sigma(t)\frac{T_o^*}{T}$ (psi x in./fringe) Temperature (°F)			
	75	40	20	2
0.1	1.00	11.9	26.2	60.0
1	0.86	6.6	17.8	45.2
10	0.83	3.3	11.1	31.3
100	0.82	1.65	6.6	20.2
1000	0.80	1.17	3.7	11.9

*$\frac{T_o}{T}$ is the ratio of the reference absolute temperature to the given temperature in degrees Rankine.

*DER x/y denotes mixture of x-parts of Dow Epoxy Resin DER 732 and y-parts of DER 331.

An additional check was obtained by means of sinusoidal oscillation tests at various frequencies. The same simple shear specimen mounted with load cells at the end was tested in the shaker as described previously (Refs. 2,10). In the present case, readings were greatly facilitated by using a frequency independent and sensitive photodiode as the photosensitive device and a Helium-Neon gas laser as the light source. The latter proved to be an ideal light source for the purpose because of its high intensity and monochromatic nature. Some values of the stress fringe value were converted from a function of frequency to one of time and plotted in Fig. 33.

The amount of horizontal shift on a logarithmic time scale necessary to produce the composite curve for either the relaxation modulus or the stress fringe value can be represented by a function of temperature, called the shift function. This function is measured in decades of time shift. Values of this function for the relaxation modulus and stress fringe value are plotted versus temperature in Fig. 34. Both mechanical and optical properties seem to be governed by the same shift function.

Poisson's ratio as a function of time was obtained from the shear and Young's modulus curves of Fig. 29 using the following approximate relation:

$$\nu(t) \cong \frac{E(t)}{2G(t)} - 1 \qquad (37)$$

An interesting result is the continuous variation of Poisson's ratio with time.

All the material functions above were plotted over the time scale of interest, 0.1 to 100 μ sec, in Fig. 35.

4. Properties of DER 73/27* and DER 85/15*

These are the two materials selected for the high- and low-impedance layers of the air shock loaded specimens. Optical properties were determined by conducting photocreep tests at various temperatures. Disk specimens were loaded under diametral compression in the same environmental chamber. Tests were conducted at 75°, 45°, 18°, and 2°F for DER 73/27, and at 75°, 45°, 17°, and -2°F for DER 85/15. The time-dependent stress fringe value at various temperatures for these two materials is plotted in Figs. 36 and 37. Values of the stress fringe value at discrete times were multiplied by the appropriate ratio of absolute temperatures and plotted in Figs. 38 and 39 for the two materials above. The individual curves for different temperatures,

*Der x/y denotes mixture of x-parts of Dow Epoxy Resin DER 732 and y-parts of DER 331.

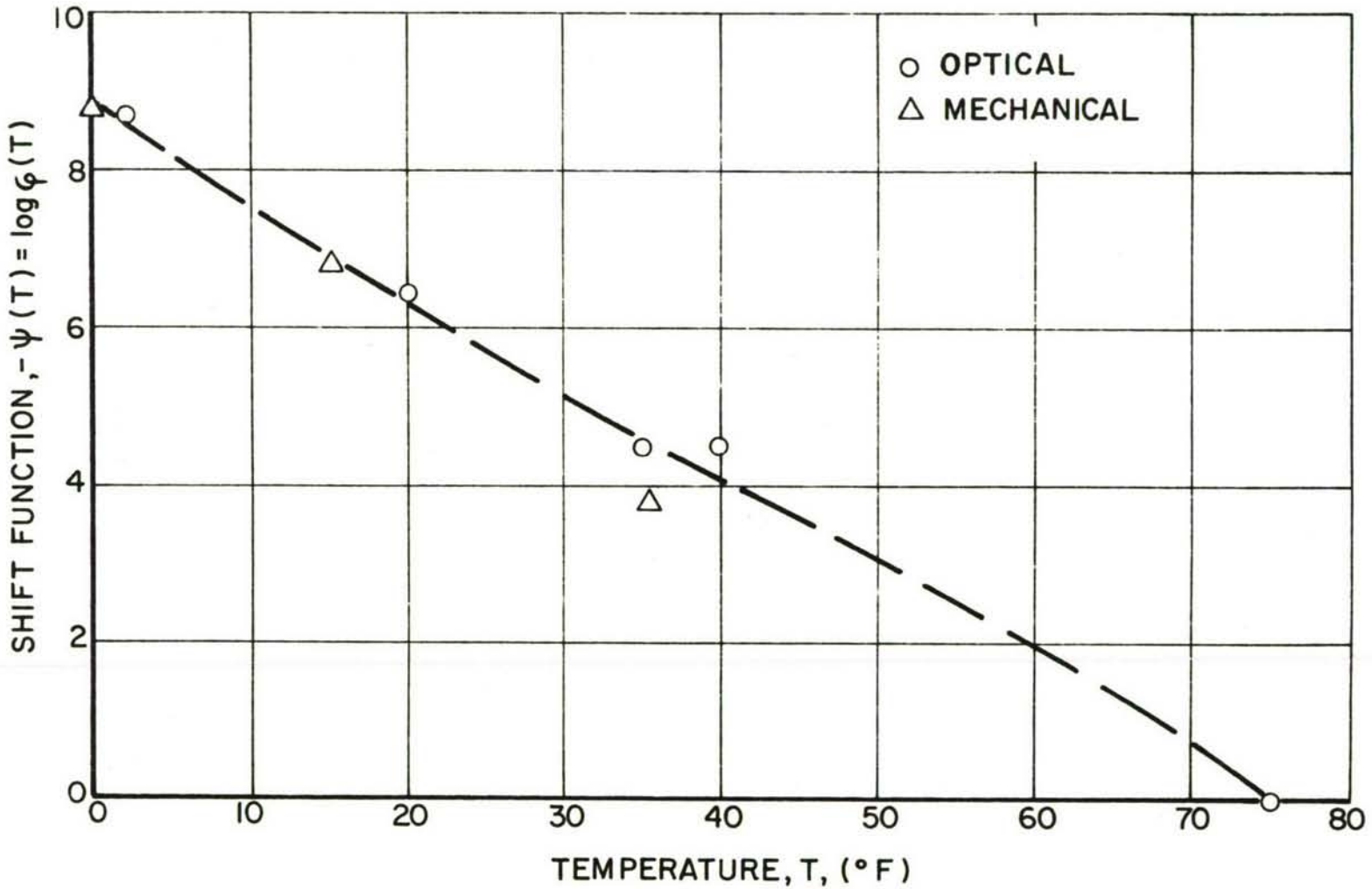


Figure 34. TEMPERATURE-TIME SHIFT FUNCTION FOR RELAXATION MODULUS AND STRESS FRINGE VALUE FOR DER 60/40

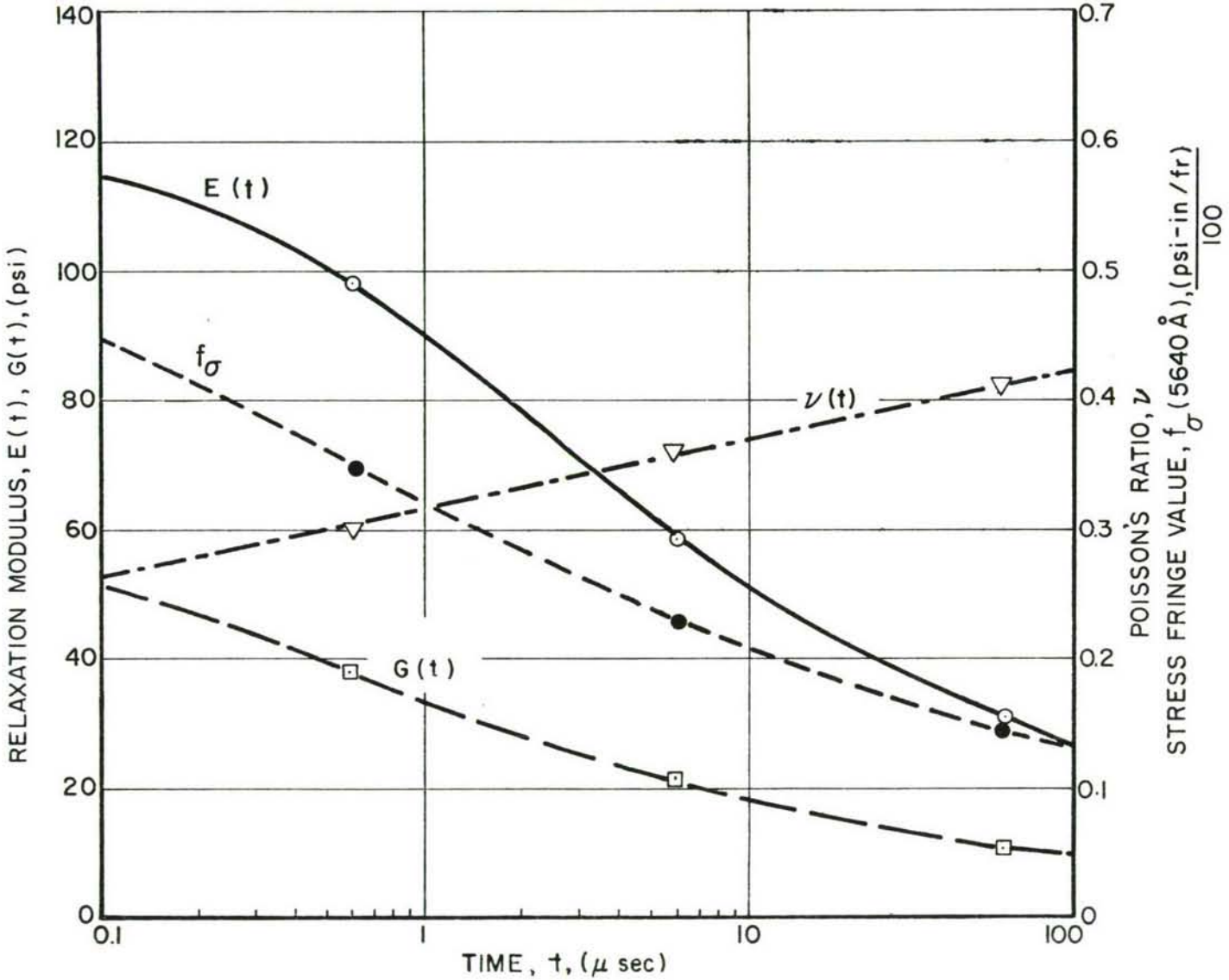


Figure 35. YOUNG'S AND SHEAR RELAXATION MODULI, STRESS FRINGE VALUE AND POISSON'S RATIO AS FUNCTIONS OF TIME FOR DER 60/40

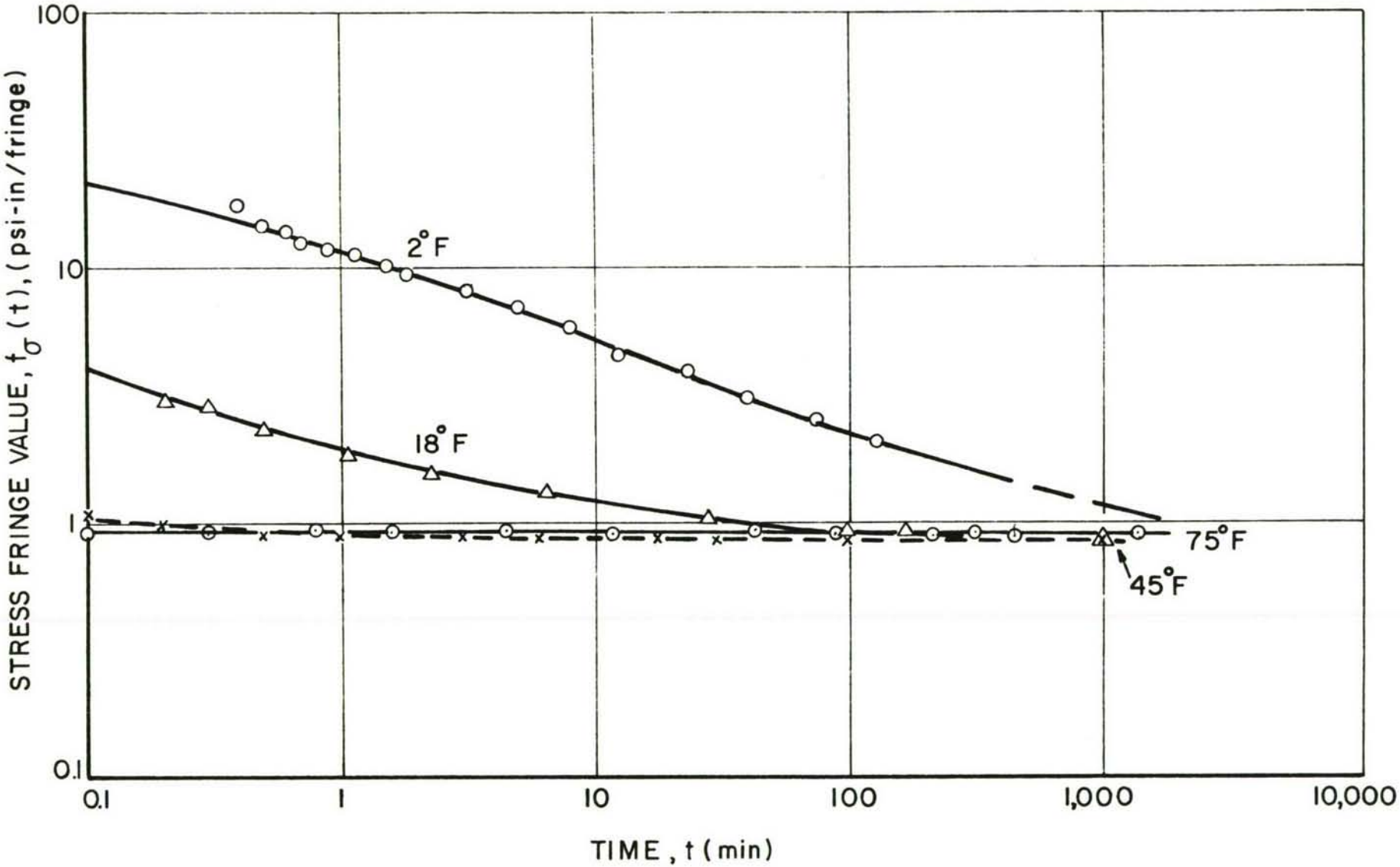


Figure 36. STRESS FRINGE VALUE AS A FUNCTION OF TIME AT VARIOUS TEMPERATURES FOR DER 73/27

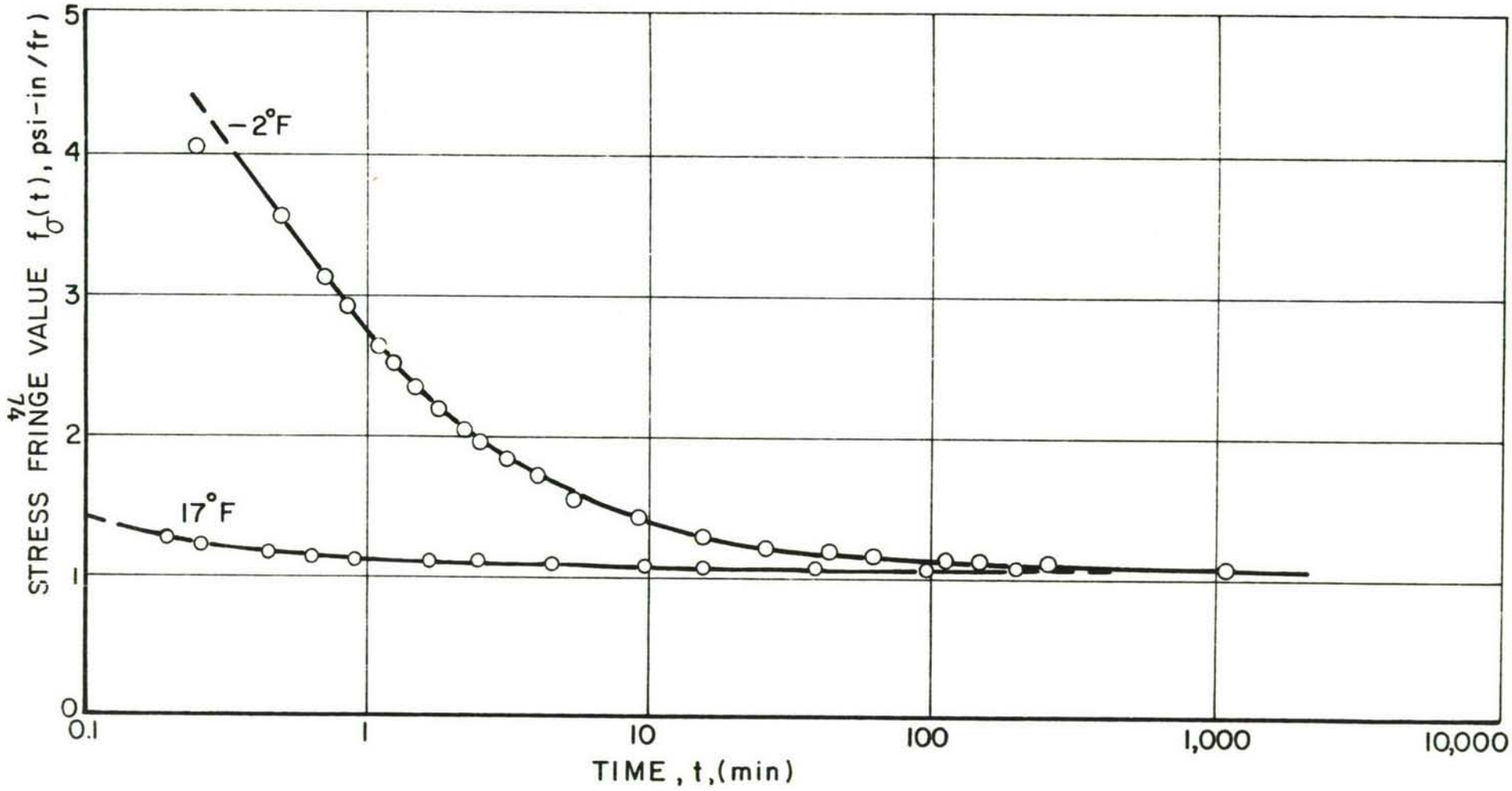


Figure 37. STRESS FRINGE VALUE AS A FUNCTION OF TIME AT VARIOUS TEMPERATURES FOR DER 85/15

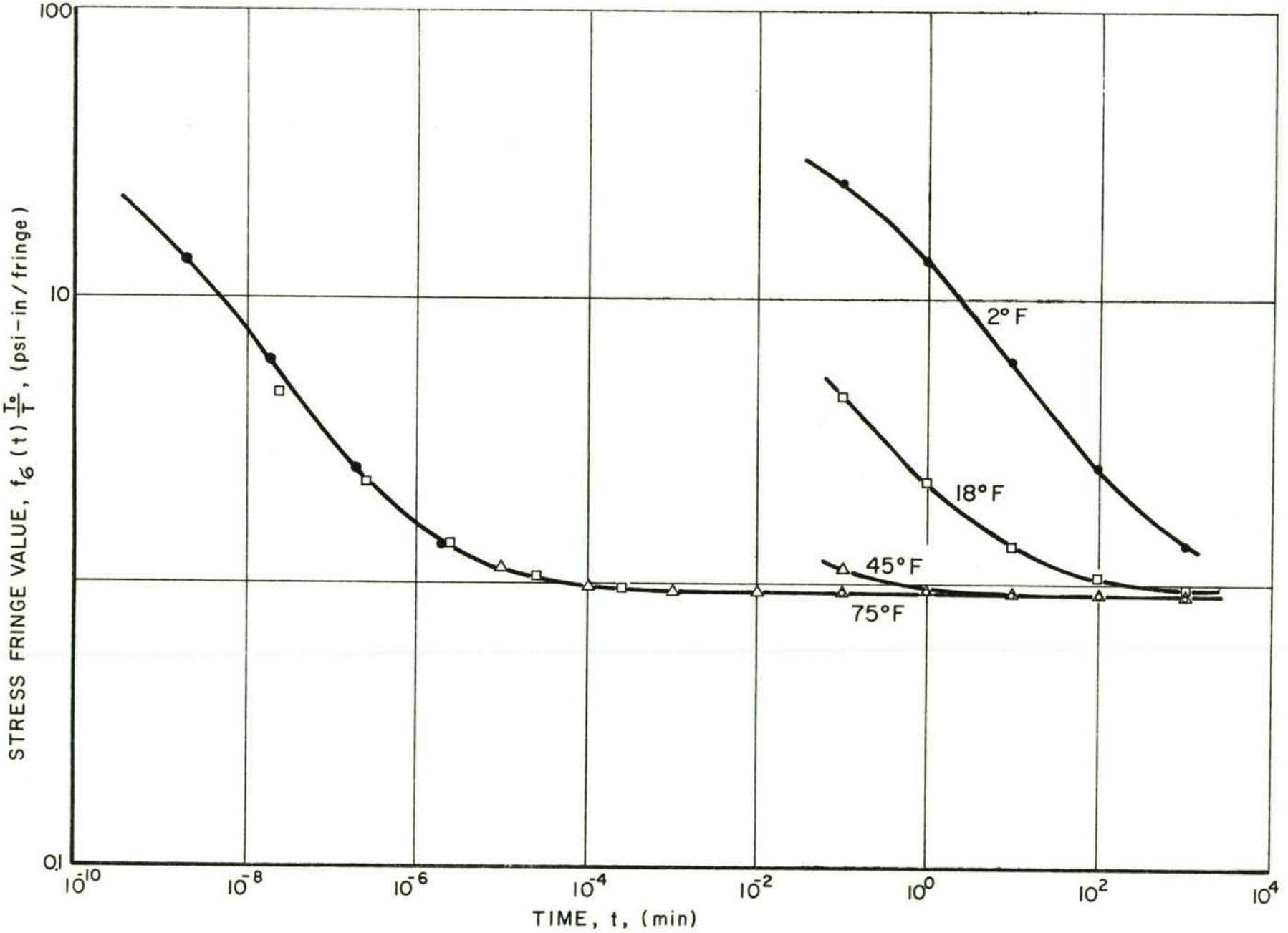


Figure 38. INDIVIDUAL AND COMPOSITE CURVES FOR STRESS FRINGE VALUE OF DER 73/27

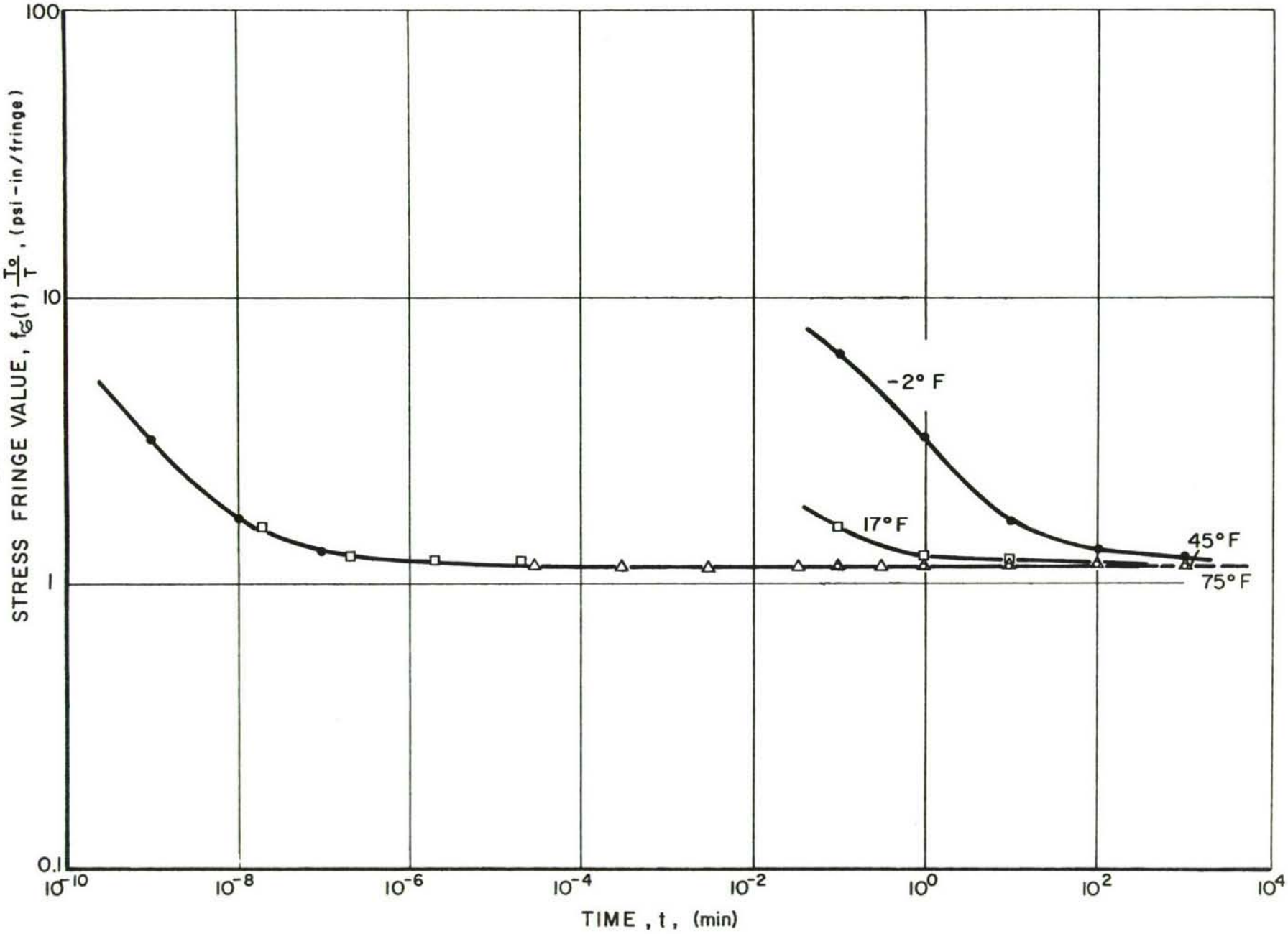


Figure 39. INDIVIDUAL AND COMPOSITE CURVES FOR STRESS FRINGE VALUE OF DER 85/15

except the one corresponding to room temperature, were shifted to form composite curves corresponding to room temperature.

One significant observation that can be made is that the transition region, the region of greatest variation with time, shifts to shorter times with increasing proportion of flexible resin. Transition regions occur at around 10^{-4} min, 10^{-7} min and 10^{-10} min for DER 60/40, DER 73/27 and DER 85/15, respectively. The last two materials exhibit long rubbery plateaus as seen in Figs. 38 and 39. The most flexible DER 85/15 appears to behave elastically even in the timescale of the air shock tests. All three materials, being chemically similar, seem to be governed by the same shift function.

SECTION VI

WAVE PROPAGATION IN LAYERED MODEL DUE TO AIR-BLAST LOADING ON ONE EDGE

1. Introduction

This type of loading has been used in earlier studies of elastic and viscoelastic wave propagation (Refs. 1,2). The model is subjected to a moving pressure pulse of sharp rise as shown in Fig. 6. The resulting stress wave in the model travels with a constant velocity initially and, therefore, has a plane wavefront. The elastic and viscoelastic cases for a semi-infinite space have been solved theoretically (Refs. 13,14,15) and experimentally (Refs. 1,2). The present study deals with the wave propagation in a two-layer specimen with the two media having an impedance ratio of 2:1. The depth of the upper (low-impedance) medium is a variable parameter.

2. Experimental Procedure

As described in the preceding two sections, the model materials selected for this phase of the study were DER 85/15 and DER 73/27 for the low-impedance and high-impedance layers, respectively. The models were made of sheets of these materials 3/8 in. thick. The lower layer was a 6 in. x 16 in. x 3/8 in. sheet of DER 73/27 and the upper layer was a sheet of DER 85/15 of variable depth (Fig. 40). Initially, three models with varying values of the depth of the low-impedance medium were prepared:

Model I-1: $h = 2$ in.
Model I-2: $h = 3$ in.
Model I-3: $h = 4$ in.

The two layers were cemented with a soft silicone rubber adhesive (Silastic 140, Dow Corning). They were tested under air blast loading on the free edge of the low-impedance medium as described in

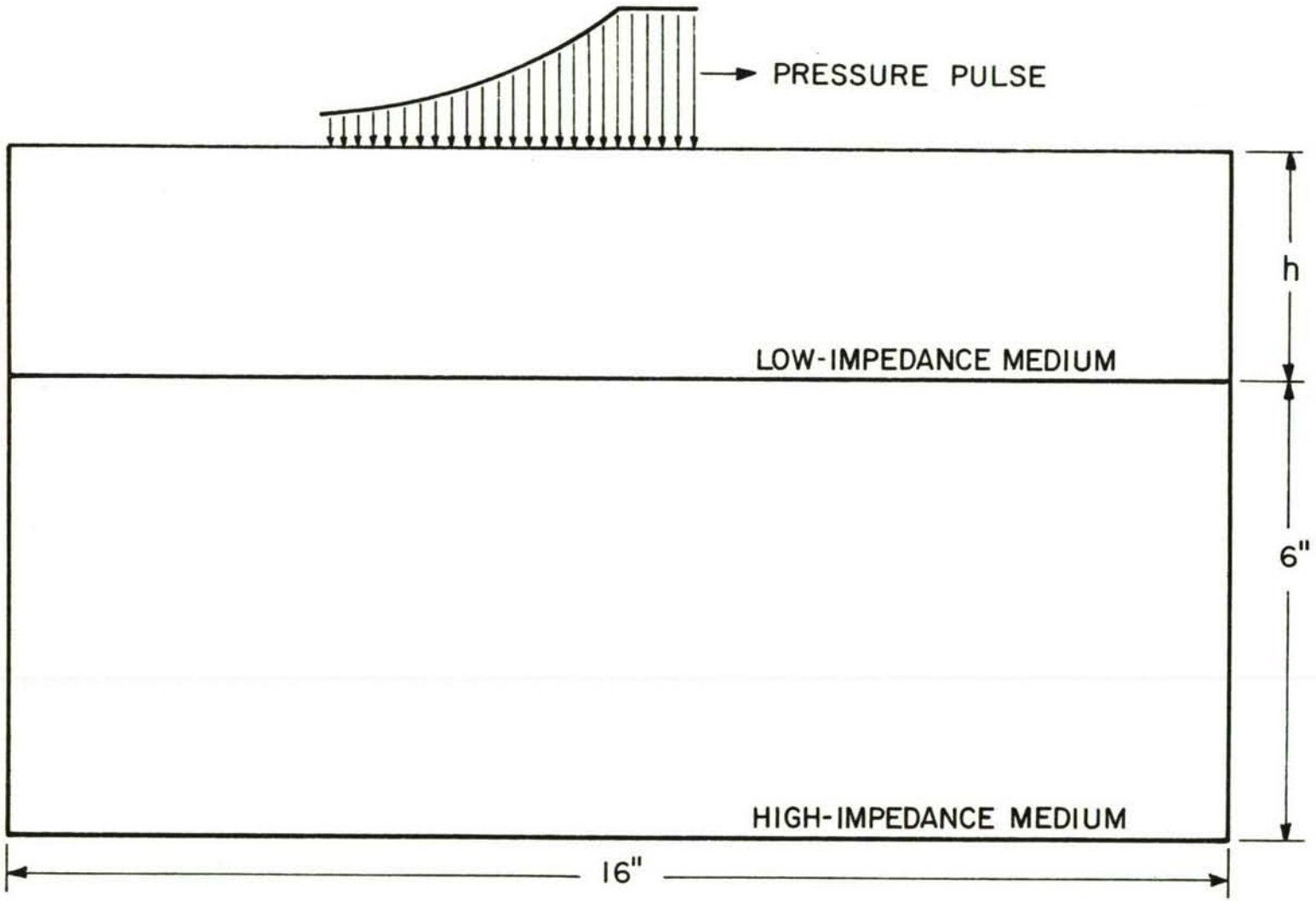


Figure 40. SKETCH OF MODEL SUBJECTED TO AIR-BLAST LOADING ON THE EDGE (PHASE I)

Section III-3-b. The pressure pulse traveling along the edge of the model shown in Fig. 6 indicates a peak pressure of approximately 52 psi. Transient isochromatic fringe patterns recorded with the Fastax camera at rates between 7,700 and 8,100 frames per second are shown in Figs. 41 through 43.

Two additional models were tested. Model I-4 was made by cementing the 2 - inch layer from model I-1 to the top layer of Model I-2. The purpose of this test was to study the case of a layer depth of h = 5 in. and the effect of the cement, if any, on the transmission of waves. It was found that the cement did not introduce any noticeable disturbance on the wave transmission. Model I-5 had a 6 in. deep low-impedance layer. Isochromatic fringe records for this model obtained with the Fastax camera are shown in Fig. 44.

To obtain supplementary information for the subsequent analysis a series of moiré experiments were planned. Two arrays of 1,000 lines per inch, one vertical and one horizontal, were photoprinted on two halves of model I-5 using the Kodak Photosensitive Resist (KPR) process as discussed previously (Section III-2). The two arrays are used for obtaining horizontal and vertical strains in the two layers of the model. The moiré fringe patterns were recorded with the Fastax camera as in the case of isochromatic patterns. A typical record is shown in Fig. 45. As can be seen from these records, the response is so high that the horizontal fringes soon wash out. The shock tube driver pressure was then reduced to 350 psi, which resulted in a peak pulse pressure of 23 psi. This time again the horizontal fringes were washed out due to excessive deformation. It was concluded that a 300 line array would have been more appropriate for measuring vertical deformations but no further work was done due to lack of time.

3. Results and Discussion

The fringe patterns of Figs. 41 through 44 were analyzed to obtain the wave propagation characteristics. The fringes initially appear to be straight lines of varying inclinations which indicates a plane wave with attenuation along its direction of propagation. A

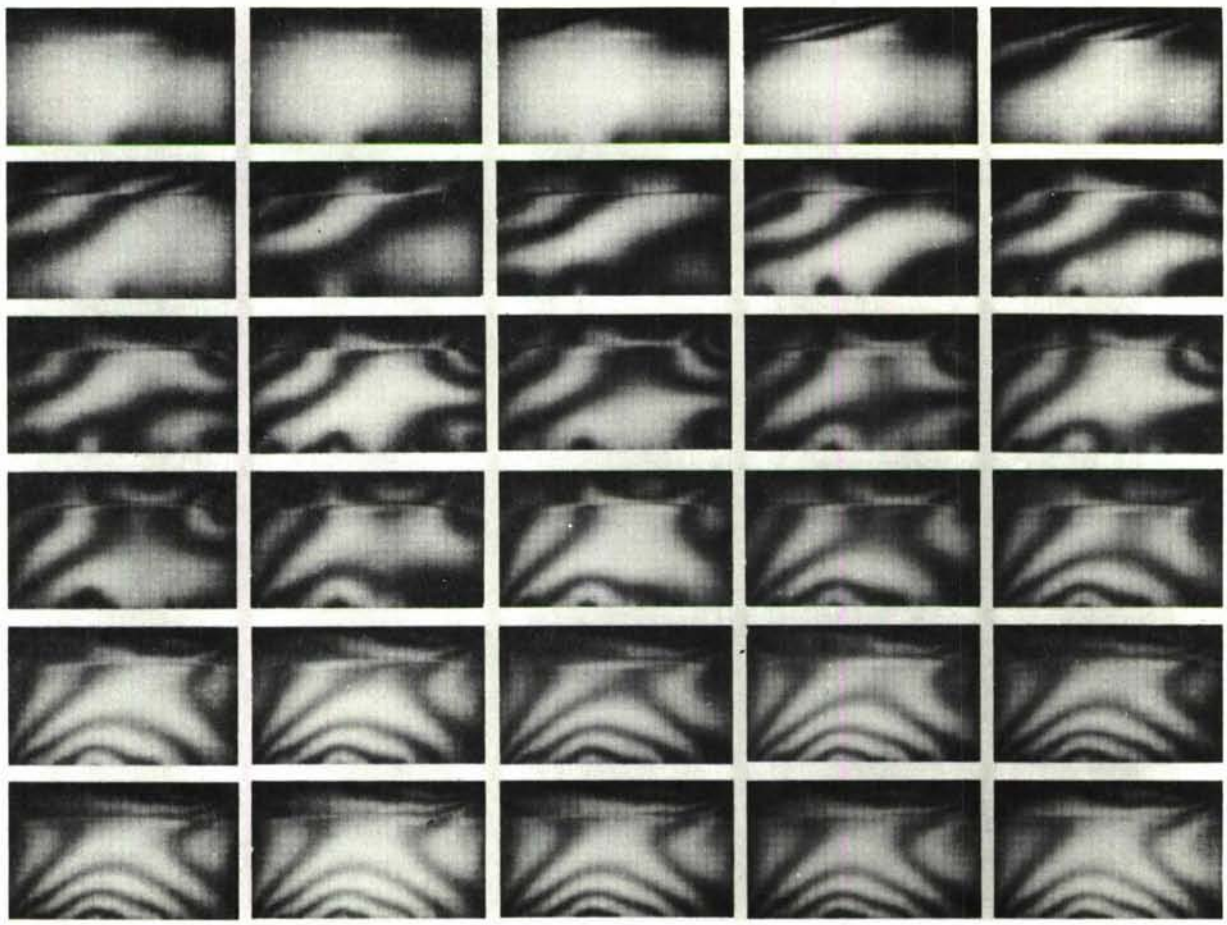


Figure 41. SERIES OF 30 CONSECUTIVE PHTOGRAPHS SHOWING TRANSIENT ISOCHROMATIC FRINGE PATTERNS IN LAYERED MODEL I-1 (CAMERA SPEED: 7,700 FRAMES/SECOND)

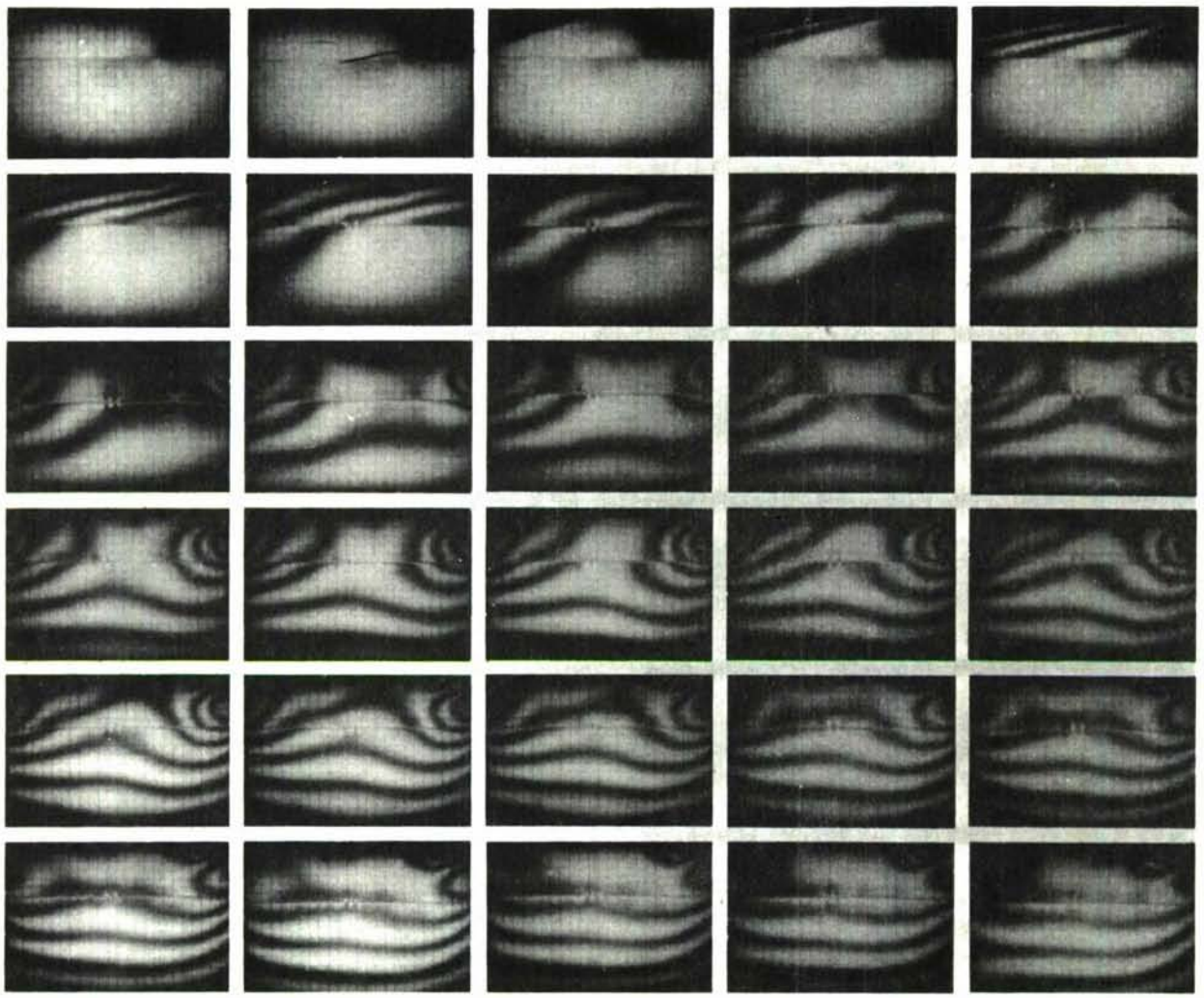


Figure 42. SERIES OF 30 CONSECUTIVE PHOTOGRAPHS SHOWING TRANSIENT ISOCHROMATIC FRINGE PATTERNS IN LAYERED MODEL I-2 (CAMERA SPEED: 7,700 FRAMES/SECOND)

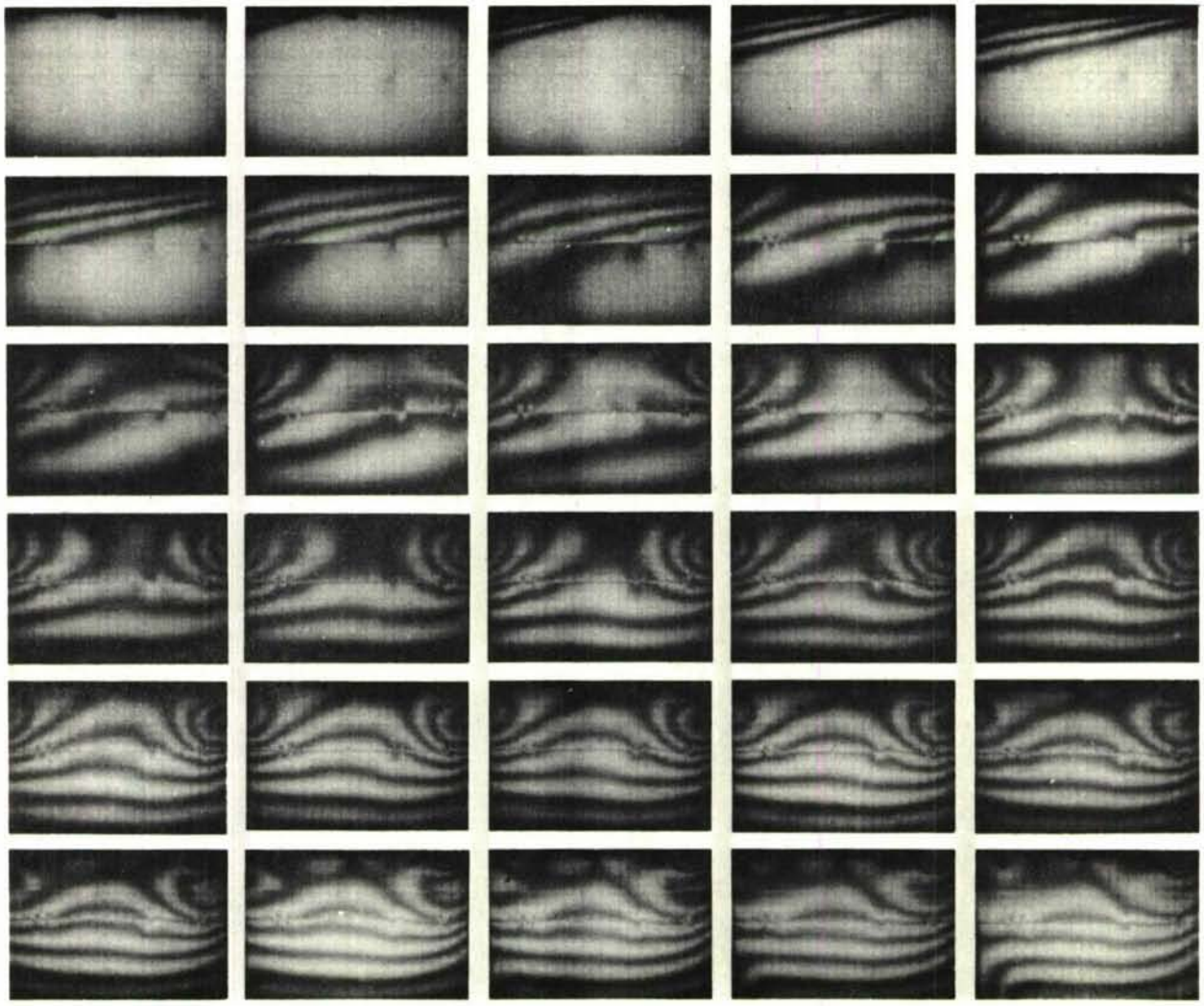


Figure 43. SERIES OF 30 CONSECUTIVE PHOTOGRAPHS SHOWING TRANSIENT ISOCHROMATIC FRINGE PATTERNS IN LAYERED MODEL I-3 (CAMERA SPEED: 8,100 FRAMES/SECOND)

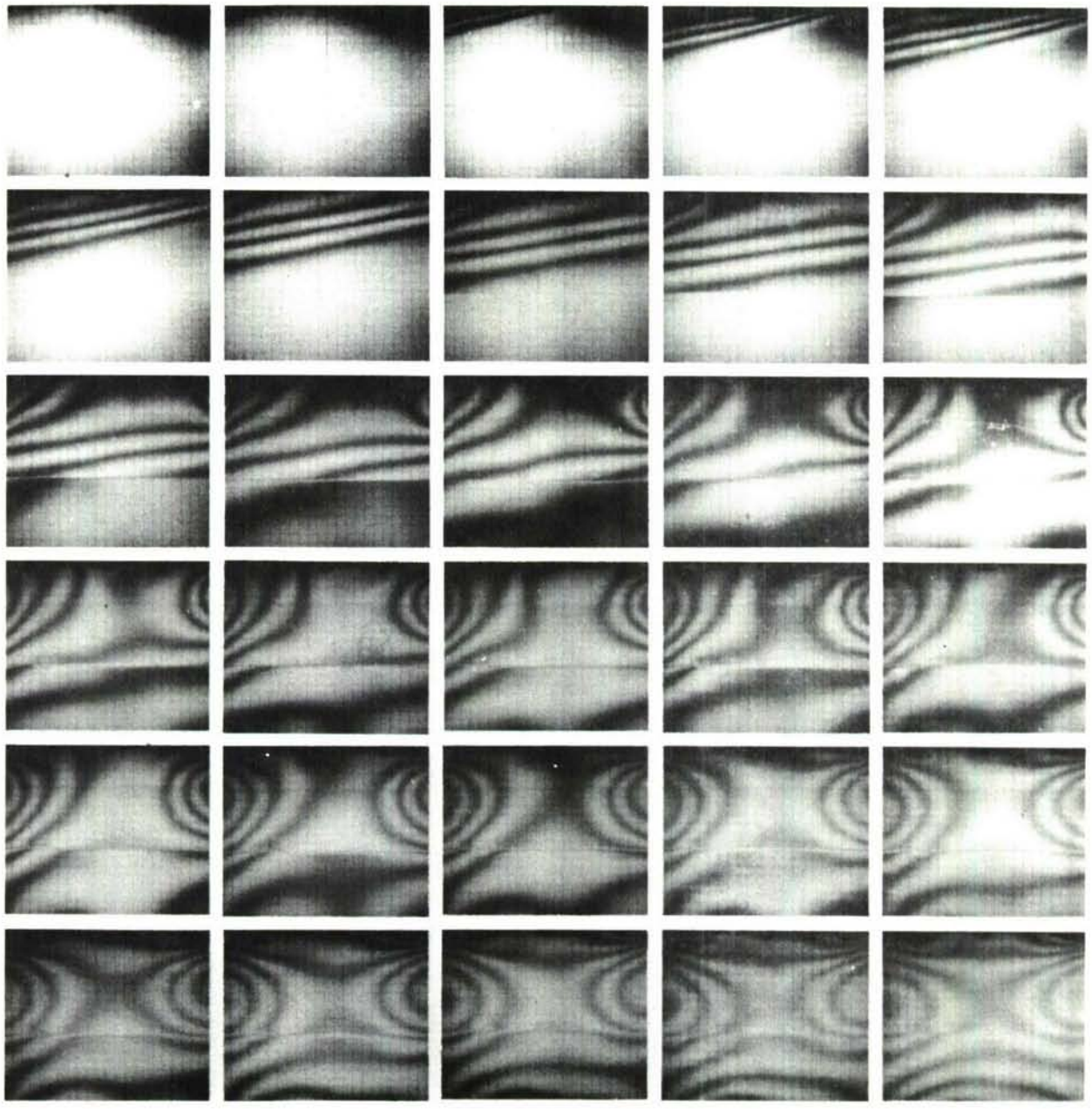


Figure 44. SERIES OF 30 CONSECUTIVE PHOTOGRAPHS SHOWING TRANSIENT ISOCHROMATIC FRINGE PATTERNS IN LAYERED MODEL I-5 (CAMERA SPEED: 7,500 FRAMES/SECOND)

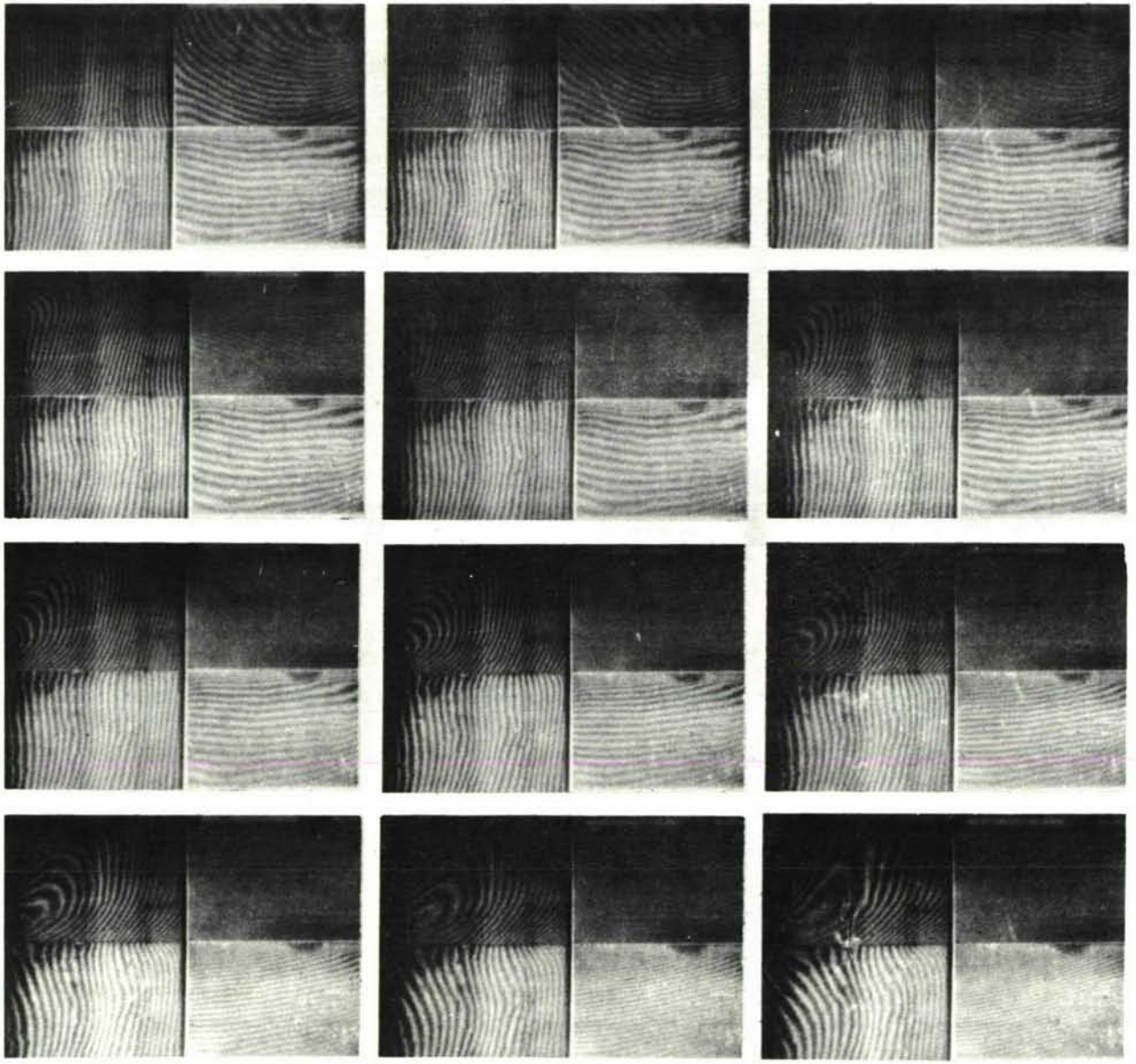


Figure 45. SERIES OF 12 CONSECUTIVE PHOTOGRAPHS SHOWING TRANSIENT MOIRE FRINGE PATTERNS IN LAYERED MODEL I-5 (CAMERA SPEED: 7,500 FRAMES/SECOND)

combination of factors makes these fringes change with time in many respects. The interaction of the wave with the high-impedance medium makes the fringes in the low-impedance medium curve a little toward the wavefront. This phenomenon becomes more pronounced with higher order fringes mainly because a given percentage of change in fringe order is more noticeable in that case. Reflections from the interface and the other edges of the specimen soon alter considerably the initially straight-line fringe pattern.

Fringe inclination and fringe location versus time along a vertical line were measured and plotted in all cases. Figure 46 shows curves of fringe location versus time (frame number) in the two media. Initially, all plots are straight but those for the higher order fringes in the low-impedance medium curve toward the direction of shorter times. Since the slopes of these curves represent propagation velocity, this phenomenon might indicate increasing propagation velocity with time near the interface for the higher order fringes.

The straight line slopes were measured and the velocities of propagation (in the vertical direction) were plotted versus fringe order in Fig. 47. The propagation velocities of the wavefront in the vertical direction were obtained by extrapolation to the zero fringe order. The true wave velocity is the component of this vertical velocity normal to the wavefront. The direction of the wavefront can be deduced from the inclination of the fringes. In this particular case, the half-order fringe inclination increases from 15° to 18°, that of the one and one-half order fringe increases from 11° to 15° and the inclination of the two and one-half order fringe increases from 8° to 13°. The angle for the half-order fringe in the high-impedance medium also varies from 22° to 35°. Taking the values of 16° and 30° for the inclination of the wavefronts the following wave velocities in the two media were computed:

$$\alpha_1 = 6{,}700 \text{ in./sec}$$

$$\alpha_2 = 13{,}450 \text{ in./sec}$$

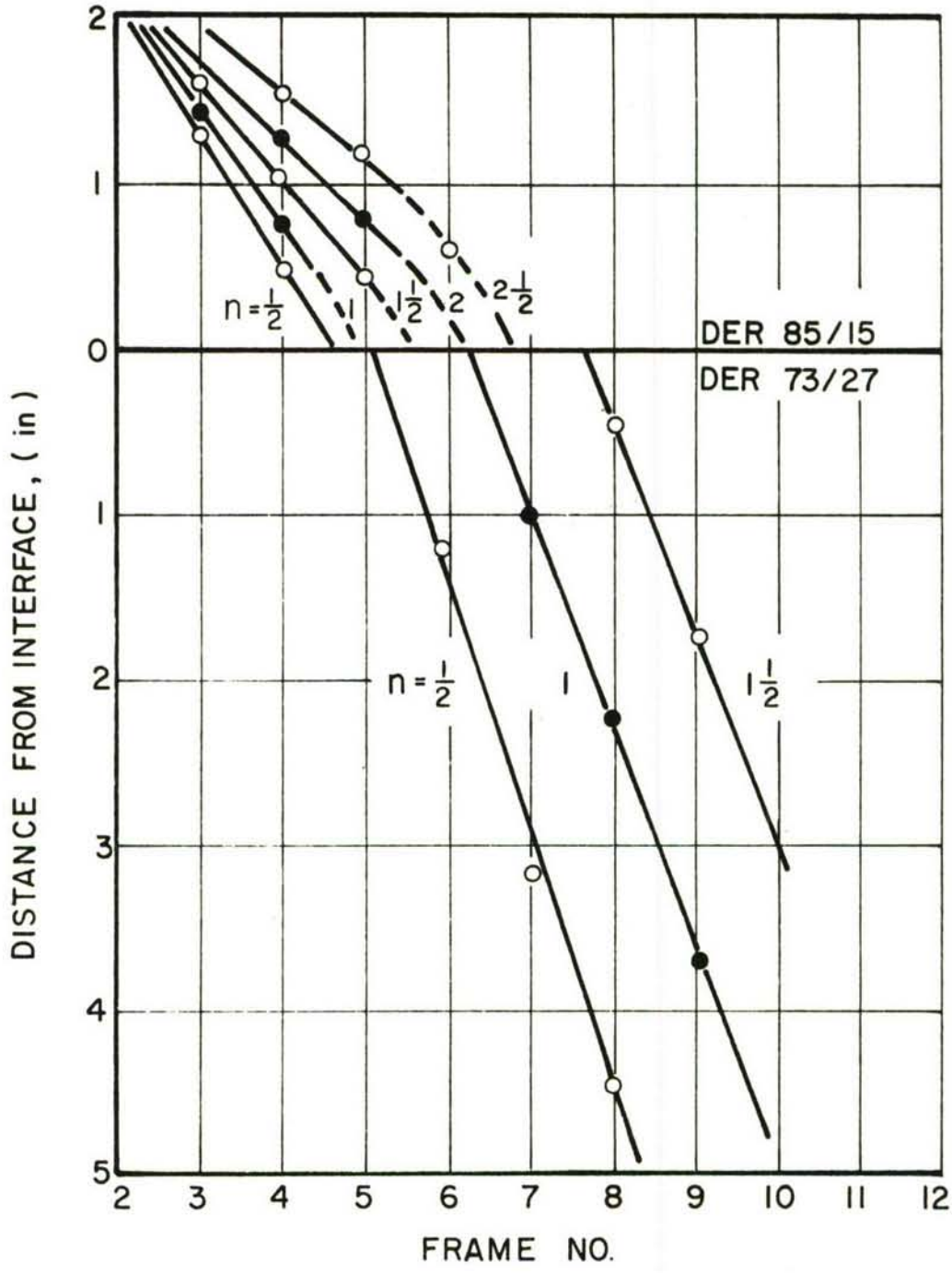


Figure 46. FRINGE POSITION AS A FUNCTION OF TIME IN MODEL I-1

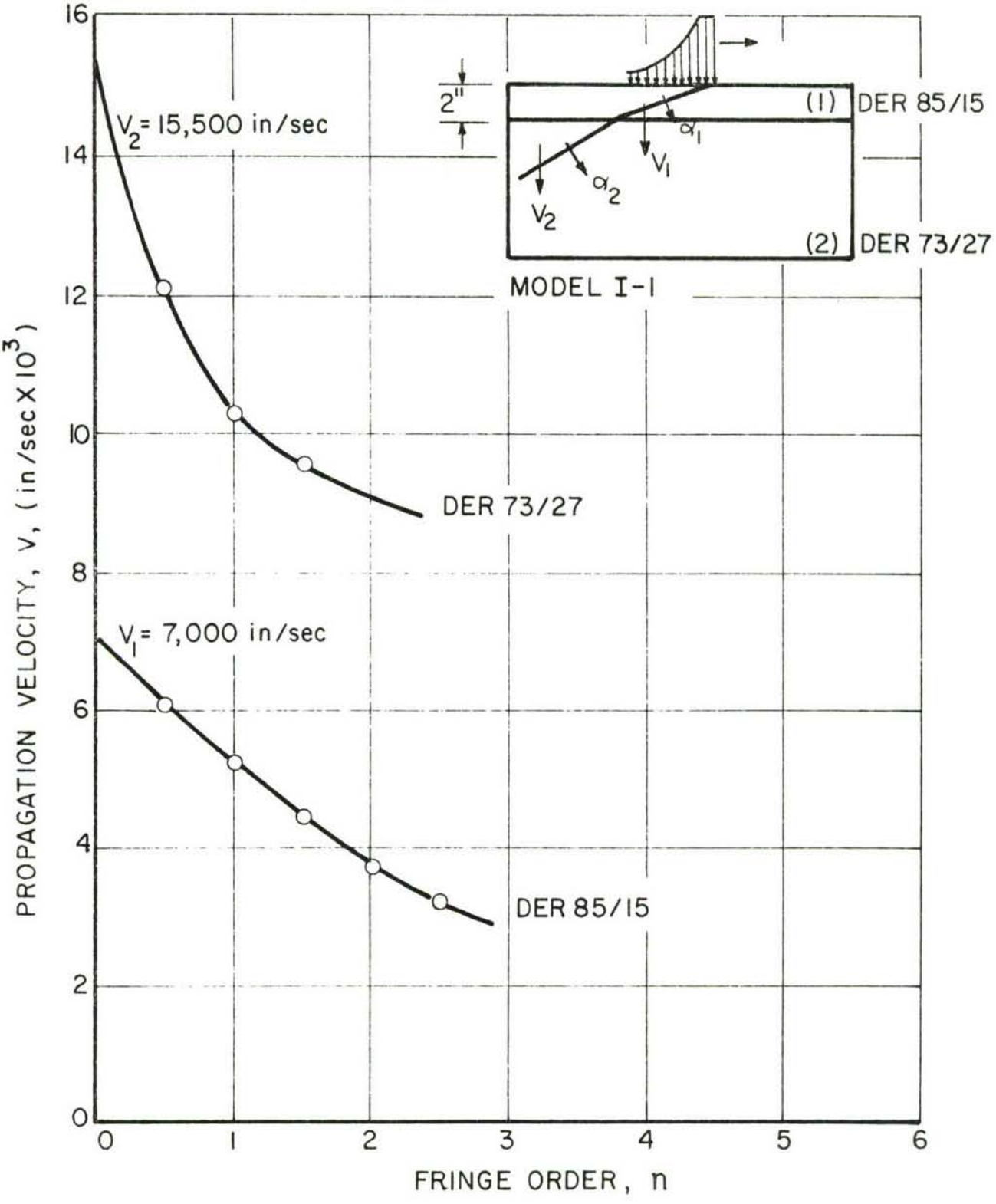


Figure 47. WAVE PROPAGATION VELOCITY IN TWO LAYERS OF MODEL I-1 AS A FUNCTION OF FRINGE ORDER

For equal densities this results in an impedance ratio:

$$\text{Impedance Ratio:} \quad \frac{\alpha_2}{\alpha_1} = 2.01$$

Figure 48 shows curves of fringe location versus time for Model I-2. As before, the plots for the higher order fringes in the low-impedance layer begin to curve toward the shorter times. The plots for the high-impedance medium also become nonlinear for higher order fringes, indicating a decreasing propagation velocity. The velocities of propagation in the vertical direction were measured as before and plotted in Fig. 49 as a function of fringe order. The angle of inclination of several fringes was measured as before. The angle for the half-order fringe decreased from 16° to 11°, those of fringe order one and one-half and two and one-half leveled at about 11° and started increasing thereafter. The angle for the half-order fringe of medium 2 fluctuated around 30°. Again, 16° and 30° were taken as the values of the wavefront inclinations and the same velocities and impedance ratio resulted as in the case of Model I-1.

Figure 50 shows plots of fringe position versus time for Model I-3. The effect of the interface on the linearity of these curves is clearly evident for the higher order fringes. Velocities of propagation in the vertical direction based on the linear portions of these curves are plotted in Fig. 51 versus fringe order. The inclination angle of several fringes was measured at several frames and plotted in Fig. 52. The fringe inclination angle decreases with time in all cases as would be expected. In the low-impedance medium the angle levels off at approximately 10°, 8°, and 7° for the 1/2, 1 1/2 and 2 1/2 fringe orders, respectively. In the high-impedance medium the corresponding angles seem to be approximately twice as large, as might be expected for a medium of double impedance. A good estimate of the inclination of the wavefronts at the time of frame 8 is 12° and 24° for the low- and high-impedance media, respectively. From the results of Fig. 51 and these angles the following wave propagation velocities are computed:

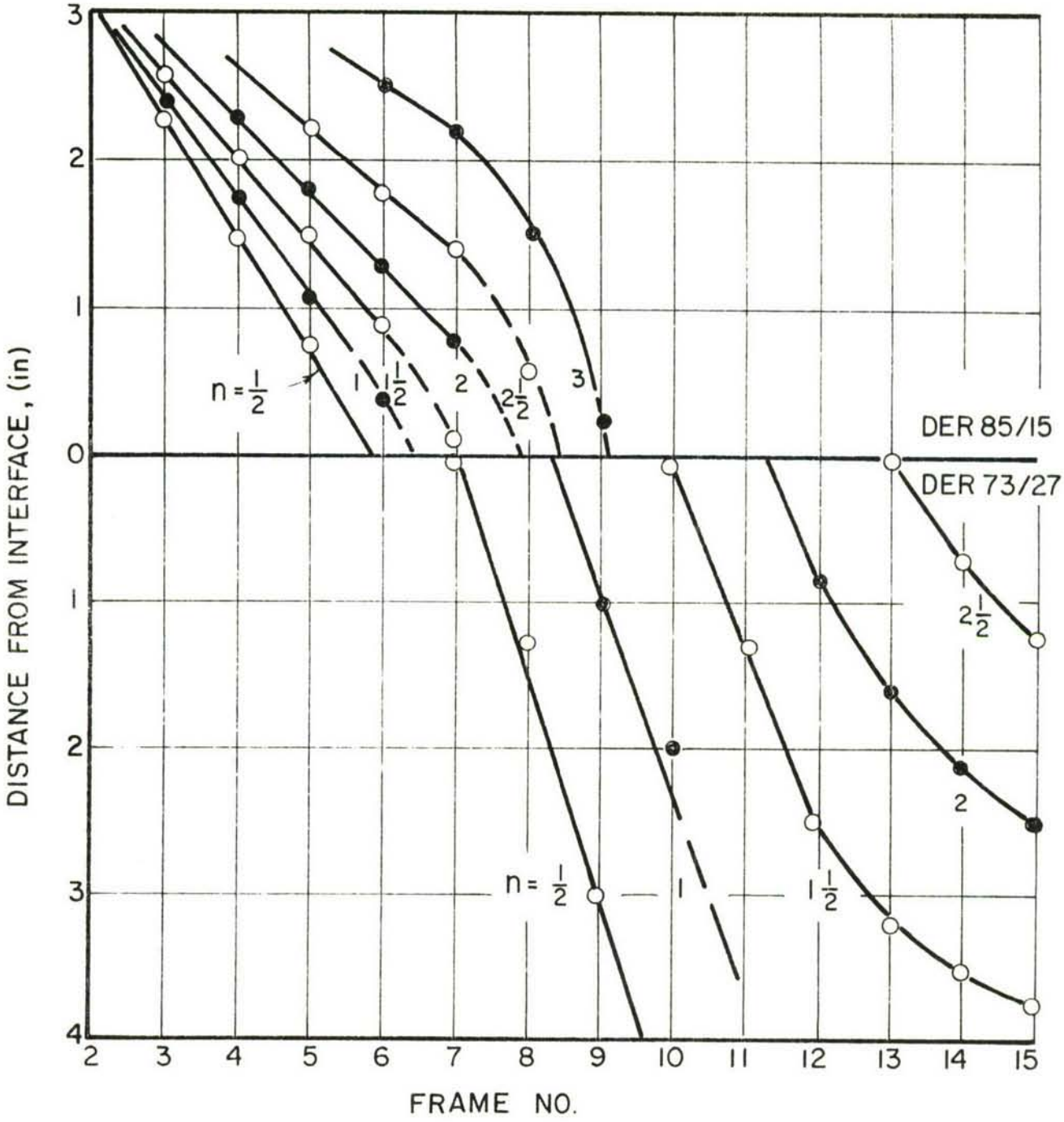


Figure 48. FRINGE POSITION AS A FUNCTION OF TIME IN MODEL I-2

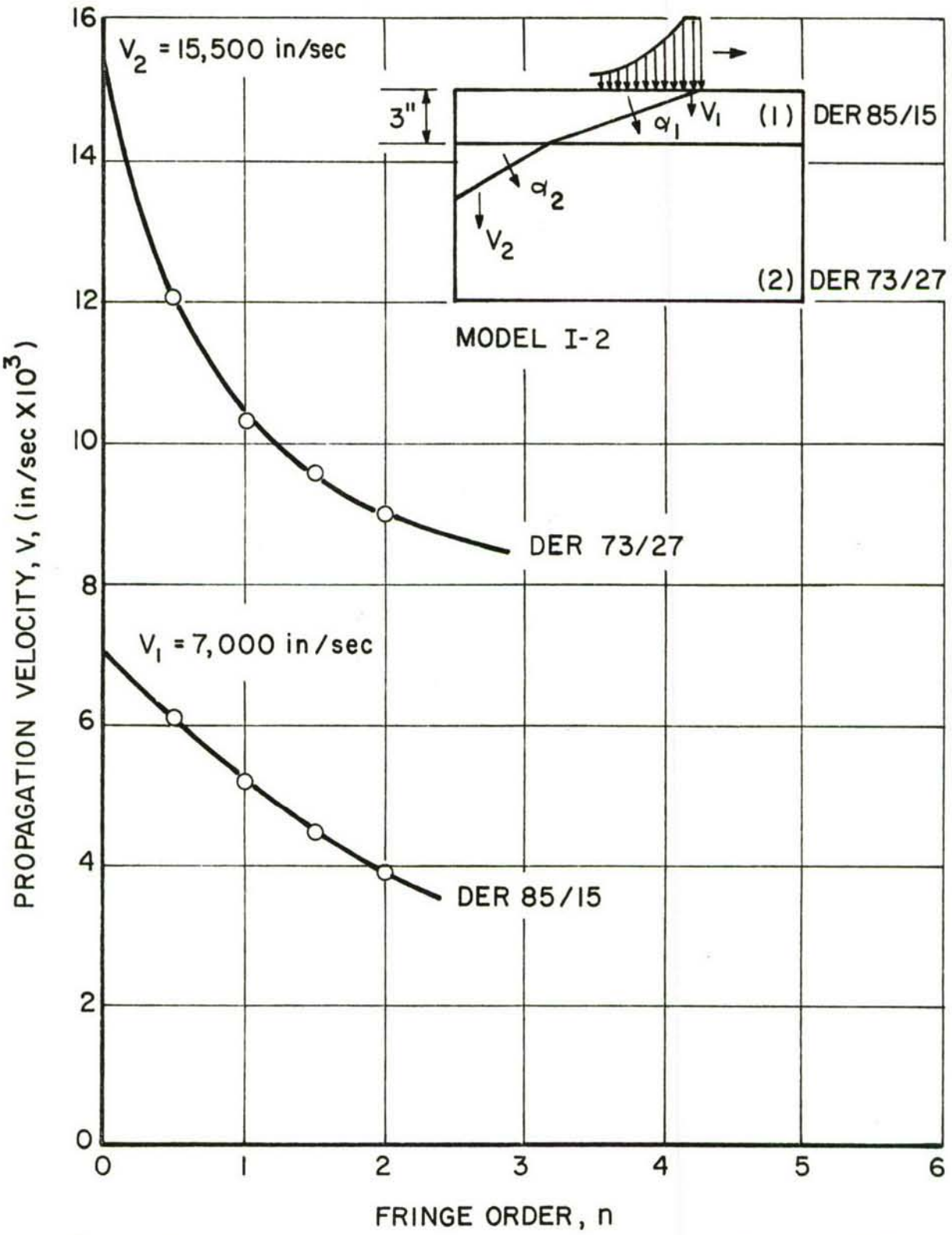


Figure 49. WAVE PROPAGATION VELOCITY IN TWO LAYERS OF MODEL I-2 AS A FUNCTION OF FRINGE ORDER

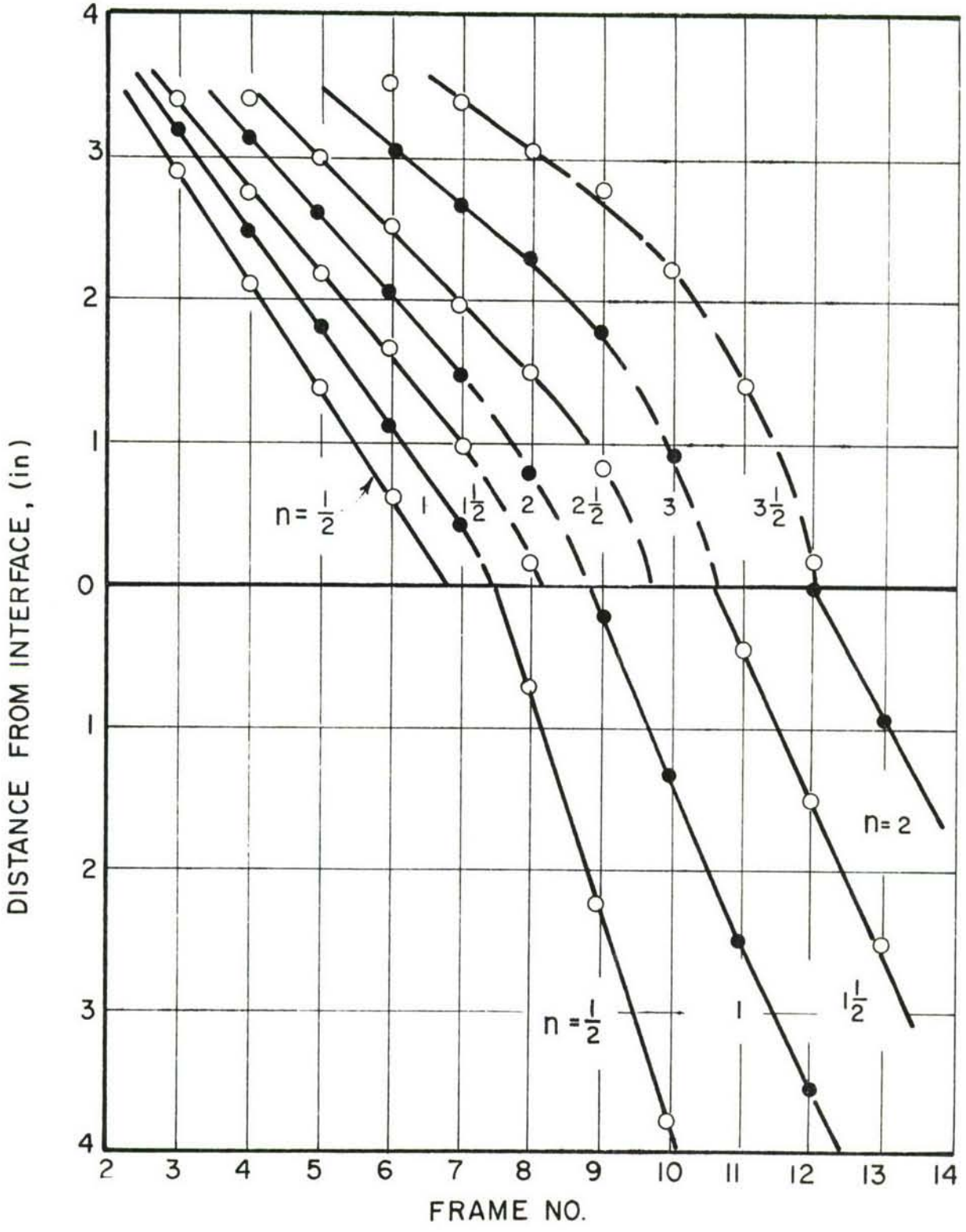


Figure 50. FRINGE POSITION AS A FUNCTION OF TIME IN MODEL I-3

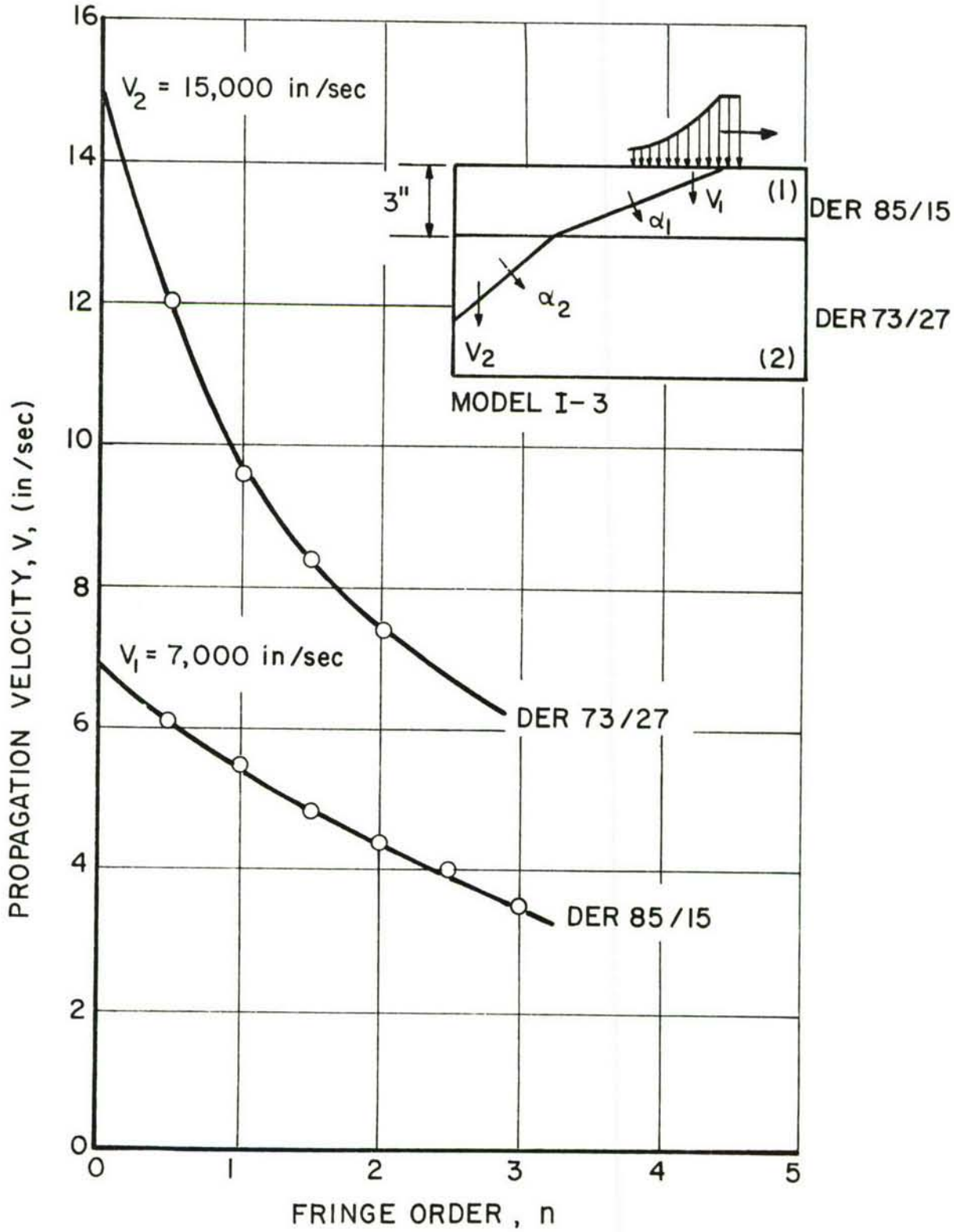


Figure 51. WAVE PROPAGATION VELOCITY IN TWO LAYERS OF MODEL I-3 AS A FUNCTION OF FRINGE ORDER

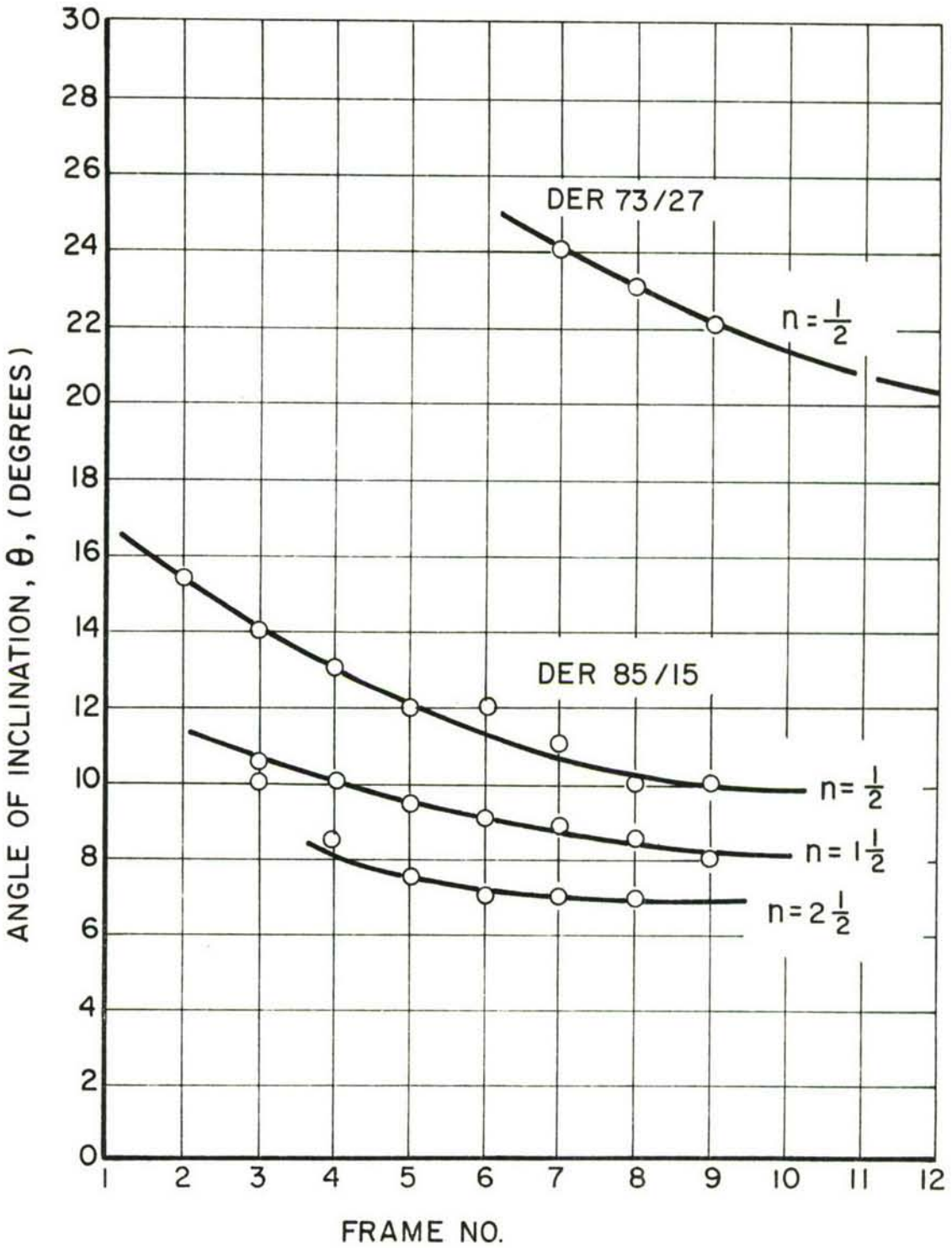


Figure 52. ANGLE OF FRINGE INCLINATION IN MODEL I-3 AS A FUNCTION OF TIME

α_1 = 6,850 in./sec

α_2 = 13,750 in./sec

which give an impedance ratio of

$$\text{Impedance Ratio} = \frac{\alpha_2}{\alpha_1} = 2.01$$

A similar analysis with similar results was conducted on Model I-5, with a 6 in. depth of low-impedance layer. (Figs. 53, 54, and 55.) The wave propagation velocities in this case, based on wavefront inclinations of 11° and 20°, are

α_1 = 6,700 in./sec

α_2 = 13,400 in./sec

and the impedance ratio is then exactly 2.00.

In general, as can be seen in Figures 46, 48, 50, and 53, the dispersion is much more pronounced in the low-impedance medium than in the high-impedance one. This is manifested by the fanlike appearance of the fringe curves in the upper layer. In contrast, the fringe curves for the lower layer appear nearly parallel indicating low dispersion.

The attenuation could not be measured quantitatively due to the absence of a peak in the pulse during the timescale of observation. However, from the fringe velocity curves it is evident that the attenuation is pronounced in both media. The fact that the inclination angle of the fringes, and hence that of the wavefront, changes (decreases) indicates attenuation along the wavefront. This phenomenon of "general plane waves" is predicted in viscoelastic materials by Cooper (Ref. 16). Also predicted in the above mentioned reference is the dependence of wave velocities on the angle of incidence. This possible variation of wave velocity was not studied due to the nearly fixed angle of incidence

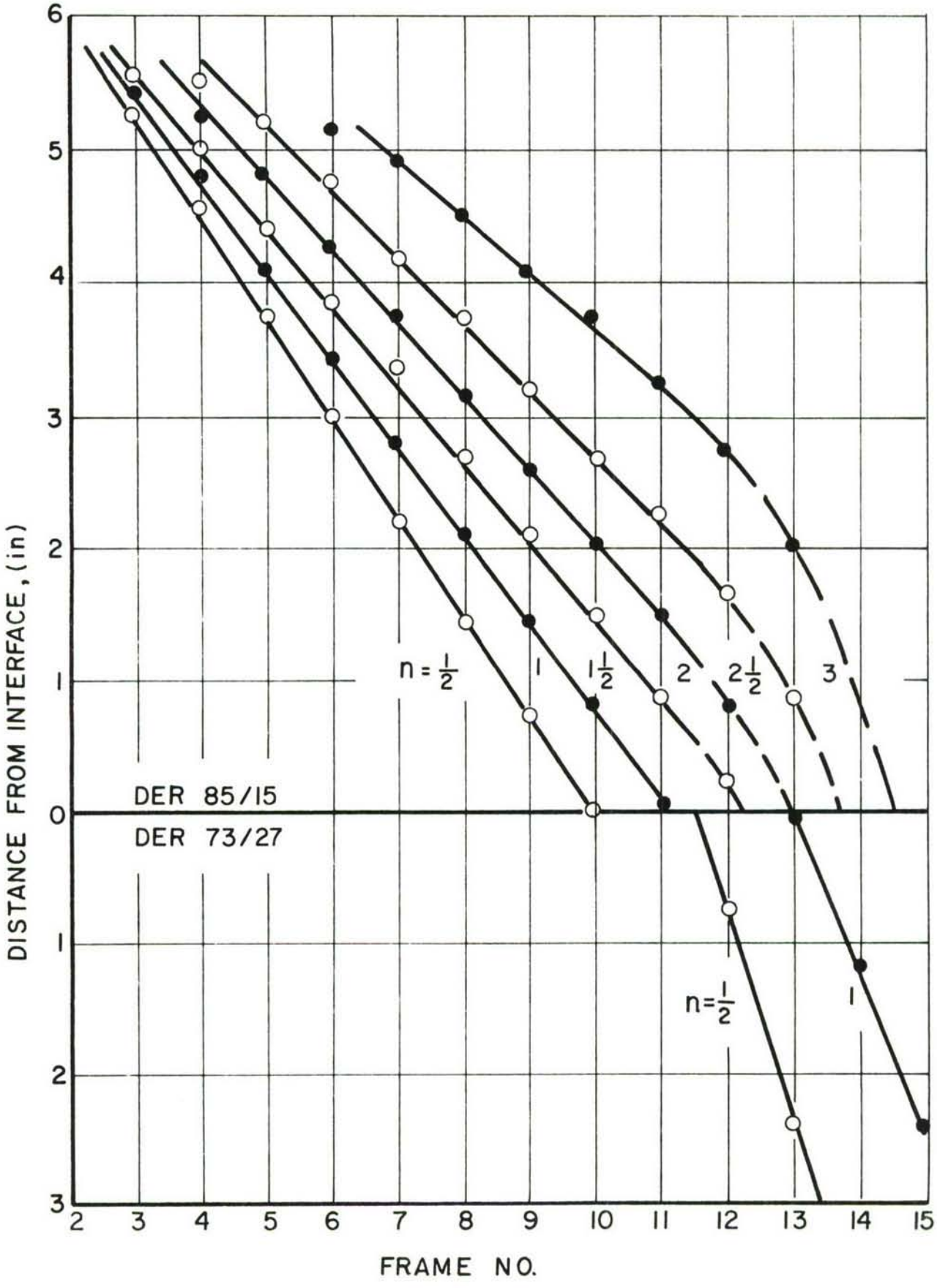


Figure 53. FRINGE POSITION AS A FUNCTION OF TIME IN MODEL I-5

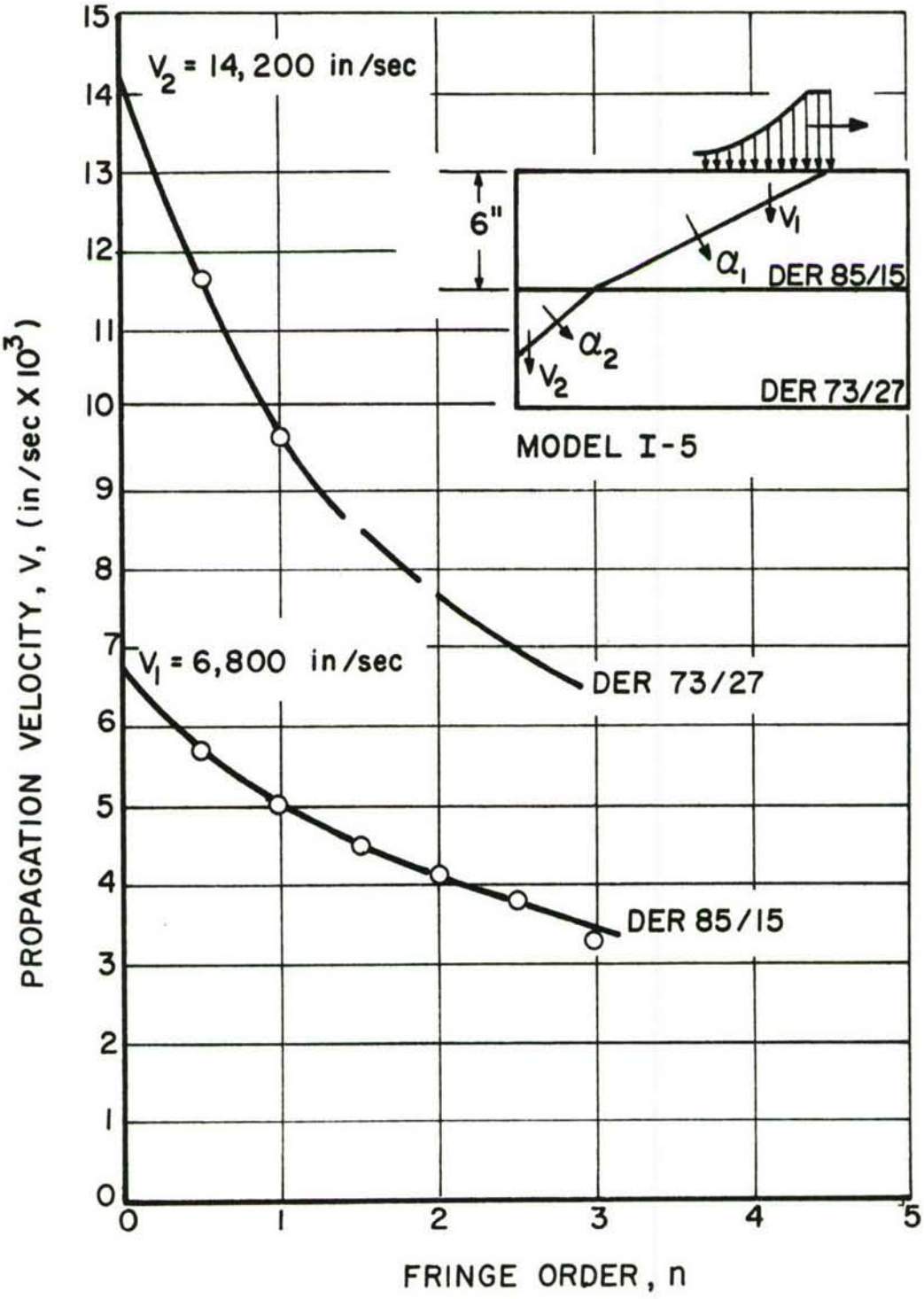


Figure 54. WAVE PROPAGATION VELOCITY IN TWO LAYERS OF MODEL I-5 AS A FUNCTION OF FRINGE ORDER

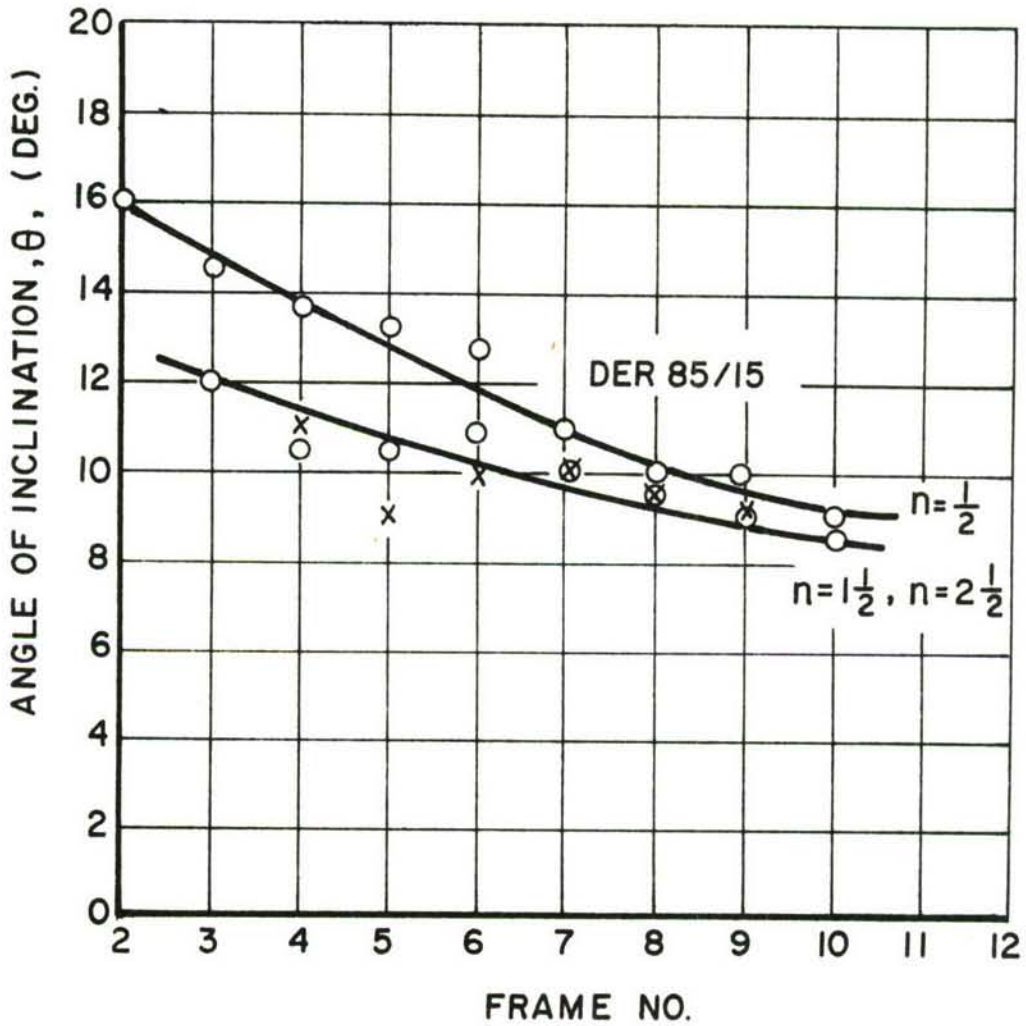


Figure 55. ANGLE OF FRINGE INCLINATION IN MODEL I-5 AS A FUNCTION OF TIME

used in the present study.

The effect of the high-impedance medium on the low-impedance one is manifested in the curvature of the otherwise straight line fringes, especially noticeable with higher orders. This is due to superposition of reflected waves upon the incident one. A local intensification of the pulse, and hence an increase in stress, results near the interface. A 2 1/2-order fringe occurs where normally a 2-order fringe would be, thus indicating a 25 percent increase in maximum shear stress at the interface. No noticeable influence of the upper layer on the lower one can be detected near the interface. Fringes in the lower layer show some curvature, however, it is not known for certain whether this is due to reflections from the side of the model or to attenuation along the wavefront. Separation of principal stresses was not possible within the time limitations of the program. A complete set of moiré data and a viscoelastic analysis would be required for a complete stress analysis.

SECTION VII

WAVE PROPAGATION IN LAYERED MODEL DUE TO EXPLOSIVE LOADING IN LOW-IMPEDANCE MEDIUM

1. Introduction

The problem of wave propagation due to point source loading is more complex analytically than the case of plane waves. Experimentally, no additional complications are introduced by the point source loading and the same methods of analysis of experimental results are used. Explosive loadings used in this case produce short and intense pressure pulses and allow the use of harder birefringent materials. In addition, this type of loading allows the observation of many types of waves, such as transmitted, reflected and refracted dilatational and shear waves and headwaves predicted theoretically (Section II). In this phase of the study, layered models with materials having an impedance ratio of 2:1 were tested under buried explosive loading in the low-impedance medium. The distance between the loading source and the interface between the two media was varied parametrically.

2. Experimental Procedure

As described in Sections IV and V, the model materials selected for this phase of the study were DER 60/40 and Columbia Resin CR-39 for the low- and high-impedance layers, respectively. The models were made by cementing together along one edge two sheets of these materials 20 in. x 8 in. x 1/4 in. (Fig. 56). Three models were used with varying distances between the explosive source and the interface:

Model II-1: $h = 1$ in.
Model II-2: $h = 2$ in.
Model II-3: $h = 3$ in.

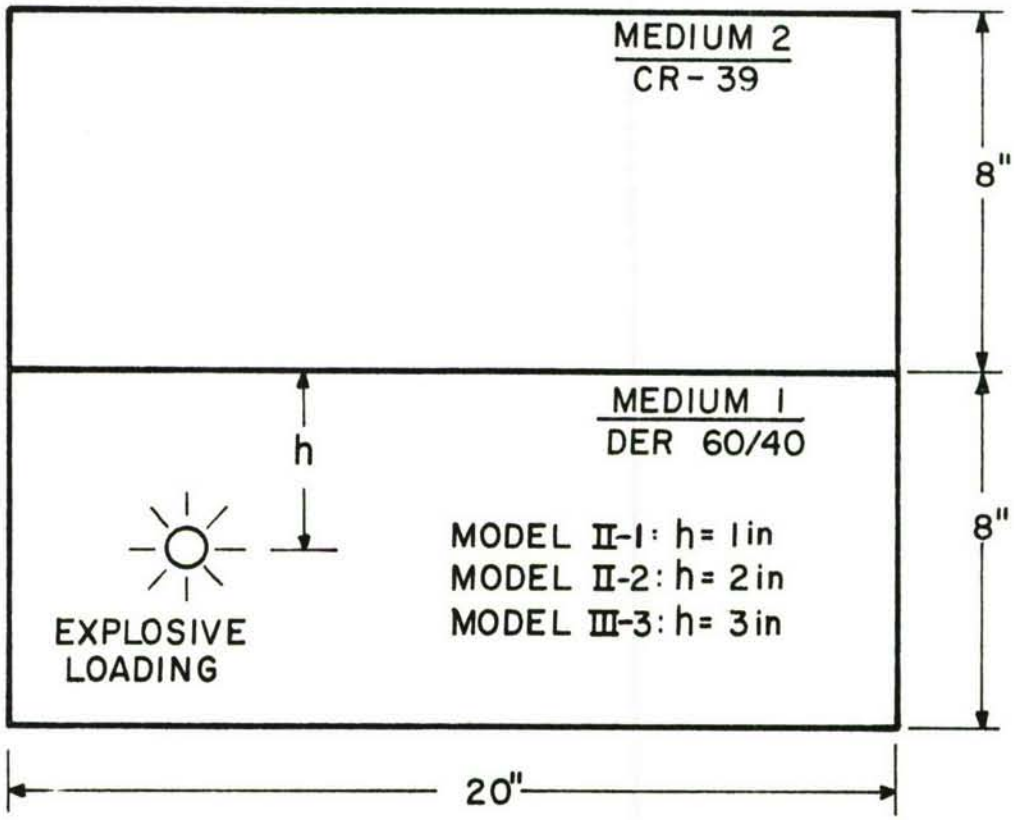


Figure 56. SKETCH OF MODEL SHOWING DIMENSIONS AND LOCATIN OF EXPLOSIVE LOADING SOURCE IN LOW-IMPEDANCE MEDIUM (PHASE II)

After a number of preliminary tests, it was found that the low-impedance material (DER 60/40) ages and its wave propagation velocity increases. Changes in this velocity, from 41,000 in./sec shortly after casting to 51,000 in./sec a few weeks later, were measured. This change resulted in a reduction of the impedance ratio from 2:1 to 1.6:1. Subsequent tests also showed that the impedance of the cementing material, even though it is used in a very small layer, plays an important role in the interaction of waves at the interface.

The final series of tests was conducted with models made of newly cast material and cemented with an epoxy cement matching the impedance characteristics of Columbia Resin. The explosive testing was conducted following procedures described previously (III-3a). Isochromatic fringe patterns were recorded with the Schardin camera.

3. Results and Discussion

Figure 57 shows the isochromatic fringe pattern for Model II-1D tested shortly after the low-impedance material was cast. This results in a somewhat lower wave propagation velocity in the low-impedance medium and a higher than 2:1 impedance ratio. The wave propagation velocities of several fringe orders were determined for the two media and plotted in Fig. 58 as a function of fringe order. By extrapolation to the zero order fringe the following wave velocities were obtained for the two media

$$\alpha_1 = 34,000 \text{ in./sec}$$
$$\alpha_2 = 71,500 \text{ in./sec}$$

where α denotes the velocity of the P-wave and the subscripts 1 and 2 denote the low- and high-impedance media, respectively. The resulting impedance ratio is 2.4:1. This higher impedance ratio produces a more detailed fringe pattern at the interface with at least three headwaves discernible.

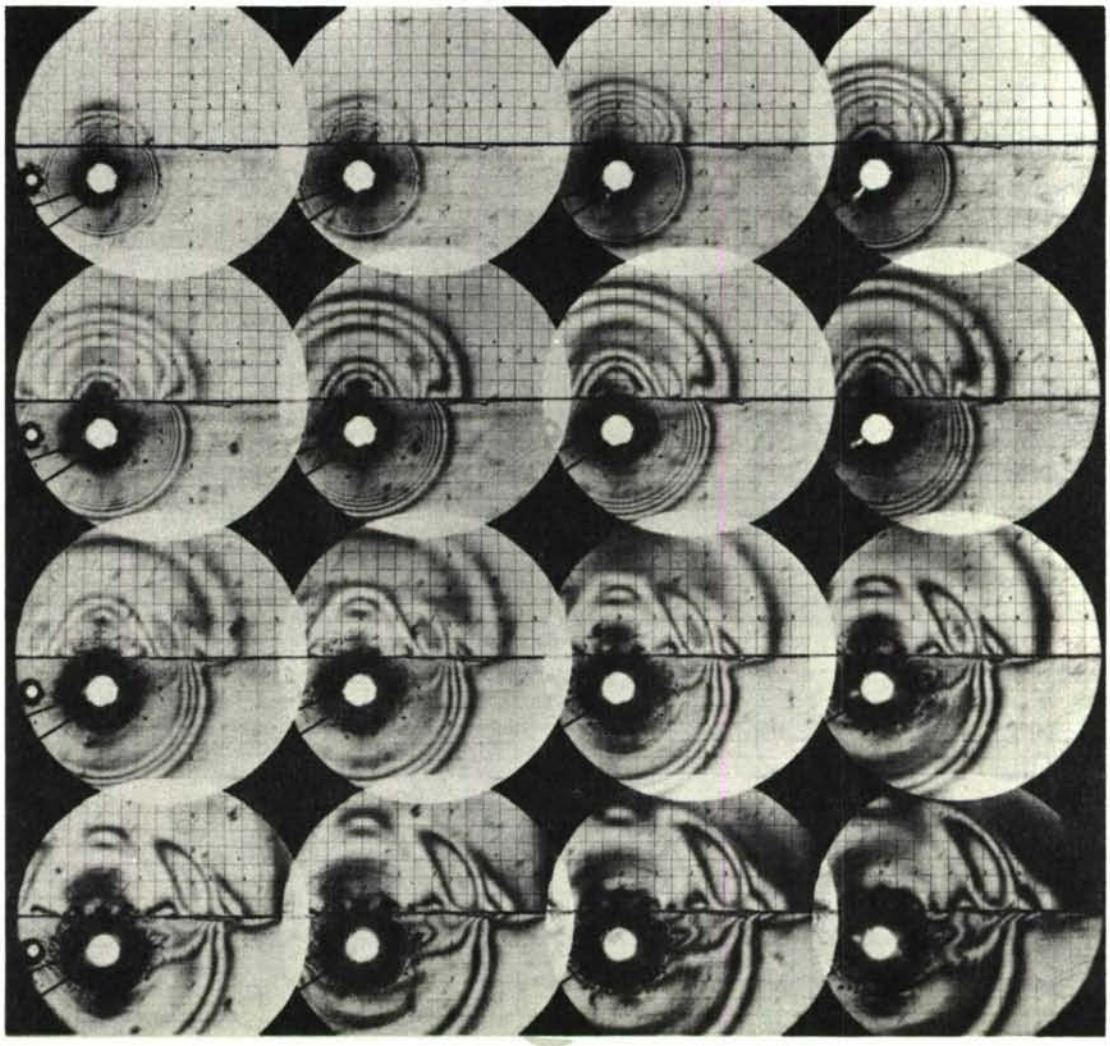


Figure 57. ISOCHROMATIC FRINGE PATTERNS IN MODEL II-1D (EXPLOSIVE SOURCE IN LOW-IMPEDANCE MEDIUM 1 IN. FROM INTERFACE; IMPEDANCE RATIO 2.40:1; CAMERA SPEED: 187,000 FRAMES/SEC)

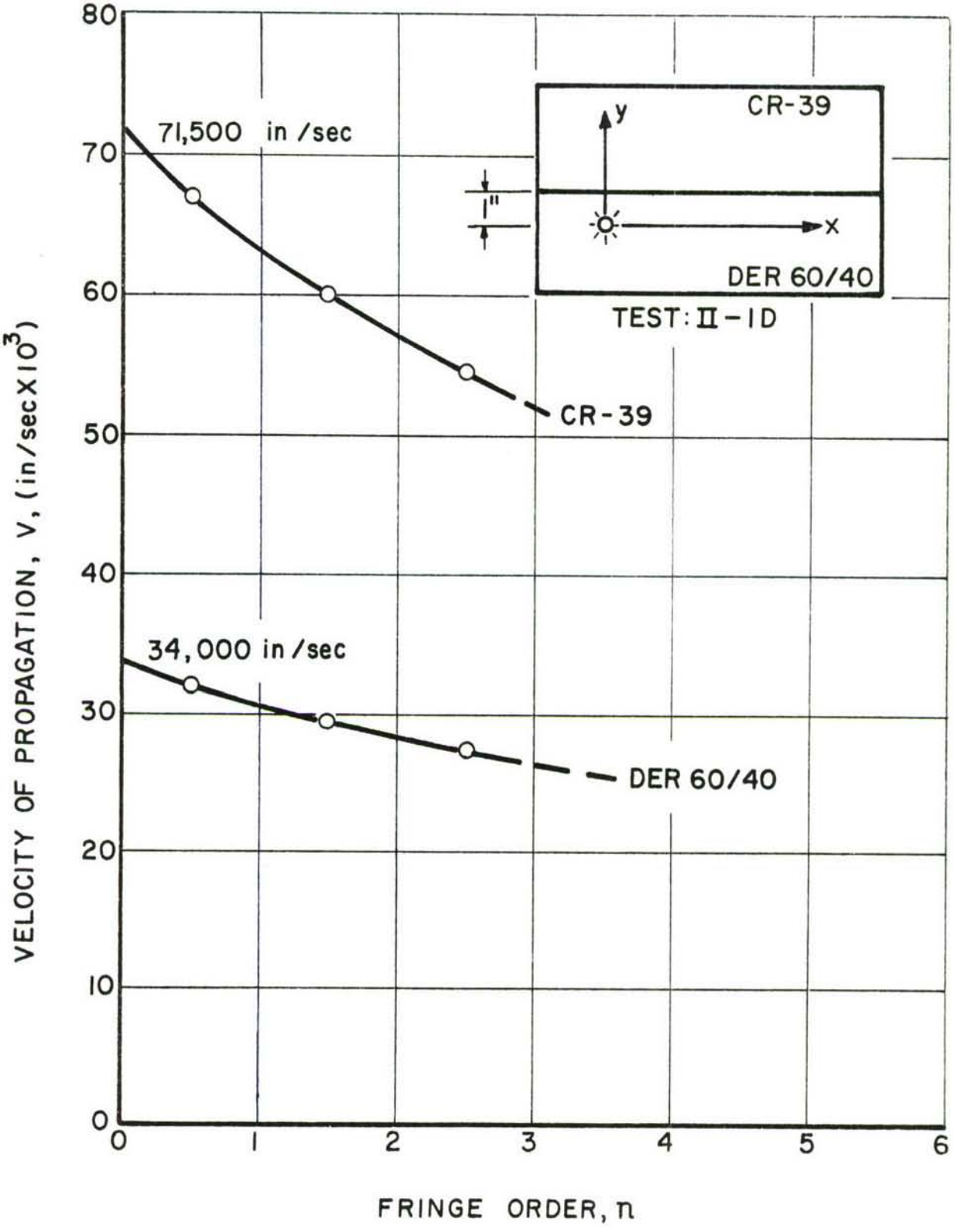


Figure 58. VELOCITY OF WAVE PROPAGATION AS A FUNCTION OF FRINGE ORDER IN TWO MEDIA OF MODEL II-1D

The nature of the incident P_1 wave was studied by plotting birefringence versus location along a horizontal line through the point source with time as a parameter (Fig. 59). The dispersion of the pulse is evident as it gets wider and its leading slope gets shallower with time. The attenuation is very pronounced and it is due to both the geometry of the wave (cylindrical) and to the viscoelastic nature of the material. The attenuation can be described by a curve drawn through the peaks of the pulse at different times. This curve cannot be described adequately by a rectangular hyperbola as was done in the past, mainly due to the viscoelastic nature of the material. Plotting the maximum fringe order versus location on semilog paper proved that an exponential fit of the following form was very satisfactory:

$$n_{max} = e^{k\,(x_o - x)} \tag{38}$$

In the present case, the two parameters had the following values:

$$k = 0.71$$
$$x_o = 3.96$$

A similar analysis was conducted for the refracted $P_1\,P_2$ wave in the high-impedance medium in the direction perpendicular to the interface. Figure 60 shows plots of birefringence versus location with time as a parameter. Although the peak of the pulse is rounded off with time, the base of the pulse does not widen. The attenuation is not as high as in the case of the P_1 wave, due to the less dissipative nature of CR-39. A similar exponential fit was found satisfactory.

$$n_{max} = e^{k\,(y_o' - y')} \tag{39}$$

with

$$k = 0.46 \quad \text{and} \quad y_o' = 4.00$$

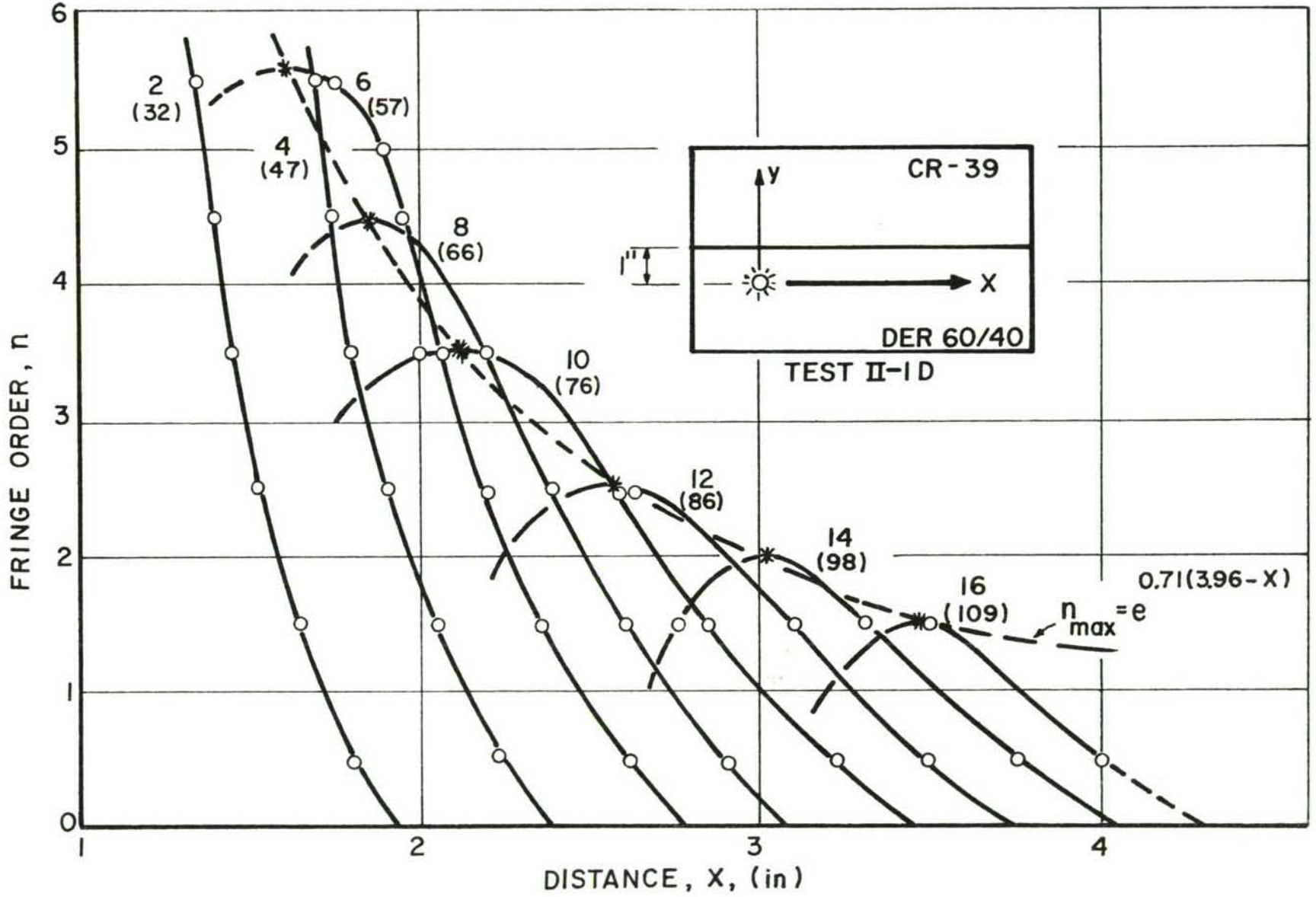


Figure 59. FRINGE ORDER AS A FUNCTION OF POSITION WITH TIME AS A PARAMETER FOR INCIDENT WAVE P_1 IN LOW-IMPEDANCE MEDIUM OF MODEL II-1D

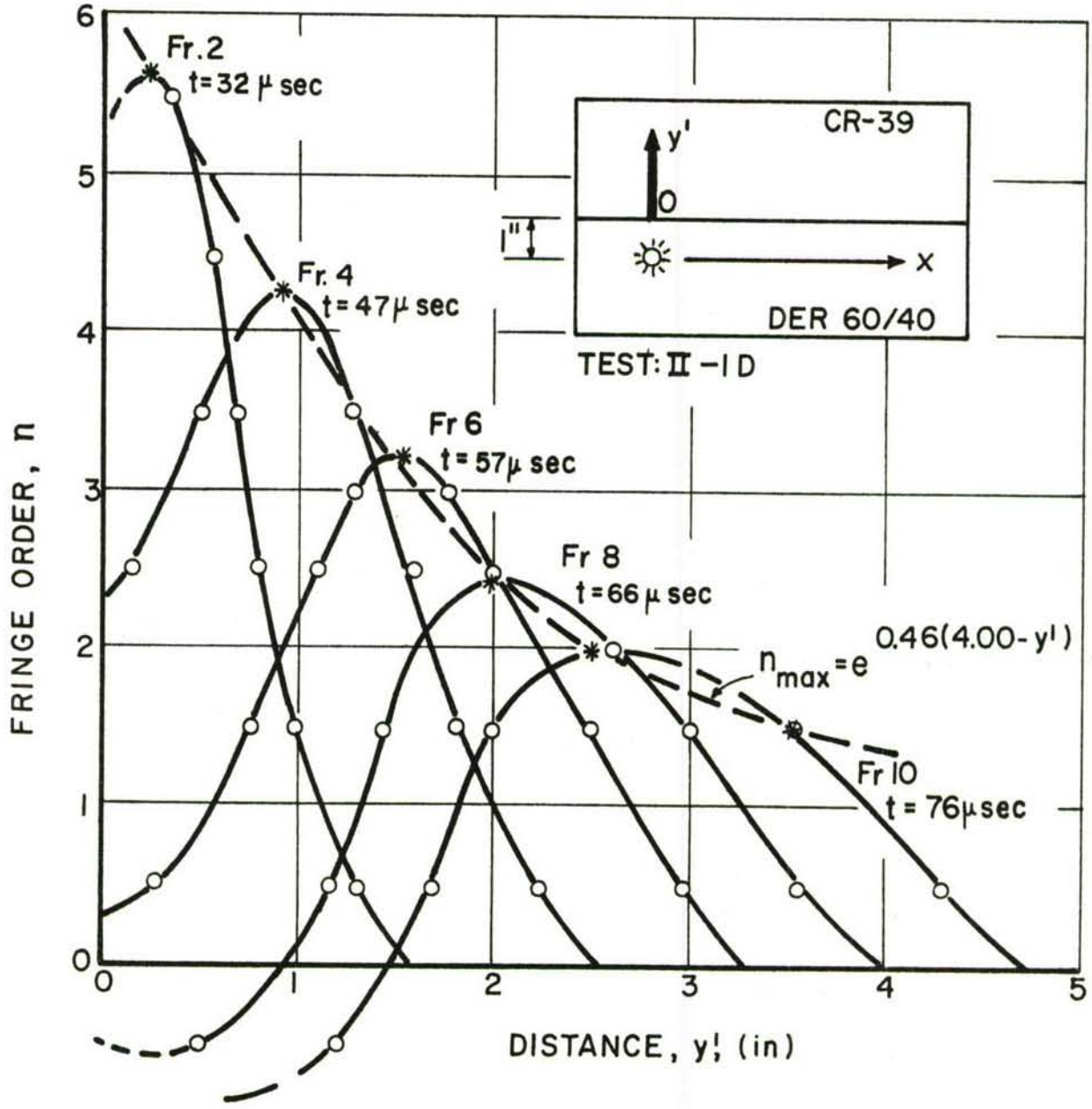


Figure 60. FRINGE ORDER AS A FUNCTION OF POSITION WITH TIME AS A PARAMETER FOR REFRACTED WAVE P_1P_2 IN HIGH-IMPEDANCE MEDIUM OF MODEL II-1D

and y' the distance from the interface. The parameter k, being a measure of the attenuation, shows that the attenuation of the $P_1\ P_2$ wave is appreciably lower than that of the P_1 wave.

The birefringence in the high-impedance medium along the interface is due for the most part to a combination of the two refracted waves $P_1\ P_2$ and $P_1\ S_2$. Birefringence versus position along the interface with time as a parameter is plotted in Fig. 61. Initially, the pulse shape is simple but later on it takes an undulatory shape as the influence of the $P_1\ P_2\ S_2$ wave comes in. An exponential fit for the variation of maximum fringe order with location along axis Ox' was found satisfactory

$$n_{max} = e^{k\ (x_o' - x')} \qquad (40)$$

with $k = 0.51$ and $x_o' = 3.58$. Here, the coefficient of attenuation is close to that for the $P_1\ P_2$ wave along the axis perpendicular to the interface.

The birefringence in the low-impedance medium along the interface is influenced by the incident P_1 wave as well as the reflected $P_1\ P_1$, $P_1\ S_1$ waves and the headwaves preceding the P_1 wave. Birefringence versus position along the interface with time as a parameter is plotted in Fig. 62. The pulse has two peaks, the one in front being much smaller and corresponding to the $P_1\ P_2\ S_1$ headwave. The larger of the peaks corresponding primarily to the incident P_1 wave attenuates according to the following equation

$$n_{max} = e^{0.39\ (6.38 - x')}$$

The smaller of the peaks shows hardly any attenuation which is characteristic of the headwaves. It is entirely possible then that the amplitude of the headwave becomes of the same order of magnitude or even overshadows that of the P_1 wave at some later time.

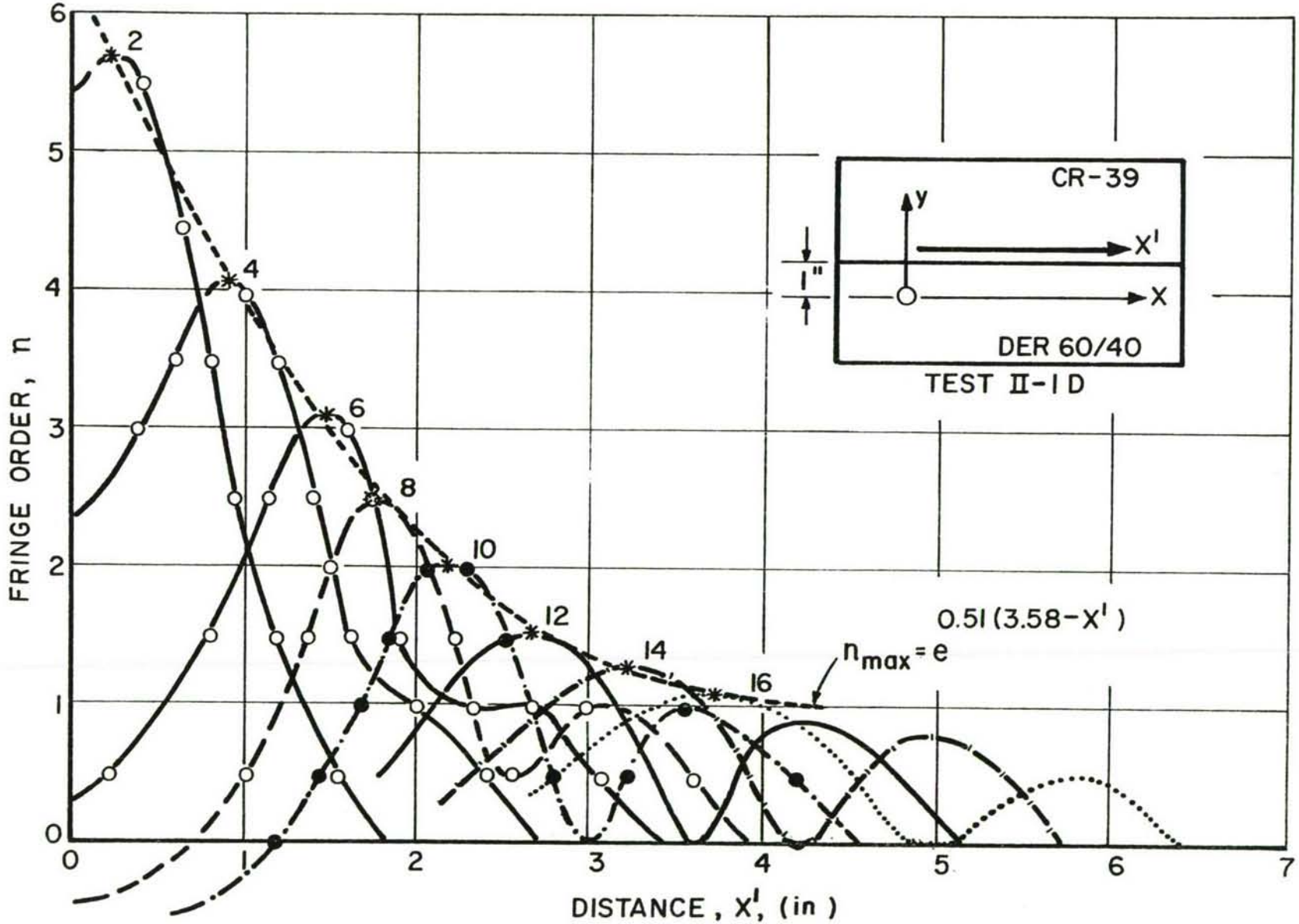


Figure 61. FRINGE ORDER AS A FUNCTION OF POSITION WITH TIME AS A PARAMETER FOR REFRACTED WAVES IN HIGH-IMPEDANCE MEDIUM ALONG INTERFACE (MODEL II-1D; FRAME NUMBERS ARE MARKED)

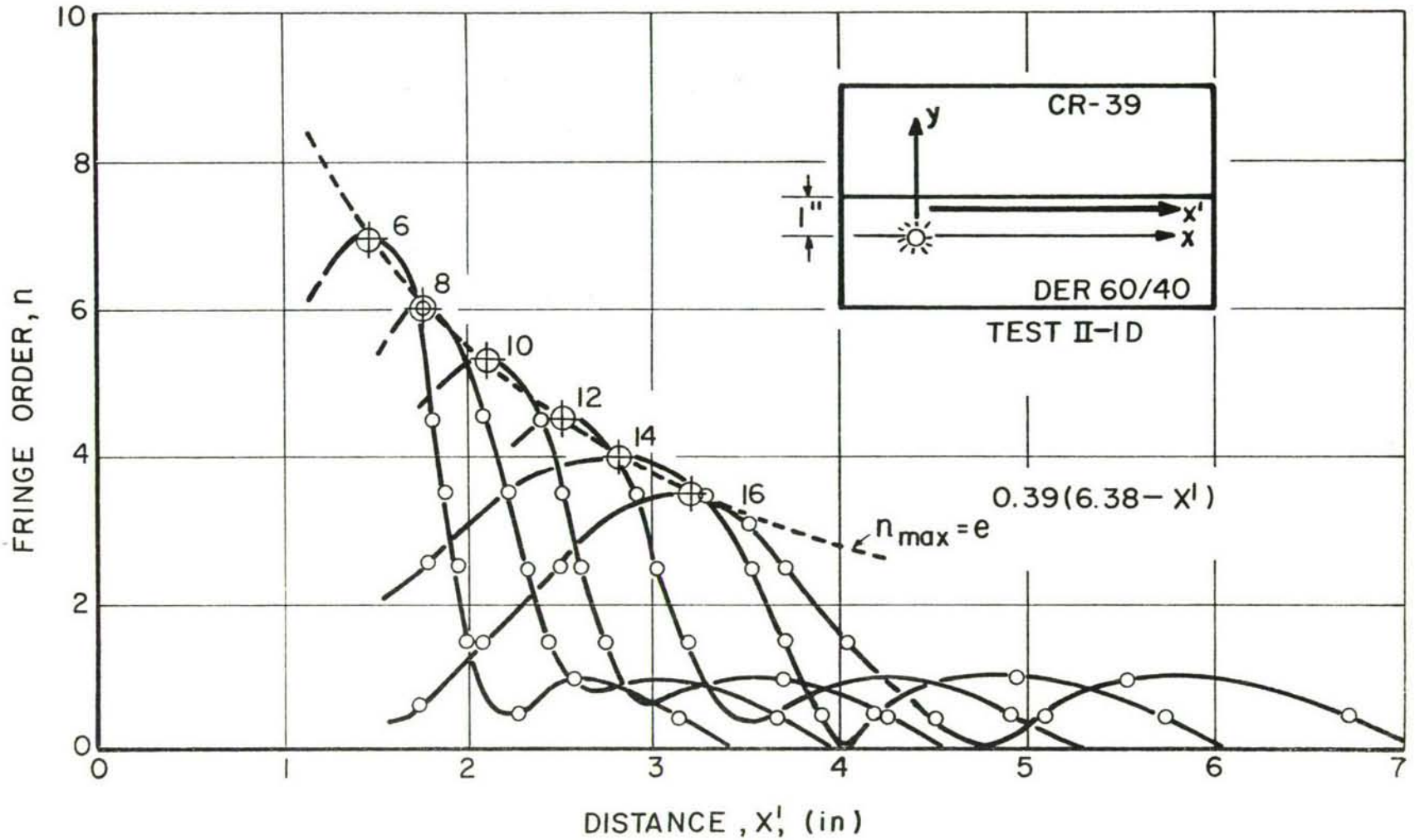


Figure 62. FRINGE ORDER AS A FUNCTION OF POSITION WITH TIME AS A PARAMETER IN LOW-IMPEDANCE MEDIUM ALONG INTERFACE (MODEL II-1D; FRAME NUMBERS ARE MARKED)

Based on the velocities determined above and an estimated value of Poisson's ratio values for Young's modulus corresponding to the wavefront were obtained for both media. Thus, for medium 2 (CR-39) we have

$$\alpha_2 = c_L = 71{,}500 \text{ in./sec}$$

$$\nu = 0.33$$

$$\rho = 122 \times 10^{-6} \text{ lb sec}^2/\text{in.}^4$$

Hence,

$$E_{CR\text{-}39} = c_L^2 \rho (1 - \nu^2) = 555{,}000 \text{ psi}$$

The corresponding velocity of the distortional wave would be

$$\beta_2 = \left[\frac{E}{2\rho(1+\nu)}\right]^{1/2} = \alpha_2 \left(\frac{1-\nu}{2}\right)^{1/2} = 41{,}400 \text{ in./sec}$$

Referring the value of the modulus above to the curve of Young's modulus of CR-39 versus loading time (Fig. 26), we find a corresponding time of loading of less than a microsecond (approximately 0.4 μ sec).

For the low-impedance medium we have

$$\alpha_1 = c_L = \left[\frac{E}{\rho(1-\nu^2)}\right]^{1/2} = 34{,}000 \text{ in./sec}$$

$$\rho = 107 \times 10^{-6} \text{ lb sec}^2/\text{in.}^4$$

$$\nu = 0.30 \text{ (corresponding to loading time of 0.4 } \mu \text{ sec)}$$

Then,

$$E_{DER\ 60/40} = 110{,}000 \text{ psi}$$

The corresponding velocity of the distortional wave would be

$$\beta_1 = \alpha_1 \left(\frac{1 - \nu}{2}\right)^{1/2} = 20{,}000 \text{ in./sec}$$

The elastic theory of wave propagation predicts the formation of an incident P wave, reflected P and S waves, refracted P and S waves and five conical or headwaves. The formation of these various waves depends on the wave propagation characteristics of the media and on time. The following various stages of wave formation are predicted for model II-1D:

1) For $0 < t < \frac{h}{\alpha_1}$ or $0 < t < 29$ μ sec there is only the incident P_1 wave. Actually the upper limit is lower since we do not have a mathematical point source but a cylindrical cavity loaded by the explosive.

2) When the incident P_1 wave reaches the interface, two reflected waves P_1P_1 and P_1S_1 and two refracted waves P_1P_2 and P_1S_2 are generated. These waves and the incident P_1 wave remain connected until a certain time when the incident wave propagation along the interface equals the refracted P_1P_2 wave velocity (Fig. 63)

$$\frac{\alpha_1}{\sin \theta_{CR}} = \alpha_2 \tag{41}$$

In the present case

$$\theta_{CR} = \text{arc sin} \left(\frac{\alpha_1}{\alpha_2}\right) = 28.4° \tag{42}$$

The time period for this stage of wave formation is

$$\frac{h}{\alpha_1} < t < \frac{h}{\alpha_1 \cos \theta_{CR}} \quad \text{or} \quad 29 \text{ μ sec} < t < 34 \text{ μ sec}$$

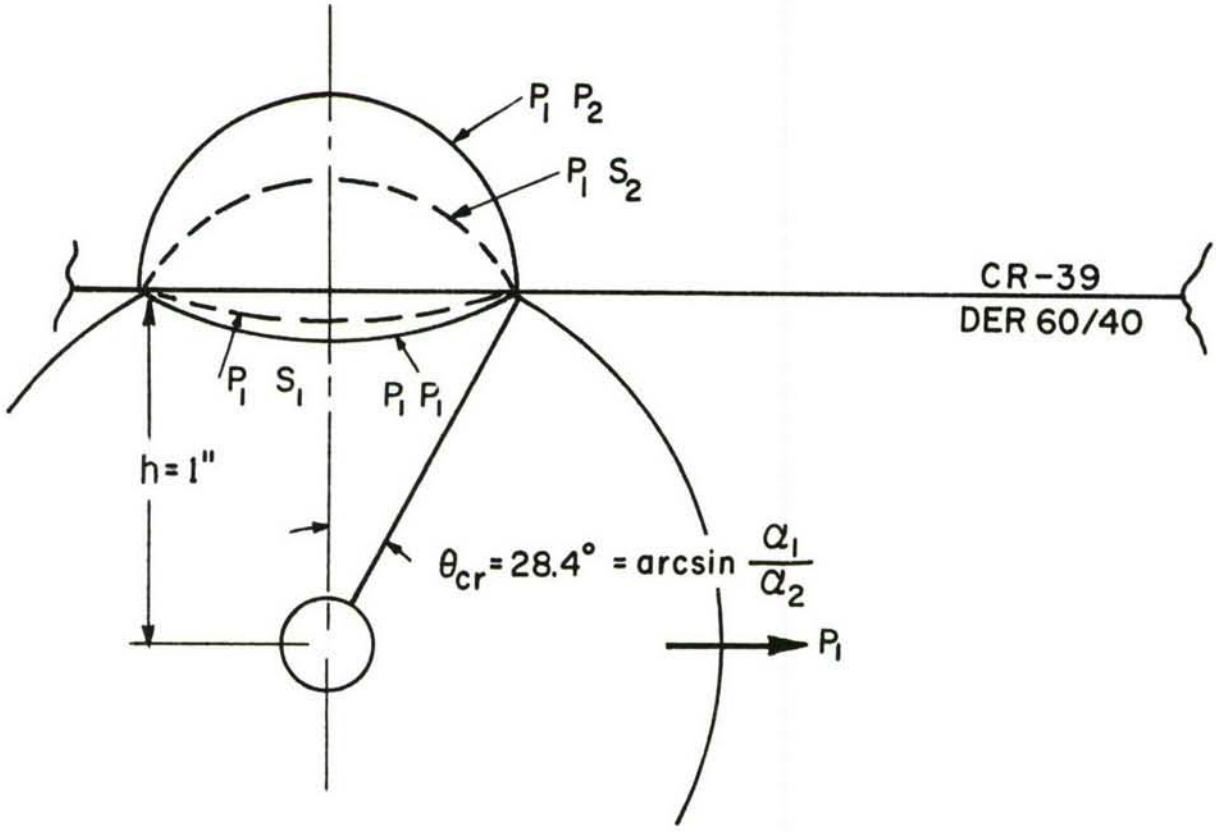


Figure 63. WAVE PROPAGATION IN TIME PERIOD $h/\alpha_1 < t < h/\alpha_1 \cos\theta_{CR}$ OR 29 μ sec $< t <$ 34 μ sec FOR MODEL II-1D

3) For times $t > h/\alpha_1 \cos \varphi_{CR}$ or $t > 34$ μ sec, the theory predicts the development of three headwaves $P_1P_2P_1$, $P_1P_2S_1$ and $P_1P_2S_2$ (Fig. 64). This information cintunues until $t = h/\alpha_1 \cos \varphi_{CR} = 43$ sec, where

$$\varphi_{CR} = \text{arc sin} \frac{\alpha_1}{\beta_2} = 55.2° \tag{43}$$

when the refracted P_1S_2 wave begins to outrun the incident P_1 wave.

4) For $t > h/\alpha_1 \cos \varphi_{CR}$ or $t > 42$ μ sec, two additional headwaves develop as the P_1S_2 wave outruns the P_1 wave. These headwaves are $P_1S_2P_1$ at an angle of $\varphi_1 = \text{arc sin} \frac{\alpha_1}{\beta_2} = 55.2°$ and $P_1S_2S_1$ at an angle of $\varphi_2 = \text{arc sin} \frac{\beta_1}{\beta_2} = 29.0°$. This complete set of waves is illustrated in Fig. 3.

Some of the wave formations discussed here are evident in the record of Fig. 57. More detail is seen in enlargements of individual frames. Frame 6 for example, corresponding to $t = 57$ μ sec, shows clearly the two headwaves $P_1P_2S_1$ and $P_1P_2S_2$ inclined at the calculated angles of $\theta_2 = 16.3°$ and $\theta_3 = 35.3°$. (Fig. 65.) Frame 12 corresponding to $t = 86$ μsec shows the two headwaves above inclined at the same angles and the beginning of a third headwave $P_1S_2S_1$ inclined at an angle $\varphi_2 = 29.0°$. (Fig. 66.) Figure 67 shows the last frame of the record (Frame 16, $t = 109$ μ sec). The wavefronts of the headwaves have been drawn on the photograph as calculated above. The match with the fringe patterns is very satisfactory. One feature, especially noticeable in Frame 16, is the curvature of the half-order fringe of the $P_1P_2S_1$ headwave. This may be due to attenuation along the wavefront. This headwave may then be a "general plane wave" as described by Cooper (Ref. 16), since the model materials used here are definitely viscoelastic.

An elastic analysis was used to separate stresses in the refracted P_1P_2 wave taking advantage of an approximate polar symmetry.

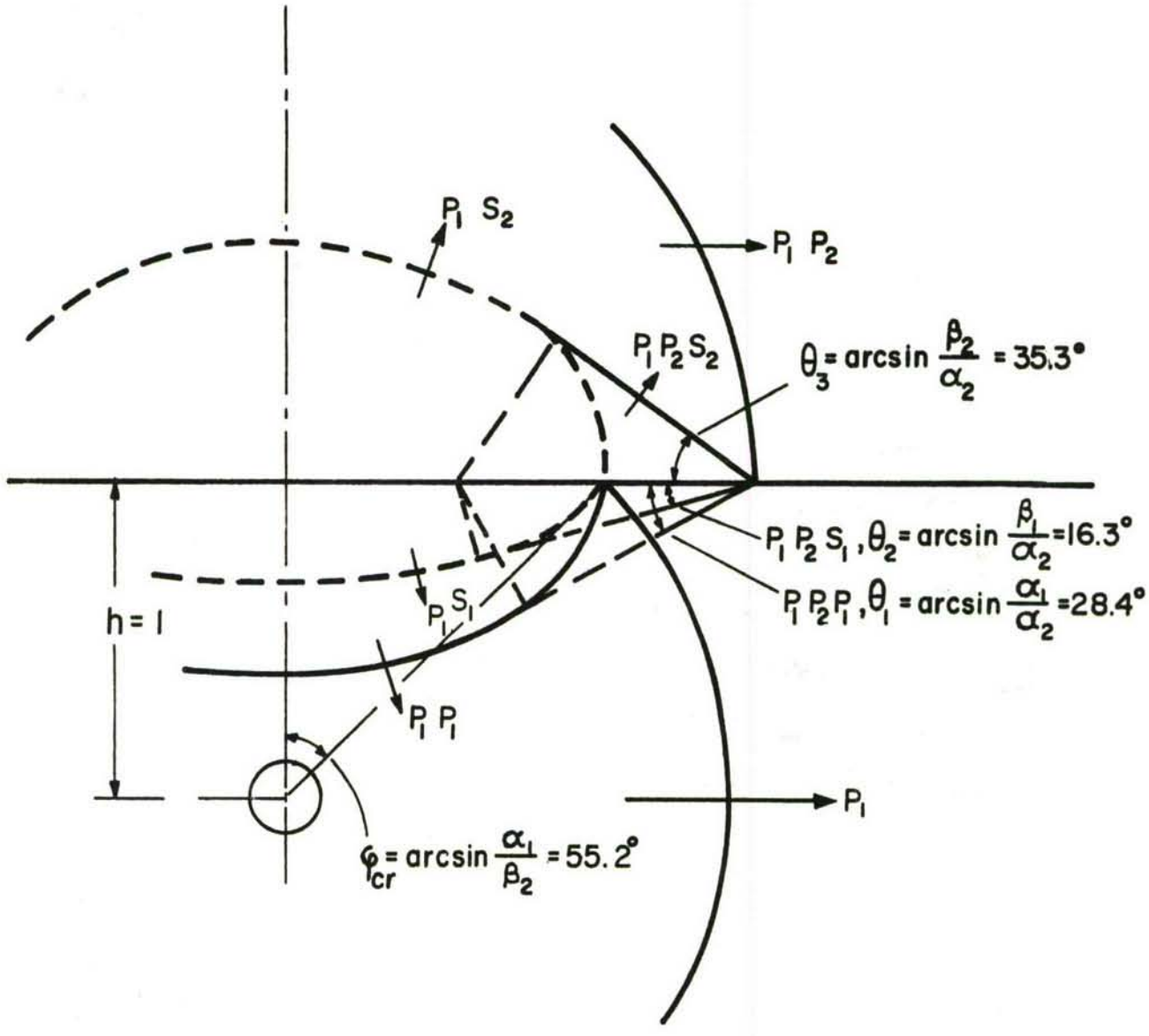


Figure 64. WAVE PROPAGATION IN TIME PERIOD $h/\alpha_1 \cos\theta_{CR} < t < h/\alpha_1 \cos \varphi_{CR}$ OR 34 μ sec $< t <$ 42 μ sec

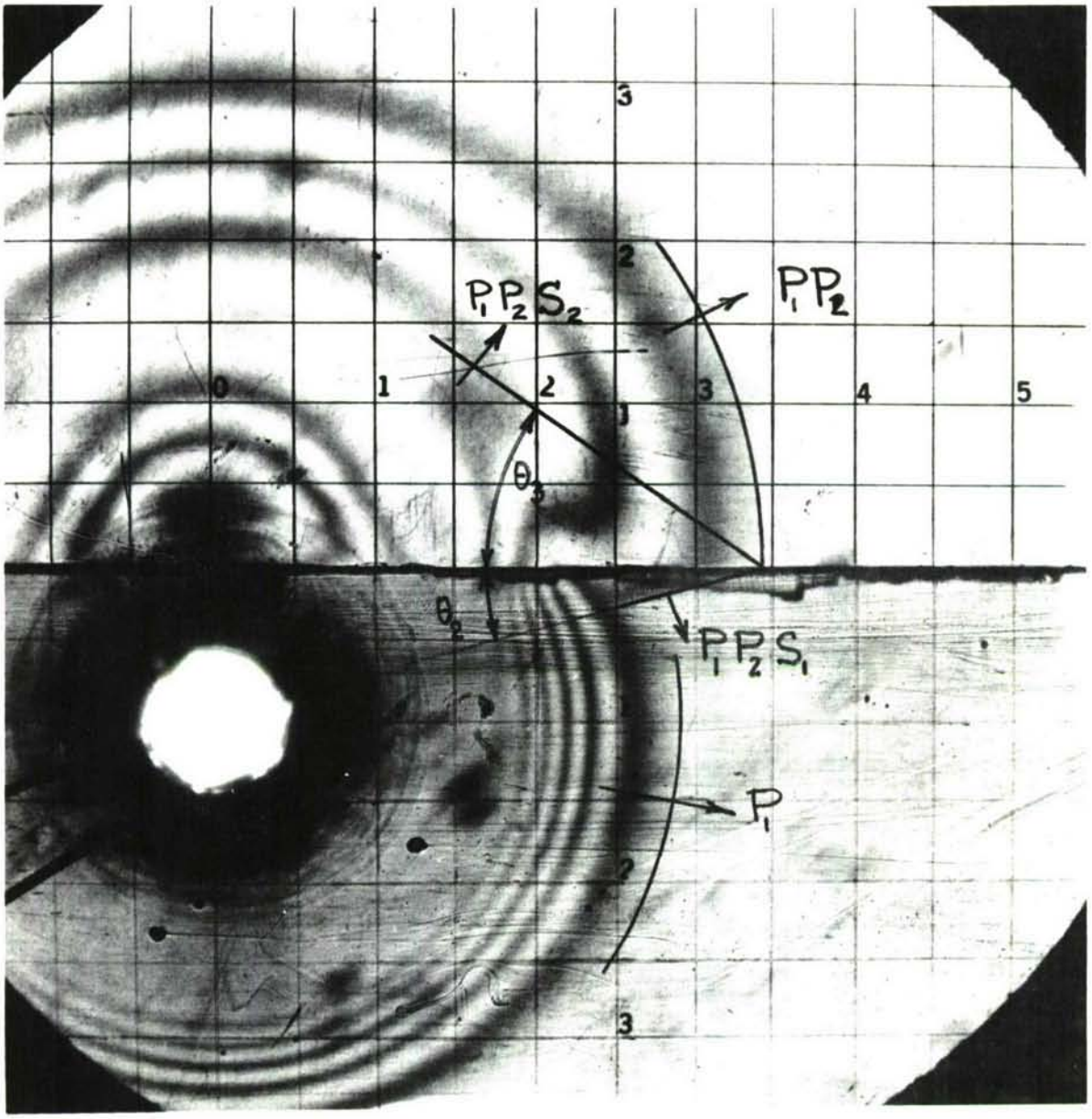


Figure 65. DETAIL OF FRAME 6 (t = 57 μ sec) SHOWING TWO HEADWAVES

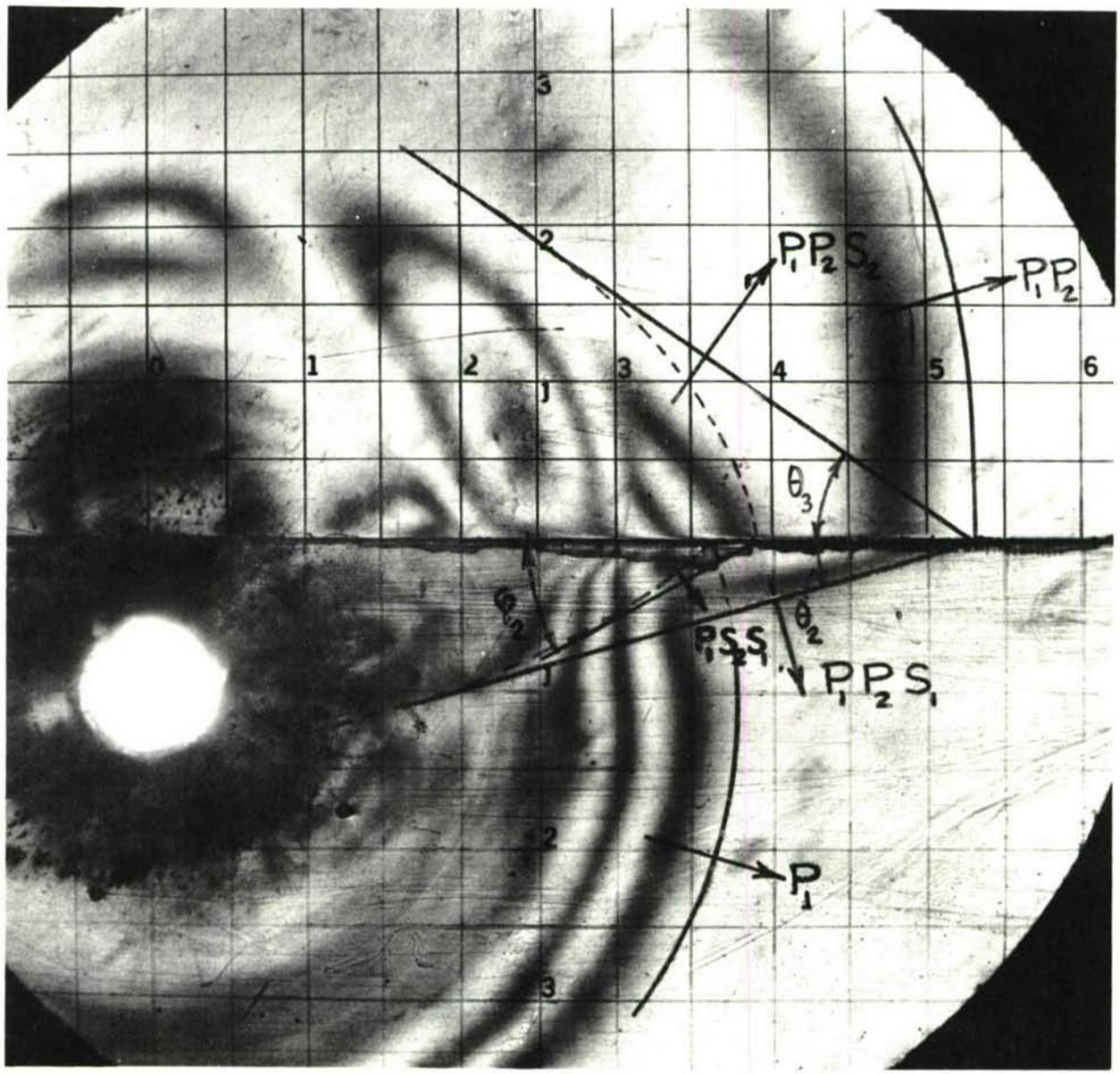


Figure 66. DETAIL OF FRAME 12 (t = 86 μ sec) SHOWING THREE HEADWAVES

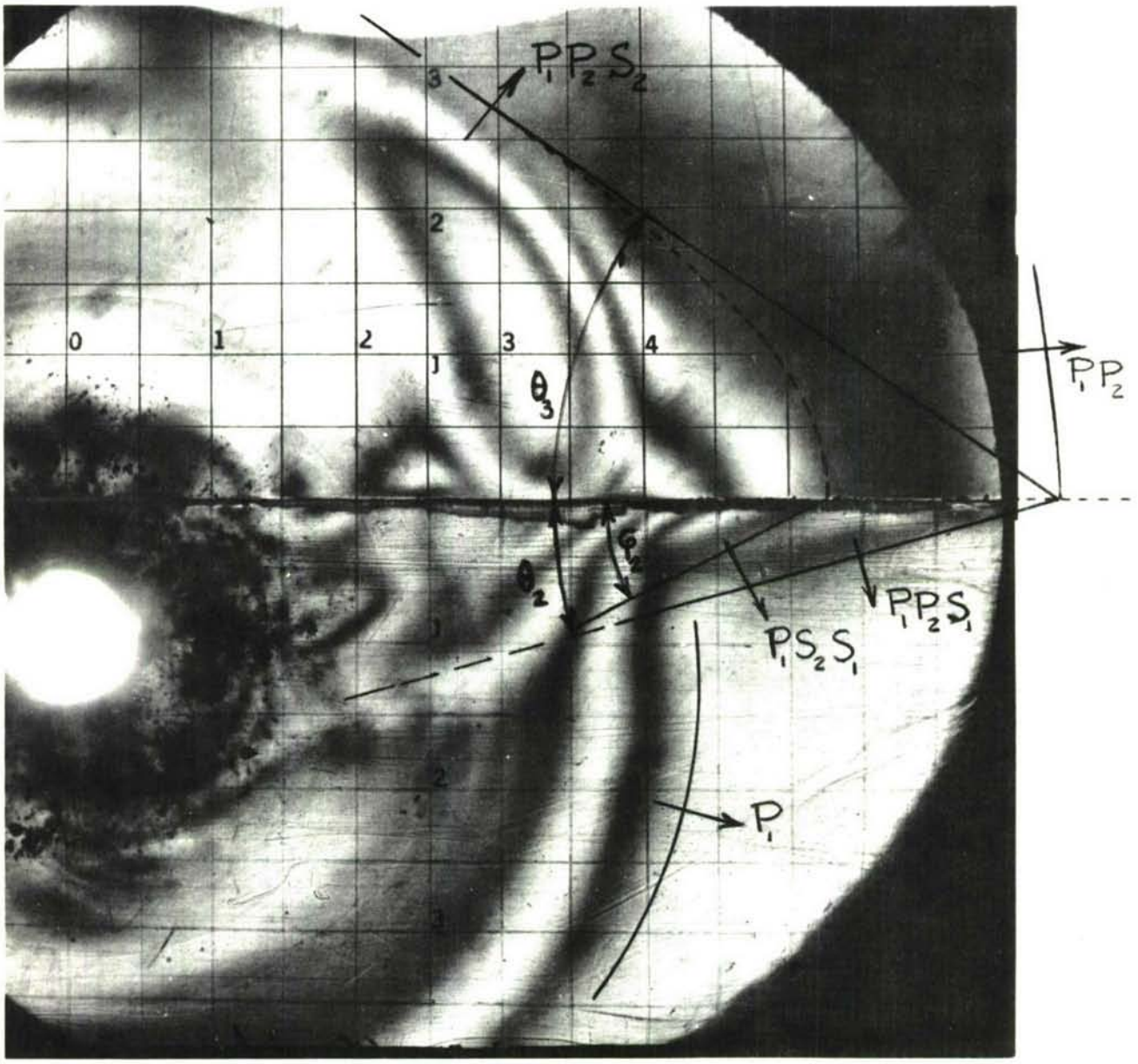


Figure 67. DETAIL OF FRAME 16 (t = 109 μ sec) SHOWING THREE HEADWAVES

The same procedure as that described by Dally and Riley (Ref. 3) was used. The strain displacement equations for polar symmetry are

$$\varepsilon_{rr} = \frac{du_r}{dr}$$
$$\varepsilon_{\theta\theta} = \frac{u_r}{r} \tag{44}$$

where u_r is the radial displacement and r the radial distance. Substituting these relations in the stress-strain relation

$$\sigma_{\theta\theta} - \sigma_{rr} = \frac{E}{1 + \nu} (\varepsilon_{\theta\theta} - \varepsilon_{rr}) \tag{45}$$

integrating and applying the stress-optic law, we obtain for the circumferential strain

$$\varepsilon_{\theta\theta} = \frac{u_r}{r} = - \frac{2 (1 + \nu) f_\sigma}{E h} \int_r \frac{n}{r} dr \tag{46}$$

where h is the model thickness. Then, the radial strain is given by

$$\varepsilon_{rr} = \varepsilon_{\theta\theta} - \frac{2 (1 + \nu) f_\sigma}{E h} n \tag{47}$$

To select the appropriate values for modulus and fringe value for CR-39 from the curves shown in Fig. 26, it was necessary to determine the relevant time parameter. Fringe orders at two distances from the interface ($y' = 1$ in. and $y' = 2$ in.) were plotted versus time as shown in Fig. 68. It can be noted that the time from zero to peak for both locations is approximately 20 μ sec. For this time parameter, the following values of modulus and fringe value were obtained

$$E = 460{,}000 \text{ psi}$$
$$f_\sigma(5445\text{Å}) = 58.6 \text{ psi-in./fringe}$$

or

$$f_\sigma(4300\text{Å}) = 46.3 \text{ psi-in./fringe}$$

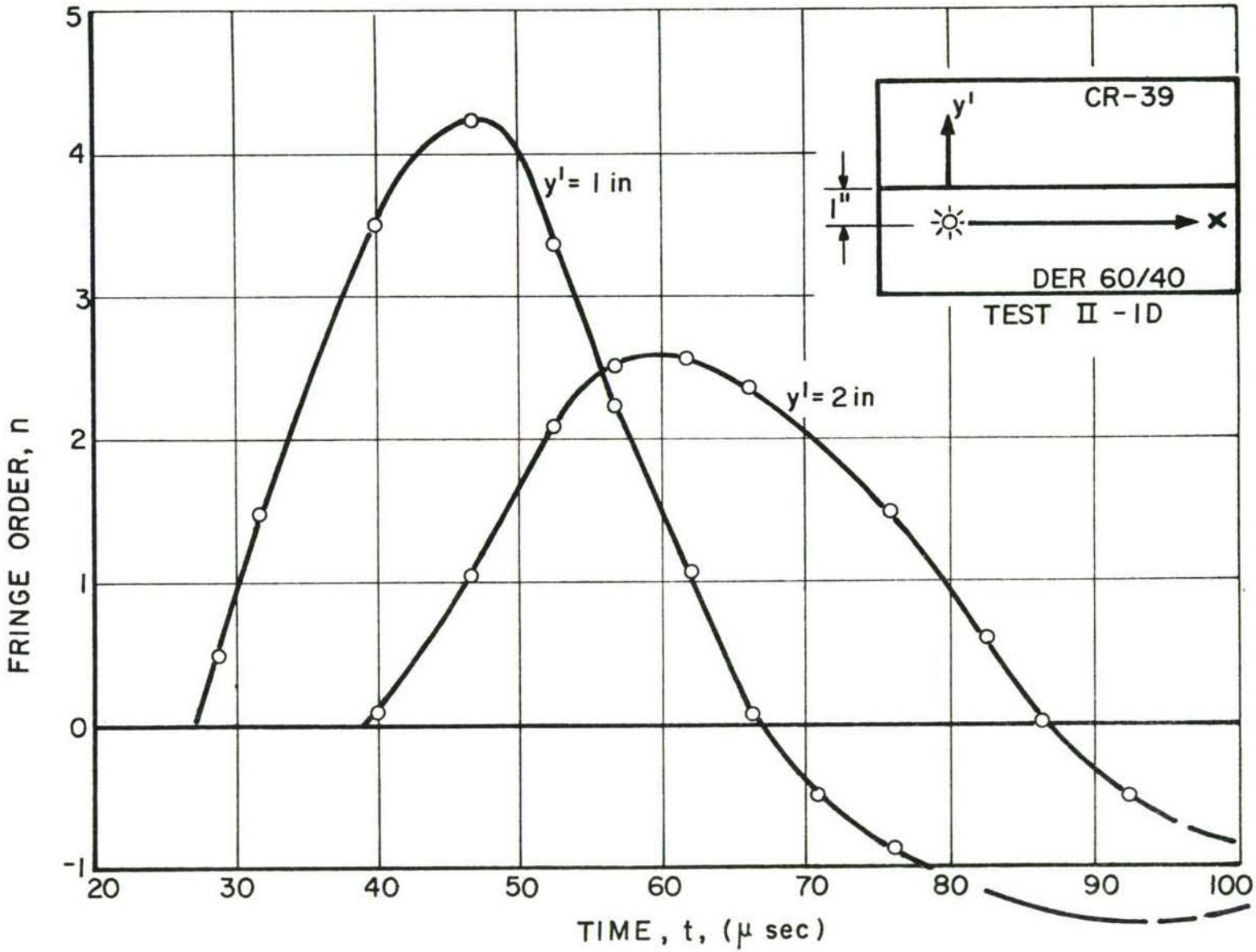


Figure 68. VARIATION OF FRINGE ORDER WITH TIME IN HIGH-IMPEDANCE MEDIUM FOR MODEL II-1D

Substituting these values into Eqs. (46) and (47) and denoting

$$A = \int_r \frac{n}{r}\, dr \tag{48}$$

we obtain

$$\begin{aligned} \varepsilon_{\theta\theta} &= 1.072 \times 10^{-3} A \\ \varepsilon_{rr} &= 1.072 \times 10^{-3} (A - n) \\ u_r &= 1.072 \times 10^{-3} Ar \end{aligned} \tag{49}$$

From measurements of the isochromatic fringe patterns, it was found that the fringes entering this analysis were nearly concentric with a common center located approximately 0.3 in. below the interface. Then, $\frac{n}{r}$ was plotted versus the distance r from this center and the area A under the curve was measured with a planimeter. This was done for several frames. The radial displacement was computed from the last of Eqs. (49) and plotted versus position in Fig. 69. Subsequently, the strains and then the stresses were computed and plotted in Fig. 70. These results indicate that both radial and circumferential stresses are compressive near the wavefront with the radial stress much higher than the other. The circumferential stress becomes tensile at some distance from the wavefront. The peak of this tensile stress could not be established as the analysis above is approximate and it is not valid beyond a certain distance behind the wavefront.

Separation of stresses based on photoelastic results is possible only under special circumstances, such as the case of polar symmetry. In general, some complementary data are used in the form of displacements or strains. In this case, it was attempted to obtain strain data directly from moiré fringe patterns. A two-layer specimen was photoprinted with arrays of 1,000 lines per inch, one half of the

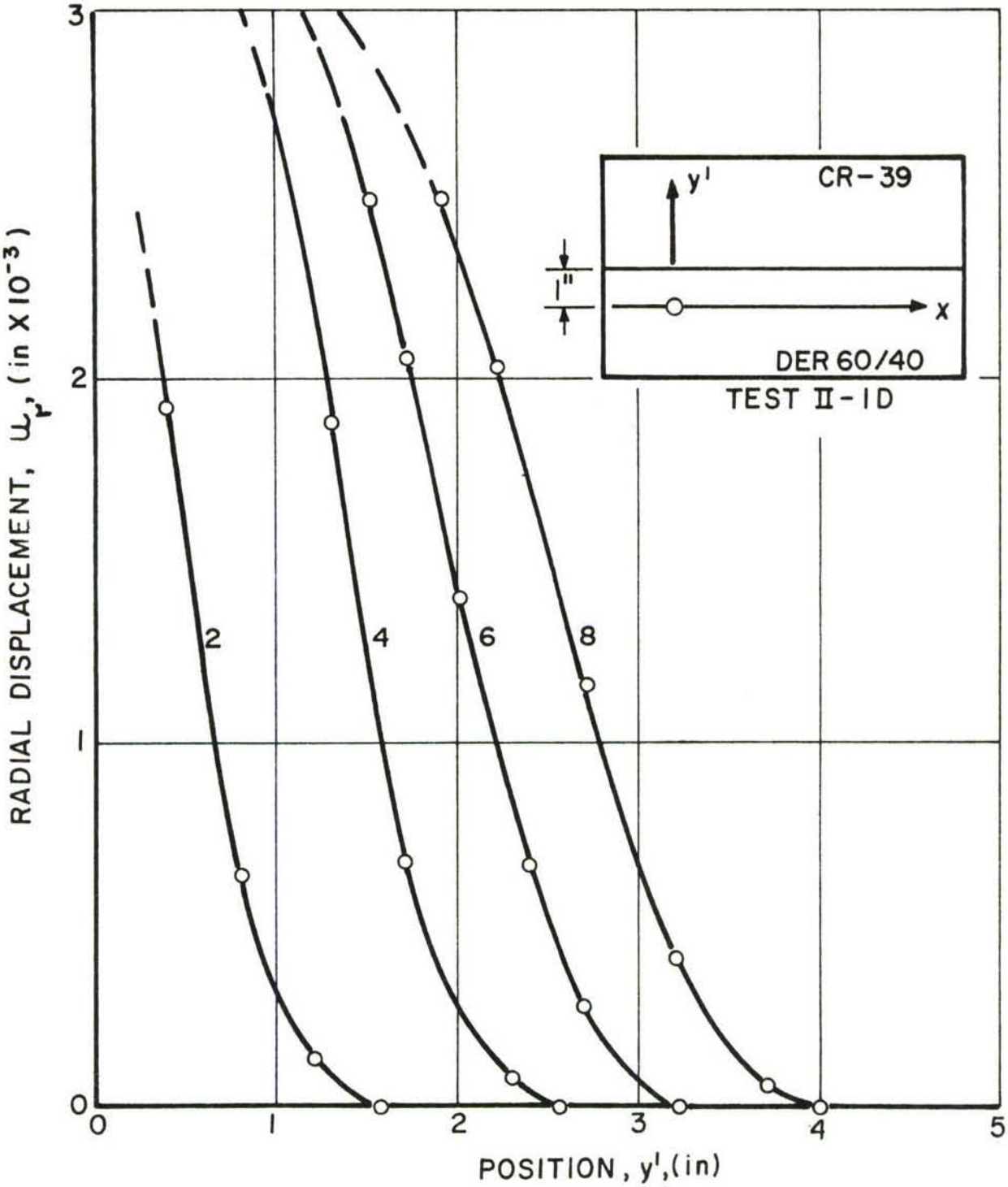


Figure 69. RADIAL (VERTICAL) DISPLACEMENTS IN HIGH-IMPEDANCE MEDIUM AS A FUNCTION OF DISTANCE FROM INTERFACE WITH TIME AS A PARAMETER FOR SPECIMEN II-1D (FRAME NUMBERS ARE MARKED ON THE CURVES)

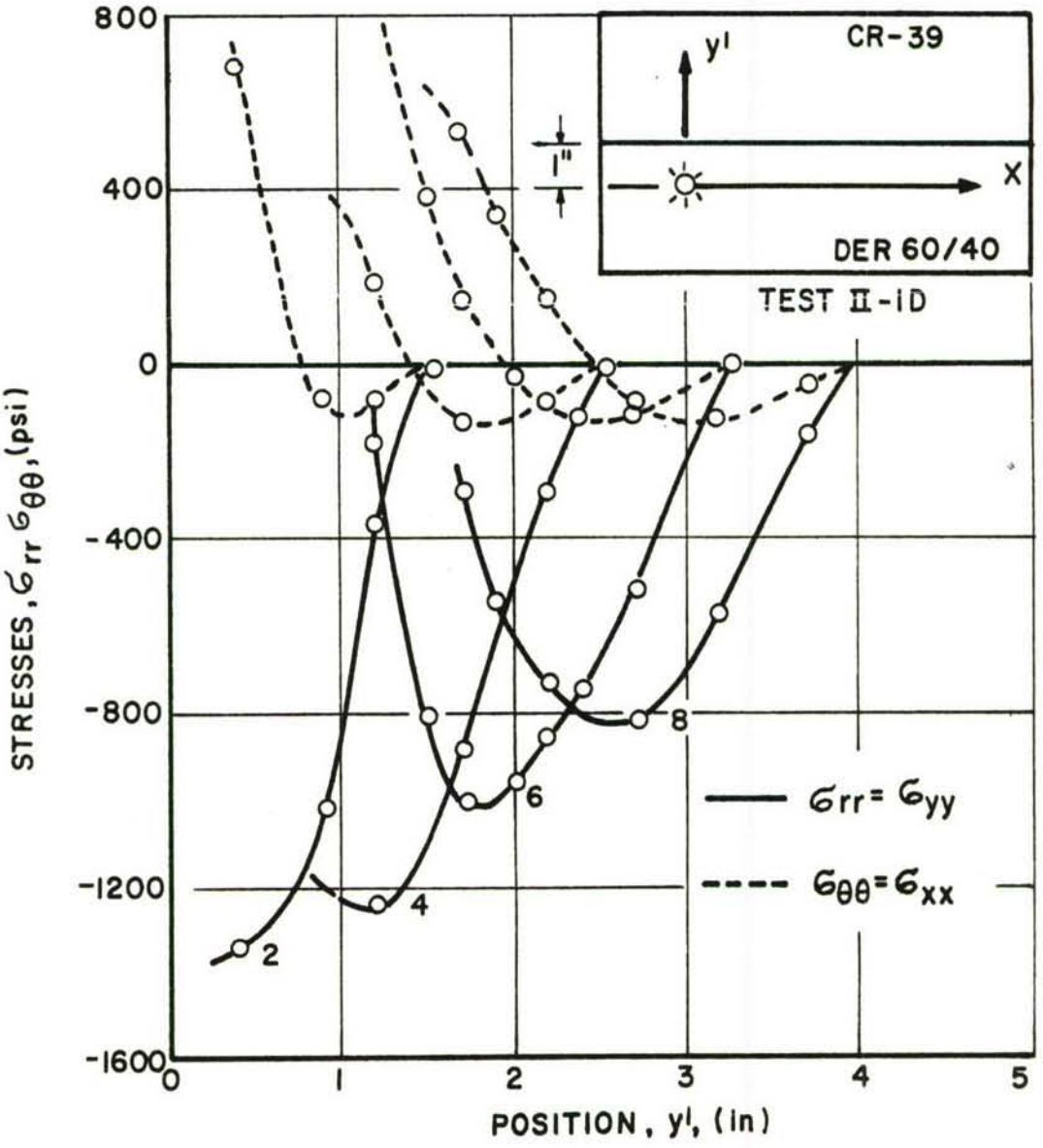


Figure 70. PRINCIPAL STRESSES IN HIGH-IMPEDANCE MEDIUM AS A FUNCTION OF DISTANCE FROM INTERFACE WITH TIME AS A PARAMETER FOR SPECIMEN II-1D (FRAME NUMBERS ARE MARKED ON THE CURVES; RESULTS OBTAINED FROM PHOTOELASTIC DATA)

specimen with horizontal lines and the other half with vertical lines. The model was loaded with an explosive charge in the DER 60/40 layer at a distance of 1 in. from the interface (Model II-1). Two such tests were conducted to obtain two families of moire fringes for the horizontal and vertical displacements (Figs. 71 and 72.).

The moiré fringe patterns were first analyzed in the high-impedance medium along the line through the point source and normal to the interface. The vertical displacements as a function of location for different frames are shown in Fig. 73 where they are compared with those obtained from the approximate photoelastic analysis. The agreement seems to be very satisfactory. Without making any assumptions of polar symmetry, horizontal and vertical strains were determined by graphical differentiation of the corresponding displacement curves. Stresses were computed from the strains and plotted versus location in Fig. 74 for several frames. The frame numbers in this figure do not correspond to the same times as in Fig. 70 so that a frame for frame comparison is not possible. However, the general appearance and magnitude of the stresses are comparable. More detail was obtained in this case on the tensile circumferential stresses at some distance behind the wavefront.

Strain data from the moiré fringe records were also obtained in the high-impedance medium along the interface. From these strains, horizontal and vertical stresses were computed and plotted as a function of position for various frames in Figs. 75 and 76. The horizontal stress σ_{xx} is always compressive near the wavefront but it becomes tensile at some distance behind it. The vertical stress σ_{yy} is initially compressive but takes appreciable tensile values at later times as it assumes an undulatory shape. This points out to the importance of a complete bond between layers in tests of this kind.

Figure 77 shows the isochromatic fringe pattern for Model II-2D loaded with an explosive charge located in the low-impedance medium 2 in. below the interface. The wave propagation velocities were

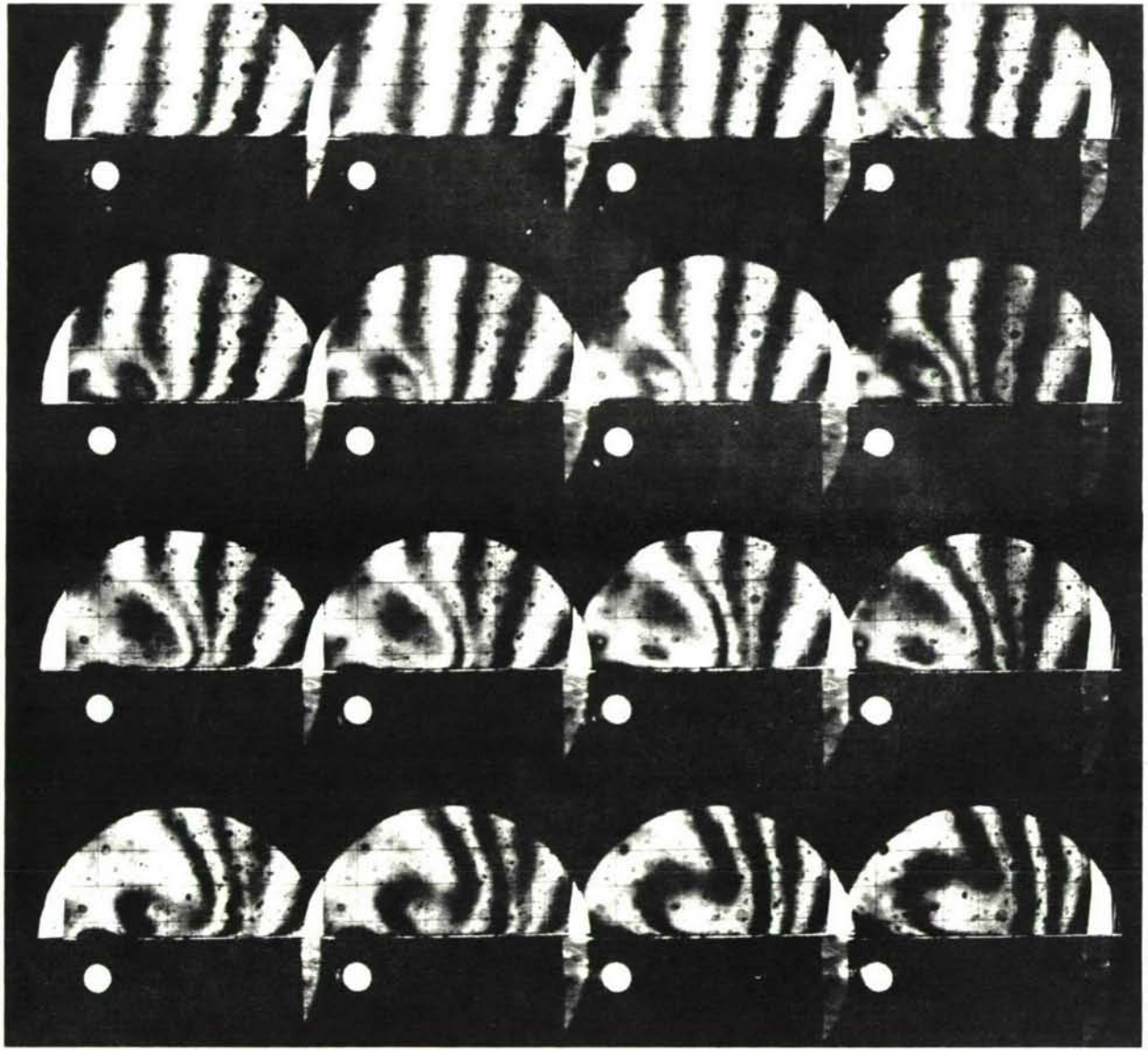


Figure 71. MOIRE FRINGE PATTERNS FOR HORIZONTAL DISPLACEMENTS IN MODEL II-1F (EXPLOSIVE SOURCE IN LOW-IMPEDNACE MEDIUM 1 IN. FROM INTERFACE; CAMERA SPEED 190,000 FRAMES/SECOND)

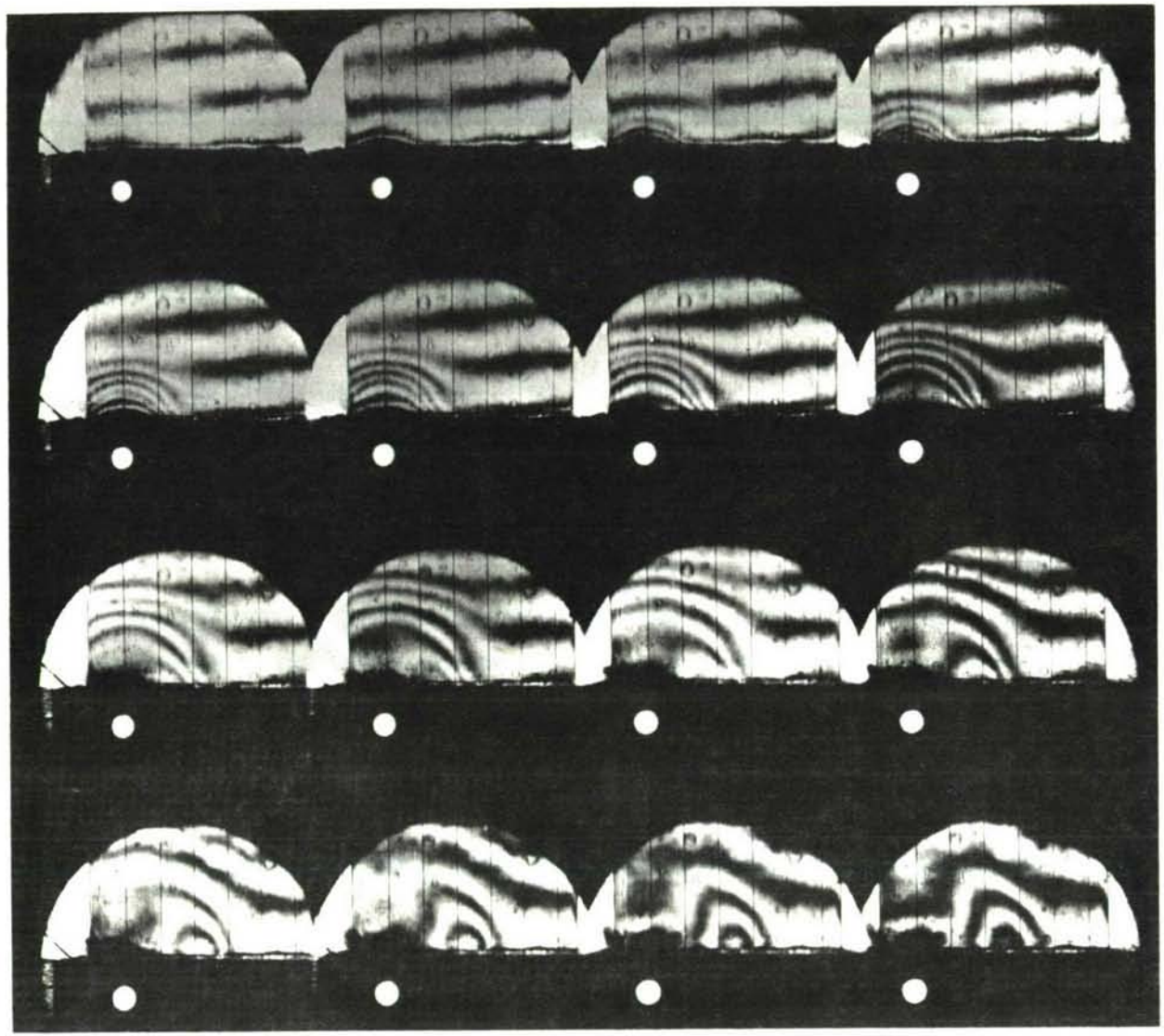


Figure 72. MOIRE FRINGE PATTERNS FOR VERTICAL DISPLACEMENTS IN MODEL II-1F (EXPLOSIVE SOURCE IN LOW-IMPEDANCE MEDIUM 1 IN. FROM INTERFACE; CAMERA SPEED 190,000 FRAMES/SECOND)

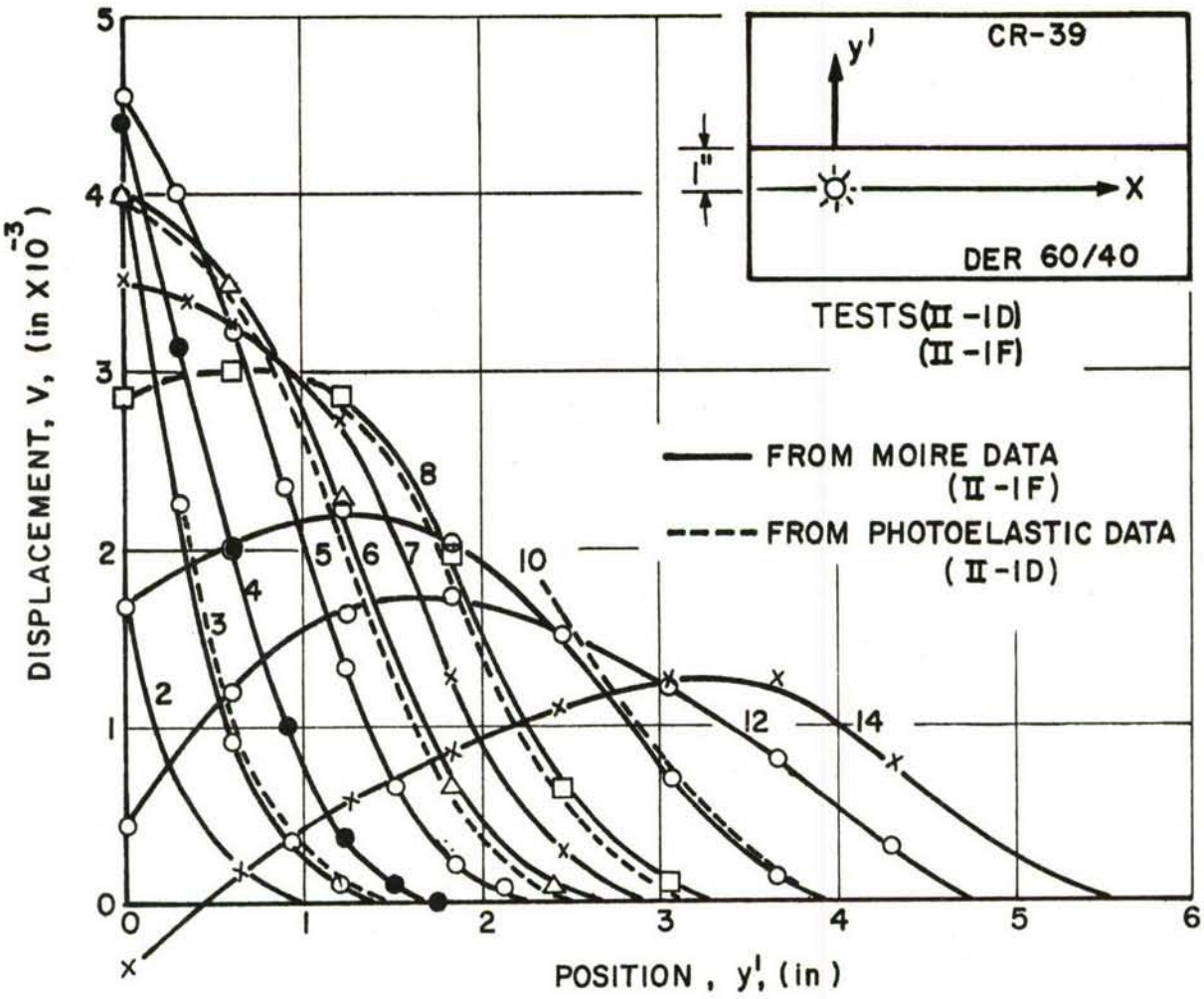


Figure 73. VERTICAL DISPLACEMENTS IN HIGH-IMPEDANCE MEDIUM AS A FUNCTION OF DISTANCE FROM INTERFACE WITH TIME AS A PARAMETER FOR SPECIMENS II-1D AND II-1F (FRAME NUMBERS ARE MARKED ON THE CURVES)

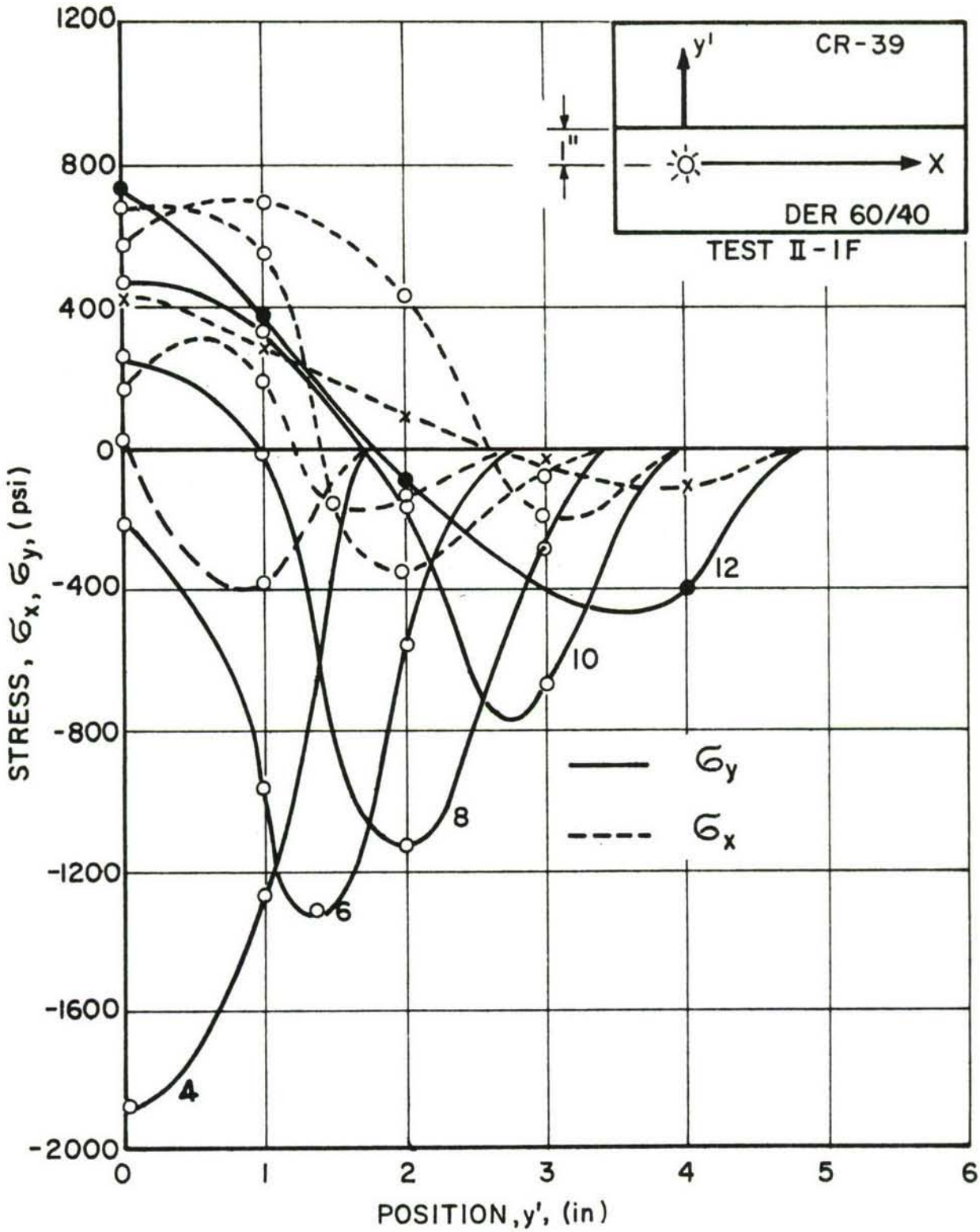


Figure 74. PRINCIPAL STRESSES IN HIGH IMPEDANCE MEDIUM AS A FUNCTION OF DISTANCE FROM INTERFACE WITH TIME AS A PARAMETER FOR SPECIMEN II-1F (FRAME NUMBERS ARE MARKED ON THE CURVES; RESULTS OBTAINED FROM MOIRÉ DATA)

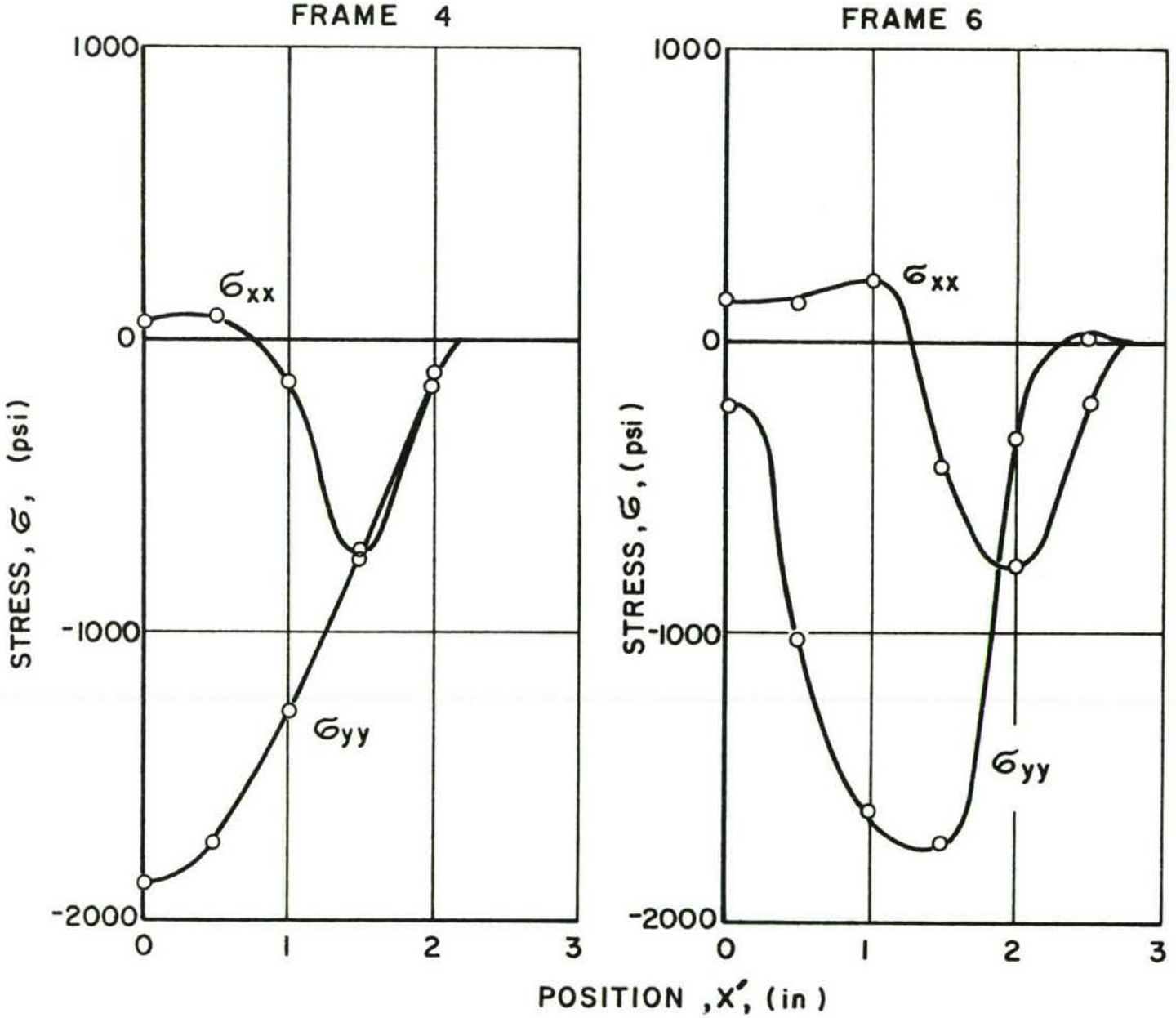


Figure 75. HORIZONTAL AND VERTICAL STRESSES IN HIGH-IMPEDANCE MEDIUM ALONG INTERFACE IN SPECIMEN II-1F

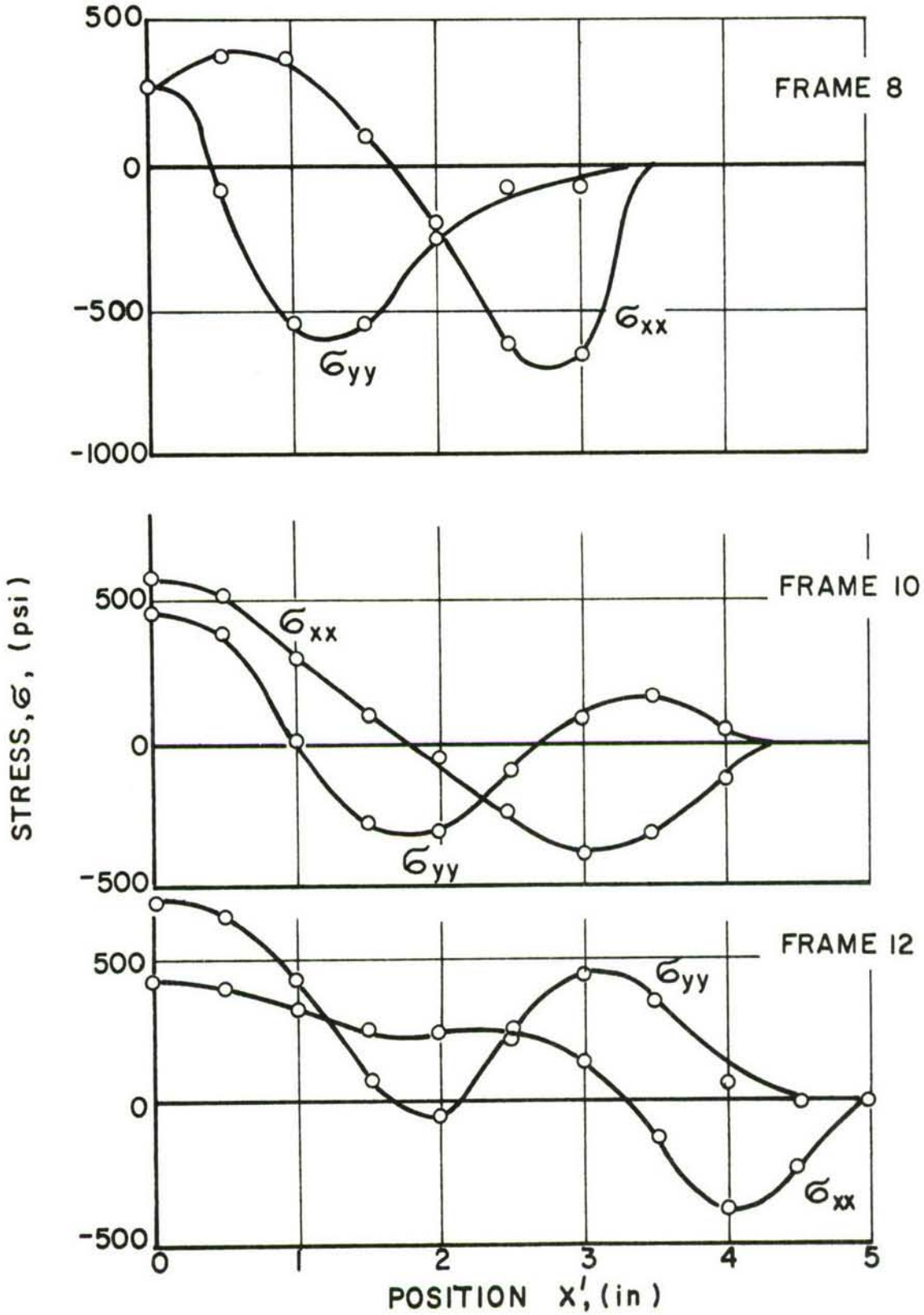


Figure 76. HORIZONTAL AND VERTICAL STRESSES IN HIGH-IMPEDANCE MEDIUM ALONG INTERFACE IN SPECIMEN II-1F

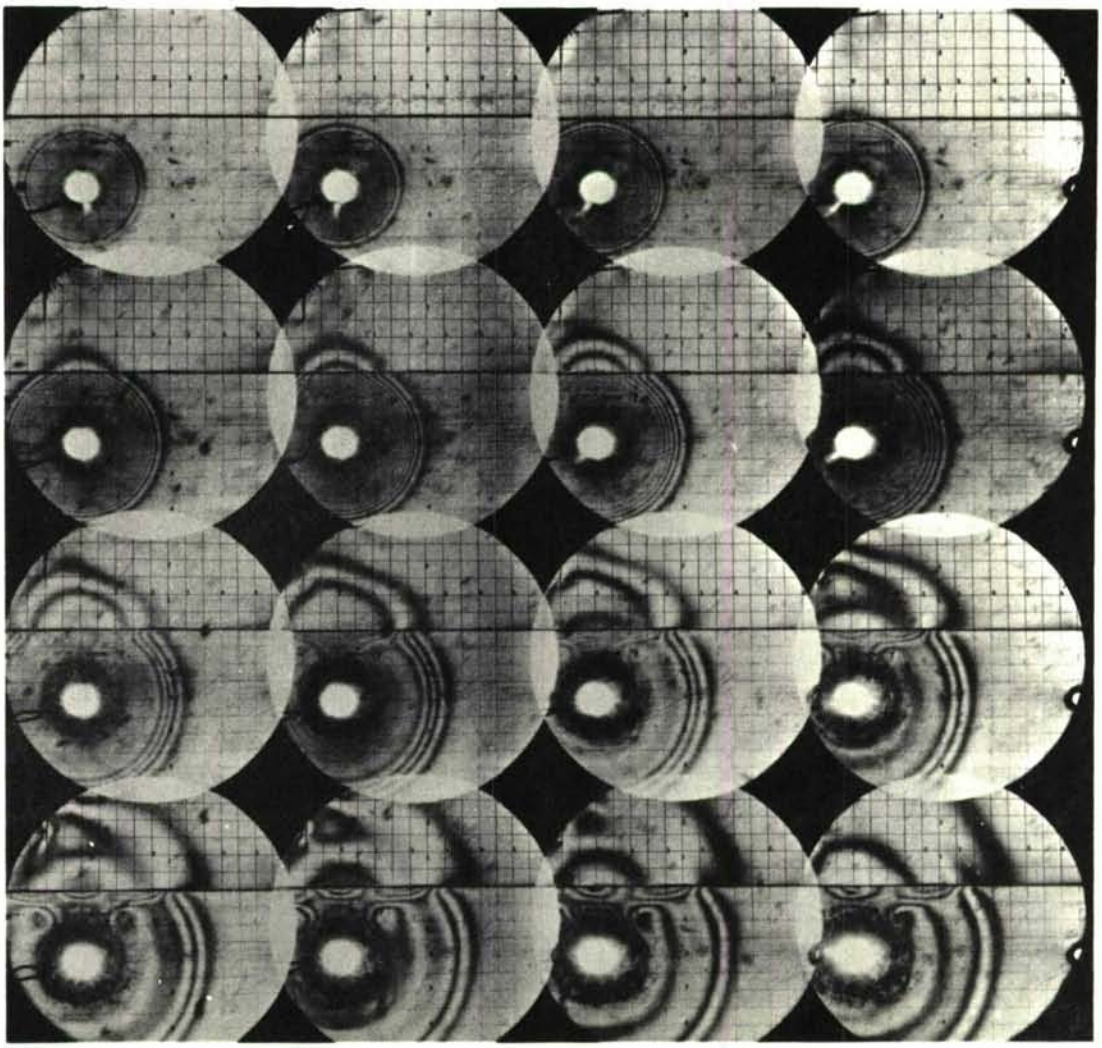


Figure 77. ISOCHROMATIC FRINGE PATTERNS IN MODEL II-2D (EXPLOSIVE SOURCE IN LOW-IMPEDANCE MEDIUM 2 IN. FROM INTERFACE; IMPEDANCE RATIO 2.31:1; CAMERA SPEED 200,000 FRAMES/SECOND)

measured as before and plotted as a function of fringe order in Fig. 78. The wavefront wave velocities were computed as

$$\alpha_1 = 35{,}500 \text{ in./sec}$$
$$\alpha_2 = 72{,}000 \text{ in./sec}$$

The resulting impedance ratio is 2.31:1. The nature of the incident P_1 wave is depicted in Fig. 79 where the fringe order is plotted versus position along a horizontal line through the loading source. The dispersion of the pulse seems to be more pronounced than in Model II-1D (Fig. 59) although there is no real reason for this difference except experimental variability in loading and material properties. An exponential fit through the peaks of the pulse gives

$$n_{max} = e^{0.87\ (3.60 - x)}$$

This shows that the coefficient of attenuation here (k = 0.87) is somewhat higher than that obtained from Model II-1D.

A similar analysis was conducted along a vertical line through the loading source. Figure 80 shows birefringence as a function of position for several frames. No appreciable attenuation can be noticed in the refracted wave in the high-impedance medium.

The variation of birefringence along the interface in the low-impedance medium is shown in Fig. 81. The influence of a possible headwave is not indicated at all. The peak of the pulse attenuates according to the following equation

$$n_{max} = e^{0.29\ (7.10 - x')}$$

Here again the attenuation coefficient of 0.29 is a little lower than the corresponding coefficient (0.39) for Model II-1D.

Figure 82 shows the variation of birefringence along the interface in the high-impedance medium. This reflects for the most part a combination of the two refracted waves P_1P_2 and P_1S_2. Curves cor-

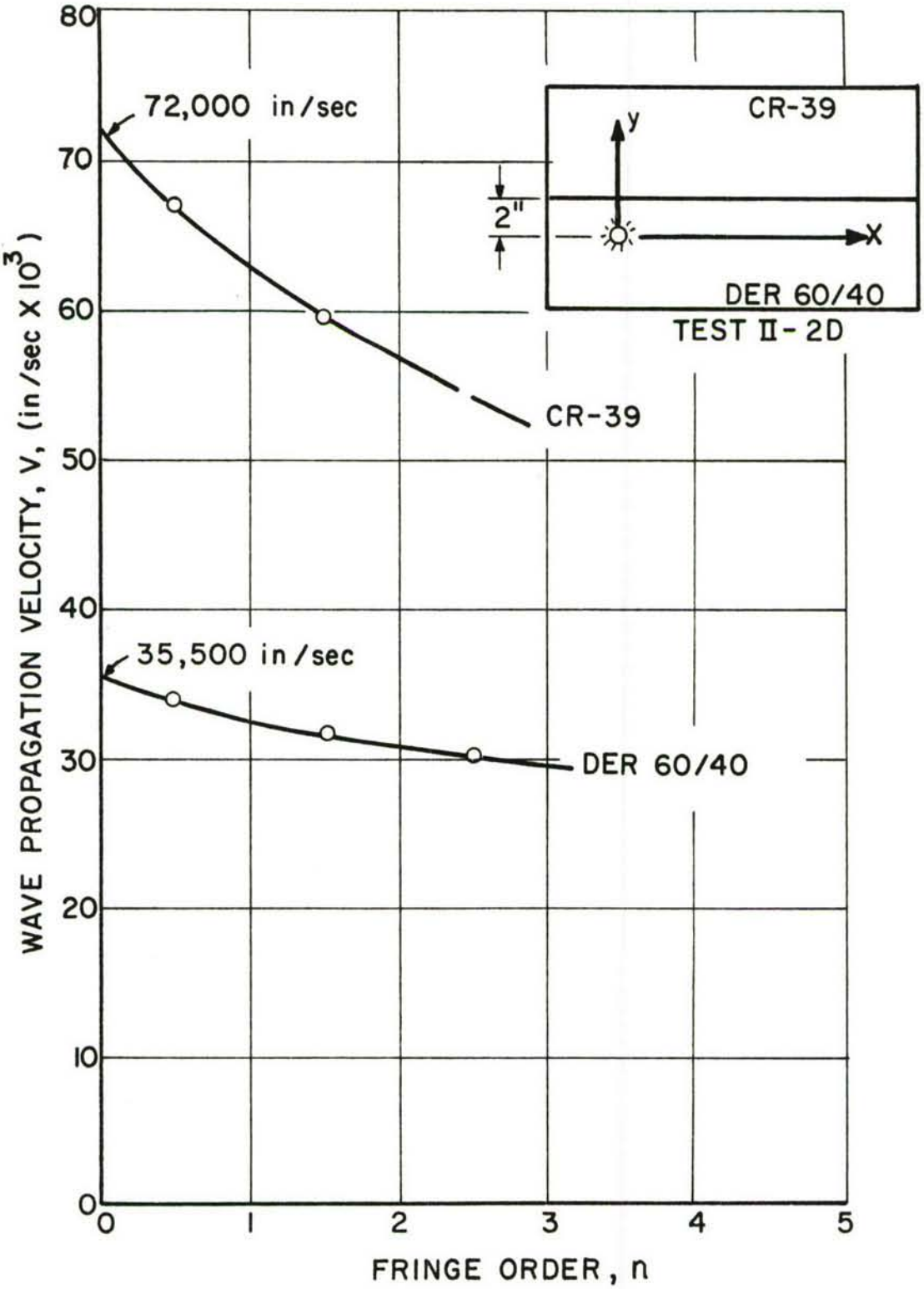


Figure 78. VELOCITY OF WAVE PROPAGATION AS A FUNCTION OF FRINGE ORDER IN TWO MEDIA OF MODEL II-2D

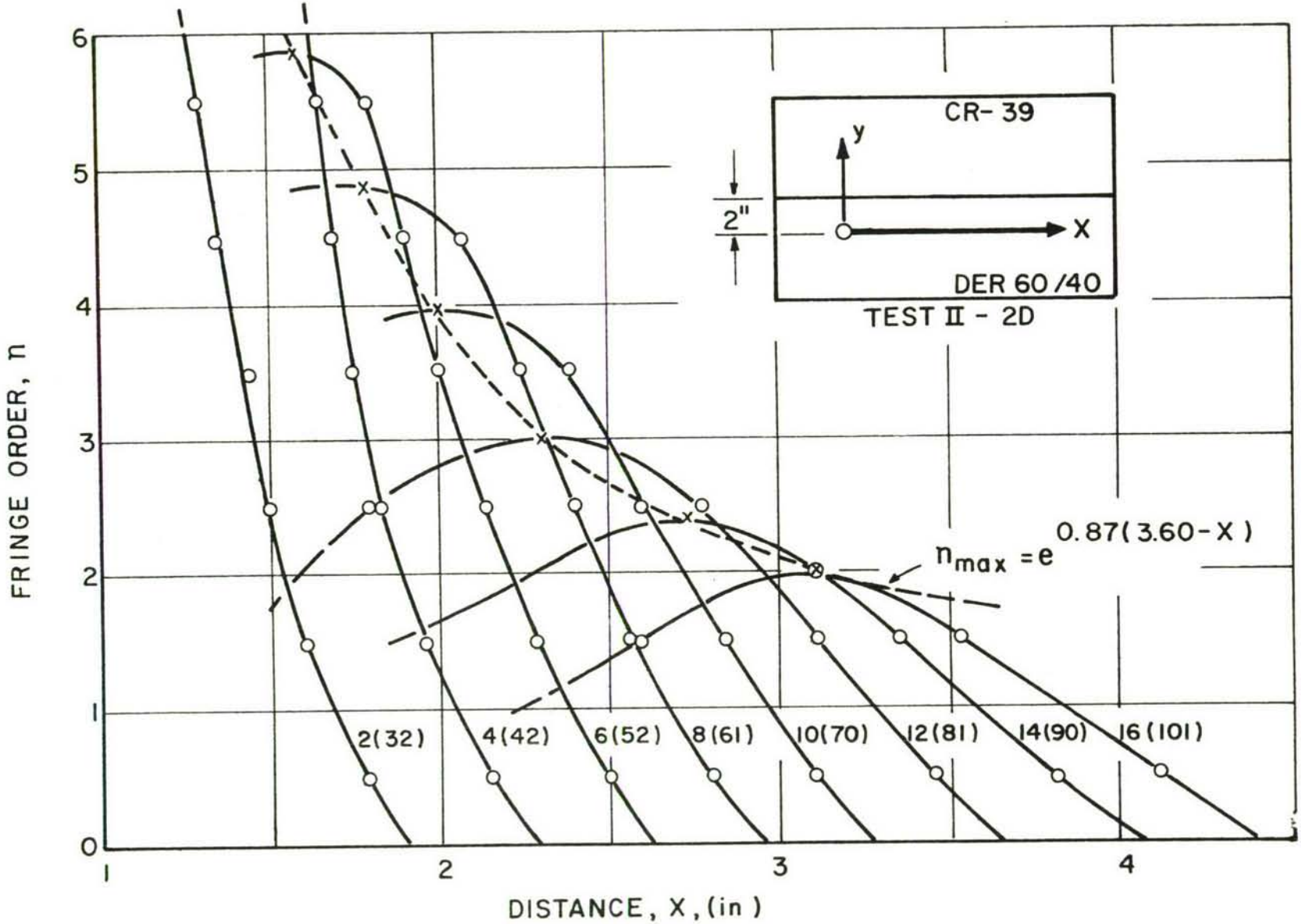


Figure 79. FRINGE ORDER AS A FUNCTION OF POSITION WITH TIME AS A PARAMETER FOR INCIDENT WAVE P_1 IN LOW-IMPEDANCE MEDIUM OF MODEL II-2D (FRAME NUMBERS AND TIMES IN MICROSECONDS ARE INDICATED)

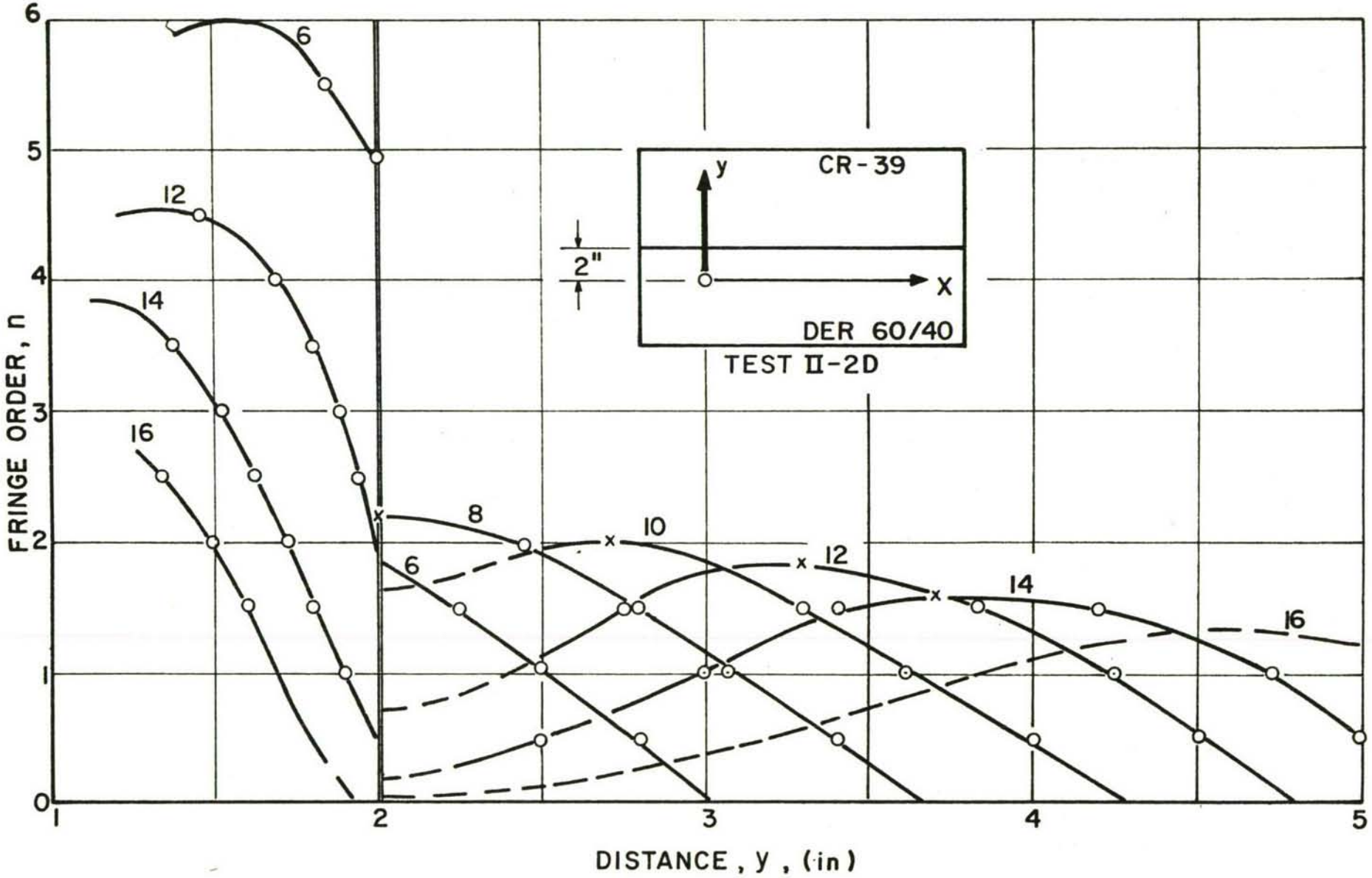


Figure 80. FRINGE ORDER AS A FUNCTION OF POSITION WITH TIME AS A PARAMETER ALONG LINE THROUGH EXPLOSIVE SOURCE NORMAL TO INTERFACE (MODEL II-2D; FRAME NUMBERS ARE INDICATED)

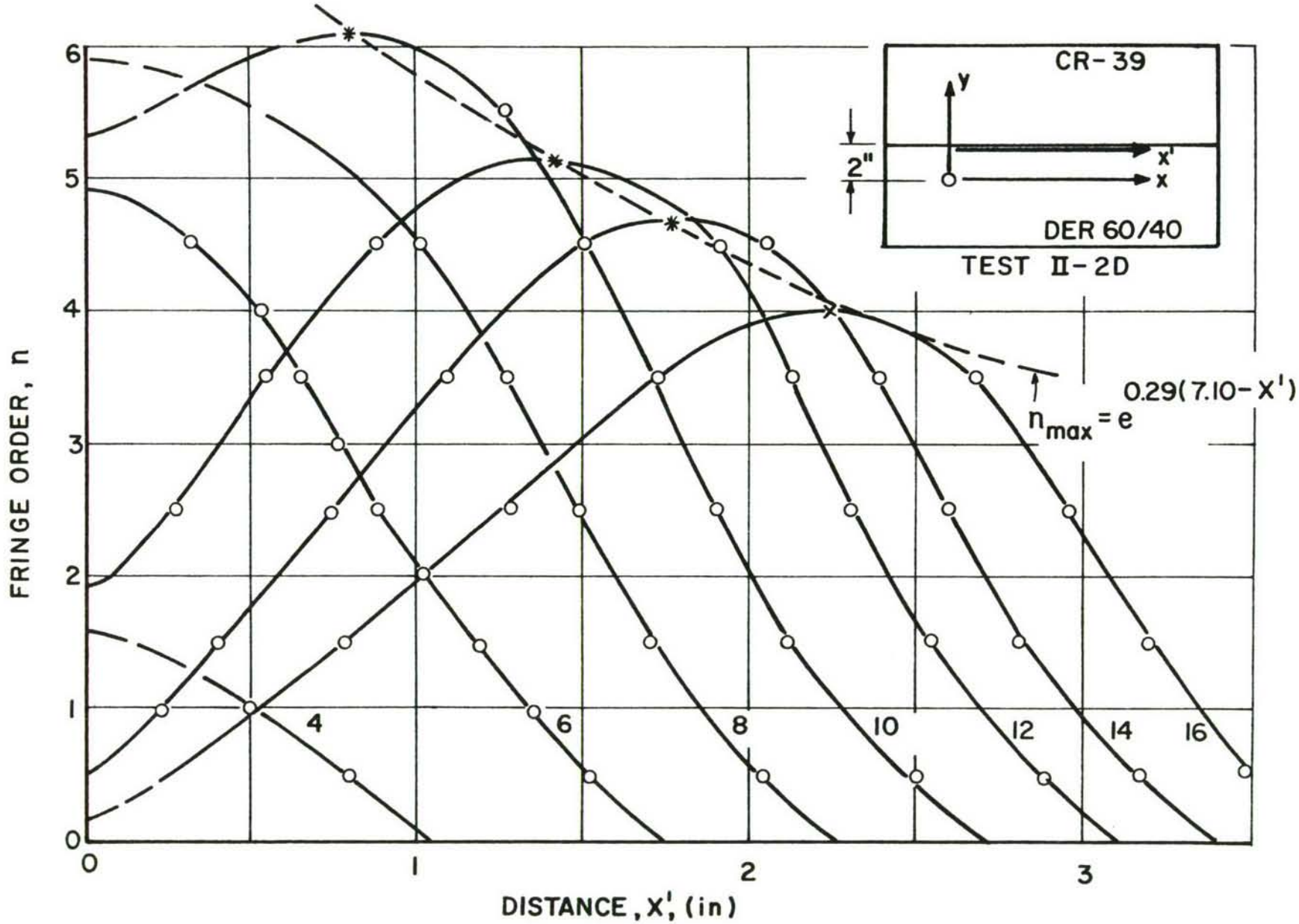


Figure 81. FRINGE ORDER AS A FUNCTION OF POSITION WITH TIME AS A PARAMETER IN LOW-IMPEDANCE MEDIUM ALONG INTERFACE (MODEL II-2D; FRAME NUMBERS ARE INDICATED)

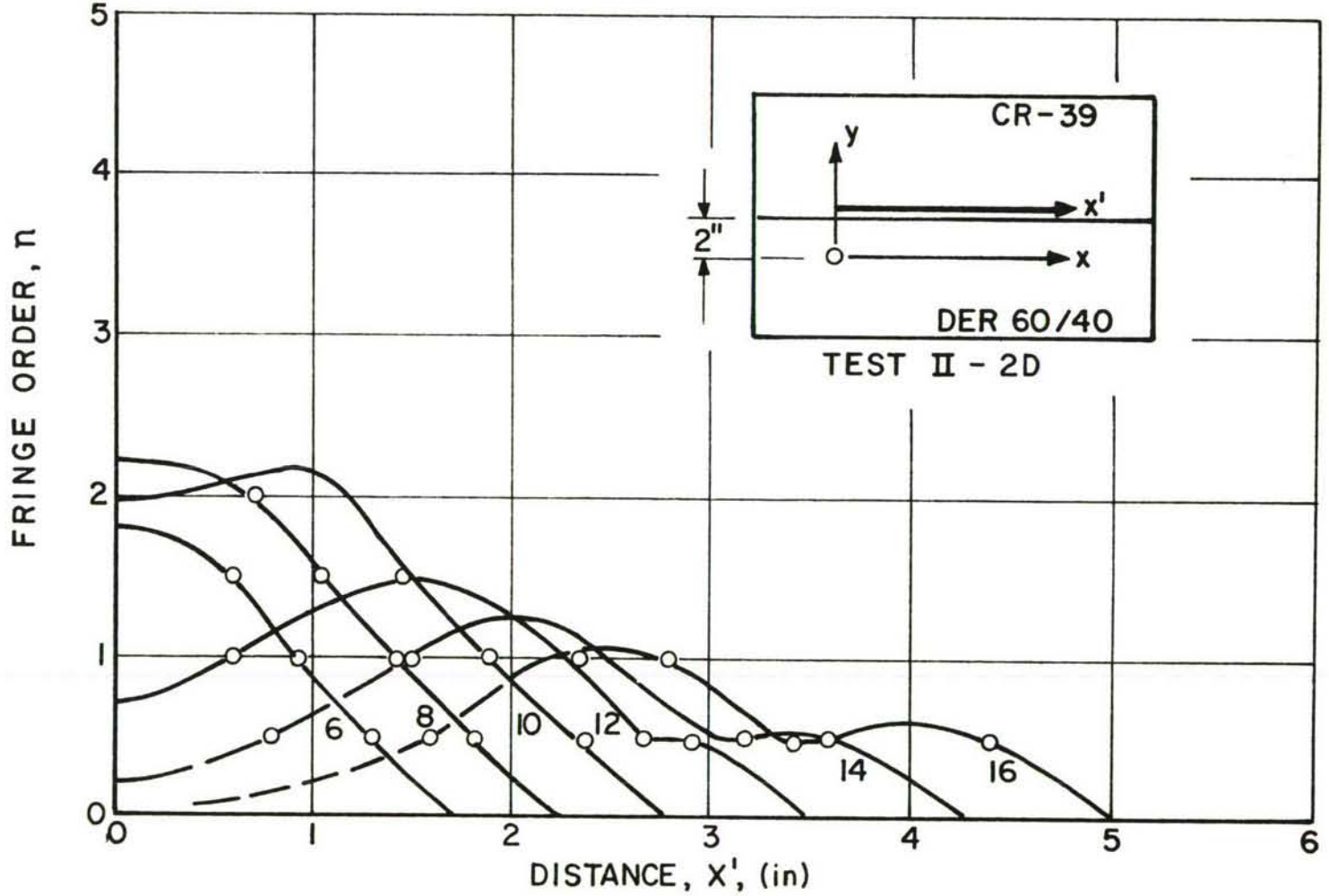


Figure 82. FRINGE ORDER AS A FUNCTION OF POSITON WITH TIME AS A PARAMETER FOR REFRACTED WAVES IN HIGH-IMPEDANCE MEDIUM ALONG INTERFACE (MODEL II-2D; FRAME NUMBERS ARE MARKED)

responding to times beyond frame 12 show a bend which is due to the influence of the $P_1P_2S_2$ headwave. The effect of the latter on the fringe pattern is barely visible as can be seen in the enlargement of frame 16 (Fig. 83).

The third model in this series, Model II-3D, was loaded in the low-impedance medium at a distance of 3 in. from the interface. Figure 84 shows the isochromatic fringe patterns obtained. Wave propagation velocities, measured and computed as before, are

$$\alpha_1 = 32{,}000 \text{ in./sec}$$
$$\alpha_2 = 60{,}500 \text{ in./sec}$$

The resulting impedance ratio is 2.16:1. One reason for the noticeable lower velocity in the high-impedance medium is the fact that due to the increased distance from the interface a more dispersed and attenuated pulse reaches that interface to load the upper layer.

Birefringence along the vertical line through the loading source was plotted versus position in Fig. 85. As in the case of Model II-2D, the attenuation is not pronounced. Figure 86 shows the variation of birefringence along the interface in the low-impedance medium. Again, in this case the attenuation is not pronounced.

Comparing results from all three specimens, the following observations may be made regarding the influence of distance of explosive source from the interface. Headwaves are evident only in Model II-1D where the distance $h = 1$ in. is the shortest. Apparently, the appearance of headwaves is a function of distance from the interface and intensity of the pulse besides the impedance mismatch. The refracted wave in the high-impedance medium shows peaks of 5-6 fringes and high attenuation in Model II-1D. In Models II-2D and II-3D, the peaks are approximately 2 and 1 fringes, respectively and the attenuation is slight. The same observation can be made regarding birefringence along the interface in the high-impedance medium. Comparison of Figs. 62, 81, and 86 shows that the peaks and attenuation in the low-impedance medium also decrease with increasing distance of loading source from interface.

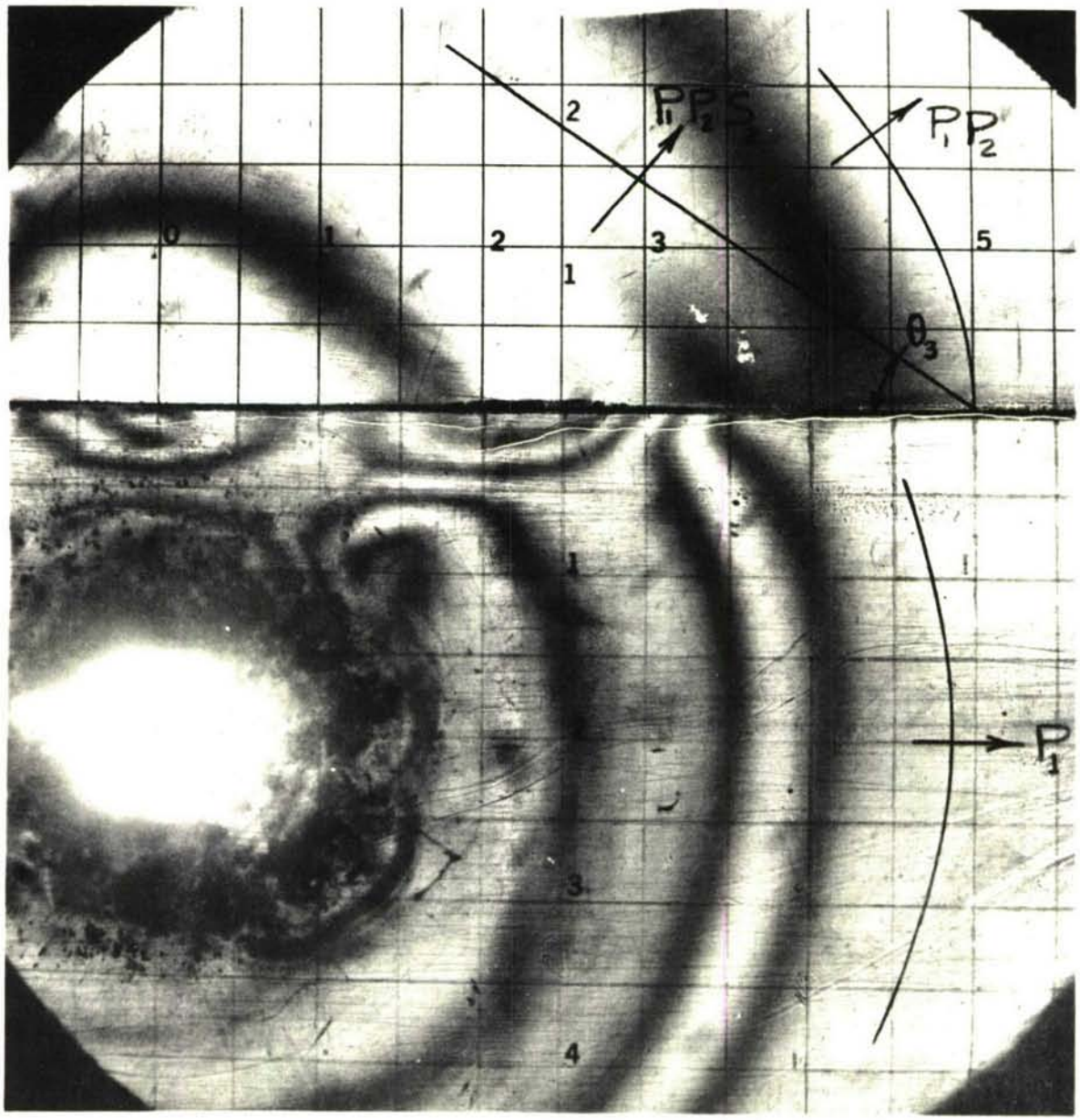


Figure 83. DETAIL OF FRAME 16 (t = 101 μ sec) FOR MODEL II-2D

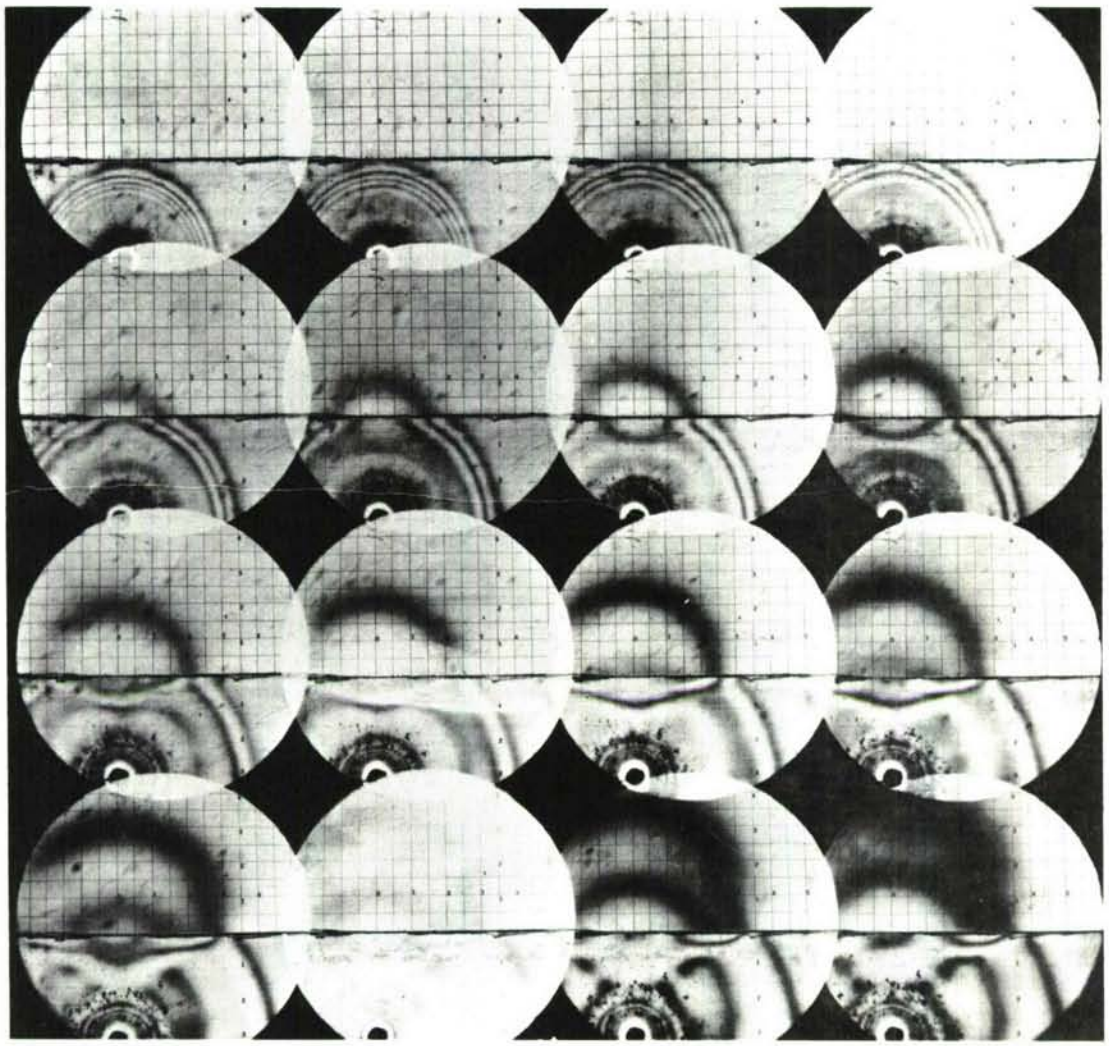


Figure 84. ISOCHROMATIC FRINGE PATTERNS IN MODEL II-3D (EXPLOSIVE SOURCE IN LOW-IMPEDANCE MEDIUM 3 IN. FROM INTERFACE; IMPEDANCE RATIO 2.16:1; CAMERA SPEED 200,000 FRAMES/SECOND)

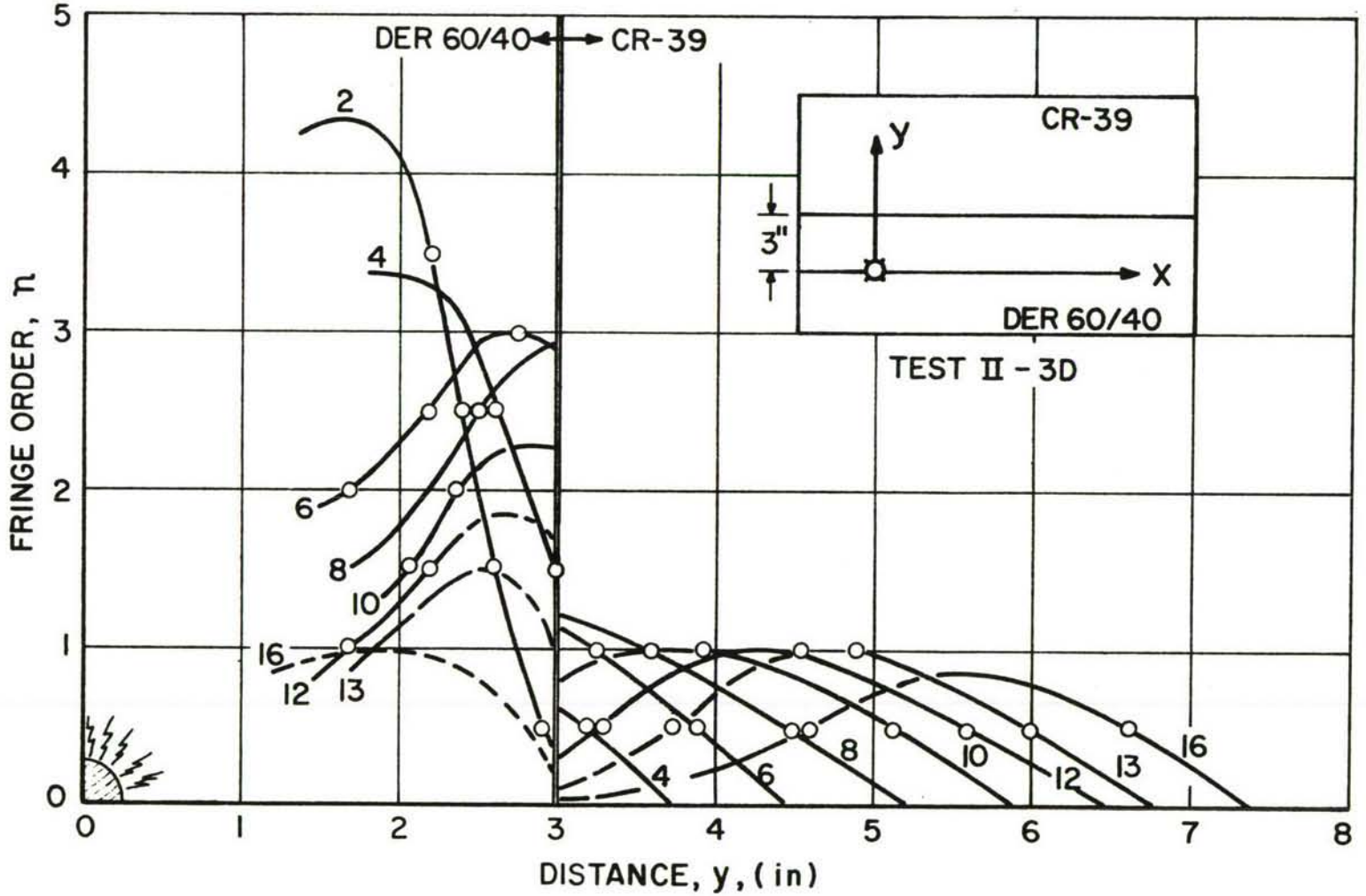


Figure 85. FRINGE ORDER AS A FUNCTION OF POSITION WITH TIME AS A PARAMETER ALONG LINE THROUGH EXPLOSIVE SOURCE NORMAL TO INTERFACE (MODEL II-3D; FRAME NUMBERS ARE INDICATED)

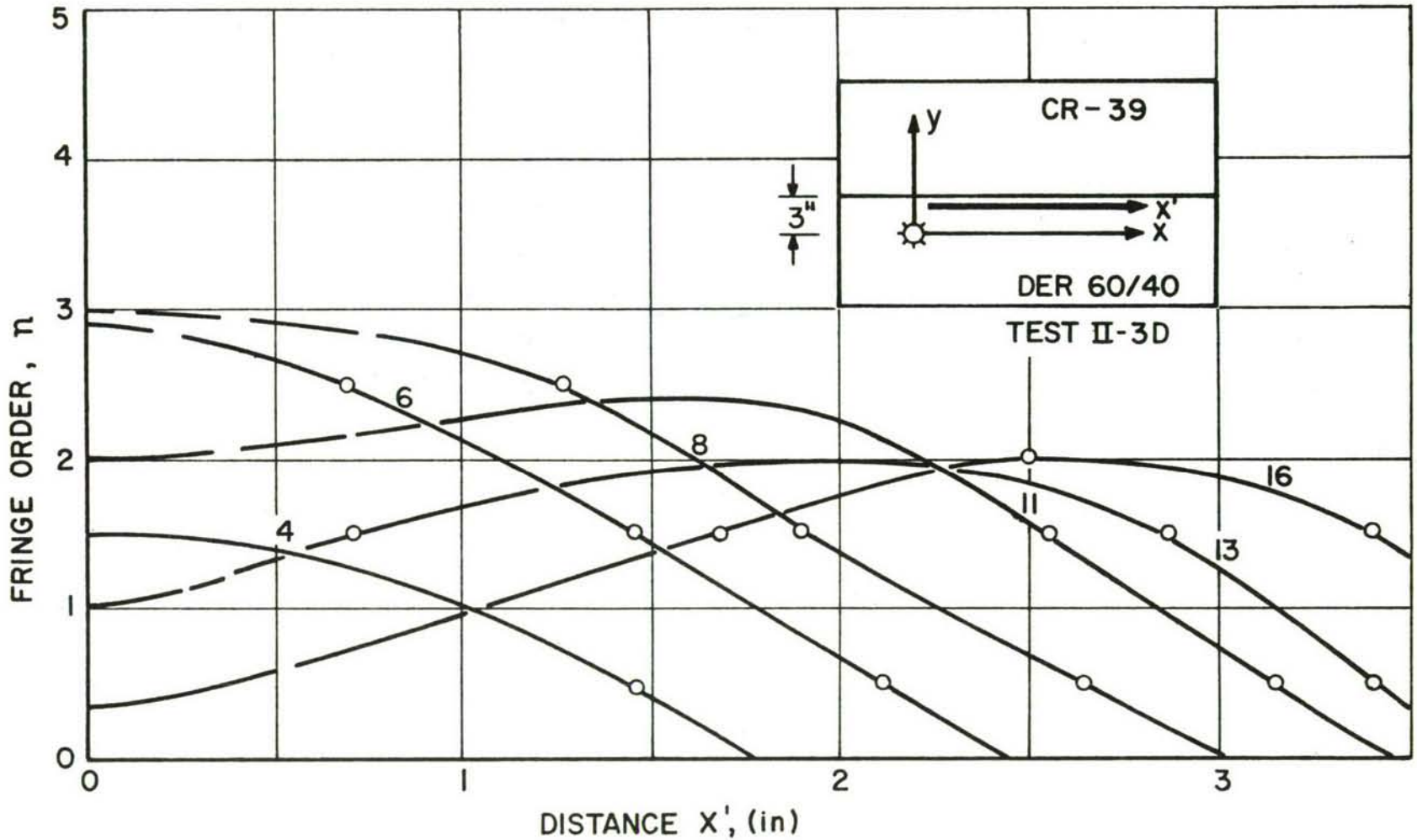


Figure 86. FRINGE ORDER AS A FUNCTION OF POSITION WITH TIME AS A PARAMETER IN LOW-IMPEDANCE MEDIUM ALONG INTERFACE (MODEL II-3D; FRAME NUMBERS ARE INDICATED)

SECTION VIII

WAVE PROPAGATION IN LAYERED MODEL DUE TO EXPLOSIVE LOADING IN HIGH-IMPEDANCE MEDIUM

1. Introduction

In this series of tests, layered models with model materials having an impedance ratio of 2:1 were tested under buried explosive loading in the high-impedance medium. Refracted headwaves are not possible under this condition as will be seen from the experimental results. The distance between the loading source and the interface between the two media was varied parametrically.

2. Experimental Procedure

The same model materials used in the previous phase of the work (Section VII), i.e., DER 60/40 and Columbia Resin CR-39, were used in this series of tests. The models were made by cementing 20 in. x 8 in. x 1/4 in. sheets of these materials along one edge (Fig. 87). Three models were used with varying distances between the explosive source and the interface:

Model III - 1: $h = 1$ in.
Model III - 2: $h = 2$ in.
Model III - 3: $h = 3$ in.

The explosive testing was conducted following previously described procedures (Section III-3a). Isochromatic fringe patterns were recorded with the Schardin camera.

3. Results and Discussion

Figure 88 shows the isochromatic fringe pattern for Model III-1D. The wave propagation velocities were measured as before and plotted as a function of fringe order in Fig. 89. The wavefront wave velocities were computed as

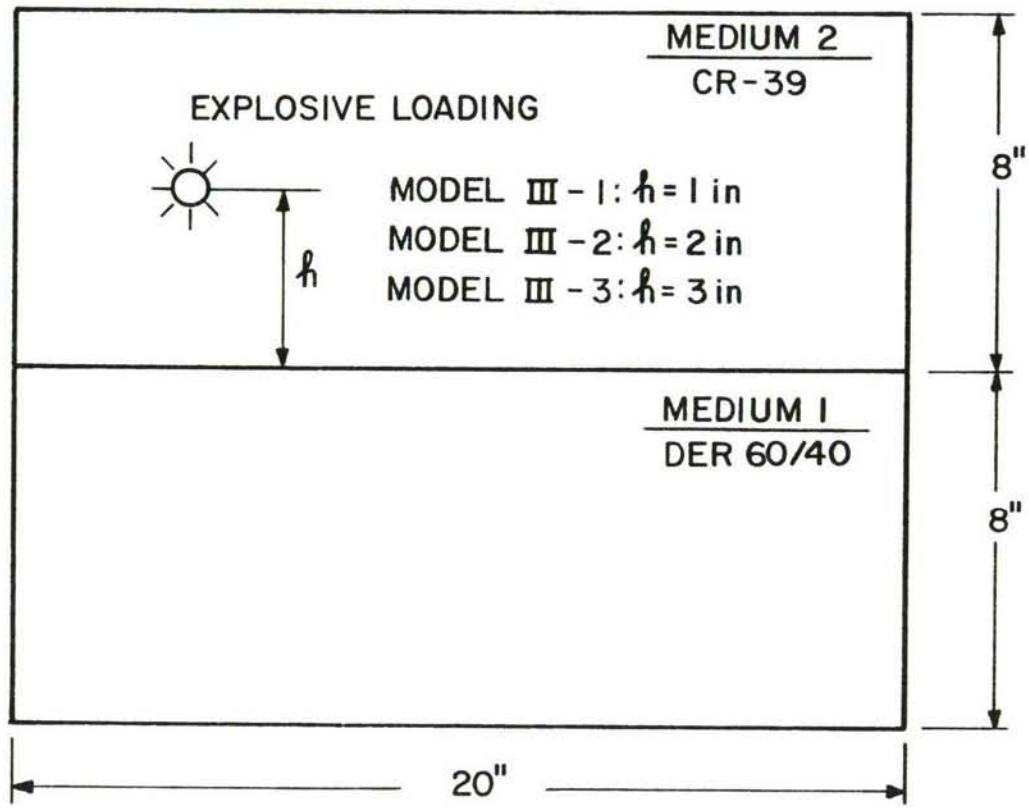


Figure 87. SKETCH OF MODEL SHOWING DIMENSIONS AND LOCATION OF EXPLOSIVE LOADING SOURCE IN HIGH-IMPEDANCE MEDIUM (PHASE III)

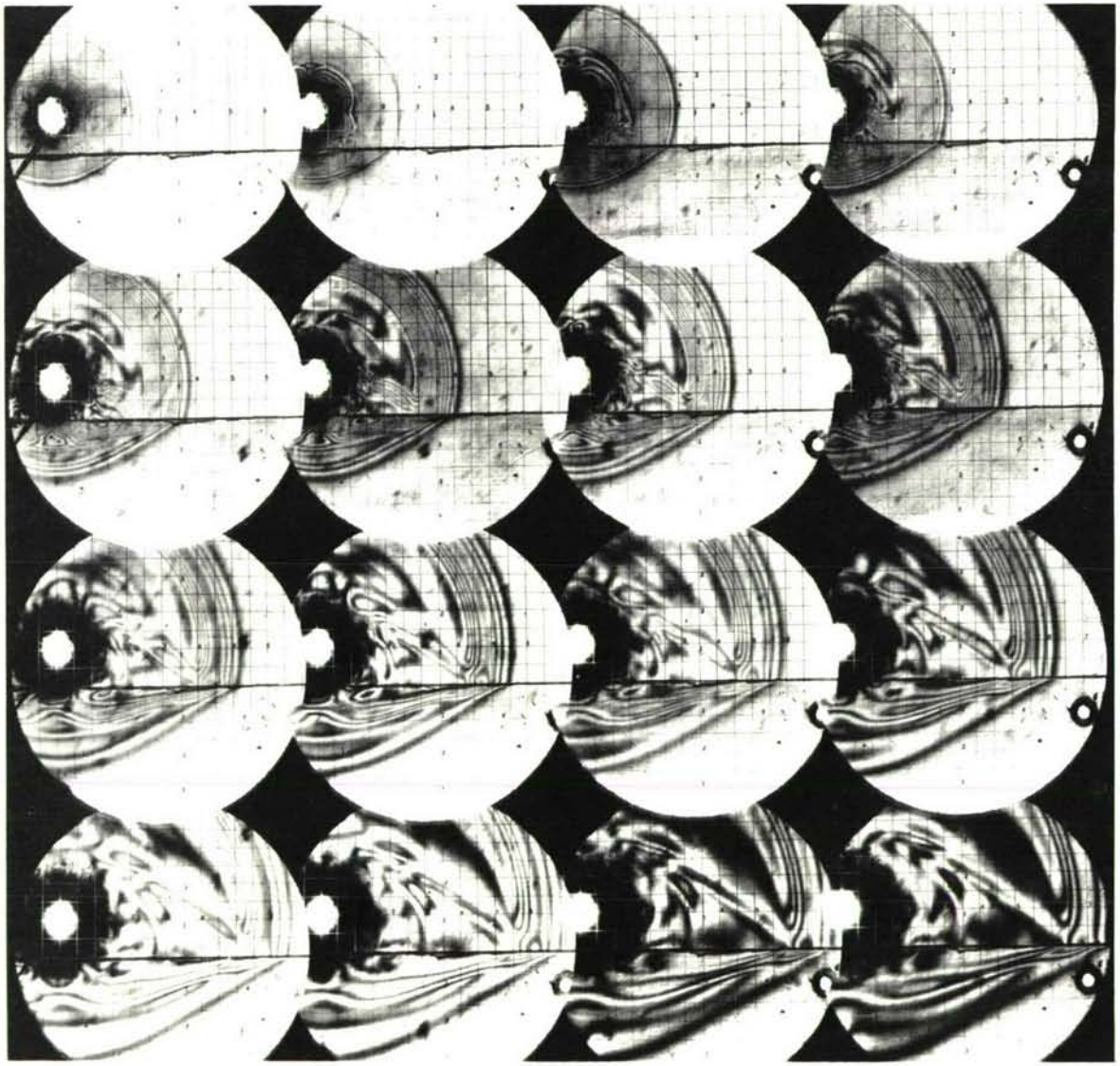


Figure 88. ISOCHROMATIC FRINGE PATTERNS IN MODEL III-1D (EXPLOSIVE SOURCE IN HIGH-IMPEDANCE MEDIUM 1 IN. FROM INTERFACE; IMPEDANCE RATIO 2.23:1; CAMERA SPEED: 200,000 FRAMES/SECOND)

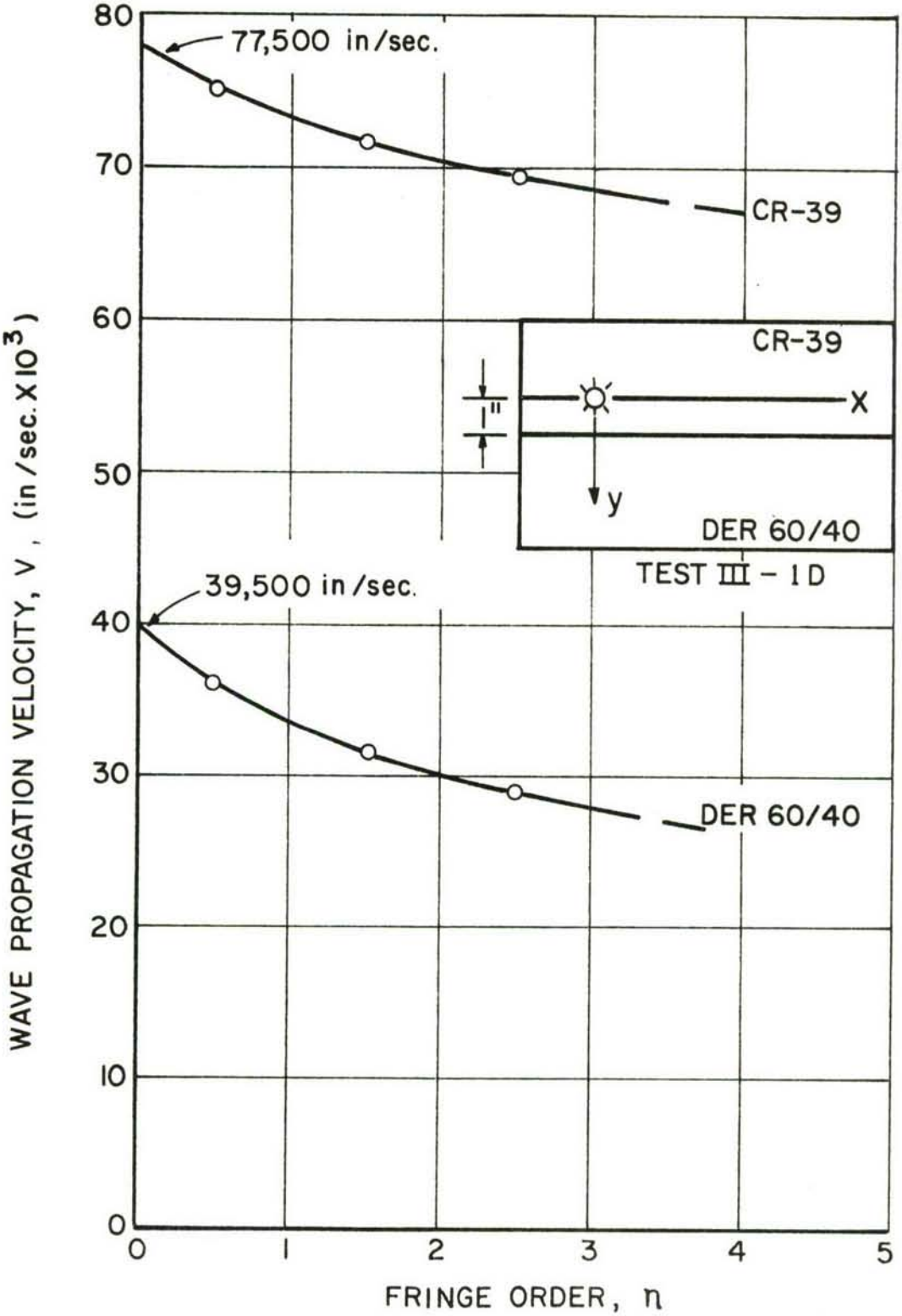


Figure 89. VELOCITY OF WAVE PROPAGATION AS A FUNCTION OF FRINGE ORDER IN TWO MEDIA OF MODEL III-1D

α_1 = 39,500 in./sec

α_2 = 77,500 in./sec

The resulting impedance ratio is 2.23:1. Worthy of notice are the higher propagation velocities than in models of Phase II although the same materials were used for the models of both series. The higher velocity in the high-impedance medium is to be expected since it is loaded directly by the explosive in this case and therefore subjected to a much steeper pulse.

The refracted P_2P_1 wave in the low-impedance layer is described by the birefringence variation with distance from the interface plotted in Fig. 90. Appreciable attenuation and dispersion are evident. The attenuation can be described by the exponential curve fitted through the peaks of the pulse at different times:

$$n_{max} = e^{0.85\ (2.66-y')}$$

The attenuation coefficient of k = 0.85 here is one of the highest observed in DER 60/40.

The birefringence in the high impedance medium along the interface is plotted in Fig. 91. It is the result of a combination of the incident P_2 and the reflected P_2S_2 waves. The dispersion seems to be moderate. The attenuation can be described by the following exponential curve:

$$n_{max} = e^{0.27\ (10.0\ -\ x')}$$

The birefringence in the low-impedance medium along the interface is influenced by the refracted P_2P_1 and P_2S_1 waves. Birefringence versus position along the interface is plotted in Fig. 92. The pulse is single-peaked with no appreciable dispersion and relatively low attenuation.

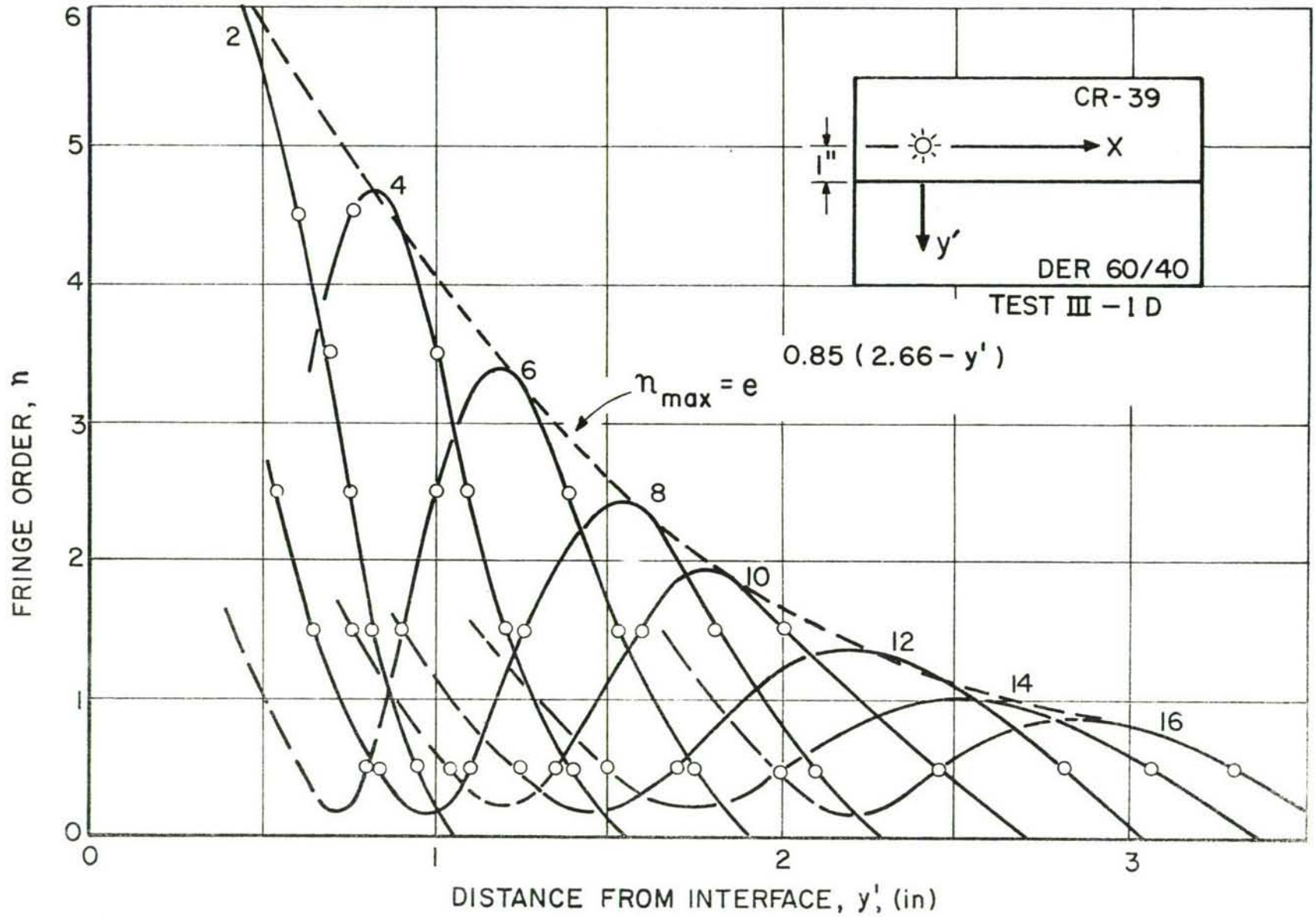


Figure 90. FRINGE ORDER AS A FUNCTION OF POSITION WITH TIME AS A PARAMETER FOR REFRACTED P_2P_1 WAVE IN LOW-IMPEDANCE MEDIUM OF MODEL III-1D

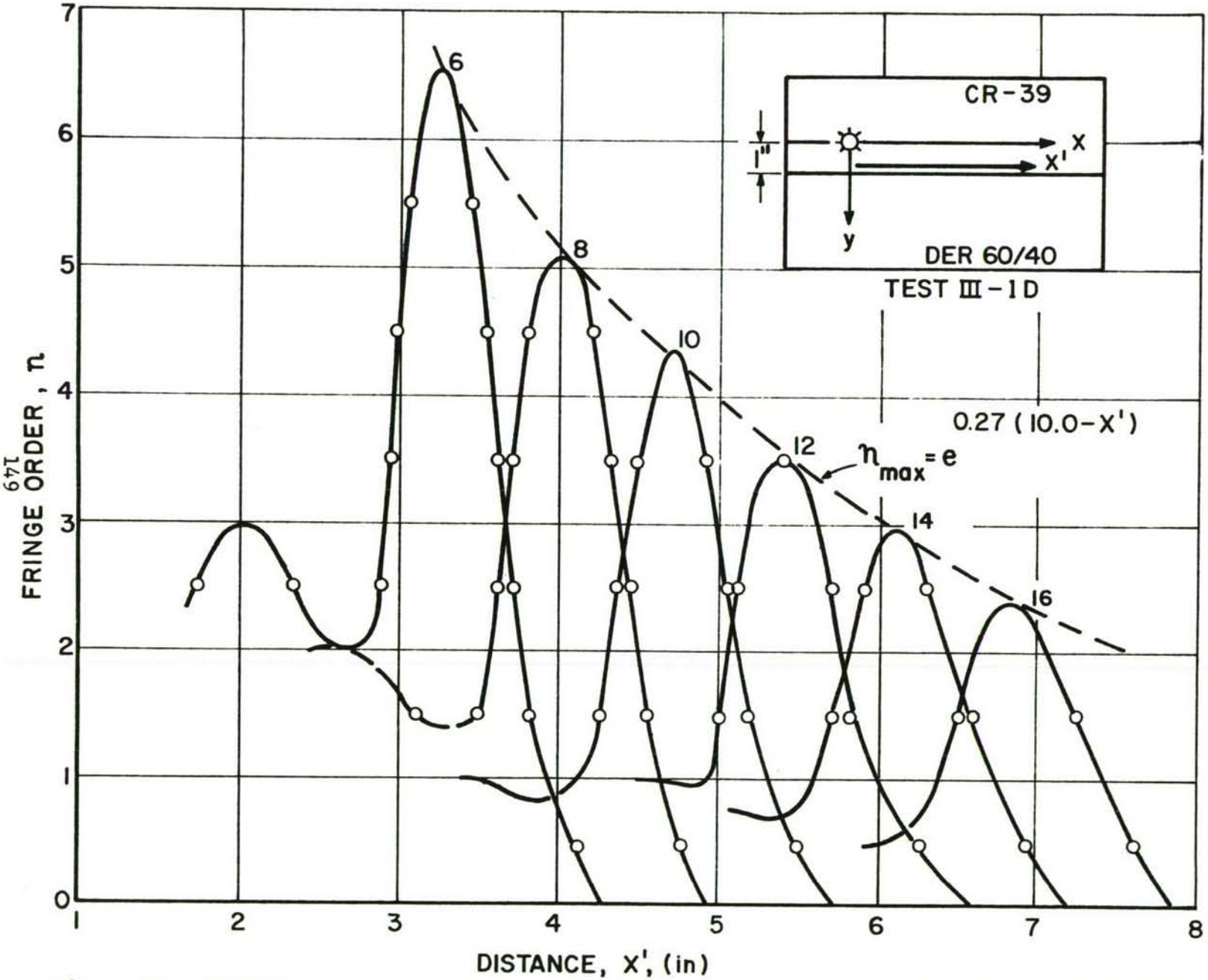


Figure 91. FRINGE ORDER AS A FUNCTION OF POSITION WITH TIME AS A PARAMETER IN HIGH-IMPEDANCE MEDIUM ALONG INTERFACE (MODEL III-1D; FRAME NUMBERS ARE MARKED)

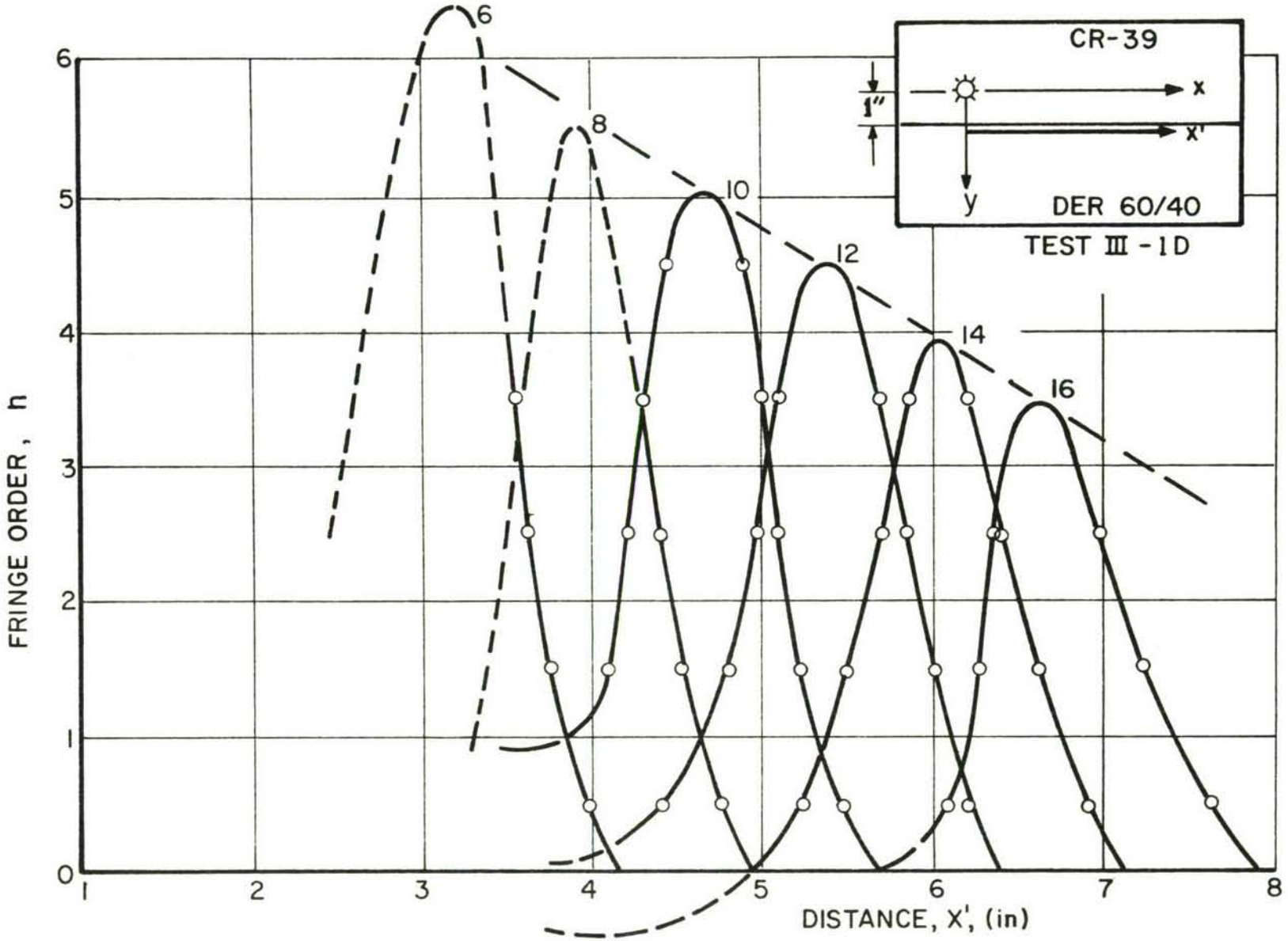


Figure 92. FRINGE ORDER AS A FUNCTION OF POSITION WITH TIME AS A PARAMETER FOR REFRACTED WAVES IN LOW-IMPEDANCE MEDIUM ALONG INTERFACE (MODEL III-1D; FRAME NUMBERS ARE MARKED)

The distortional wave velocities were computed from the dilatational velocities as before:

$$\beta_1 = 23,300 \text{ in./sec}$$

$$\beta_2 = 45,000 \text{ in./sec}$$

On the basis of these measured and computed velocities, the angles of the reflected and refracted wavefronts near the interface were calculated:

$$\text{Refracted } P_2P_1: \quad \theta_1 = \arcsin \frac{\alpha_1}{c} = 30.3° \tag{50}$$

$$\text{Refracted } P_2S_1: \quad \theta_2 = \arcsin \frac{\beta_1}{c} = 17.3° \tag{51}$$

$$\text{Reflected } P_2S_2: \quad \theta_3 = \arcsin \frac{\beta_2}{c} = 35.1° \tag{52}$$

where c is the wave velocity along the interface

$$c = \frac{\alpha_2}{\cos e} \tag{53}$$

and e is the angle of incidence. The computation of the angles above corresponds to an angle of incidence occurring around frames 10 and 12. Enlargements of these frames are shown in Figs. 93 and 94 where the calculated wavefronts have been drawn. The agreement with the fringe patterns is satisfactory.

Figure 95 shows the isochromatic fringe pattern for Model III-2D loaded in the high-impedance medium at a distance of 2 in. from the interface. The wave propagation velocities were measured as before and plotted as a function of fringe order in Fig. 96. The wavefront velocities were computed as

$$\alpha_1 = 40,000 \text{ in./sec}$$

$$\alpha_2 = 77,000 \text{ in./sec}$$

The resulting impedance ratio is 2.20:1. These propagation velocities and impedance ratio are almost the same as in Model III-1D.

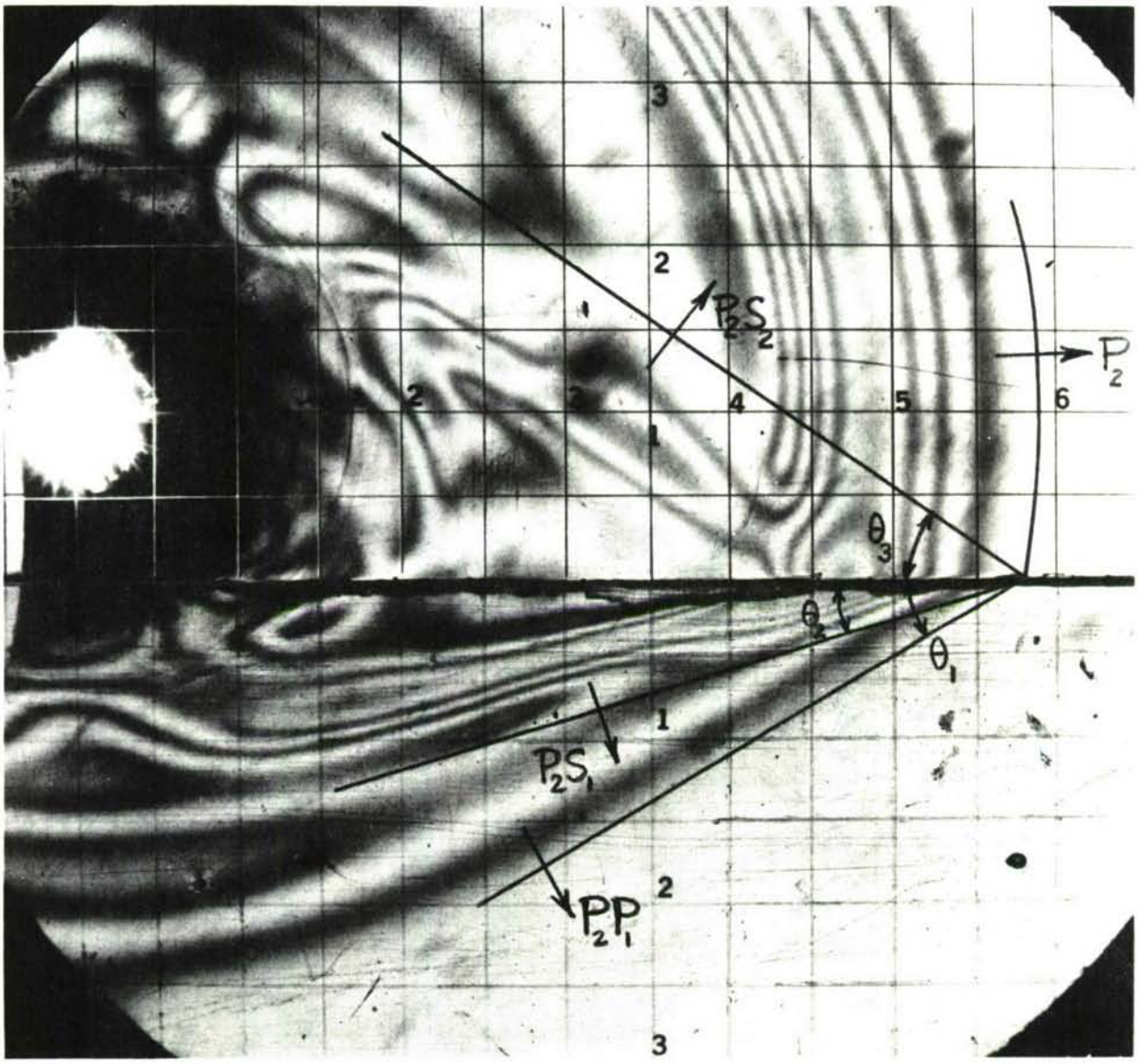


Figure 93. ENLARGEMENT OF FRAME 10 (t = 70 μ sec)
SHOWING REFLECTED AND REFRACTED WAVES

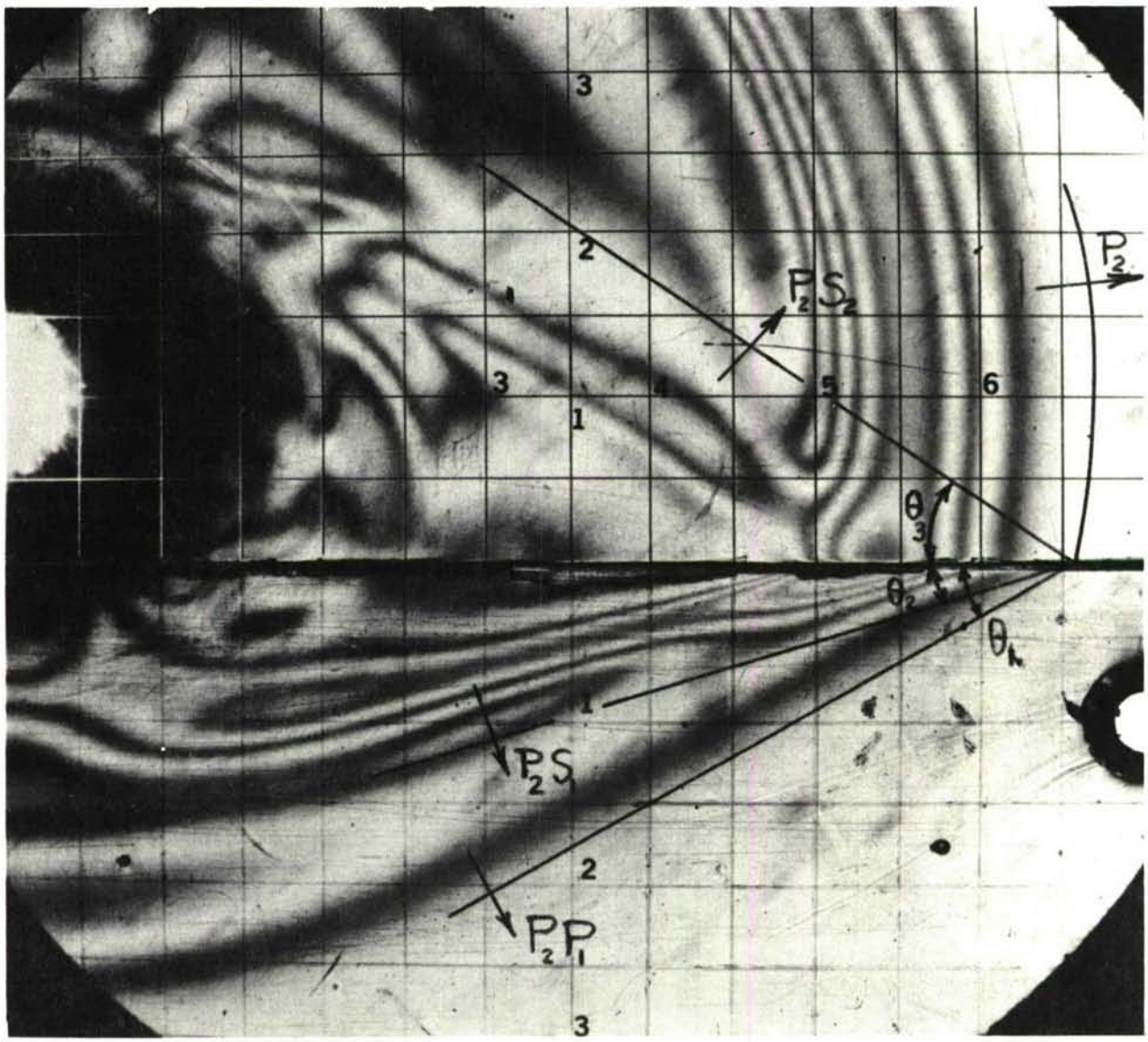


Figure 94. ENLARGEMENT OF FRAME 12 (t = 80 μ sec) SHOWING REFLECTED AND REFRACTED WAVES

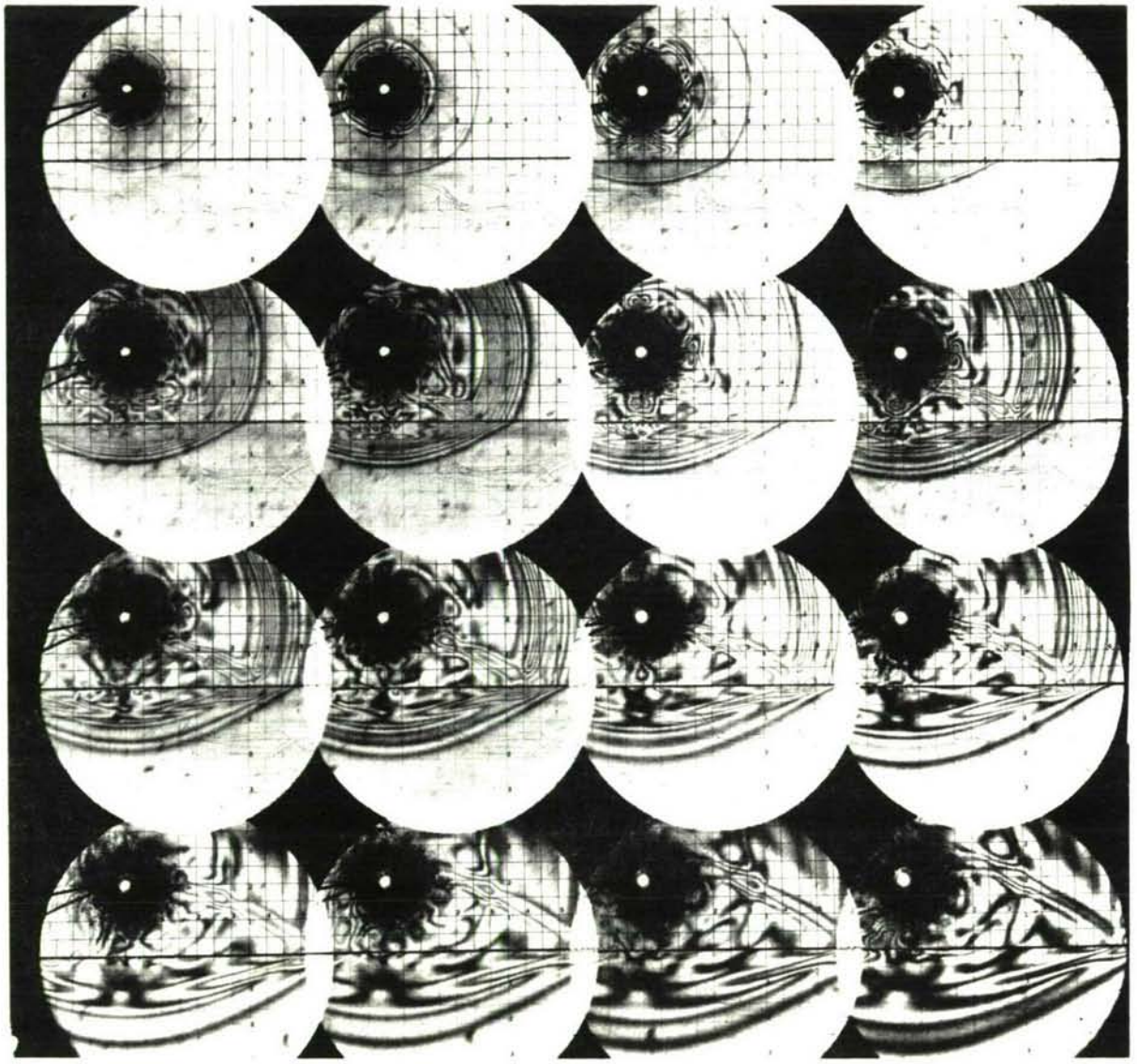


Figure 95. ISOCHROMATIC FRINGE PATTERNS IN MODEL III-2D (EXPLOSIVE SOURCE IN HIGH-IMPEDANCE MEDIUM 2 IN. FROM INTERFACE; IMPEDANCE RATIO 2.20:1; CAMERA SPEED: 200,000 FRAMES/SECOND)

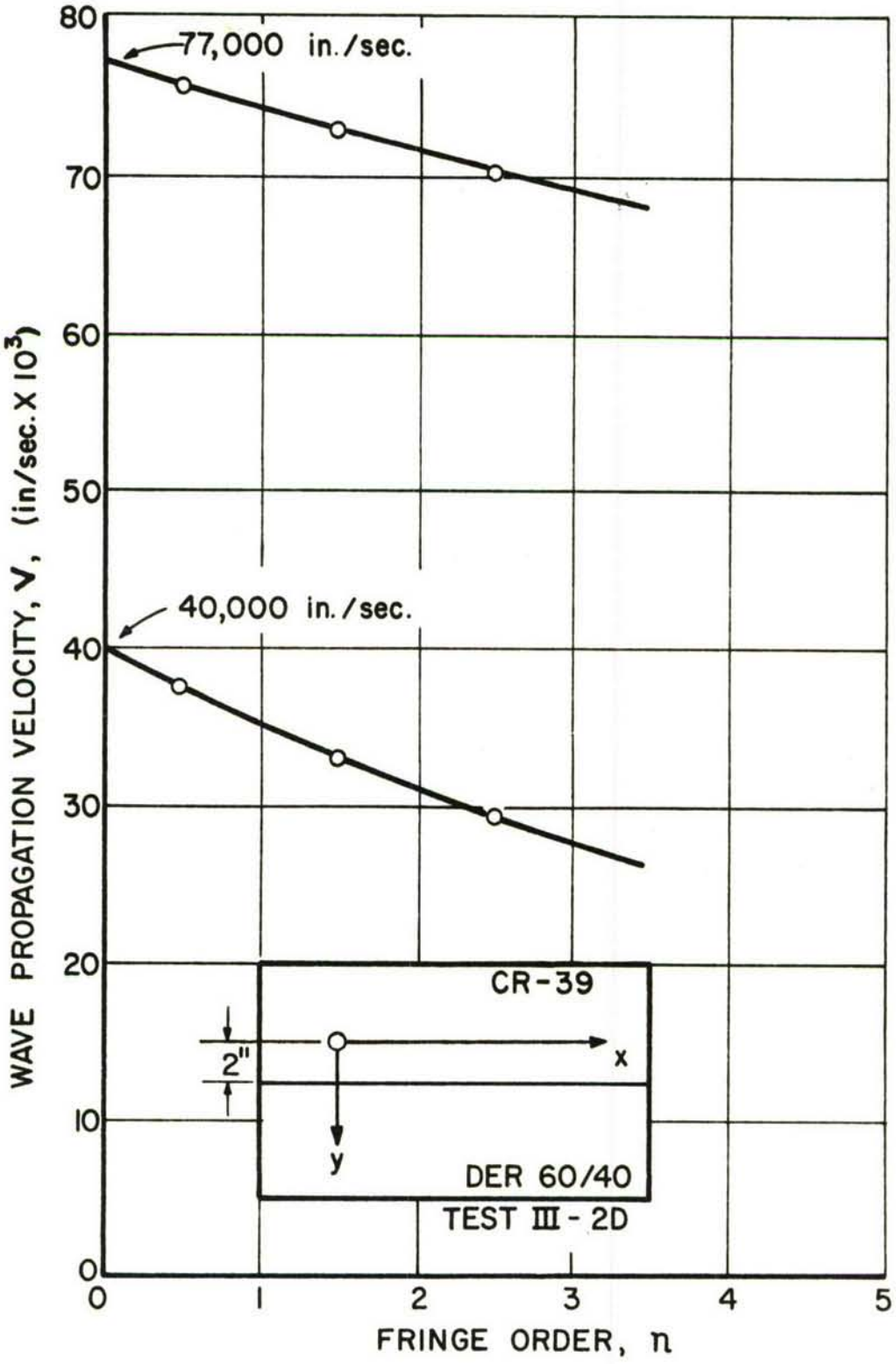


Figure 96. VELOCITY OF WAVE PROPAGATION AS A FUNCTION OF FRINGE ORDER IN TWO MEDIA OF MODEL III-2D

The refracted P_2P_1 wave is described by the birefringence variation with distance from interface plotted in Fig. 97. High attenuation and dispersion are evident. The attenuation is described by the exponential curve

$$n_{max} = e^{0.95\ (2.07 - y')}$$

The attenuation coefficient $k = 0.95$ is somewhat higher than in the corresponding case of Model III-1D. One other characteristic of these pulses is that they dip below zero and show sign changes. (The negative sign indicates a change of sign of the stress difference $(\sigma_x - \sigma_y)$ and not a negative fringe order, since the latter by definition is always a positive quantity.)

The birefringence in the high-impedance medium along the interface is plotted in Fig. 98. The dispersion seems to be moderate, if any. In fact, the slope of the front of the pulse does not seem to change noticeably with time. The attenuation also seems to be low. Another noticeable characteristic of the pulse is the formation of a secondary peak on the trailing side. Figure 99 shows the variation of birefringence with location along the interface in the low-impedance medium. In this case also, the dispersion is not noticeable and the attenuation is moderate as can be measured with the low attenuation coefficient in the exponential curve

$$n_{max} = e^{0.21\ (13.0 - x')}$$

The secondary trailing peak is much more pronounced than in the high-impedance medium.

The distortional wave velocities were computed as follows:

β_1 = 23,700 in./sec

β_2 = 44,500 in./sec

At frame 12, the angle of incidence of wave P_2 at the interface is $e = 18°$, therefore, the wave propagation velocity along the

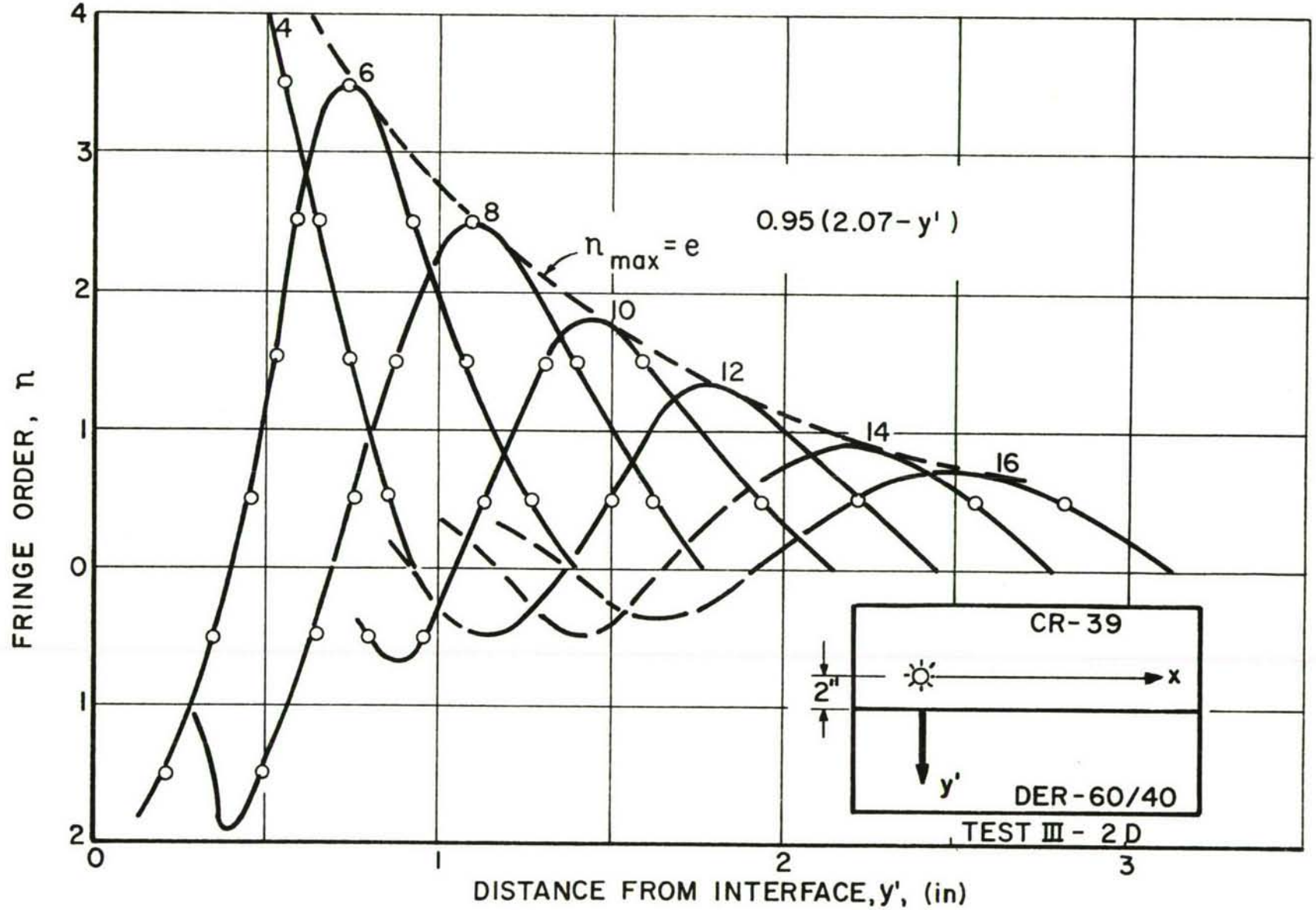


Figure 97. FRINGE ORDER AS A FUNCTION OF POSITION WITH TIME AS A PARAMETER FOR REFRACTED P_2P_1 WAVE IN LOW-IMPEDANCE MEDIUM OF MODEL III-2D

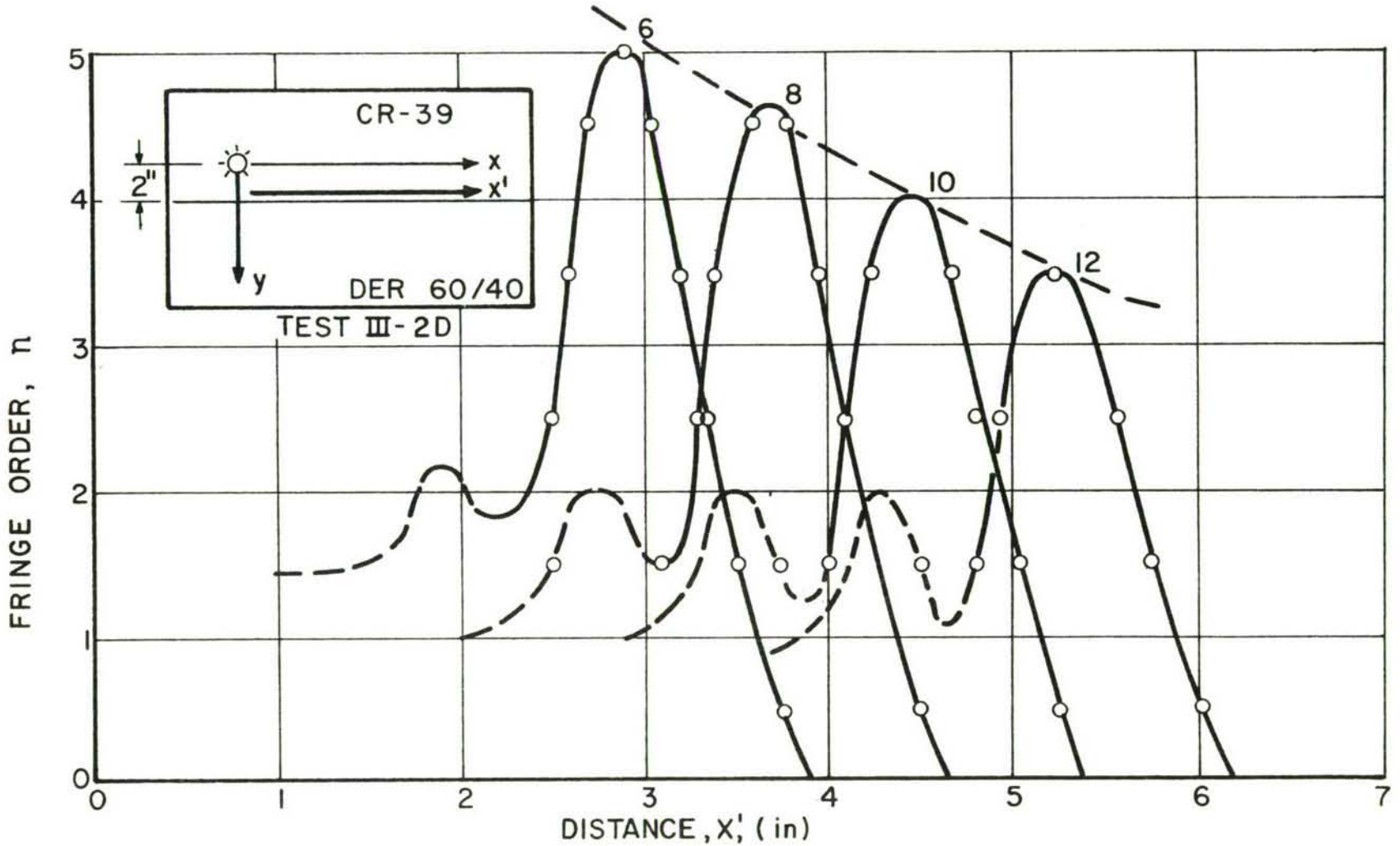


Figure 98. FRINGE ORDER AS A FUNCTION OF POSITION WITH TIME AS A PARAMETER IN HIGH-IMPEDANCE MEDIUM ALONG INTERFACE (MODEL III-2D; FRAME NUMBERS ARE MARKED)

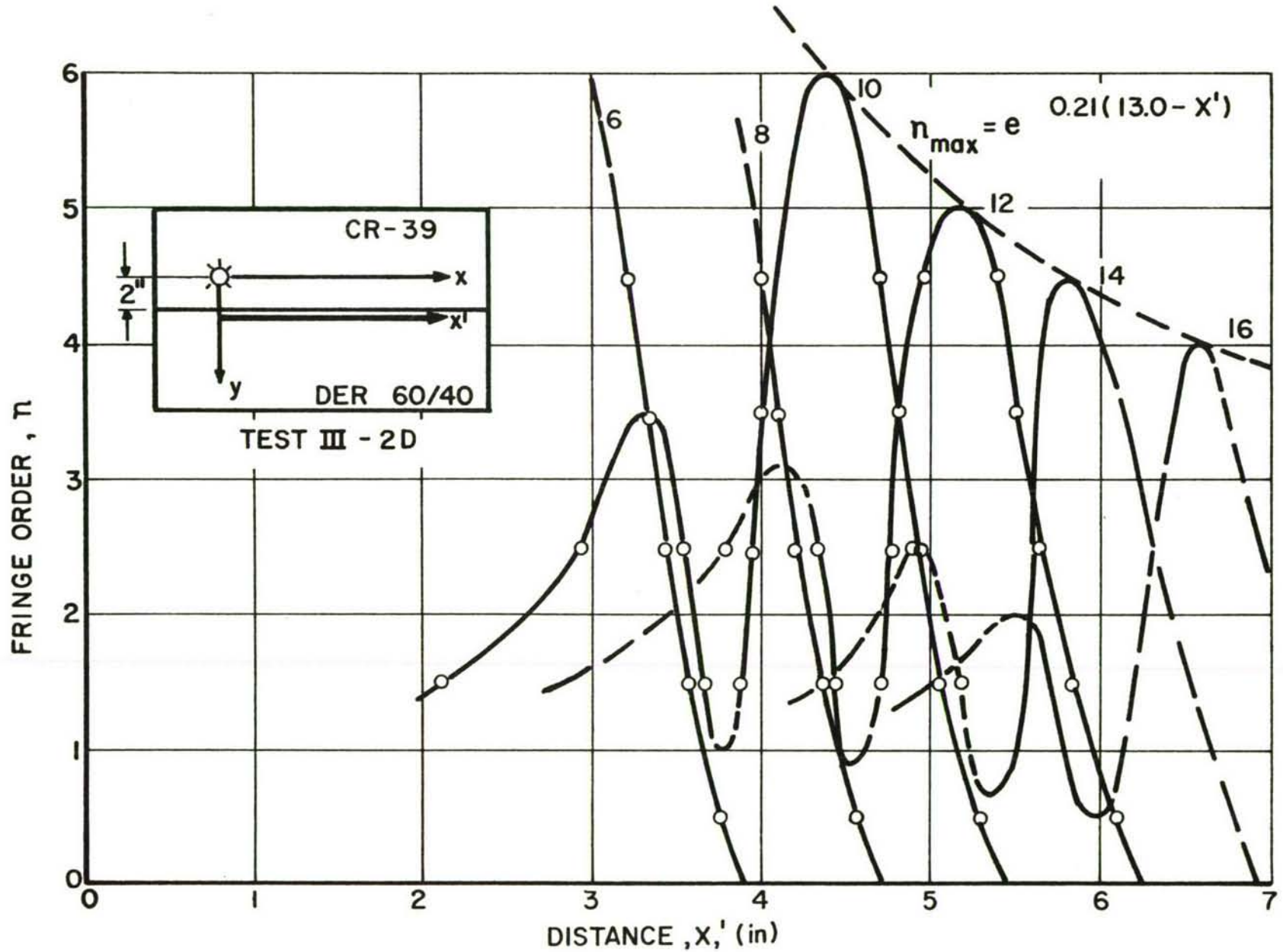


Figure 99. FRINGE ORDER AS A FUNCTION OF POSITION WITH TIME AS A PARAMETER FOR REFRACTED WAVES IN LOW-IMPEDANCE MEDIUM ALONG INTERFACE (MODEL III-2D; FRAME NUMBERS ARE MARKED)

interface is

$$c = \frac{\alpha_2}{\cos e} = 81{,}000 \text{ in./sec}$$

and the angles of the refracted and reflected waves computed according to Eqs. (50), (51), and (52) are

$$\theta_1 = 29.6°$$
$$\theta_2 = 17.0°$$
$$\theta_3 = 33.3°$$

The calculated wavefronts drawn on an enlargement of frame 12 in Fig. 100 show remarkable agreement with the fringe patterns.

Figure 101 shows the isochromatic fringe pattern for Model III-3D loaded in the high-impedance medium at a distance of 3 in. from the interface. The wave propagation velocities were measured as before and plotted as a function of fringe order in Fig. 102. The wavefront velocities were computed as

$$\alpha_1 = 39{,}000 \text{ in./sec}$$
$$\alpha_2 = 74{,}500 \text{ in./sec}$$

The resulting impedance ratio is 2.18:1.

The incident and reflected waves are described by the birefringent variation in the high-impedance medium along a line through the loading source normal to the interface. (Fig. 103.) Initially (Frame 2), the pulse is almost wholly compressive but at later times, with the influence of the reflected waves, it becomes almost totally tensile (Frames 5 and 6).

The refracted P_2P_1 wave is described by the birefringence variation with distance from interface plotted in Fig. 104. Pronounced attenuation and dispersion are evident. The sign reversal of the pulse is significant. Both positive and negative peaks of the

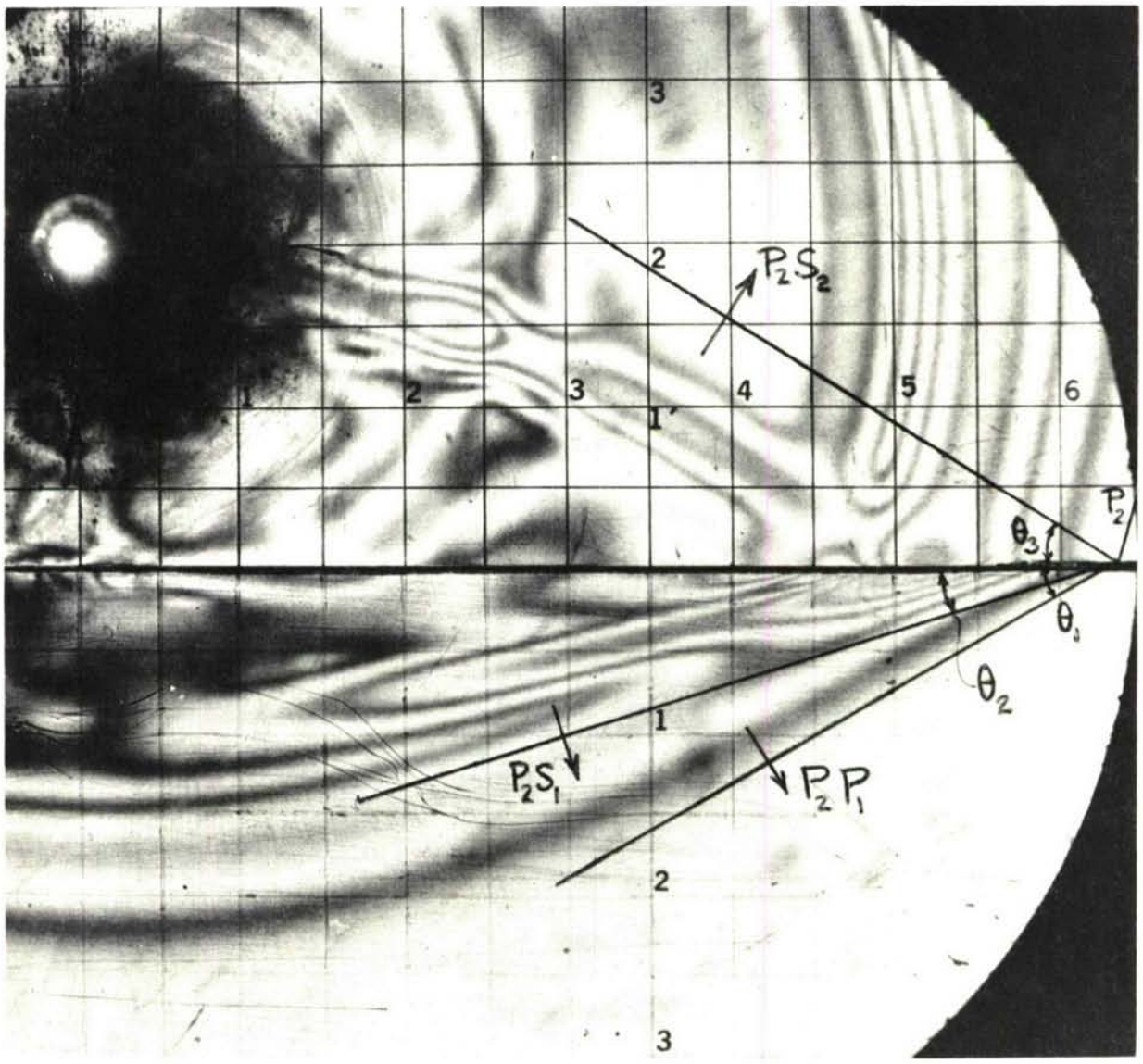


Figure 100. ENLARGEMENT OF FRAME 12 (t = 81 μ sec) SHOWING REFLECTED AND REFRACTED WAVES IN MODEL III-2D

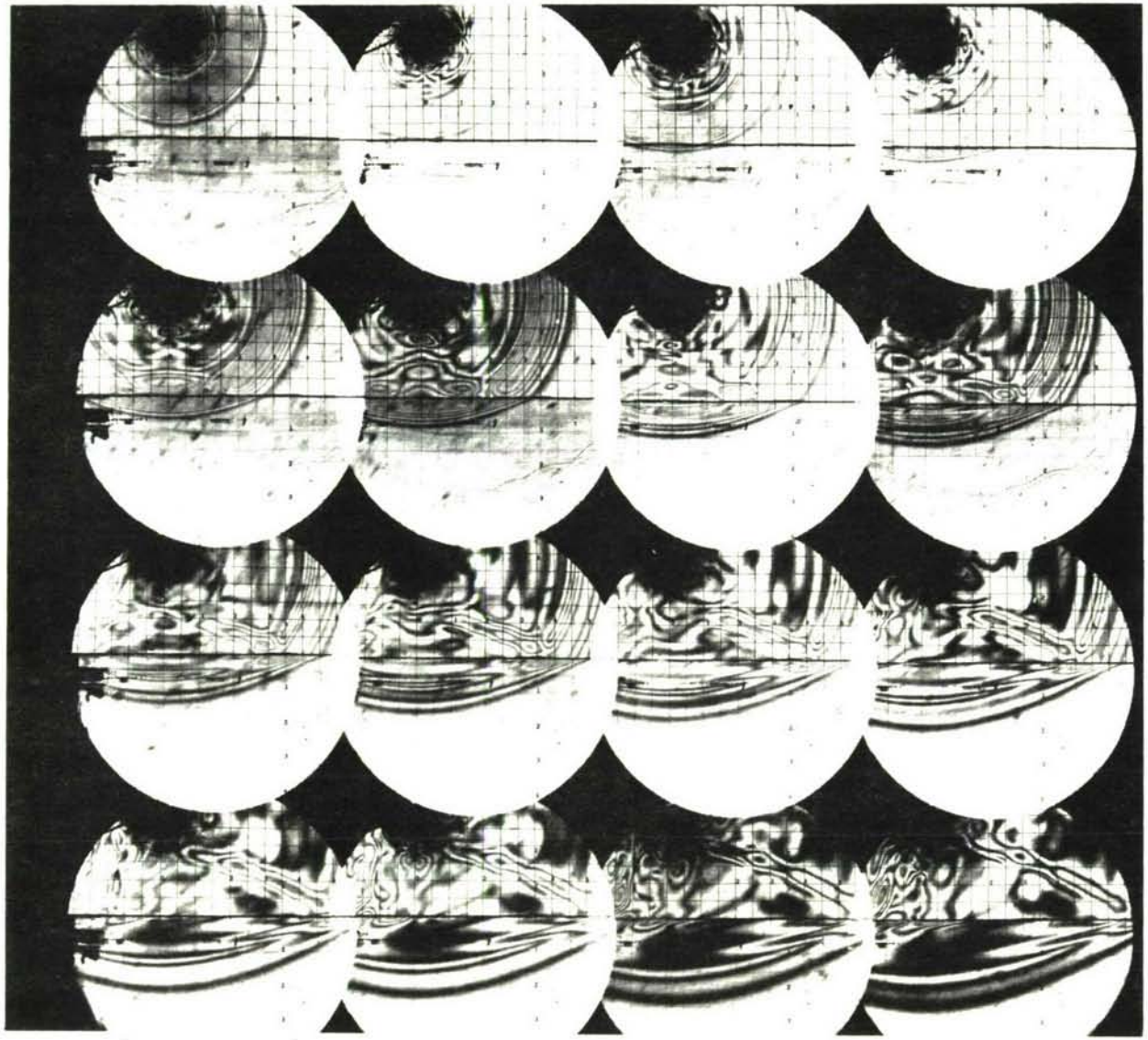


Figure 101. ISOCHROMATIC FRINGE PATTERNS IN MODEL III-3D (EXPLOSIVE SOURCE IN HIGH-IMPEDANCE MEDIUM 3 IN. FROM INTERFACE; IMPEDANCE RATIO 2.18:1; CAMERA SPEED: 200,000 FRAMES/SECOND)

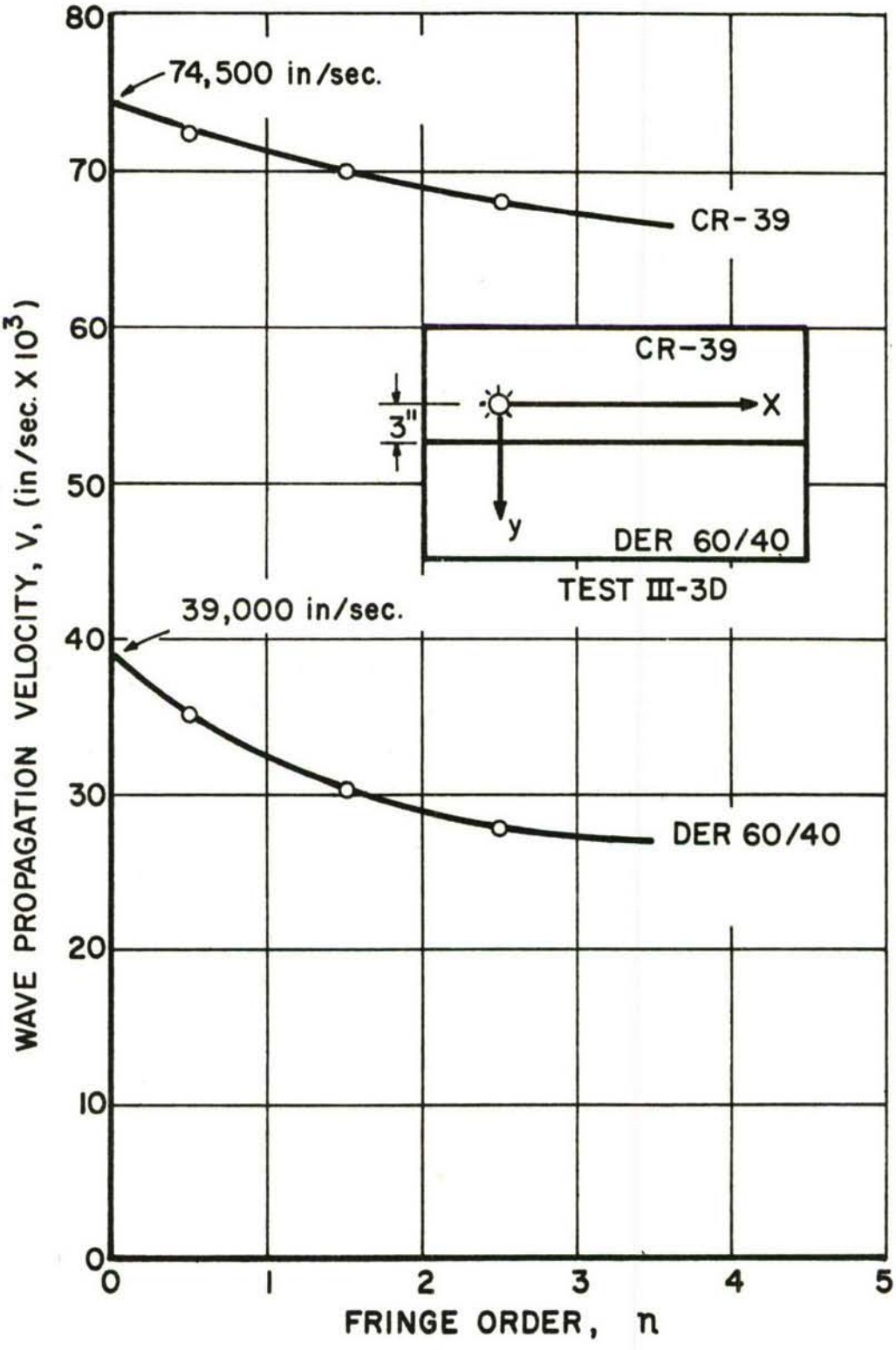


Figure 102. VELOCITY OF WAVE PROPAGATION AS A FUNCTION OF FRINGE ORDER IN TWO MEDIA OF MODEL III-3D

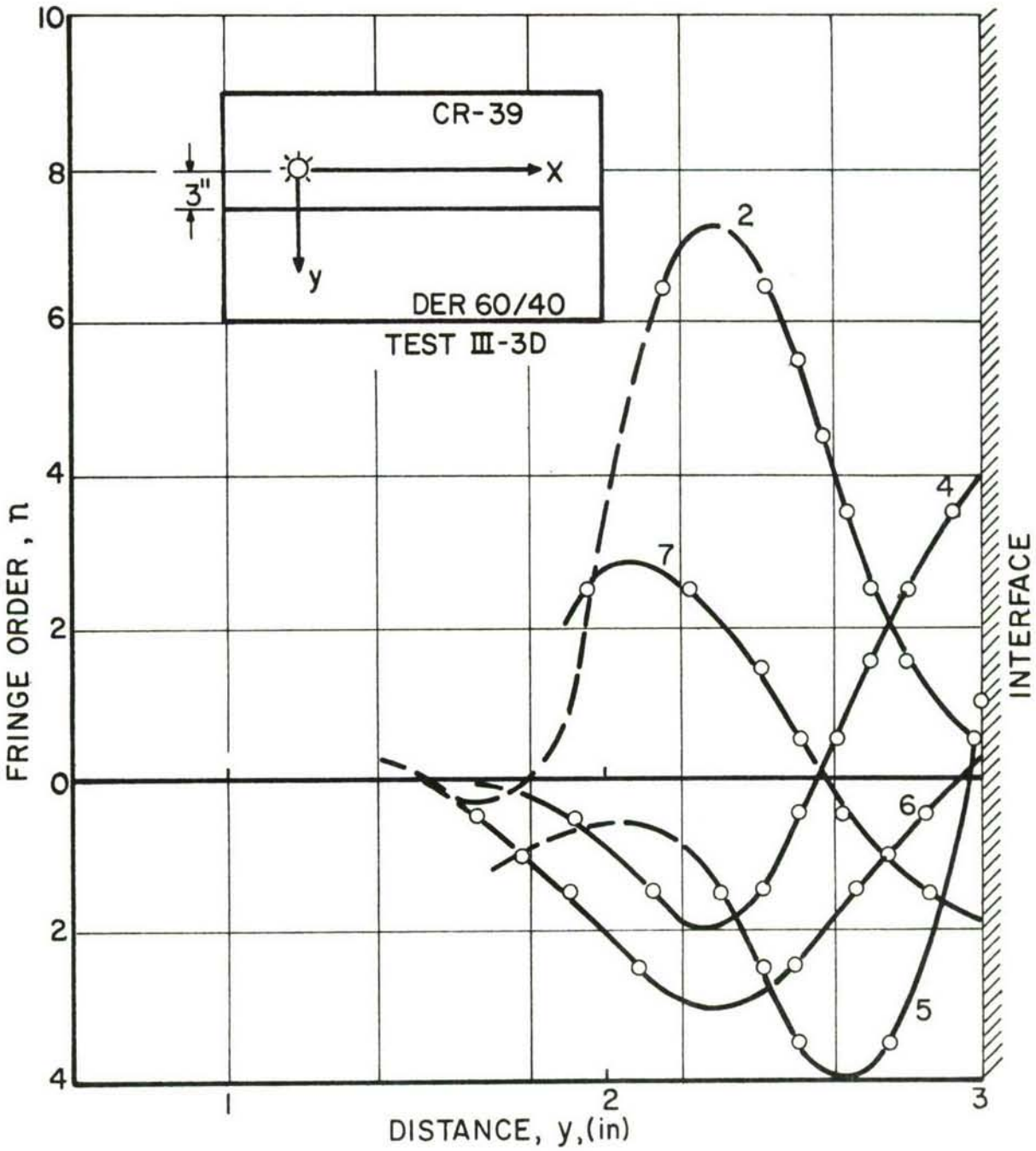


Figure 103. FRINGE ORDER AS A FUNCTION OF POSITION IN HIGH-IMPEDANCE MEDIUM ALONG LINE THROUGH EXPLOSIVE SOURCE NORMAL TO INTERFACE FOR MODEL III-3D; (FRAME NUMBERS ARE MARKED)

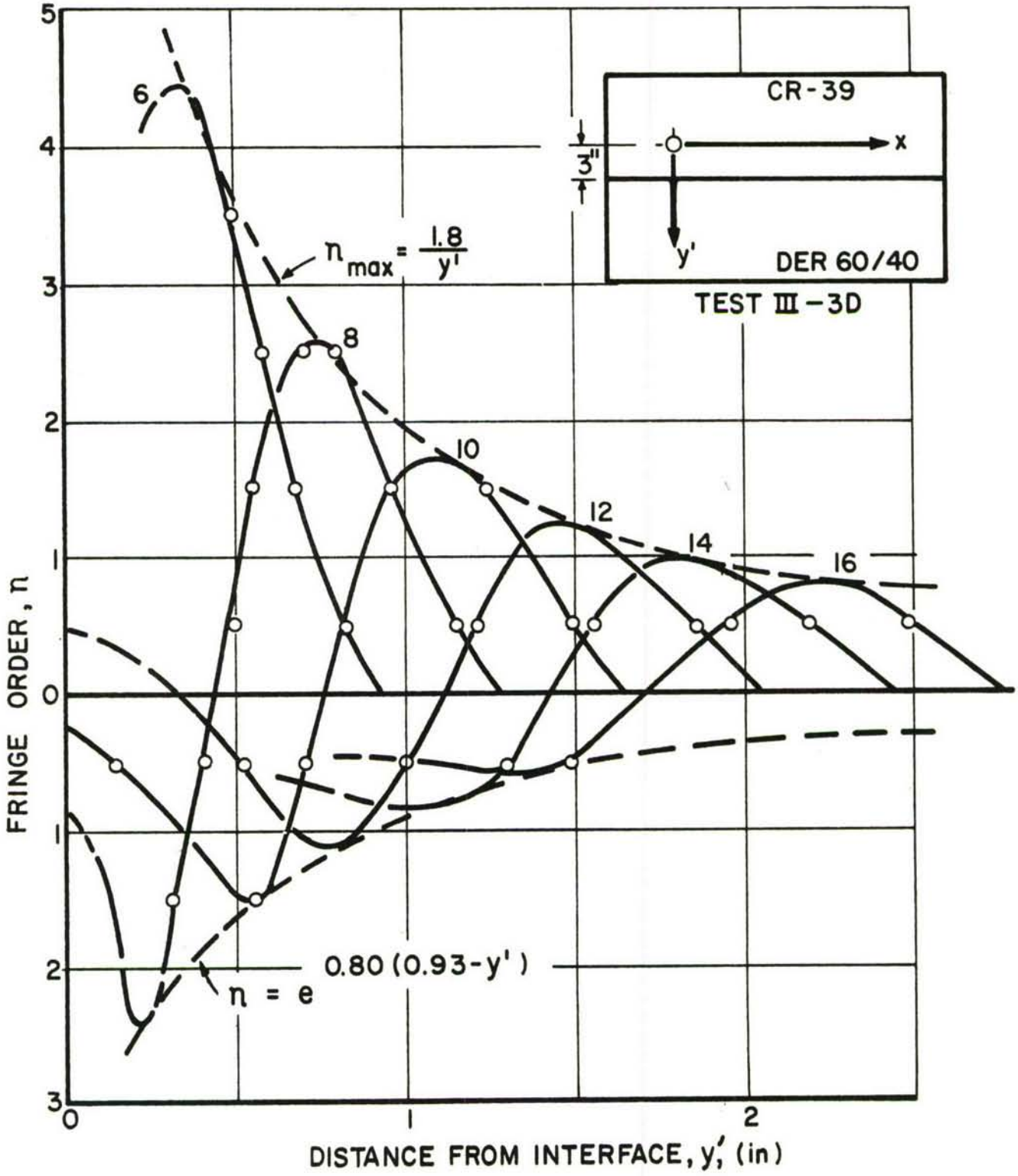


Figure 104. FRINGE ORDER AS A FUNCTION OF POSITION WITH TIME AS A PARAMETER FOR REFRACTED P_2P_1 WAVE IN LOW-IMPEDANCE MEDIUM OF MODEL III-3D

pulse show orderly attenuation. The best fit for the attenuation of the positive peak in this case was a rectangular hyperbola

$$n_{max} = \frac{1.8}{y'}$$

while an exponential curve was found more suitable for the negative peak

$$n_{max} = e^{0.80\ (0.93 - y')}$$

The degree of attenuation here is comparable to that encountered in Models III-1D and III-2D.

The birefringence in the high impedance medium along the interface is plotted in Fig. 105. The leading slope of the pulse seems to remain unchanged and the secondary peak on the trailing side is present. No conclusion can be drawn regarding the attenuation.

Figure 106 shows the variation of birefringence with location along the interface in the low-impedance medium. The dispersion is insignificant as the slopes of the pulse remain essentially unchanged. The attenuation is very low as can be measured with the low attenuation coefficient (k = 0.08) in the exponential curve through the peaks of the pulse

$$n_{max} = e^{0.08\ (25.5 - x')}$$

The secondary trailing peak is much more pronounced than in Model III-2D and there is evidence of an incipient tertiary trailing peak.

The distortional wave velocities were computed as follows:

β_1 = 23,100 in./sec

β_2 = 43,000 in./sec

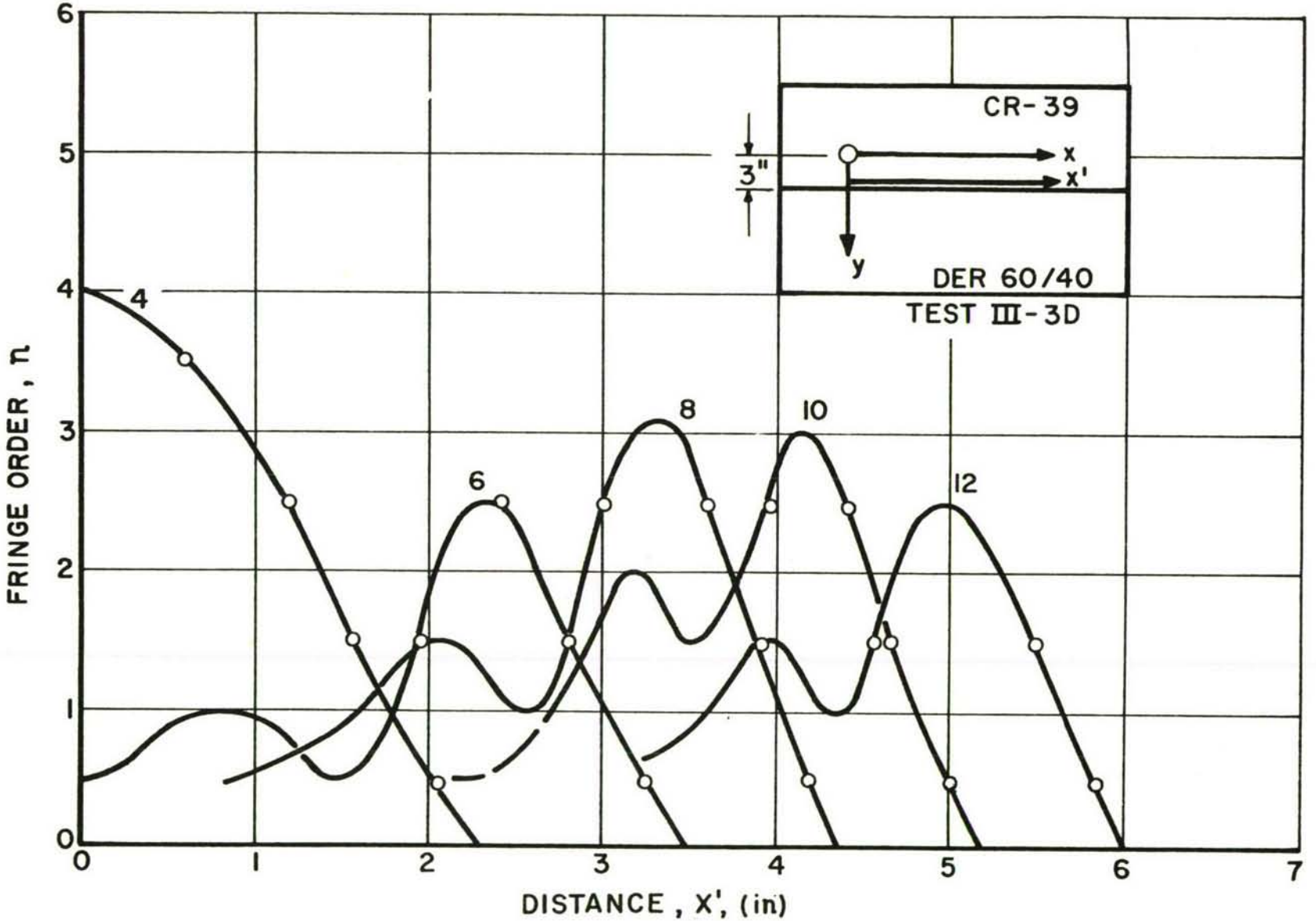


Figure 105. FRINGE ORDER AS A FUNCTION OF POSITION WITH TIME AS A PARAMETER IN HIGH-IMPEDANCE MEDIUM ALONG INTERFACE (MODEL III-3D; FRAME NUMBERS ARE MARKED)

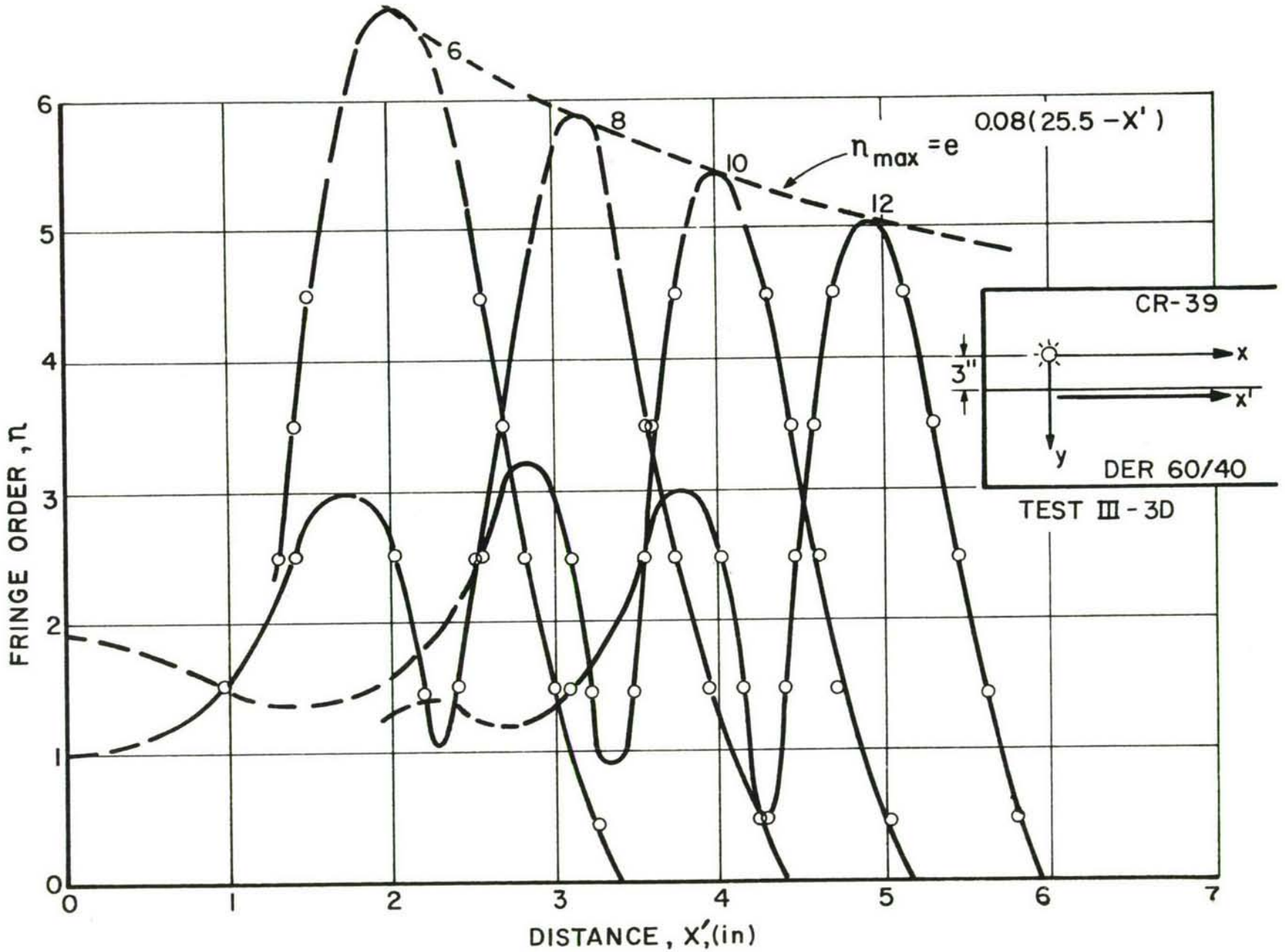


Figure 106. FRINGE ORDER AS A FUNCTION OF POSITION WITH TIME AS A PARAMETER FOR REFRACTED WAVES IN LOW-IMPEDANCE MEDIUM ALONG INTERFACE (MODEL III-3D; FRAME NUMBERS ARE MARKED)

At frame 12, the angle of incidence of wave P_2 at the interface is $e = 26.5°$; therefore, the wave propagation velocity along the interface is

$$c = \frac{\alpha_2}{\cos e} = 83,000 \text{ in./sec}$$

and the angles of the refracted and reflected waves computed according to Eqs. (50), (51), and (52) are

$$\theta_1 = 28.0°$$
$$\theta_2 = 16.2°$$
$$\theta_3 = 31.2°$$

The calculated wavefronts drawn on an enlargement of frame 12 in Fig. 107 show good agreement with the fringe patterns.

Reviewing the results from the three models of Phase III, we note the following. Wave velocities varied between 74,500 and 77,500 in./sec for the high-impedance medium and between 39,000 and 40,000 in./sec in the low-impedance medium. The impedance ratio varied between 2.18:1 and 2.23:1. The refracted P_2P_1 wave in the low impedance medium shows pronounced attenuation increasing slightly with distance of explosive source from interface. The shape of this pulse changes appreciably with this parameter. In Model III-1D, this pulse is wholly compressive, in Model III-2D, it begins to show sign reversal on the trailing side and in Model III-3D the sign reversal is appreciable. In the latter case, the negative peak of the pulse shows similar attenuation characteristics as the positive one.

The combination of incident and reflected waves in the high-impedance medium along the interface shows little or no dispersion and low attenuation decreasing further with distance of loading source from interface. Secondary and tertiary peaks develop on the trailing side of the pulse with increasing distance of loading source from interface.

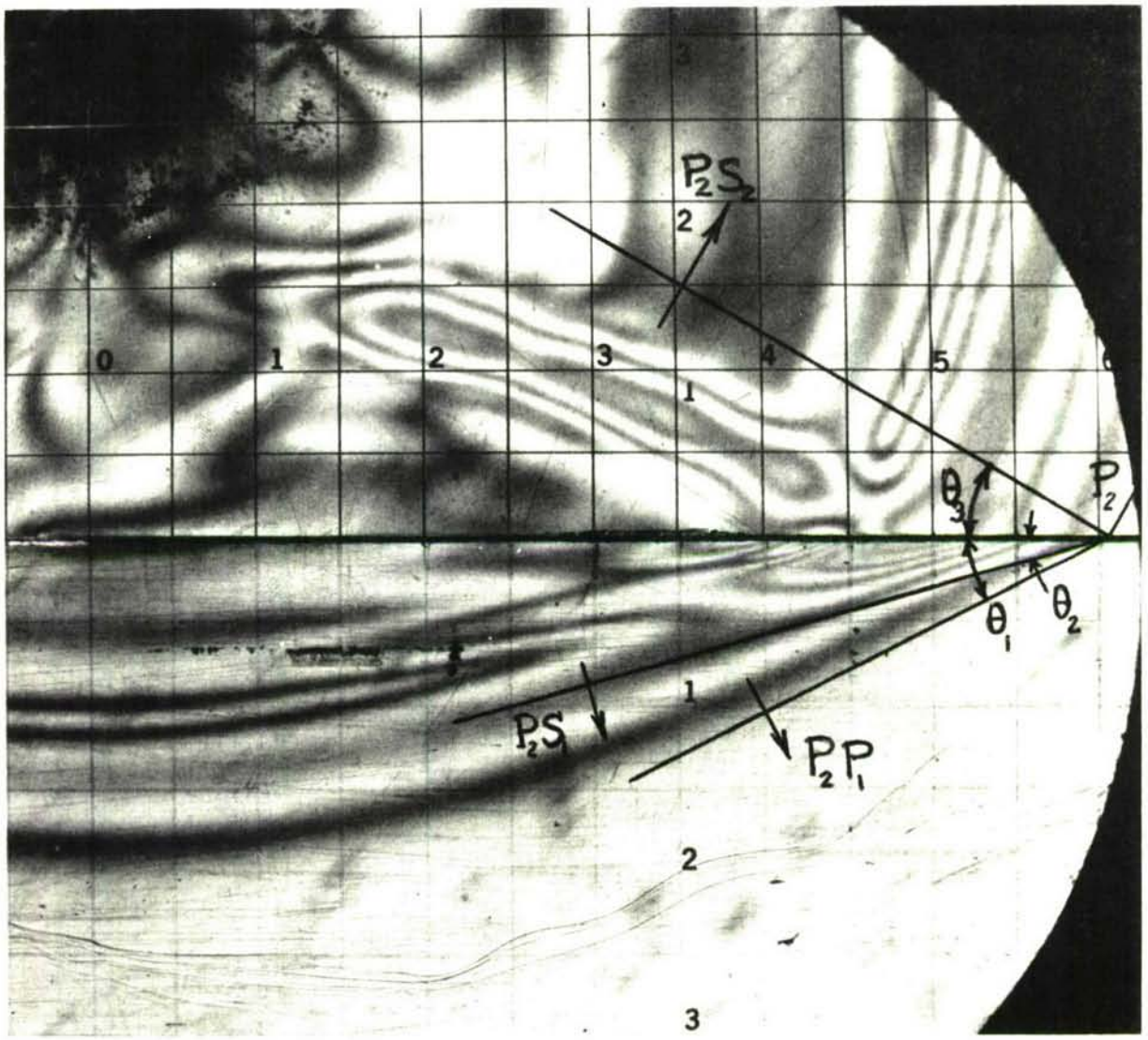


Figure 107. ENLARGEMENT OF FRAME 12 (t = 85 μ sec) SHOWING REFLECTED AND REFRACTED WAVES IN MODEL III-3D

The combination of refracted waves in the low-impedance medium along the interface shows no noticeable dispersion and low and decreasing attenuation (attenuation coefficient decreasing from $k = 0.21$ to $k = 0.08$). Model III-2D shows pronounced secondary trailing peaks and Model III-3D shows even more pronounced secondary peaks with a tertiary peak developing at later times.

SECTION IX

SUMMARY, CONCLUSIONS AND RECOMMENDATIONS FOR FUTURE WORK

This report deals with a photoelastic study of wave propagation in layered media. Specifically, the propagation and attenuation characteristics were studied of transmitted, reflected and refracted waves generated by air-shock or explosive loading in birefringent layered media having an impedance ratio of 2:1. Some of the significant developments of this study are summarized below.

A new explosive charge, Pentaerythritol Tetranitrate (PETN), was developed for dynamic point source loading of photoelastic models. This explosive was found to be safer than previously used lead azide requiring a high level of energy for detonation. It has a higher detonation velocity and does not produce too much smoke or light that would interfere with photography of fringes in the vicinity of the loading source. The PETN charges were detonated by means of an exploding bridge wire detonator.

The same multiple spark Cranz-Schardin camera used in previous similar studies (Ref. 3) was used here with only minor modifications. In the present investigation, isochromatic and moiré fringe records were photographed with this camera at rates around 200,000 frames per second.

Considerable effort was devoted to the development and characterization of model materials meeting the necessary requirements of birefringence and impedance ratio (2:1). Two classes of materials were investigated, high-modulus materials for the explosive loading tests and low-modulus materials for the air blast loading tests. In the first category, a large number of materials were evaluated by subjecting samples to explosive point loading and measuring the wave propagation velocity. In the second category, samples were subjected to air-blast loading in a shock tube and the wave propagation velocity

measured. The most important development was that of a birefringent material with easily controllable impedance. This was accomplished by mixing a flexible resin (DER 732) and a rigid resin (DER 331) in varying proportions. For the explosive loading tests, Columbia Resin (CR-39) and DER 60/40 (60 percent of DER 732 and 40 percent of DER 331) were selected as the high- and low-impedance layers, respectively. For the air blast loading tests, DER 73/27 and DER 85/15 were selected.

All materials used in this study are viscoelastic. Properties of Columbia Resin under dynamic conditions were extracted from published results (Ref. 12). The mixture DER 60/40 was completely characterized by conducting mechanical and optical creep tests at different temperatures and using the temperature-time equivalence principle. Thus, a relaxation Young's modulus, shear modulus, Poisson's ratio and stress fringe value as functions of time were obtained for a time span of 14 decades. The optical properties of DER 73/27 and DER 85/15 were similarly obtained.

In the first phase of this study, layered models were subjected to air-blast loading along the free edge of the low-impedance layer. Five models with five different depths of low-impedance layer were tested. The dispersion of the pulse was appreciable in the upper (low-impedance) layer and very low in the lower (high-impedance) layer. Evidence of appreciable attenuation in both layers exists, both in the direction of wave propagation and along the wavefronts. The latter is manifested by the changing inclination of the fringes with time and has been predicted for viscoelastic materials (Ref. 16). No interface (Stoneley) waves were noticed. In materials with approximately equal densities (as is the case here), such waves are only possible when the shear wave velocities are approximately equal (Ref. 4). No headwaves were noticed. However, the influence of the high-impedance medium on the low-impedance one was manifested in the curvature of the otherwise straight line fringe position versus time curves. This curvature, especially noticeable for higher fringe orders, is due to superposition of reflected waves upon the incident one and causes local stress intensitication. A typical increase of 25 percent

in maximum shear stress near the interface can be predicted from the experimental results. No noticeable influence of the upper (low-impedance) layer on the lower one was detected.

In the second phase of this study, two-layer models were loaded with explosive charges in the low-impedance layer at varying distances from the interface. The propagation and attenuation characteristics of the waves were studied from the isochromatic fringe records. The attenuation was described by fitting curves through the peaks of the pulse. The best fit was an exponential one indicating the influence of the viscoelastic nature of the model materials. The incident wave (in the low-impedance medium) had an attenuation coefficient varying between 0.7 and 0.9. The refracted waves in the high-impedance medium along a line normal to the interface and passing through the loading source showed appreciable attenuation ($k = 0.5$) for the first model with the shortest distance between loading and interface ($h = 1$ in.) and no measurable attenuation for the other models. The same conclusions apply for the waves in the high-impedance medium along the interface. This pulse along the interface results from a combination of refracted dilatational, shear and conical shear waves. It changes shape with increasing time forming a second lower peak near the leading end. Whereas the main peak of the pulse shows the attenuation characteristics discussed above the leading lower peak seems to be of nearly constant amplitude (approximately 0.8 fringes for Model II-1D and 0.5 fringes for Model II-2D). The pulse along the interface in the low-impedance medium results from a combination of incident and reflected waves and headwaves which seem to have a reinforcing effect as shown by the low attenuation coefficient of 0.4 for Model II-1D. This attenuation decreases further with increasing distance of loading source from interface. It is interesting to note that the attenuation in the low-impedance medium along the interface is lower than that in the high-impedance medium which is known to be less "lossy."

Headwaves ($P_1P_2S_1$, $P_1S_2S_1$ and $P_1P_2S_2$) were evident in Model II-1D with the shortest distance between load and interface (h = 1 in.). The wavefronts of these headwaves calculated from the wave propagation velocities were in agreement with the isochromatic fringe patterns. The headwaves in the low-impedance medium show a characteristic lack of attenuation which implies that their amplitude may become comparable to or even overshadow that of the incident wave at some distance along the interface. One feature, especially noticeable in the last frame of the photoelastic record (Fig. 67), is the curvature of the half-order fringe of the $P_1P_2S_1$ headwave. This may be due to attenuation along the wavefront as predicted for a "general plane wave" in a viscoelastic material (Ref. 16). Model II-2D (h = 2 in.) shows only a slight evidence of a headwave ($P_1P_2S_2$). Apparently, the appearance of headwaves is a function of distance of loading from interface and the intensity of the pulse, in addition to the impedance mismatch of the materials.

A quasi-elastic stress analysis of the refracted waves in the high-impedance medium was conducted. Stress separation was achieved for the refracted P_1P_2 wave using photoelastic data only and taking into consideration polar symmetry. A similar analysis was conducted for this wave and the combination of waves along the interface using moiré data. One conclusion from this analysis is that both horizontal and vertical stresses along the interface can reach appreciable tensile values, especially when the loading source is near the interface. This should be an important consideration in the design of underground structures located near the interface of earth strata.

Relative magnitudes of the transmitted, reflected and refracted waves can be obtained approximately from the fringe patterns. Since the comparison of amplitudes must be in terms of stress, fringe order ratios must be multiplied by the ratio of stress fringe values for the two materials. For the timescale of interest in the present study (1 to 20 μ sec), the ratio is approximately 4.5. Thus, in

comparing the incident P_1 and the refracted P_1P_2 waves in Model II-1D, we note that a maximum fringe order of four is reached at a distance of 2 in. from the source in both media. This would indicate an approximate stress amplitude ratio of 4.5:1. In comparing the pulses along the interface we note that the fringe order amplitudes in the low-impedance medium are two to three times the corresponding fringe orders in the high-impedance medium. This would indicate an approximate stress ratio of 1.50 to 2.25 between the high-impedance and the low-impedance media.

Reflection from the high-impedance medium has a reinforcing effect on the incident wave in the low-impedance medium near the interface. Approximate amplitude ratios (in terms of maximum shear stress) between 1.3 and 1.5 were computed at a distance of 2 in. from the source. This compares with a typical ratio of 1.25 computed from one of the shock tube tests. This ratio, of course, would vary with distance of source from the point in question and with the type of wave (plane or cylindrical).

In the third phase of this investigation, two-layer models were loaded with explosive charges in the high-impedance medium at varying distances from the interface. The wavefronts of the reflected and refracted waves were calculated on the basis of the measured propagation velocities and drawn over the isochromatic fringe patterns. The agreement with the fringe patterns is very satisfactory.

An exponential fit on the incident P_2 wave gave an attenuation coefficient of $k = 0.29$ which is much lower than the attenuation of refracted waves in the same medium when the loading source is in the low-impedance medium. The combination of incident and reflected waves along the interface shows little or no dispersion and low attenuation. Secondary and tertiary peaks develop on the trailing end of the pulse with increasing distance between explosive and interface. As in the previous phase of work (explosive in low-impedance medium),

the incident wave is reinforced by the reflected ones. An approximate ratio of amplitudes between the pulse along the interface and the incident one is 1.35 for Model III-1D. This ratio decreases with increasing distance between source and interface.

The refracted P_2P_1 wave shows pronounced attenuation increasing slightly with distance of explosive from interface. The shape of the pulse changes with this parameter. In Model III-1D (h = 1 in.), it is wholly compressive, in Model III-2D (h = 2 in.), it begins to show sign reversal on the trailing side becoming more pronounced in Model III-3D (h = 3 in.). The combination of refracted waves along the line through the source and normal to the interface reaches a maximum amplitude at the interface. This amplitude has a nearly constant value (approximately seven fringes) independent of the distance from the source. For points located a fixed distance from the source the amplitude ratio between the refracted P_2P_1 wave and the incident P_2 wave increases with increasing distance between source and interface. For example, for a distance of 3 in. from the source the approximate amplitude ratio is 0.07, 0.11, and 0.30 for values of h = 1, 2 and 3 in., respectively.

The refracted waves along the interface show characteristics similar to the pulse in the high-impedance medium along the interface, i.e., no noticeable dispersion, low attenuation and multiple peaks. The amplitude ratio at corresponding points along the interface between the pulses in the two media is of the order of 0.30.

One general conclusion from all experiments conducted is that the incident wave upon impingement on the interface and combination with reflected waves is reinforced by approximately 25 to 50 percent. This is true in all cases, whether the wave is plane or cylindrical and whether the loading source is in the low- or high-impedance medium. The highest stresses in the high-impedance medium occur at the interface when the loading source is in that medium. The highest stresses in the low-impedance medium occur at the interface and are of the same order of magnitude whether the source is in the low- or high-impedance medium. In the former case, however, this stress falls off rapidly with increasing distance of source from interface.

The present work clearly demonstrates that the photoelastic methods developed and used heretofore provide illuminating insights into wave propagation problems and they can yield solutions to specific problems and useful conclusions regarding the influence of material, geometrical and loading parameters. Although a great many cases were treated in this investigation, the treatment can not be considered complete. Complete separation of stresses would require moiré data in all cases and a rigorous viscoelastic analysis. Experimental methods for such analyses have been developed previously but could not be applied here due to time limitations. Future research could deal with more complete analyses of a few critical problems using all available methods and techniques. The potential of holographic and interferometric methods in connection with these problems should be investigated.

The problem of wave propagation in layered media could be extended to include more than two layers or include curved interfaces. The possibility of stress waves reflected from a curved interface and focusing in a small area should be of interest. The influence of wavefront orientation with respect to the interface should be studied. Then, it would be possible to see if phase velocities are functions of the incident angle as predicted theoretically (Ref. 16). Also, the conditions (critical angle) for which interface waves are produced should be established experimentally. The extension of these studies to three-dimensions is now entirely feasible owing to recent developments in the scattered-light technique using a multiple-pulse ruby laser (Ref. 11). The problem of an explosively loaded spherical cavity in an infinite medium or near interfaces is of great importance.

A systematic study of the influence of material parameters should also be undertaken. In the study of wave propagation in layered media, the different layers can be elastic, viscoelastic (linear or nonlinear), viscoplastic or fluid. In the latter case, the influence of a solid-liquid interface is of special interest and could be studied using birefringent fluids. Feasibility studies of scattered-light photoelasticity in birefringent fluids have been conducted recently at IITRI.

Another approach which has not been explored much is the study of wave propagation in actual rock materials. Moiré methods and birefringent coatings would be eminently suitable for such studies. In such studies, the effects of material anisotropy on wave propagation would be of great interest. Loads could be increased to sufficiently high levels to produce failure and crack propagation characteristics under dynamic loading could be studied.

REFERENCES

1. Riley, W. F., Daniel, I. M. and Carey, J. J., "A Study of Stress Wave Interaction with Buried Structures," Air Force Special Weapons Center, AFSWC-TDR-62-47.

2. Daniel, I. M., "Experimental Study of Stress Wave Interaction in Photoviscoelastic Plates," Air Force Weapons Lab., AFWL-TR-65-43.

3. Dally, J. W., and Riley, W. F., "Photoelastic Study of Wave Propagation," Air Force Weapons Lab., AFWL-TR-66-54.

4. Ewing, W. M., Jardetsky, W. S. and Press, F., Elastic Waves in Layered Media, McGraw-Hill, New York, 1957.

5. Cooper, Jr., H. F. and Reiss, E. L., "Reflection of Plane Viscoelastic Waves from Plane Boundaries," J. Acoust. Soc. of America, v. 39, June 1966, pp. 1133-1138.

6. Muskat, M. and Meres, M. W., "Reflection and Transmission Coefficients for Plane Waves in Elastic Media," Geophysics, v. 5, 1940, pp. 149-155.

7. Ewing, W. M., Jardetsky, W. S. and Press, F., Elastic Waves in Layered Media, McGraw-Hill, New York, 1957, p. 109.

8. Cagniard, L., "Reflection et refraction des ondes seismiques progressives," (These), Gauthier-Villars et Cie., Paris, 1939.

9. Daniel, I. M., "Experimental Methods for Dynamic Stress Analysis in Viscoelastic Materials," J. Appl. Mechanics, v. 32, September 1965, pp. 598-606.

10. Daniel, I. M., "Mechanical and Optical Characterization of Plasticized Polyvinyl Chloride," Trans. of the Soc. of Rheology, v. 10, Part 1, 1966, pp. 25-49.

11. Rowlands, R. E., Taylor, C. E. and Daniel, I. M., "A Multiple-Pulse Ruby Laser System for Dynamic Photomechanics: Applications to Transmitted and Scattered-Light Photoelasticity," presented at annual meeting of the Soc. for Exper. Stress Analysis, San Francisco, October 1968.

12. Clark, A.B.J., "Static and Dynamic Calibration of a Photoelastic Model Material, CR-39," Proc. SESA, v. XIV, Part 1, 1956, pp. 195-204.

REFERENCES (Cont'd.)

13. Cole, J. and Huth, J., "Stresses Produced in a Half Plane by Moving Loads," J. Appl. Mech., v. 25, 1961, pp. 62-68.

14. Ang, D. D., "Transient Motion of a Line Load on the Surface of an Elastic Half-Space," Quart. Appl. Math., v. 18, 1960, pp. 251-256.

15. Arenz, R. J., "Two-Dimensional Wave Propagation in Realistic Viscoelastic Materials," J. Appl. Mech., v. 32, 1965, pp. 303-314.

16. Cooper, Jr., H. F., "Reflection and Transmission of Oblique Plane Waves at a Plane Interface Between Viscoelastic Media," J. Acoust. Soc. of Amer., v. 42, 1967, pp. 1064-1069.

DISTRIBUTION

No. cys.

HEADQUARTERS USAF

Hq USAF, Wash, DC 20330

1 (AFOCE)

2 (AFRDQSN)

1 (AFRDQSS)

1 (AFRDDC)

1 (AFRSTG)

1 (AFOCEK)

1 (AFOCEKA)

1 (AFOCELA)

1 (AFOCELB)

1 USAFCEC (CEC-E), Wright-Patterson AFB, OH 45433

MAJOR AIR COMMANDS

AFSC, Andrews AFB, Wash, DC 20331

1 (SCTP)

1 (SCTSW)

1 (SCTTS)

1 (SCLSC)

1 (SCSSM)

1 (SCOCC)

1 (SCLAS)

1 (SCAP)

1 SAC (DE), Offutt AFB, Nebraska 68113

1 AFLC (MCE), Wright-Patterson AFB, OH 45433

DISTRIBUTION (cont'd)

No. cys.	
1	ADC (ADEDC), Box 5, Ent AFB, CO 80912
	AFIT, Wright-Patterson AFB, OH 45433
1	(CES)
1	(SEB (Dept of Mechanics)/Maj Johnson
1	(SEP (Dept of Physics)/Dr. Bridgeman
1	USAFE (DE), New York, NY 09633
1	CINPACAF, (DCE), APO San Francisco 96553
1	USAF Academy (DFSFR), Colorado 80840
	AFSC ORGANIZATIONS
1	AFML, Wright-Patterson AFB, OH 45433
1	AF Avionics Lab, Wright-Patterson AFB, OH 45433
1	AF Flight Dynamics Lab, Wright-Patterson AFB, OH 45433
1	ASD, Wright-Patterson AFB, OH 45433
	SAMSO, AFUOP, Los Angeles, CA 90045
1	(SMQ)
1	(SMT)
1	(SMQH)
1	(SMQNM)/LtCol J. Cahoon
1	ADTC (PGU), Eglin AFB, FL 32542
1	AFFTC, Edwards AFB, CA 93523
1	RADC (EMEAM), Griffiss AFB, NY 13442
1	AFRPL, Edwards AFB, CA 93523
	KIRTLAND AFB ORGANIZATIONS
1	AFSWC (SWEH), Kirtland AFB, NMex 87117
1	AFSWC (SWT), Kirtland AFB, NM 87117

DISTRIBUTION (cont'd)

No. cys.

AFWL, Kirtland AFB, NMex 87117

12 (WLIL)

1 (WLAW)

1 (WLD)

12 (WLDC-I)

1 (WLDM)

1 (WLRA)

1 (WLRE)

1 (WLRP)

OTHER AIR FORCE AGENCIES

Dir, USAF Proj RAND, Via: AFLO, The Rand Corp, 1700 Main Street, Santa Monica, CA 90401

1 (Dr. H. Brode)

1 (Dr. C.C. Mow)

1 Hq OAR (RROS), 1400 Wilson Blvd, Arlington, VA 22209

1 AFOSR, 1400 Wilson, Arlington, VA 22209

1 AFCRL, L.G. Hanscom Fld, Bedford, MS 01731

1 FTD (TD-PTN), Wright-Patterson AFB, OH 45433

ARMY ACTIVITIES

1 Comdg Off, Ballistic Rsch Lab, Aberdeen Proving Ground, MD 21005

1 Comdg Off, Picatinny Arsenal, Dover, NJ 07801

1 Chief of Engineers, DOA, (ENGMC-EM), Wash, DC 20315

1 Chief, R&D, DOA (CRD/P, Sci-Tech Info), Wash, DC 20310

1 Dept of Army, Nike-X Fld Ofc, (AMCPM-NXE-FB), Bell Tele Lab, Inc, Whippany, NJ 07981

1 Comdg Off, USA Rsch Ofc-Durham, Box CM, Duke Sta, Durham, NC 27705

DISTRIBUTION (cont'd)

No. cys.

1 Dir, USA Waterways Exper Sta, P.O. Box 631 (WESRL), Vicksburg, Miss 39181, Mr. Guy Jackson, Mr. Bob Walker, Dr. J. Zelasko, Dr. Don Day

1 USA Engr Div, Ohio River, Corps of Engr, 5851 Mariemont Ave, Cincinnati, OH 45227

1 Dir, Nuclear Cratering Group, USA Corps of Engineers, Lawrence Radiation Laboratories, P.O. Box 808, Livermore, California 94551

NAVY ACTIVITIES

1 Comdg Off and Dir, NCEL, Port Hueneme, CA 93041

1 Comdg Off and Dir, NCEL (Mr. J.R. Allgood), Port Hueneme, CA 93041

1 Ofc Nav Rsch, Dept of the Navy, Wash DC 20360

1 Dir, NRL (Tech Lib), Wash DC 20390

1 Comdg Off and Dir, NEL (Code 4223), San Diego, CA 92152

1 Supt, Nav Postgrad Sch (Code 2124, Tech Rpts), Monterey, CA 93940

1 Comdr, NWC (Code 753), China Lake, CA 93557

1 USNOL (Code 730), White Oak, Silver Sprint, MD 20910

OTHER DOD ACTIVITIES

2 Dir, DASA (SPSS), Wash, DC 20305

20 DDC (TCA), Cameron Station, Alexandria, VA 22314

1 Comdr, Fld Comd, DASA (FCAG3), Sandia Base, NM 87115

1 Dir, ARPA, DOD, Pentagon, Washington, DC 20301

AEC ACTIVITIES

Sandia Corp, Box 5800, Sandia Base, NM 87117 (Info Dist Div)

1 (Dr. M.L. Merritt)

1 (Dr. W. Herrmann)

1 Dir Ofc, UCLRL, P.O. Box 808, Livermore, CA 94551, Dr. T. Cherry, Dr. R.B. Carr, Maj G.P. D'Arcy

DISTRIBUTION (cont'd)

No. cys.

1	Sandia Corp (Tech Lib), P.O. Box 969, Livermore, CA 94550
1	Dir, LASL (Rpt Lib), P.O. Box 1663, Los Alamos, NM 87554
	Courant Inst Math Sci, AEC Comp and Appl Math Cen, 251 Mercer Street, New York, NY 10012
1	(Tech Lib)
1	UCLRL (Tech Info Div), Berkeley, CA 94720
1	Oak Ridge National Lab (Tech Lib), Oak Ridge, Tenn 37831
	OTHER
	Aerospace Corp, San Bernardino Opns, P.O. Box 1308, San Bernardino, CA 92402
1	(Tech Lib)
1	(Dr. M. Watson)
1	(Dr. T. Alley)
1	(Dr. S. Batdorf)
1	Aerospace Corp (Acquis Gp), P.O. Box 95085, Los Angeles, CA 90045
1	Applied Theory (John G. Trulio), 1950 Cotner Avenue, West Los Angeles, CA 90025
1	Atlantic Research Corp, Henry G. Shirley Memorial Highway at Edsall Road, Alexandria, VA 20301
1	Auburn University (D.A. Sawyer), Civil Engineering, Auburn, Alabama 36830
1	Battelle Memorial Inst, 505 King Avenue (William L. Buckel), Columbus, OH 43201
	Bell Telephone Lab, Inc., Whippany Rd, Whippany, NJ 07981
1	(Mr. J.W. Foss)
1	(Mr. C. Fu)
1	(Dr. F. Flaherty)
1	(Tech Library)
1	Boeing Co, 1707 First National Bank Bldg East, 5201 Central NE, Albuquerque, New Mexico 87108

DISTRIBUTION (cont'd)

No. cys.	
1	Burlingame Research Center (A.B. Willoughby, 1811 Trousdale Drive, Burlingame, CA 94011
1	Clemson University (Dr. R.W. Moorman), Dept of Eng Mechanics, Clemson, SC
1	Carnegie Institute of Technology (T.E. Stelson), Schenley Park, Pittsburgh, Pennsylvania 15213
1	Columbia University (R.D. Stoll), Dept of Civil Engineering and Engineering Mechanics, Seeley Mudd Building, New York, NY 10027
1	Detroit Edison Co., 2000 Second Avenue, Detroit, Michigan 48226 (J.H. McCarthy)
1	Duke University (Aleksandar S. Vesic), Dept of Civil Engineering, Durham, North Carolina 27706
1	Engineering Mechanics Laboratory (M.V. Barton), TRW Systems, 1 Space Park, Redondo Beach, CA 90278
1	General American Research Division, General American Transportation Corp, 7449 N. Natchez Ave, Niles, Illinois 60648
1	General Electric Company, Missile and Space Division (L.I. Chasen), P.O. Box 8555, Philadelphia, Pennsylvania 19101
	IITRI, 10 West 35 Street, Chicago, Illinois 60616
1	(Dr. E. Vey)
1	(Library, Dr. E. Sevin)
10	(Dr. Isaac Daniel)
1	Lovelace Foundation for Medical Education and Research (C.S. White), 5200 Gibson Blvd, SE, Albuquerque, NMex 87108
1	Michigan Technological University (G.A. Young) Dept of Civil Engineering, Houghton, Michigan 49931
1	National Engineering Science Company, 711 South Fair Oaks Avenue, Pasadena, CA 91105
1	NASA Scientific & Technical Information Facility (Doc Svcs Dept), P.O. Box 33, College Park, MD 20740
1	North Carolina State University (R.E. Fadum), School of Engineering, Office of the Dean, Box 5518, Raleigh, North Carolina 27607

DISTRIBUTION (cont'd)

1 OSA-OCD, The Pentagon (E.J. Taylor) A/E Services Division, University Projects Branch, Washington, DC 20301

1 Paul Weidlinger, 777 Third Avenue, New York, NY 10017

1 Pennsylvania State University (D. Kummer), 101 Eng. A., University Park, Pennsylvania 16802

Physics International, 2700 Merced, San Leoandro, CA 94557

1 (Dr. C. Godfrey)
1 (Mr. F. Sauer)

1 MIT, 77 Massachusetts Avenue (Dr. R.V. Whitman), Cambridge, MS 02739

1 Polytechnic Institute of Brooklyn, 333 Jay Street, Brooklyn, NY 11201 (R.B.B. Moorman), Head, Dept of Civil Engineering

1 Portland Cement Association (Eivind Hognestad), R&Division, 5420 Old Orchard Road, Skokie, Illinois 60078

1 Princeton University (N.J. Sollenberger), School of Engineering and Applied Science, Princeton, NJ 08540

1 Purdue University (G.A. Leondards/M.B. Scott) School of Civil Engineering, Lafayette, Indiana 47907

1 Rensselaer Polytechnic Institute (E.C.W.A. Geuze), Dept of Civil Engineering, Troy Building, Troy, NY 12180

1 Rice University (A.S. Veletsos), Dept of Civil Engineering, Houston 1, Texas 77001

1 Rutgers University (M.L. Granstrom), University Heights Campus, New Brunswick, NJ 08903

1 Sacramento State College (L.H. Gabriel), 6000 Jay Street, Sacramento, CA 95819

1 San Jose State College (F.J. Agardy), Dept of Civil Engineering, San Jose, CA 95100

1 Shannon and Wilson, Inc. (E.A. Sibley), 1105 N. 38th Street, Seattle, Wash 98103

1 South Dakota School of Mines, Rapid City, South Dakota 57701

1 Southwest Research Institute (R.C. DeHart), Dept of Structural Research, 8500 Culebra Road, San Antonio, TX 78228

1 Stanford Research Institute, Menlo Park, CA 94025

DISTRIBUTION (cont'd)

No. cys.	
1	Dr. E.T. Selig, Dept of Civil Engineering, State University of New York, Buffalo, New York 14214
1	Susquehanna Instruments Company (Mr. B. Granath), Box 399, R.D. 1, Bel Air, Maryland 21014
1	Teledyne Industries (Mrs. Lula H. Layton), Earth Sciences Division, P.O. Box 1650, Library, Pasadena, CA 91109
1	Shock Hydrodynamics, 15010 Ventura Blvd, Sherman Oaks, CA 91403
1	Systems, Science, and Software, P.O. Box 1620, La Jolla, CA 92037
1	Thomas G. Morrison, Consulting Engineer, 881 Apple Tree Lane, Highland Park, Illinois 60035
1	Tulane University (W.E. Blessey), Dept of Civil Engineering, New Orleans, Louisiana 70112
1	The University of Arizona (C.H. Peyton), College of Engineering, Tucson, Arizona 85721
1	University of California (C. Martin Duke) Dept of Civil Engineering, Los Angeles, CA 90024
1	University of Colorado (G.K. Vetter), School of Architecture, Boulder, CO 80302
1	University of Dayton (S.J. Ryckman), Dept of Civil Engineering and Engineering Mechanics), Dayton, OH 45409
1	University of Denver (Dr. R. Szilard), Senior Engineer, Denver Resch Institute, University Park, Denver, CO 80210
1	University of Florida (J.A. Samuel), Dept of Mechanical Engineering, Gainesville, FL 32601
1	University of Illinois, 1114 Civ Engr Bldg (Civ Engr Dept/ Dr. N.M. Newmark, Head), Urbana, Illinois 61801
1	University of Massachusetts, Head, Civ Engr Dept, Amherst, Mass 01002
1	University of Michigan (Proj K.C. Johnston), Dept of Civil Engineering, Ann Arbor, Michigan 48104
1	University of Missouri (Adrain Pauw), College of Engineering, Dept of Civil Engineering, Columbia, Missouri 65201

DISTRIBUTION (cont'd)

No. cys.	
1	The University of New Mexico (College of Engineering), Albuquerque, New Mexico 87106
1	UNM, CERF (Dr. Zwoyer, Dr. R. Shunk), Box 188, University Station, Albuquerque, New Mexico 87103
	TRW Systems, One Space Park, Redondo Beach, CA 90278
1	(Mr. F. Peiper - 427/710)
1	(Mr. N. Lipner - 73/3049)
1	(Dr. J. Merritt - 427/702)
1	(Mr. M. Anthony - 427/710)
1	(Dr. J. Carpenter - 73/3049)
1	(Dr. F. Safford - 73/3049)
1	University of Notre Dame (B.B. Schimming), Dept of Civil Engineering, Notre Dame, Indiana 46556
1	University of Rhode Island (Vito A. Nacci) Dept of Civil Engineering, Kingston, Rhode Island 02881
1	University of Washington (Bill Miller) Dept of Civil Engineering, 307 More Hall Seattle, Washington 98105
1	West Virginia University (J.H. Schaub) Dept of Civil Engineering, Morgantown, West Virginia 26506
1	Worcester Polytechnic Institute (Carl Koontz), Dept of Civil Engineering, Worcester, MS 01600
1	US Dept of Commerce, Bureau of Public Roads, (Mr. F.J. Tamanini, Dept Chief), Structures and Applied Mechanics Division, Washington, DC 20235
1	West Virginia University (Dr. E.F. Byars), Dept of Theoretical and Applied Mechanics, Morgantown, West Virginia 26506
1	University of California (Dr. E.L. Wilson), Structural Engineering Laboratory, Berkeley, California 94720
1	Official Record Copy (Dr. Henry F. Cooper, Jr.,/WLDC)

UNCLASSIFIED

Security Classification

DOCUMENT CONTROL DATA - R & D

(Security classification of title, body of abstract and indexing annotation must be entered when the overall report is classified)

1. ORIGINATING ACTIVITY *(Corporate author)*
IIT Research Institute
Technology Center
Chicago, Illinois 60616

2a. REPORT SECURITY CLASSIFICATION
UNCLASSIFIED

2b. GROUP

3. REPORT TITLE

PHOTOELASTIC STUDY OF WAVE PROPAGATION IN LAYERED MEDIA

4. DESCRIPTIVE NOTES *(Type of report and inclusive dates)*
31 May 1967 to 30 September 1968

5. AUTHOR(S) *(First name, middle initial, last name)*
I. M. Daniel

6. REPORT DATE
July 1969

7a. TOTAL NO. OF PAGES
204

7b. NO. OF REFS
16

8a. CONTRACT OR GRANT NO. F29601-67-C-0079

b. PROJECT NO. 5710

c. Subtask: SB144

d. Program Element 61102H

9a. ORIGINATOR'S REPORT NUMBER(S)
AFWL-TR-68-153

9b. OTHER REPORT NO(S) *(Any other numbers that may be assigned this report)*
Contractor's report no. D6038

10. DISTRIBUTION STATEMENT This document is subject to special export controls and each transmittal to foreign governments or foreign nationals may be made only with prior approval of AFWL (WLDC), Kirtland AFB, New Mexico 87117.

11. SUPPLEMENTARY NOTES

12. SPONSORING MILITARY ACTIVITY
AFWL (WLDC)
Kirtland AFB, New Mexico 87117

13. ABSTRACT (Distribution Limitation Statement No. 2)

This program studies photoelastically the transmitted, reflected and refracted waves resulting when a wave generated by explosive or air-shock loading reaches the plane interface between two birefringent materials of different impedances. Dynamic photoelastic and photoviscoelastic methods complemented by moiré techniques were used. A special explosive loading system using PETN (Pentaerythritol Tetranitrate) was developed. A shock tube was used for air-shock loading. The photoelastic and moiré fringe patterns in the explosively loaded models were photographed with a Cranz-Schardin multiple spark camera operating at a rate of 200,000 frames per second. A Fastax camera was used in recording similar patterns in the air-shock loaded models. A class of birefringent model materials with controllable impedance was developed. All models consisted of two layers of birefringent materials having an impedance ratio of 2:1. The models were loaded by a buried explosive source in the low-impedance medium, a buried explosive source in the high-impedance medium. The distance of the point of loading from the interface was varied. Propagation and attenuation characteristics of incident, reflected and refracted waves were studied. The formation of headwaves at the interface was clearly evident in one case. Stress determinations were made in some instances using photoelastic and moiré data.

DD FORM 1 NOV 65 1473 REPLACES DD FORM 1473, 1 JAN 64, WHICH IS OBSOLETE FOR ARMY USE.

UNCLASSIFIED

Security Classification

14. KEY WORDS	LINK A		LINK B		LINK C	
	ROLE	WT	ROLE	WT	ROLE	WT
Wave propagation						
Photoelasticity						
Layered media						
Airblast induced ground motions						
Ground motions						
Elasticity						